POLISH ACADEMY OF SCIENCES
ELECTRICAL ENGINEERING COMMITTEE

ARCHIVES OF ELECTRICAL ENGINEERING

Volume 66(259) • 1/2017

QUARTERLY JOURNAL

www.aee.put.poznan.pl
www.degruyter.com/view/j/aee

POZNAŃ 2017

www.aee.put.poznan.pl
www.degruyter.com/view/j/aee

ISSN 1427-4221
eISSN 2300-2506

Edition co-sponsored by
Polish Academy of Sciences

EDITORIAL OFFICE

Archives of Electrical Engineering
Piotrowo 3A (room: 612X)
60-965 Poznań, Poland
tel.: +48 616652636, *fax*: +48 616652381
e-mail: aee@put.poznan.pl

Centrum Poligrafii Sp. z o.o.
ul. Łopuszańska 53
02-232 Warszawa

Printed in Poland

Contents

ARCHIVES OF ELECTRICAL ENGINEERING VOL. 66(1), pp. 5-16 (2017)

DOI 10.1515/aee-2017-0001

Quad channel software defined receiver for passive radar application

TAMÁS PETŐ, RUDOLF SELLER

Department of Broadband Infocommunication and Electromagnetic Theory
Budapest University of Technology and Economics
Egry József 18, 1111 Budapest, Hungary
e-mail: peto@hvt.bme.hu, seller@hvt.bme.hu

(Received: 08.12.2015, revised: 19.07.2016)

Abstract: In recent times the growing utilization of the electromagnetic environment brings the passive radar researches more and more to the fore. For the utilization of the wide range of illuminators of opportunity the application of wideband radio receivers is required. At the same time the multichannel receiver structure has also critical importance in target direction finding and interference suppression. This paper presents the development of a multichannel software defined receiver specifically for passive radar applications. One of the relevant feature of the developed receiver platform is its up-to-date SoC (System on hip) based structure, which greatly enhance the integration and signal processing capacity of the system, all while keeping the costs low. The software defined operation of the discussed receiver system is demonstrated with using DVB-T (Digital Video Broadcast – Terrestrial) signal as illuminator of opportunity. During this demonstration the multichannel capabilities of the realized system are also tested with real data using direction finding and beamforming algorithms.

Key words: DPIS, multichannel receiver, passive radar, PCL, SDR

1. Introduction

Passive radars take advantage of already existing radio sources to detect targets. Researches have investigated the potential illuminators of opportunity such as the FM radio, GSM, UMTS, Wi-Fi, WiMAX, DAB, DVB-T, DVB-S signals. The basic proof of concept has been verified extensively so far for the different illuminator signals [4-6]. Software defined radio platforms are commonly used in a passive radar demonstrator system due to the flexibility of such receiver structures [1-3, 10]. The application of multiple IOPs (Illuminator of Opportunity) located in different bands at the same time is also a field of interest in high range resolution and imaging application [10]. However these modular systems are very high-priced and inhibit the dissemination of passive radar technology. Low cost software defined receivers that are currently available in wide range are also investigated for passive radar application, how-

ever the high dynamic range and precise multichannel operation is not achievable with these units.

One of the most significant limitation factor of passive radars is the direct path interference [6].The suppression of the strong direct path reference signal in the surveillance channel is essential in order to achieve a reasonable signal-to-noise ratio in large bistatic target distances. One of the most straightforward solution for this issue is the use of spatial filtering with beamforming algorithms [7-9]. FM radio based beamforming passive radars have been developed successfully in recent times [8].

In this paper we describe our developed multichannel passive radar receiver structure which is based on SoC (System on Chip) architecture. Our approach not only reduces the cost of the system, but increases the system integration and provides an up-to-date high performance platform for passive radar signal processing. The demonstration of basic spatial filtering implementation on the designed system is also presented. The design considerations (Section 2), the structure (Section 3) and the results (Section 4) of the developed hardware platform are described in detail. The effective operation of the platform is tested via field measurements.

2. Design considerations

The required parameters of the receiver system are fundamentally dependent on the properties of the used illuminator signals. The receiver must be able to cover sufficiently high dynamic range to the simultaneous reception of the high power direct path signal and the weak target echoes. At the same time the bandwidth of the used reference signal is also significant to achieve fine range resolution. For a given illuminator signal the achievable bistatic range resolution can be calculated using Eq. (1). In Eq. (1) c stands for the speed of light, B denotes the bandwidth of the signal and β denotes the bistatic angle.

$$\Delta_r = \frac{c}{2B\cos\left(\frac{\beta}{2}\right)}. \tag{1}$$

Table 1 summarizes the main parameters of the most common illuminators of opportunity. To determine a real requirement for the dynamic range of the receiver system, the power level of the direct path signal has been calculated for the different applicable illuminators using Eq. (2) with the baseline distance of L = 10 km. (Antennas with 0 dBi gain are assumed both on the transmitter and the receiver side.)

$$P_{\text{direct}} = \frac{\left(P_t\lambda^2\right)}{(4\pi)^2 L^2}, \tag{2}$$

where P_t is the power of the transmitter, λ denotes the wavelength of the IOP and L denotes the distance from the reference transmitter. In order not to lose sensitivity because of digita-

lization, the quantization noise of the ADC (Analog Digital Converter) must be lower than the thermal noise floor for the given illuminator bandwidth plus the external noise. The thermal noise floors have been calculated with Eq. (3).

$$P_n = kT_sB, \tag{3}$$

where k is the Boltzmann constant, T_s=300 K is the system temperature and B denotes the bandwidth of the signal. The power of the external noise that is originating from man-made or natural sources can be estimated using the ITU-R [P.372-8] recommendation. This recommendation is intended to use for system performance determinations and design. The external noise figure denoted with F_a expresses the power of the external noise above thermal noise with reference temperature of 300 K (our assumed system temperature). For frequencies bellow 1 GHz the values indicated in Table 1 belong to the curve of the man-made noise in business environment. In frequencies above ~1 GHz noise from individual sources such as galactic noise, atmospheric gasses, etc. have usually less noise temperature than 300 K (Expect the noise of the Sun).

Table 1. Relevant parameters of the most common illuminators

Illuminator	**EIRP**	**Frequency**	**Bandwidth**	**Received power (L = 10 km)**	**Thermal noise floor**	**External noise factor**
FM	100 kW	~100 MHz	~75 kHz	−12 dBm	−125 dBm	22 dB
GSM	100 W	900, 1800 MHz	200 kHz	−61, −67 dBm	−120 dBm	8 dB, < 0
UMTS	100 W-1 kW	2100 MHz	3.84 MHz	−59 dBm	−108 dBm	< 0
DAB	10 kW	~220 MHz	1.536 MHz	−29 dBm	−112 dBm	13 dB
DVB-T	1-100 kW	~600 MHz	7.61 MHz	−28 dBm	−105 dBm	9 dB
DVB-S	100-1000 kW	10.7-12.7 GHz	27-30 MHz	–	−99 dBm	< 0

Having examined the parameters of different illuminators the analog digital converter of the receiver system must have at least ~70 dB dynamic range in order to reduce SNR (Signal-to-Noise Ratio) degradation originating from the quantization noise. Thus for the digital conversation we are using 12 bit wide ADC with 100 MHz sampling frequency providing slightly more than 70 dB SNR. The effective number of bits and thus the SNR for illuminator signals with small bandwidth can be further increased with performing integration in the decimation stage.

Nowadays several research groups deal with using the DVB-T signal in passive radars. From among the potentially applicable illuminators of opportunity, the DVB-T signal not only has beneficial correlation properties but also has relatively wide 7.61 MHz bandwidth and high power transmitters. Thus it was expedient to test the capabilities of the receiver with this type of illuminator. The demonstration results are presented in Section 4.

3. Receiver structure

The block diagram of the designed receiver platform is illustrated in Fig. 1 and Fig. 2.

3.1. RF front-end

RF signals coming from the antenna system are first received by the front-end unit. This unit is responsible for down-mixing the RF signal to the intermediate frequency which can be processed further by the digital data acquisition card. Fig. 1 shows the detailed architecture of the RF signal path.

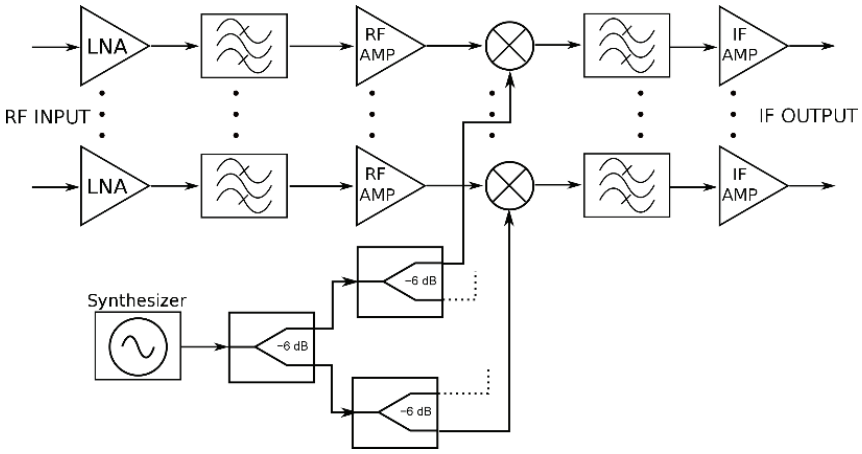

Fig. 1. Block diagram of the multichannel coherent RF receiver

The first stage of the RF front-end unit is a low noise amplifier which is responsible for achieving a low noise figure for the overall system. After the first stage the signal is filtered by an optional band pass filter. Application of the RF filter can improve the out-of-band interference tolerance capability of the system, but also limits the available illuminators for the receiver. For the demonstration presented in Section 4 a filter designed to operate in the DVB-T band has been utilized (460 MHz – 800 MHz). In order to maintain the proper signal level in the entire RF chain a second RF amplifier has been placed before the signal is mixed down to the IF (Intermediate Frequency) band. It is also important that in passive radar scenarios the reference signal often has very high power at the receiver side, thus the system must also handle the these signals. Beside this the amplifier stage must have high linearity to avoid the appearance of the undesired harmonic components in the spectrum. Thus an amplifier with high power handling capability (P_{sat}) and IP3 (third order intercept point) has been used. After the second RF amplifier the RF signal is downmixed to the IF band (38 MHz). In order to implement coherent RF signal reception all the mixers in the system have to use the sample local oscillator signal, thus the RF power divider is used to distribute the local oscillator signal for the mixers of the four individual receiver channels. In the last stage the IF signal is filtered to suppress the RF and local signal leakage. The IF filter is also used as the anti-aliasing filter

for the later digitalization step. It must be emphasized that all the components of the receiver system are wideband RF integrated circuits to ensure wideband software defined operation. The critical amplifier stages are MMICs (Monolithic Microwave Integrated Circuit) and the RF power divider is implemented as a resistive splitter.

3.2. Digital Data Acquisition

Fig. 2 highlights the structure of the digital data acquisition unit of the system.

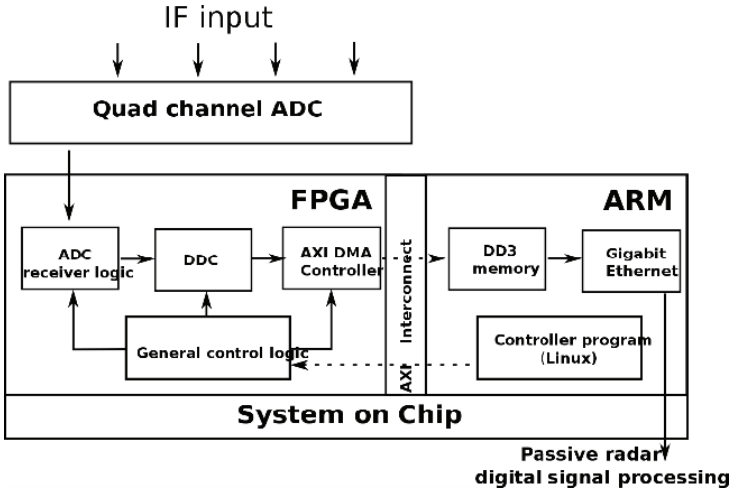

Fig. 2. Block diagram of the multichannel passive radar receiver platform

After the RF stage the IF signals are digitalized by the ADC which has serial data output. At this point of the system the data rate reach 100 MHz 12 bit 4 = 4.8 Gbit/s. This high speed data stream is split into 8 different lines which greatly facilitates the transfer of the raw data. The transferred signals then arrive to the SoC (System on Chip). A picture from the receiver platform can be seen in Fig. 3.

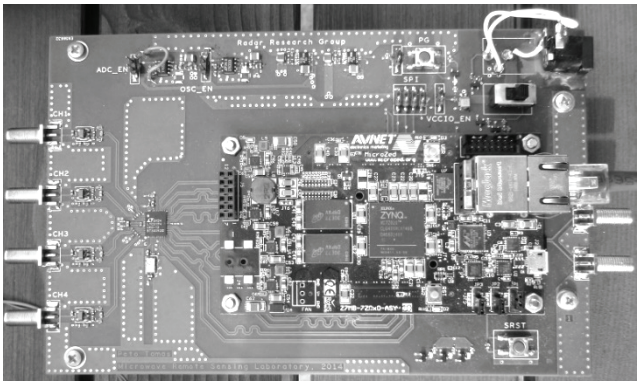

Fig. 3. Picture of the high speed digital data acquisition board

We are using the Xilinx Zynq 7020 SoC in the receiver platform. Application of SoC provides state of the art solution for mixed signal processing demands. The FPGA integrated into the chip is able to perform the critical signal processing tasks while the dual core ARM processor can handle effectively the algorithmic problems. Therefore, it is advisable to implement real time signal processing tasks with high data throughput in the FPGA logic. Accordingly, we have implemented the ADC receiver logic inside the PL (Programmable Logic). This logic is mainly responsible for the reception of the high speed raw data transferred by the ADC. The received digital samples are then forwarded to the DDC (Digital Down-Converter) circuit. The DDC circuit performs down-mixing to baseband, filtering, and decimation of the processed signal. Decimation ratio is determined according to the bandwidth of the currently used reference signal. During the presented experimental measurement, we used 12 as a decimation factor for the processing of the DVB-T signal which has 7.61 MHz bandwidth. From the output of the DDC module the baseband IQ complex samples are forwarded to the DMA (Direct Memory Access) controller module. The main task of this logic is to move the data from the FPGA to the DDR3 memory used by the ARM processors with CPU offload. The Linux system running on the ARM processors transfers the received data through Gigabit Ethernet to a computer which performs the passive radar signal processing and detection algorithms. The flexibility and signal processing capability of the system relies on the effective information exchange between the two part of the system (PL-programmable logic and PS-processing system). The operating system running on the PS manages the protocols needed to communicate with the outside world, while it is also able to reach the internal systems and registers of the PL directly. Because of this construction the passive radar receiver system can effectively change between the used reference sources by reconfiguring the internal parameters of the software defined radio blocks inside the system even during remote operation.

4. Receiver demonstration results

The wideband multichannel operation of the receiver has been tested with DVB-T transmission in the UHF band. To perform an adequate test for the beamforming capabilities, the effectiveness of the interference suppression has been analyzed as it is real demand in passive radar applications. The results of these measurement along with results of the DOA (Direction of Arrival) algorithms are presented.

4.1. Calibration procedure

Amplitude and phase response calibration of a multichannel receiver is essential for the proper and correct application of the beamforming techniques. In order to carry out relevant measurements, the receiver unit has been calibrated. This calibration procedure must be performed over the full frequency range of interest. For the presented demonstration the relative amplitude and phase responses of the individual channels have been recorded from 630 MHz to 638 MHz in the band of the used DVB-T transmission.

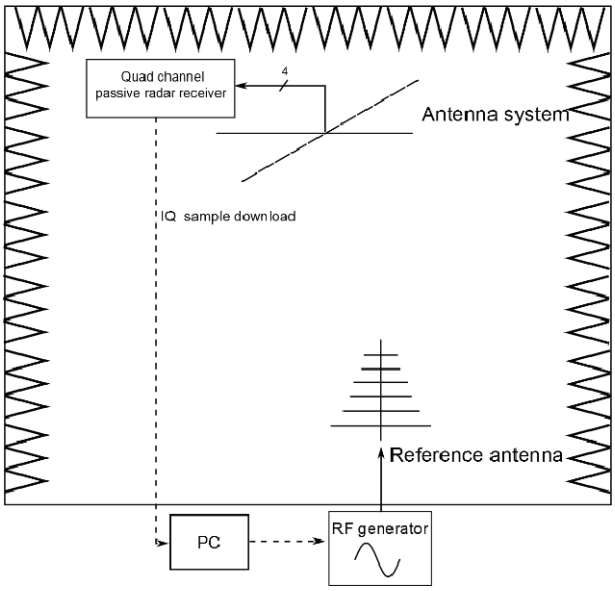

Fig. 4. Calibration measurement setup

The calibration has been performed in an anechoic chamber. The setup of this measurement is illustrated on Fig. 4. Both the RF generator and the receiver unit were, controlled from a PC. The RF CW (Continuous Wave) excitation signal had been set first, then the receiver downloaded sufficient IQ samples for the latter offline processing. For the reception of the RF signals we used an equidistant linear antenna array consisting of 4 fractal patch antenna elements with 0.52 wavelength (634 MHz) distance between elements. As a reference antenna for the transmission of the RF calibration signal a wideband log-periodic antenna was used. The relative amplitude and phase difference between the channels was finally determined in frequency domain at the currently measured frequency. It has to be noted that in this calibration setup both the RF multichannel receiver chain and the antenna array were calibrated. While measuring the calibration matrix, the main direction of the antenna system was rotated precisely in the direction of the reference antenna. The arrangement of the measurement can be seen in Fig. 5.

Since the effective interference cancelation is crucial in passive radars applications, the performance of the calibration was determined with analyzing the suppression capabilities of the system. This has been carried out with the calculation of the averaged power before and after performing a beam space processing algorithm.

The success of the calibration has been tested first. During the test measurement the antenna system was rotated from its original calibration direction to a random direction to ensure more realistic scenario. The RF generator was programed to transmit a priori known wideband excitation signal in the same setup as in the calibration procedure. The IQ samples were recorded and then after correcting the samples the DOA of the test signal has been determined. For the DOA estimation Capon's method has been applied as it has high resolution. Eq. (4) describes the used Capon method.

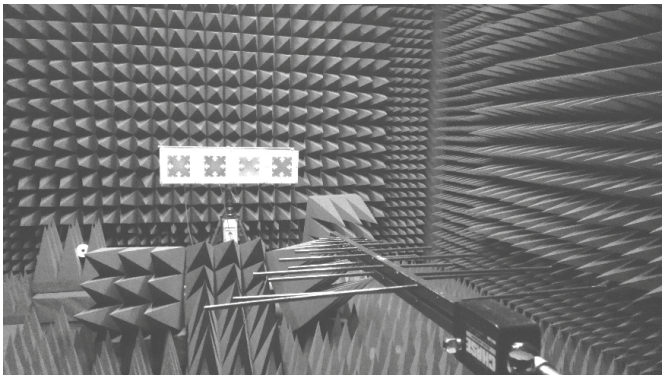

Fig. 5. Calibration measurement taken in the anechoic chamber

$$P(\Theta) = \frac{1}{\boldsymbol{s}(\boldsymbol{\Theta})^H \boldsymbol{R}_{xx}^{-1} \boldsymbol{s}(\boldsymbol{\Theta})}, \tag{4}$$

where $\boldsymbol{s}(\boldsymbol{\Theta})$ is the steering vector and $\boldsymbol{R}_{xx}$ is the spatial correlation matrix. Fig. 6 shows the calculated results.

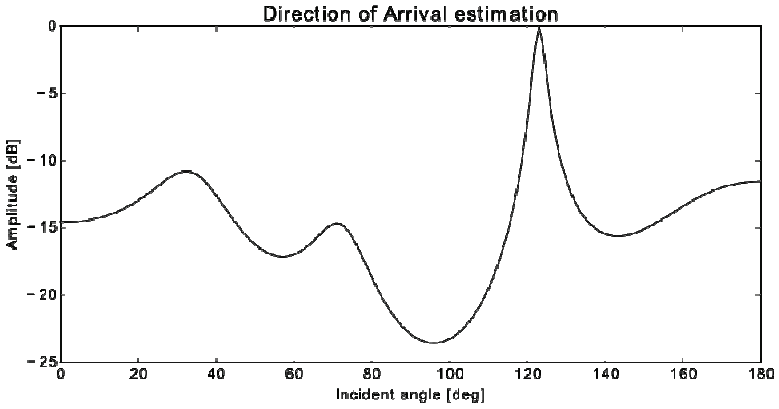

Fig. 6. Result of the DOA measurement taken in the anechoic chamber

From the result, the DOA of the test signal has been determined to 125 deg. On the basis of the knowledge on the incident angle of the transmitted test signal, the beampattern illustrated in Fig. 7 has been synthesized. The coefficient vector of the beamformer was calculated using the fixed MSIR (Maximum Signal to Interference Ratio) algorithm according to Eq. (5) which was configured to place wideband null in the direction of the interference signal.

$$\boldsymbol{w}^H = \boldsymbol{u}^H \boldsymbol{A}^{-1}. \tag{5}$$

In Eq. (5) $\boldsymbol{w}$ denotes the calculated coefficient vector of the beamformer, $\boldsymbol{u}$ means the constraint vector and $\boldsymbol{A}$ is the array response matrix.

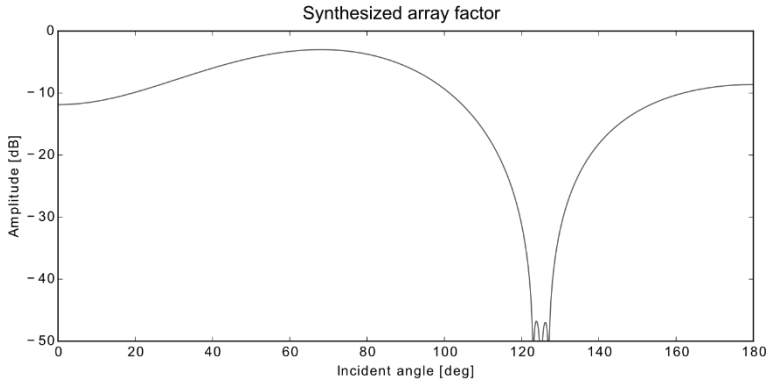

Fig. 7. Array factor of the synthesized radiation pattern for testing interference suppression in anechoic chamber

Finally, the cross correlation functions have been calculated to determine the power level of the known excitation signal. Fig. 8 shows the obtained results. The blue curve represents the autocorrelation function of the first receiver channel, while the red curve represents the cross-correlation function of the same receiver channel and the beamspace processed channel. It can be seen that the power level of the excitation signal has been effectively suppressed with 30 dB.

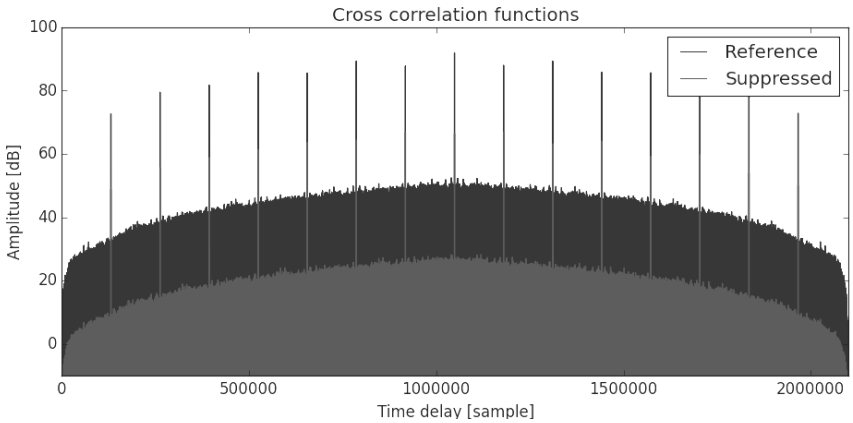

Fig. 8. Difference between cross correlation functions shows the power level reduction in the received signal

4.2. Field measurements

We have measured the beamforming capabilities of the system also in real environment using DVB-T reference signal. During the course of the experimental measurement we have first determined the exact positions of a transmitter tower applying Capon's direction of

arrival algorithm and then we applied interference suppression technique in the same way as it was used in the calibration test.

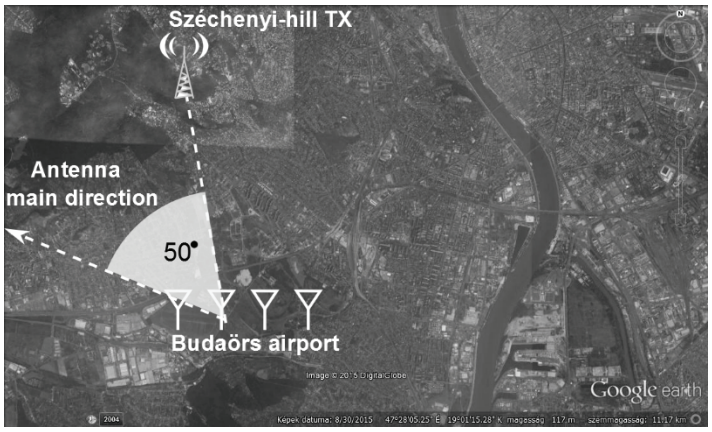

Fig. 9. Measurement scenario

For the measurement we used the signals of a DVB-T transmitter operating in Budapest. The transmitter tower is located at the Széchenyi-hill. The geometrical layout of the transmitters and the receiver system is depicted in Fig. 9. After the completion of the measurement, the downloaded IQ complex data was processed offline.

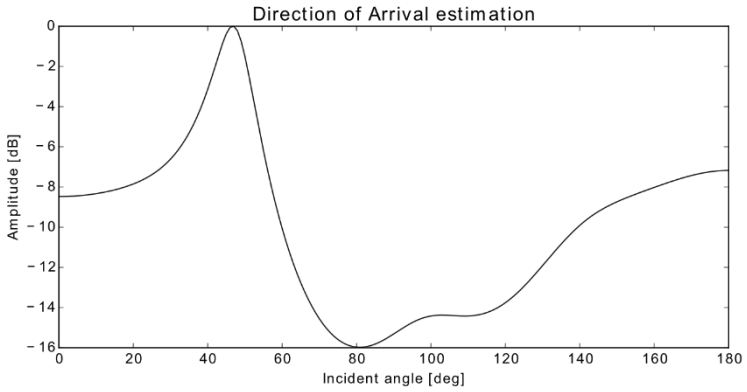

Fig. 10. Measured DOA of the DVB-T transmitter tower located at the Széchenyi-hill with Capon's method

Fig. 10 shows the results of the direction of arrival algorithm. Where, the function of the DOA estimation has its maximum at 48 deg. Based on the preliminary calculated transmitter direction we can conclude that the DOA of the DVB-T transmitter tower could be determined precisely. The results of the direction of arrival algorithms match with the expected results. After having measured the DOA of the reference signal, the antenna channels have been

processed in order to produce the surveillance channel for the passive radar. The synthesized beampattern can be seen in Fig. 11. Nulls are placed in the direction of the DVB-T transmitter.

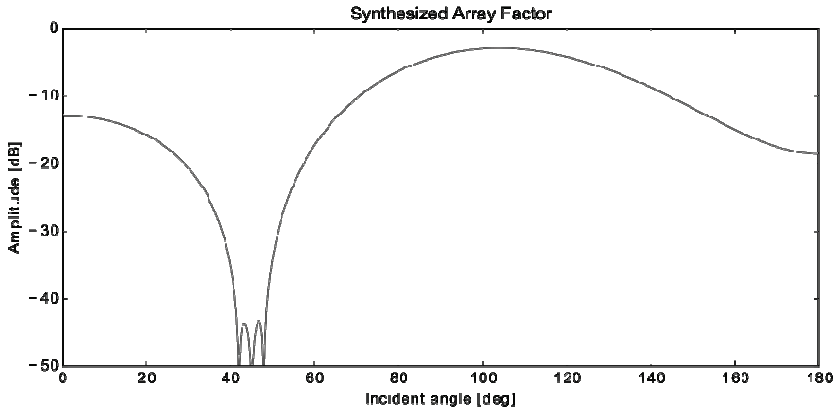

Fig. 11. Synthesized surveillance channel beampattern for the experimental measurement

Correlation functions are calculated finally to estimate the achieved DPIS (Direct Path Interference Suppression). The results are shown in Fig. 12. The reference curve shows the autocorrelation function of the first receiver channel, while the other curve represents the surveillance channel. Having examined the measurement results, 21 dB suppression has been achieved.

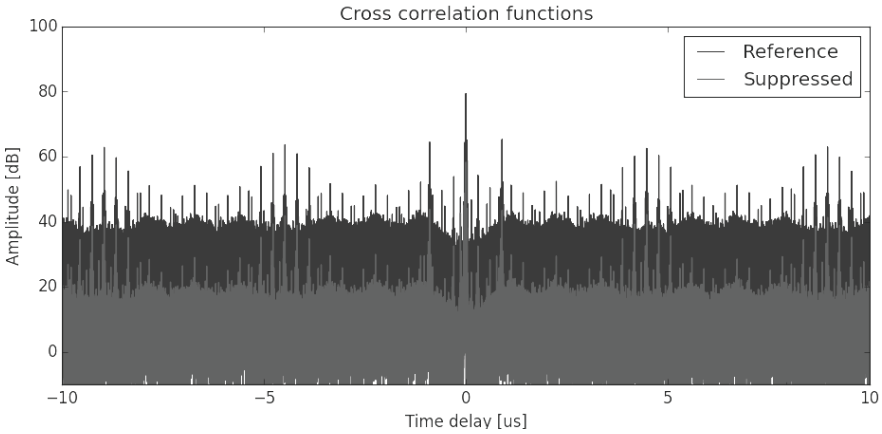

Fig. 12. Estimation of the achieved DPIS in the field measurement

Based on the presented measurement results it can be concluded that the developed multi-channel receiver platform performs properly as expected.

5. Conclusions

In order to widespread the passive radar technology it is necessary to develop such hardware supported systems that target the inherent advantages and difficulties of the passive radars. The saturation of the electromagnetic environment provides great opportunity to passive radars, however special receiver platforms are required. In this paper we presented the development of a passive radar receiver platform which applies modern system on chip architecture with high integrity, flexibility and signal processing capability. The operation of the receiver structure has been tested with the DVB-T signal. The performance of the multichannel operation including the DOA estimation, and the DPIS have been demonstrated. Further researches can be done to effectively implement high performance passive radar signal processsing algorithms utilizing the DSP capabilities of the SoC.

Acknowledgements
This work has been supported in the frame of the project "Multichannel passive ISAR imaging for military applications (MAPIS) No. B-1359 IAP2 GP" of the European Defence Agency.

References

[1] Jamil K., Alam M., M. Hadi A., Alhekail Z.O., *A multi-band multi-beam software-defined passive radar part I: System design*, IET International Conference on Radar Systems, Glasgow, United Kingdom, pp. 1-4 (2012).
[2] Alam M., Jamil K., Alhekail Z.O., Al-Humaidi S., *A multi-band multi-beam software-defined passive radar part II: Signal processing,* IET International Conference on Radar Systems, Glasgow, United Kingdom, pp. 1-5 (2012).
[3] Heunis S., Paichard Y., Inggs M., *Passive Radar using a Software-Defined Radio Platform and Opensource Software Tools,* IEEE Radar Conference 2011, Kansas City, United States of America, pp. 879-884 (2011).
[4] Wang Q., Hou C., Lu Y., *An Experimental Study of WiMAX-Based Passive Radar,* IEEE Transactions on Microwave Theory and Techniques, vol.58, no. 12, pp. 3502-3510 (2010).
[5] Tan D.K.P., Sun H., Lu Y., Liu W., *Feasibility analysis of GSM signal for passive radar,* IEEE Radar Conference 2003, Huntsville, United States of America, pp. 425-430 (2003).
[6] Peto T., Dudás L., Seller R., Péter Renner, *Digital television broadcast-based passive radar research and development*, 20th International Conference on Microwaves, Radar, and Wireless Communication (MIKON), Gdansk, Poland, pp. 1-4 (2014).
[7] Tao R., Wu H.Z., Shan T., *Direct-path suppression by spatial filtering in digital television terrestrial broadcasting-based passive radar*, IET Radar, Sonar & Navigation, vol. 4, no. 6, pp. 791-805 (2010).
[8] Malanowski M., Kulpa K., *Digital beamforming for Passive Coherent Location radar*, IEEE Radar Conference 2008, Rome, Italy pp. 1-6 (2008).
[9] Moscardini C., Conti M., Berizzi F et al., *Spatial Adaptive Processing for Passive Bistatic Radar*, IEEE Radar Conference 2014, Cincinnati, United States of America, pp. 1061-1066 (2014).
[10] Conti M., Berizzi F., Martorella M. et al, *High range resolution multichannel DVB-T passive radar*, IEEE, vol. 27, no. 10, pp. 37-42 (2012).

ARCHIVES OF ELECTRICAL ENGINEERING VOL. 66(1), pp. 17-28 (2017)

DOI 10.1515/aee-2017-0002

A new cast-resin transformer thermal model based on recurrent neural networks

DAVOOD AZIZIAN[1], MEHDI BIGDELI[2]

[1]*Department of Electrical Engineering, Abhar Branch, Islamic Azad University, Abhar, Iran*
e-mail: d.azizian@abhariau.ac.ir
tel.: +98 9122418353

[2]*Department of Electrical Engineering, Zanjan Branch, Islamic Azad University, Zanjan, Iran*
e-mail: mehdi.bigdeli@iauz.ac.ir

(Received: 06.03.2016, revised: 19.07.2016)

Abstract: Thermal modeling in the transient condition is very important for cast-resin dry-type transformers. In the present research, two novel dynamic thermal models have been introduced for the cast-resin dry-type transformer. These models are based on two artificial neural networks: the Elman recurrent networks (ELRN) and the nonlinear auto-regressive model process with exogenous input (NARX). Using the experimental data, the introduced neural network thermal models have been trained. By selecting a typical transformer, the trained thermal models are validated using additional experimental results and the traditional thermal models. It is shown that the introduced neural network based thermal models have a good performance in temperature prediction of the winding and the cooling air in the cast-resin dry-type transformer. The introduced thermal models are more accurate for the temperature analysis of this transformer and they will be trained easily. Finally, the trained and validated thermal models are employed to evaluate the life-time and the reliability of a typical cast-resin dry-type transformer.

Key words: cast-resin transformer, dynamics, recurrent neural networks, thermal modeling

1. Introduction

In many critical applications such as military and residential areas, transformers must be protected against explosion. Thus, nonflammable insulations (such as Askarel and Epoxy Resins) have been offered to be used in transformers. As the usage of Askarel has been phased out, epoxy resins have proven themselves and are widely used in transformers. Therefore, a cast-resin dry-type transformer [1, 2] has been developed as a nonflammable transformer. While a dry-type transformer lacks any cooling fluid and the life-time of insulating system depends on temperature, the thermal behaviour analysis of the dry-type transformer is crucially important.

Previously, the steady-state thermal modeling for different geometries of the dry-type transformer was introduced in [2-8]. Additionally, it is essential to study the transient thermal behaviour and the life-time of the dry-type transformers; thus, it is helpful to introduce some applicable dynamic models for this purpose. Different life-time and transient thermal models have been presented for oil-immersed transformers [9-13]. There are few researches on dynamic thermal modeling of the dry-type transformers [14-17]. References [14, 15] introduce simplified RC models for the dynamic thermal modeling of the dry-type transformers. Different heuristic algorithms have been employed to estimate the parameters of these RC thermal models. As it has been shown in [15], the simplified models are accurate enough for the thermal modeling of the dry-type transformer. Additionally, some detailed RC thermal models have been presented in [16, 17] for the thermal modeling of the cast-resin dry-type transformer. The RC models that are based on the physical structure of the transformer are accurate enough to analyse the dynamic thermal behaviour of the dry-type transformers. But the accurate thermal modeling of the transformer, especially when the current variation is high, cannot be achieved. Thus, it is needed to introduce some compatible methods to model the dynamic thermal behaviour of the dry-type transformer. Nowadays artificial neural networks (ANN) are widely used for temperature prediction in different problems and phenomena [18-24]. Several ANN based dynamic thermal models have been presented for oil-immersed transformers [21-24].

Consequently, novel dynamic thermal models based on the Elman recurrent networks (ELRN) and the nonlinear autoregressive model process with exogenous input (NARX) for the thermal modeling and temperature prediction of the cast-resin dry-type transformers are introduced in this paper. Employing the measured temperatures, the ANN models have been trained and the predicted temperatures are validated against experimental results, the RC thermal models [15-17] and the classic IEC method [25]. Afterwards, using the trained ANN models, the life-time and reliability of the cast-resin transformer are studied. It is shown that, the introduced ANN models have better efficiency in the temperature prediction of the cast-resin dry-type transformer rather than other traditional methods.

Main contributions and novelties of this paper can be listed as following:

- New and simple ANN based thermal models are introduced for the dynamic thermal modeling of the cast-resin dry-type transformer.
- The results of the introduced models are compared to experimental results, the RC based models, IEC equations and to each other.
- Using the predicted and validated ANN models, the life-time and reliability of the cast-resin transformer have been studied.

2. Cast-resin dry-type transformer thermal models

2.1. IEC thermal equations

Practically, there are few conventional models that are employed for temperature prediction of dry-type transformers [25, 26]. In these traditional models, if the required experimental

parameters are not accessible then the models cannot be employed. Here, the traditional thermal equations that have been presented by the IEC standard [25] are discussed. It is known that the dynamic behaviour of temperature is similar to a simple exponential equation. Thus, by determination of the initial and the final values of this exponential equation, the winding's temperature rise (θ_w) can be governed at each time (t) as given in (1).

$$\theta_w(t) = \theta_{w0} + \theta_{w\infty}\left(1 - e^{\frac{-t}{\tau}}\right), \tag{1}$$

where: τ is the thermal time-constant of a winding, θ_{w0} is the initial ($t = 0$) winding temperature rise at the beginning of the time period, and $\theta_{w\infty}$ is the final (steady-state) winding temperature rise that can be expressed as

$$\theta_{w\infty} = \theta_{wn} K^n, \tag{2}$$

where: θ_{wn} is the nominal steady-state winding temperature rise, K is the load factor (load current/nominal current) and n is an experimental correction coefficient. IEC standard proposes τ = 0.5-2 hours and n = 1.6 for dry-type transformers [25].

2.2. RC thermal model

A schematic view of a cast-resin transformer is shown in Fig. 1a. Thermal behaviour of the windings can be expressed as (3) [16].

$$\frac{1}{r}\frac{\partial}{\partial r}\left(r\frac{\partial \theta}{\partial r}\right) + \frac{\partial^2 \theta}{\partial z^2} + \frac{q''}{k} = \frac{1}{\alpha}\frac{\partial \theta}{\partial t}, \tag{3}$$

where: q'' is the specific loss density, θ is the temperature, k is the thermal conductivity and α is the thermal diffusion. Now, assume the solid parts to be divided into a number of cylindrical units that are related to each other by thermal resistances (Fig. 1b).

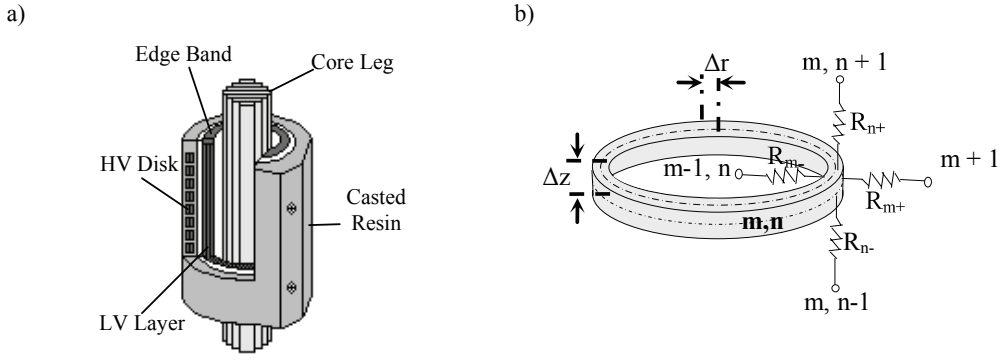

Fig. 1. Cast-resin dry-type transformer: a) schematic view; b) a partial part

In the transient condition, the transferred thermal energy to each unit appears as an increase in the total energy and the unit behaves as an integrated capacitor [16]. If only one unit is selected in the windings and if the heat transfer from horizontal surfaces is neglected (heat transfer is assumed to occur in the radial direction) [2], the thermal behaviour of the winding and the cooling air (on top of the enclosure [27]) can be explained as following [15]:

$$P_w - \frac{\theta_w - \theta_e}{R_w} = C_w \frac{\mathrm{d}\theta_w}{\mathrm{d}t}, \tag{4}$$

$$P_e - \frac{\theta_e}{R_e} = C_e \frac{\mathrm{d}\theta_e}{\mathrm{d}t}, \qquad \text{where} \qquad P_e = \frac{\theta_w - \theta_e}{R_w}, \tag{5}$$

where: θ_w/θ_e are the average temperature rises, P_w/P_e are the thermal flow sources, R_w/R_e are the thermal resistances, and C_w/C_e are the thermal capacitances of the winding/cooling air.

Consequently, (4) and (5) represent a second order RC circuit as given in [15]. Note that R_e, C_e and P_w are temperature dependent [17]. And P_w also depends on the load factor and the nominal winding losses (P_{wn}) as shown in (6).

$$P_w = P_{wn} K^n. \tag{6}$$

Combining (4)-(6), the matrix form of the thermal model can be explained as (7).

$$\begin{bmatrix} \frac{\mathrm{d}\theta_w}{\mathrm{d}t} \\ \frac{\mathrm{d}\theta_e}{\mathrm{d}t} \end{bmatrix} = \begin{bmatrix} -\frac{1}{R_w C_w} & \frac{1}{R_w C_w} \\ \frac{1}{R_w C_e} & -\frac{1}{R_w C_e} - \frac{1}{R_e C_e} \end{bmatrix} \begin{bmatrix} \theta_w \\ \theta_e \end{bmatrix} + \begin{bmatrix} \frac{P_{w0}}{C_w} \\ 0 \end{bmatrix} K^n. \tag{7}$$

Applying the forward Euler discretization rule ($\dot{\theta} = (\theta[k] - \theta[k-1])/\Delta t$), a discrete time form of (7) can be extracted as:

$$\begin{bmatrix} \theta_w[k] \\ \theta_e[k] \end{bmatrix} = \begin{bmatrix} 1 + \frac{\Delta t}{R_w C_w} & -\frac{\Delta t}{R_w C_w} \\ -\frac{\Delta t}{R_w C_e} & 1 + \frac{\Delta t}{C_e}\left(\frac{1}{R_w} + \frac{1}{R_e}\right) \end{bmatrix}^{-1} \left(\begin{bmatrix} \frac{P_{w0}}{C_w} \\ 0 \end{bmatrix} K^n + \begin{bmatrix} \theta_w[k-1] \\ \theta_e[k-1] \end{bmatrix} \right) = f(K, \theta_w[k-1], \theta_e[k-1]). \tag{8}$$

2.3. Novel thermal models based on recurrent neural networks

An artificial neural network (ANN) is a set of interconnected neurons that employs a mathematical model to simulate a biological neural network. ANN is formed by connecting the artificial neurons to each other among adjustable weights. Neural networks can be employed to model complicated interaction between a set of inputs and outputs. ANN can be trained to reach a target output for a specific set of inputs.

In this research, it is assumed that only two nodes in the winding and the cooling air can model the thermal behaviour of the cast-resin dry-type transformer with sufficient accuracy. This means that only the winding's average (or hottest spot) temperature and the cooling air

temperature on top of the winding are important and measurable. Obviously, if the measured cooling air temperature is not accessible, one can neglect the related node and thus the order (number of the outputs) of the thermal model will be reduced. As it can be seen from (8), thermal model needs one input for the load factor (K) and two outputs for the winding temperature (θ_w) and the cooling air temperature (θ_e). For more simplification in the thermal model, θ_w and θ_e are assumed to be temperature rises (absolute temperature - ambient temperature) instead of the absolute temperatures; this helps to remove the ambient temperature from the inputs and to simplify the model.

Note that temperatures are presented in both sides of (8); so the thermal models must have dynamic behaviours. Additionally, the thermal parameters in this equation are temperature dependent and consequently, the thermal model must be able to model the nonlinear behaviour of this system. In order to achieve these goals, two models based on recurrent neural networks are introduced here.

2.3.1. Elman recurrent networks (ELRN)

ELRN is a partial recurrent artificial neural network and is a widely used model for dynamic systems modeling. Previously, this network has been employed for temperature prediction in many different problems [18-24]. The ELRN is composed of input, hidden, context, and output layers (Fig. 2).

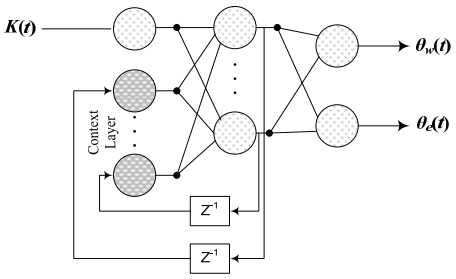

Fig. 2. Structure of the ELRN

The recurrent links in the context layer causes the ELRN to be sensitive to the output's history; dynamic behaviour of the ELRN is provided only by these internal connections. In this research, different training processes were carried out and the optimal number of neurons in the hidden layer (5), type of transfer functions ('logsig' for the hidden layer and 'purelin' for the output layer), the number of epochs, and etc. have been determined using a trial and error process. The network has been trained using the Levenberg-Marquardt method.

2.3.2. Nonlinear autoregressive model process with exogenous input (NARX)

NARX is a powerful dynamic neural network for modeling nonlinear and time variant systems. Due to better gradient descent, the NARX learning process is more effective and converges faster than in other artificial neural networks [28]. In modeling long time dependences,

the NARX model is better than other recurrent networks. The NARX networks can be implemented in different ways. A simple way is to use a feed-forward network with delayed inputs in addition to a delayed output link to input (Fig. 3).

A dynamic back-propagation method is required for learning purpose; training may be trapped in local optima. One can use the measured outputs instead of the estimated ones to train the NARX model; thus the feedback links are decoupled. The resultant neural network is a known feed-forward network that could be trained using the classical static back-propagation algorithm. But unfortunately, it was seen that this caused unsuitable results.

In this research, the optimal number of neurons in the hidden layer (5), type of the transfer functions ('logsig' for hidden layer and 'purelin' for output layer), the number of iterations, and etc. have been determined using a trial and error process. The network has been trained using the Levenberg-Marquardt method. In this problem, it has been seen that there was no need for input delays and each output was delayed twice.

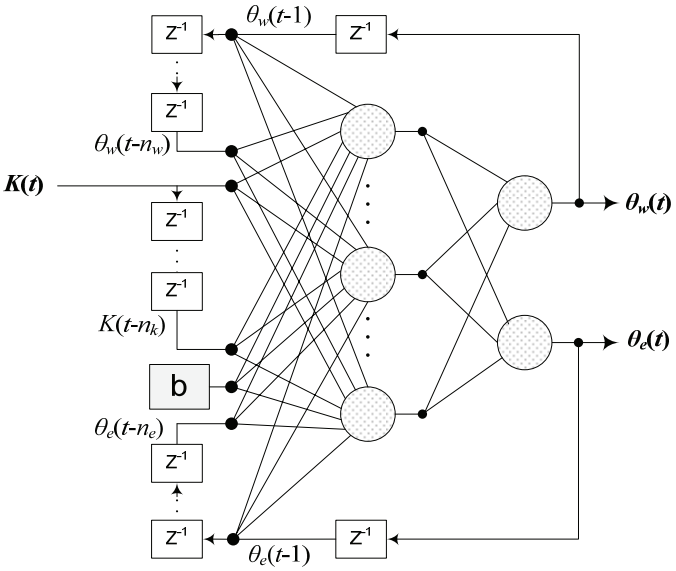

Fig. 3. Structure of the NARX

3. Reliability equations for dry-type transformer

Insulation's Life-time in a transformer depends on the winding's temperature. To compute the life-time of a cast-resin dry-type transformer, IEC [9] and IEEE [10] standards proposed some equations. In this research, the expected life-time (L) and the failure rate (λ) of the cast-resin dry-type transformer have been calculated using the following equations [15, 27]:

$$L = \frac{180000}{1875\times10^{18}}\times e^{\frac{20475}{1.25(\theta_w+\theta_{amb})+273}}, \tag{9}$$

$$\lambda = \frac{1}{L} = \frac{10^{16}}{0.96}\times e^{-\frac{20475}{1.25(\theta_w+\theta_{amb})+273}}. \tag{10}$$

The failure rate in (10) depends upon the winding temperature rise and the ambient temperature. The winding temperature is also related to the transformer load.

4. Temperature and life-time evaluation in a typical transformer

In order to train the introduced neural network models, the load cycle of Figure 4 is applied to a typical 400 kVA, 20 KV/400 V transformer [15] and the temperatures of the winding and the cooling air on top of the enclosure [29] are gathered.

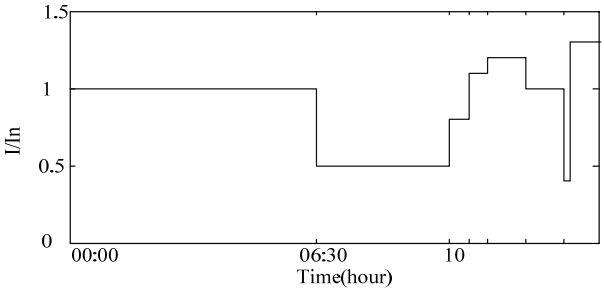

Fig. 4. A Typical load cycle employed for training the neural network models

Using the gathered experimental data, the ELRN and the NARX models have been trained. Figure 5 shows the training process of the ELRN and the NARX neural network models. From this figure, it can be seen that the NARX model is trained faster and has some better performance comparing with the ELRN model.

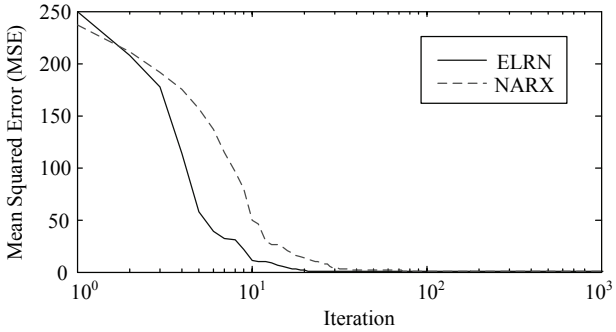

Fig. 5. Training process for neural network thermal models

In the following figures (Figs. 6-8), the predicted temperatures of the introduced neural network models are compared to the results extracted from traditional IEC and RC thermal models. The introduced neural network models are accurate in the thermal modeling of the cast-resin transformer. Note that these models need less information about the structure and the thermal behaviour of the cast-resin dry-type transformer. Unfortunately, the introduced models need gathering more experimental data for training rather than the traditional thermal models. The IEC simple thermal model is implemented easily, but it is not so accurate. The RC thermal model is accurate enough; but while the load variation is too high, the results may not be acceptable. It is seen that the introduced neural network based thermal models are rather more accurate thermal models than the traditional ones. They need no information about the system topology and its physical behaviour. But these thermal models need more gathered experimental data for training purpose.

Finally, using the introduced thermal model, the reliability of the cast-resin transformer can be evaluated according to the load and the ambient temperature variations. Consider a typical operating condition as shown in Fig. 9. By applying the mentioned load and ambient temperature to the introduced thermal model, winding temperature has been predicted as shown in Fig. 10a. Using the predicted winding temperature, the reliability indices can be calculated from (9) and (10) as shown in Fig. 10b.

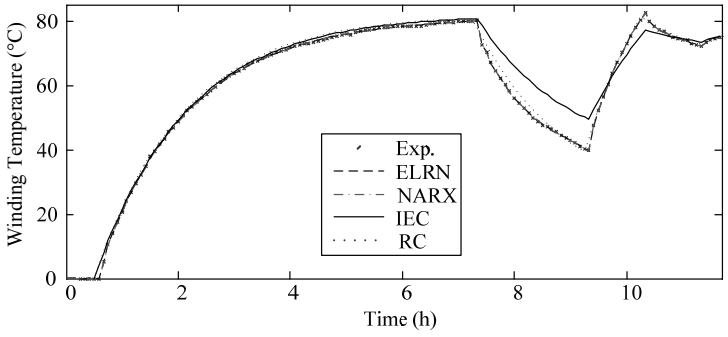

Fig. 6. Predicted winding temperature

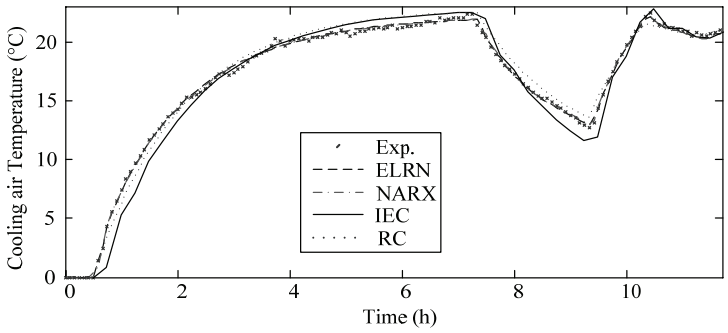

Fig. 7. Predicted cooling air temperature on top of the enclosure

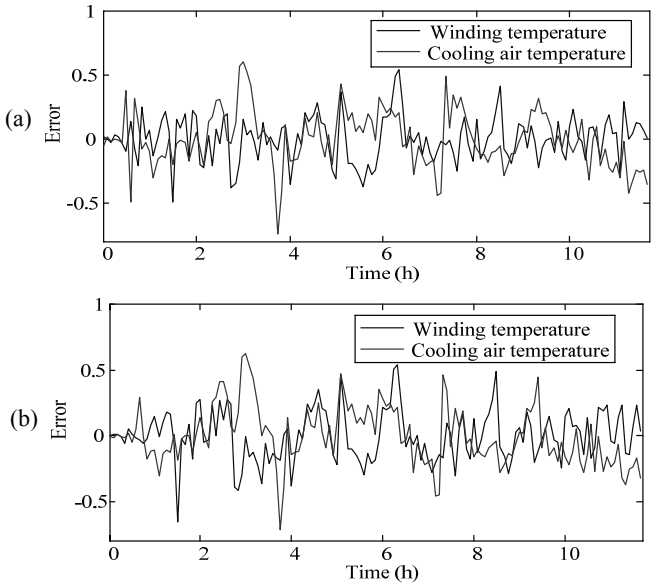

Fig. 8. Error of the predicted temperatures: a) ELRN; b) NARX

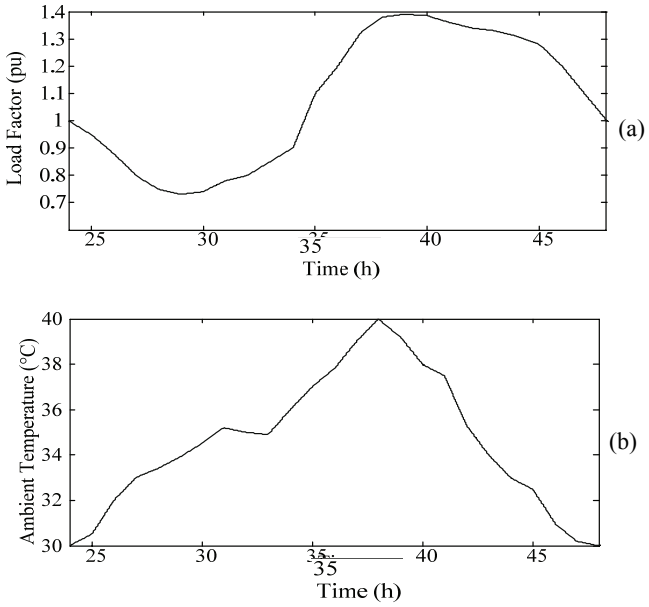

Fig. 9. A typical operating condition: a) load factor; b) ambient temperature variations

One can see that the life-time and the reliability indices of the cast-resin transformer are more sensitive to the load factor and the ambient temperatures while it is compared to the oil-immersed types [9].

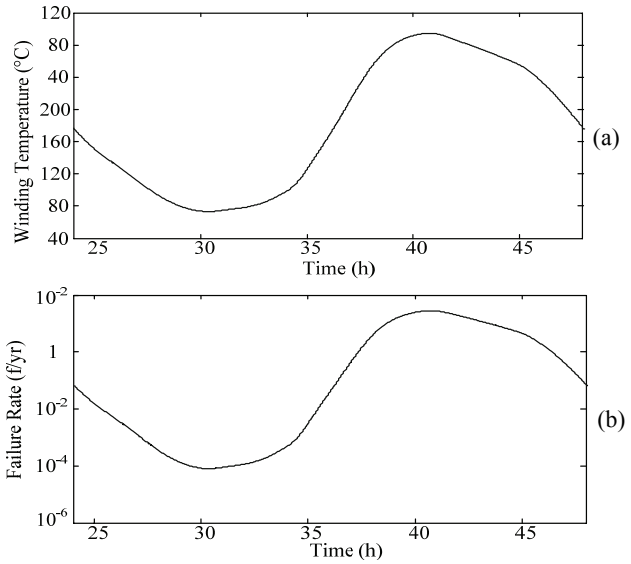

Fig. 10. a) winding temperature; b) failure rate due to variations in load and ambient temperature

It may be so interesting to analyse the effects of load and ambient temperature on the reliability of transformer separately. Fig. 11a shows the effect of load variation and Fig. 11b shows the effect of ambient temperature on the failure rate of the cast-resin dry-type transformer.

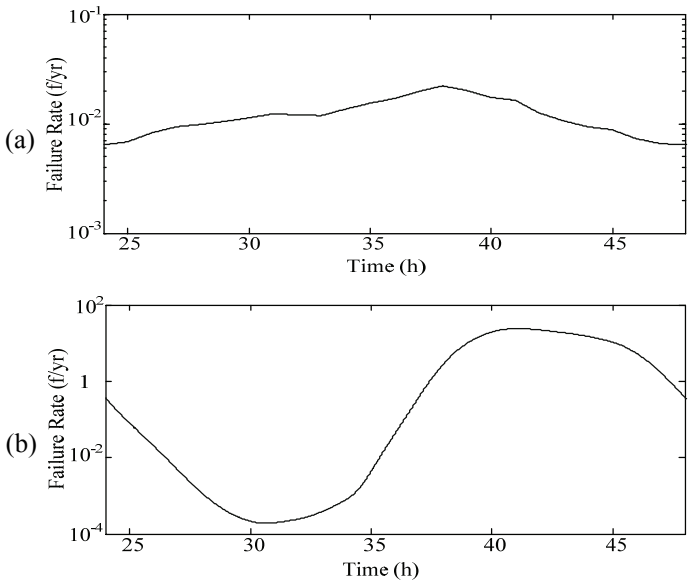

Fig. 11. Transformer failure rate due a variation in: a) load; b) ambient temperature

5. Conclusions

The analysis of the dynamic behaviour of the winding and cooling air temperatures is very important in the cast-resin dry-type transformers. Thus in this paper, new dynamic models based on ELRN and NARX neural networks were introduced for the cast-resin transformer thermal modeling. Using the gathered experimental data, the networks have been trained and with the help of additional measurements the accuracy of the thermal models are verified. As it has been presented in this paper, the introduced thermal models show a good performance in the dynamic thermal modeling of the cast-resin transformer.

The IEC equation needs less information about the design parameters of transformer; but it is very simple and it is not an accurate thermal model. The RC thermal model that depends on the physical and actual structure of the transformer is accurate enough. Although the proposed ELRN and NARX models need more data gathering, but their accuracy is higher than the traditional IEC and RC thermal models and need less information about system characteristics. The NARX model has some better training speed when it is training by experimental data.

Finally, by employing the trained and validated thermal models, the reliability indices are analysed. Variation in winding temperature affects the life-time and reliability of the cast-resin dry-type transformer. Some factors that have more effects on the temperature and reliability of the transformer are ambient temperature and load current. In comparison with the oil-immersed types, the life-time of the cast-resin dry-type transformer is more sensitive to the load factor and the ambient temperatures. It was shown that the most serious effect is due to the load current but the ambient temperature also has considerable effects on the life-time of the cast-resin dry-type transformers.

References

[1] Azizian D., Bigdeli M., Faiz J., *Design optimization of cast-resin transformer using nature inspired algorithms*, Arabian Journal for Science and Engineering, vol. 41, no. 9, pp. 3491-3500 (2016).

[2] Rahimpor E., Azizian D., *Analysis of temperature distribution in cast-resin dry-type transformers*, Electrical Engineering, vol. 89, no. 4, pp. 301-309 (2007).

[3] Pierce L.W., *An investigation of the temperature distribution in cast-resin transformer windings*, IEEE Transaction on Power Delivery, vol. 7, no. 2, pp. 920-926 (1992).

[4] Lee M., Abdullah H.A., Jofriet J.C., Patel D., Fahrioglu M., *Air temperature effect on thermal models for ventilated dry-type transformers*, Journal of Electrical Power System Research, vol. 81, no. 3, pp. 783-789 (2011).

[5] Eslamian M., Vahidi B., Eslamian A., *Thermal analysis of cast-resin dry-type transformers*, Journal of Energy Conversion and Management, vol. 52, no. 7, pp. 2479-2488 (2011).

[6] Dianchun Z., Jiaxiang Y., Zhenghua W., *Thermal field and hottest spot of the ventilated dry-type transformer*, IEEE 6th International Conference on Properties and Applications of Dielectric Materials, Xi'an, China (2000).

[7] Cho H.G., Lee U.Y., Kim S.S., Park Y.D., *The temperature distribution and thermal stress analysis of pole cast resin transformer for power distribution*, IEEE Conference International Symposium on Electrical Insulation, Boston, USA (2002).

[8] Azizian D., *Windings temperature prediction in split-winding traction transformer*, Turkish Journal of Electrical Engineering and Computer Science, vol. 24, no. 4, pp. 3011-3022 (2016).

[9] Jian H., Lin C., Zhang S.Y., *Transformer real-time reliability model based on operating conditions*, Journal of Zhejiang University, vol. 8, no. 3, pp. 378-383 (2007).
[10] Randakovic Z., Feser K.A., *New method for the calculation of hot-spot temperature in power transformers with ONAN cooling*, IEEE Transactions on Power Delivery, vol. 18, no. 4, pp. 1284-1292 (2003).
[11] Susa D., Palola J., Lehtonen M., Hyvärinen M., *Temperature rises in an OFAF transformer at OFAN cooling mode in service*, IEEE Transactions on Power Delivery, vol. 20, no. 4, pp. 2517-2525 (2005).
[12] Susa D., Lehtonen M., Nordman H., *Dynamic Thermal Modeling of Distribution Transformers*, IEEE Transactions on Power Delivery, vol. 20, no. 3, pp. 1919-1929 (2005).
[13] Taghikhani M.A., *Power transformer top oil temperature estimation with GA and PSO methods*, Energy and Power Engineering, vol. 4, no. 1, pp. 41-46 (2012).
[14] Ghareh M., Sepahi L., *Thermal modeling of dry-transformers and estimating temperature rise*, International Journal of Electrical, Computer, Electronics and Communication Engineering, vol. 2, no. 9, pp. 1789-1790 (2008).
[15] Azizian D., Bigdeli M., Firuzabad M.F., *A dynamic thermal based reliability model of cast-resin dry-type transformers*, International Conference on Power System Technology, Hangzhou, China (2010).
[16] Azizian D., Bigdeli M., *Cast-resin dry-type transformer thermal modeling based on particle swarm optimization*, 6th International Workshop on Soft Computing Applications, Timisoara, Romania (2014).
[17] Azizian D., Bigdeli M., *Application of heuristic methods for dynamic thermal modeling of cast-resin transformer*, International Journal of Advanced Intelligence Paradigms, vol. 8, no. 1, pp. 288-302 (2016).
[18] Baboo S.S., and Shereef I.K., *An efficient weather forecasting system using artificial neural network*, International Journal of Environmental Science and Development, vol. 1, no. 4, pp. 321-326 (2010).
[19] Moreno C.J.G., *Using neural networks for simulating and predicting core-end temperatures in electrical generators: power uprate application*, World Journal of Engineering and Technology, vol. 3, no. 1, pp. 1-14 (2015).
[20] De S.S., Debnath A., *Artificial neural network based prediction of maximum and minimum temperature in the summer monsoon months over India*, Applied Physics Research, vol. 1, no. 2, pp. 37-44 (2009).
[21] He Q., Si J., Tylavsky D.J., *Prediction of top-oil temperature for transformers using neural networks*, IEEE Transactions on Power Delivery, vol. 15, no. 4, pp. 1205-1211 (2000).
[22] Assunção T.C.B.N., Silvino J.L., Resende P., *Transformer top-oil temperature modeling and simulation*, World Academy of Science, Engineering and Technology, vol. 2, no. 10, pp. 1115-1120 (2008).
[23] Alias A.M., George A., Francis A., *Neural network based temperature prediction*, International Journal of Advanced Research in Electrical, Electronics and Instrumentation Engineering, vol. 2, no. 1, pp. 103-110 (2013).
[24] Smith B.A., McClendon R.W., Hoogenboom G., *Improving air temperature prediction with artificial neural networks*, International Journal of Computer, Control, Quantum and Information Engineering, vol. 1, no. 10, pp. 3100-3107 (2007).
[25] IEC Std. 60076-12, *IEC Loading Guide for Dry-Type Power Transformers*, (2008).
[26] ANSI/IEEE C57.96, *IEEE Guide for Loading Dry-Type Distribution and Power Transformers*, (April 1989).
[27] IEC Std. 60529, *IEC Degree of Protection Provided by Enclosures*, (1989).
[28] Gao Y., Er M.J., *NARMAX time series model prediction: feed-forward and recurrent fuzzy neural network approaches,* Fuzzy Sets and Systems, vol. 150, no. 2, pp. 331-350 (2005).

ARCHIVES OF ELECTRICAL ENGINEERING VOL. 66(1), pp. 29-40 (2017)

DOI 10.1515/aee-2017-0003

A novel rotor design for a hybrid excited synchronous machine

PIOTR PAPLICKI

West Pomeranian University of Technology Szczecin
Department of Power Systems and Electrical Drives
Sikorskiego 37, 70-313 Szczecin, Poland
e-mail: paplicki@zut.edu.pl

(Received: 20.11.2015, revised: 23.02.2016)

Abstract: The paper presents three novel rotor design concepts for a three-phase electric controlled permanent magnet synchronous machine (ECPMS-machine) with hybrid excitation. The influence of magnets and flux-barriers arrangement on the magnetic field distribution and field-weakening characteristics of the machine is examined, based on a three-dimensional finite element analysis (3D-FEA). Moreover, a prototype rotor design based on a new rotor concept with a good field-weakening capability is presented in detail. Finally, the experimental results of no-load back electromotive force (back-EMF) waveforms and field-weakening characteristics versus a control coil current of the machine are reported.

Key words: experimental result, field-weakening, finite element analysis, hybrid excitation, PM machine, rotor design

1. Introduction

At present, we are witnessing a continuing development of electrical machines used in variable-speed applications, such as wind turbines and automobiles. Numerous applications, such as the electric vehicle (EV) drive, require constant-voltage operation over a broad range of speeds. Depending on the operating conditions, the traction characteristics imply the use in two operation regions, namely: constant torque and constant power. An extended constant power range capability is crucial in reducing the power supply volt-ampere rating. Therefore, optimal applications for an EV drive for a hybrid electric vehicle (HEV), or a battery electric vehicle (BEV), should offer a field weakening potential of at least 1:4. It can be obtained, for instance, by connecting two kinds of excitation. Using machines with electromagnetic excitation, the required operating mode is achieved by an appropriate reduction of the field excitation current when the speed increases. In permanent magnet (PM) excited machines, constant excitation flux can only be controlled from the stator side by injecting the *d*-axis current.

It leads to an increase in winding losses and decreases efficiency of the entire drive system. In a hybrid excited PM machine (HEPM-machine), the extended constant power range is achieved by combining PM and electrical excitation. Thanks to an additional DC field excitation winding, a direct adjustment of the magnetic flux of the HEPM-machine is implemented. Various machine topologies with hybrid excitation have been described in literature, e.g. [1-5, 13].

The purpose of this paper is to explore three new rotor magnetic structure concepts for an Electric Controlled Permanent Magnet Synchronous machine (ECPMS-machine) with field weakening capability, which has been developed and widely tested in [6]. Furthermore, preliminary PM arrangement optimization methods of extending the field-weakening capability and reducing the cogging torque of the machine have been proposed in [7].

2. Flux distribution in the ECPMS-machine

The main features and properties of the ECPMS-machine shown in Fig. 1 derive from the use of a powder composite material mixture with an epoxy resin addition technology. The technology has been used to form a solid stator core and a rotor core with iron poles of the machine. As reported in [6], the implementation of this version of the machine allows to control the field excitation within the range of ±30% only. As a result, the speed of the machine is nearly doubled.

In order to explore the magnetic structure and clearly understand the role of the additional field-excitation in the magnetic field distribution of the ECPMS-machine, a cross section of the machine, including a virtual view of the magnetic flux paths, have been presented in Fig. 1. It is important to note that some of the flux paths have only appeared within a field-weakening region.

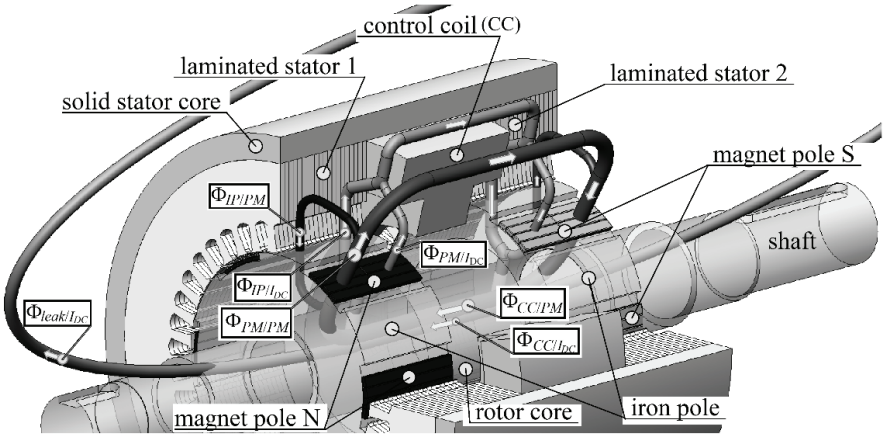

Fig. 1. Cross-section of the ECPMS-machine and virtual view of magnetic flux paths by weakening condition at $I_{DC} > 0$

By neglecting the saturation effect and the magnet flux leakage of the machine, it can be assumed that a flux component generated by PMs ($\Phi_{PM/PM}$) crosses an air-gap over magnet pole N section in the radial direction and flows through a laminated stator 1. The main part of the flux $\Phi_{PM/PM}$ is passed through a solid stator core in the axial direction and subsequently returned through an air-gap over the magnet pole S section to the magnet pole N section via a rotor core in the form of a flux $\Phi_{CC/PM}$. The remaining part of the flux $\Phi_{PM/PM}$ passes through the stator core 1 and is returned to the magnet pole N section through the air-gap over the iron pole section in the form of a flux $\Phi_{IP/PM}$.

When a current I_{DC} of a control coil (CC) is injected, additional DC field excitation is achieved. In this case, the flux Φ_{CC} passing through the control coil in the axial direction can be expressed as a combination of the flux $\Phi_{CC/PM}$ generated by the PMs and the flux $\Phi_{CC/I_{DC}}$ generated by the current I_{DC}. The flux Φ_{CC} is passed through a magnetic shaft and the rotor core in the axial direction and a significant portion of it returns to the air-gap of the machine, where it is divided into two components: flux $\Phi_{PM/I_{DC}}$ crosses the air-gap over the magnet pole section and $\Phi_{IP/I_{DC}}$ crosses the air-gap over the iron pole section.

The remaining portion of the flux Φ_{CC} creates a flux leakage, comprised of both axial and radial components.

Neglecting armature effects and saturation, using the principle of flux superposition, the resulting air-gap fluxes, excited in the field-weakening region, can be decomposed into PM excitation and additional DC field excitation by the current I_{DC}. The linear model of the resulting air-gap flux over the magnet pole section Φ_{PM} and the resulting flux over the iron pole section Φ_{IP} can be expressed as:

$$\Phi_{PM} = \Phi_{PM/PM} + \Phi_{PM/I_{DC}}, \tag{1}$$

$$\Phi_{IP} = -\Phi_{IP/PM} + \Phi_{IP/I_{DC}}. \tag{2}$$

It should be noted that, the design of a rotor magnetic circuit structure ECPMS-machine is crucial because of the field-weakening and flux leakage issues. The fixed additional DC field excitation, apart from the increase of the size of the machine also increases the leakage inductance of the control coil fixed on the stator. Hence, it is very important to determine the flux leakage of the machine particularly between no-load and under injected current of the control coil conditions. The linear model of the resultant control coil flux Φ_{CC} and the axial flux leakage $\Phi_{\text{leak}/I_{DC}}$ generated by the additional DC field excitation in the field-weakening region, can be defined as:

$$\Phi_{CC}/p = \Phi_{CC/PM} + \Phi_{CC/I_{DC}}, \tag{3}$$

$$\Phi_{\text{leak}/I_{DC}} = \Phi_{CC}/p - \Phi_{PM/I_{DC}} - \Phi_{IP/I_{DC}}, \tag{4}$$

where: $\Phi_{CC/PM}$ is the control coil flux component created by PMs, $\Phi_{CC/I_{DC}}$ is the control coil flux component created by the additional DC field excitation by the current I_{DC}, p is the number of pair of poles.

In order to show the principal change in the magnitude of fluxes from the additional DC field excitation, Fig. 2 presents the 2-D air-gap magnetic flux density distribution over a magnet and iron pole pitch. As illustrated in Fig. 2, it can be assumed that the polarity of the resulting flux over the iron pole section changes as a result of the addition field excitation by the current $I_{DC} > 0$, in this case $I_{DC} = 2.0$ A (2500 Ampere-turns).

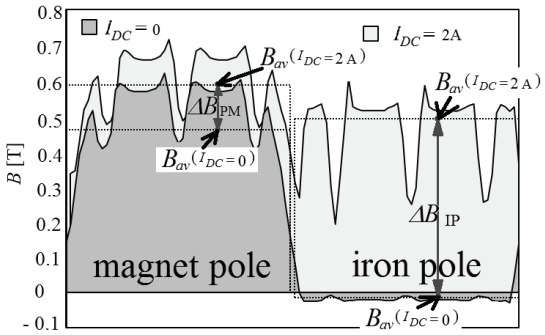

Fig. 2. Air-gap flux density distribution over magnet pole and iron pole pitch of the M1 model

The essence of increasing the flux linked with the stator phases is based on an equalization of fluxes passed through the magnet Φ_{PM} and the iron pole Φ_{IP} section. Therefore, rotor magnetic circuit structures for the ECPMS-machine should be developed, in which the additional DC field excitation strongly increases the iron pole flux Φ_{IP} only, simultaneously maintaining the magnet pole flux Φ_{PM}. This objective can be achieved by developing effective magnetic flux diverters in the rotor magnetic circuit of the machine.

Fig. 3a shows the initial, previously presented, structure of the rotor ECPMS-machine with surface-mounted PM (M1), analyzed in detail in [12], as well as three new rotor design concepts (M2-M4) for the machine. It should be noted that, in all cases, the machine has the parallel hybrid excitation system.

In the M2 model, the magnet poles are formed by quadrant-cylinder PMs and they are placed alternately between the iron poles. Due to the relatively high reluctance of the large volume quadrant-cylinder magnet, a natural path for leading flux through the ferromagnetic iron poles is formed. As a result, a substantial portion of the flux $\Phi_{CC/I_{DC}}$ component created by the control coil current can be diverted into the iron pole section. Thus, it can be assumed that the magnetic flux passing through the iron pole Φ_{IP} can be effectively regulated by the additional DC field excitation.

In the M3 model, each magnet pole is formed by a single surface-mounted PM and two magnets locked in radially arranged holes. The holes also serve as radial flux barriers (RFB). A single embedded flux barrier (EFB) is located below the RFBs.

In the M4 model, the magnet pole is formed by two embedded PMs and two magnets are locked in the RFBs. Similarly to the M3 model, a single EFB is formed in each iron pole section.

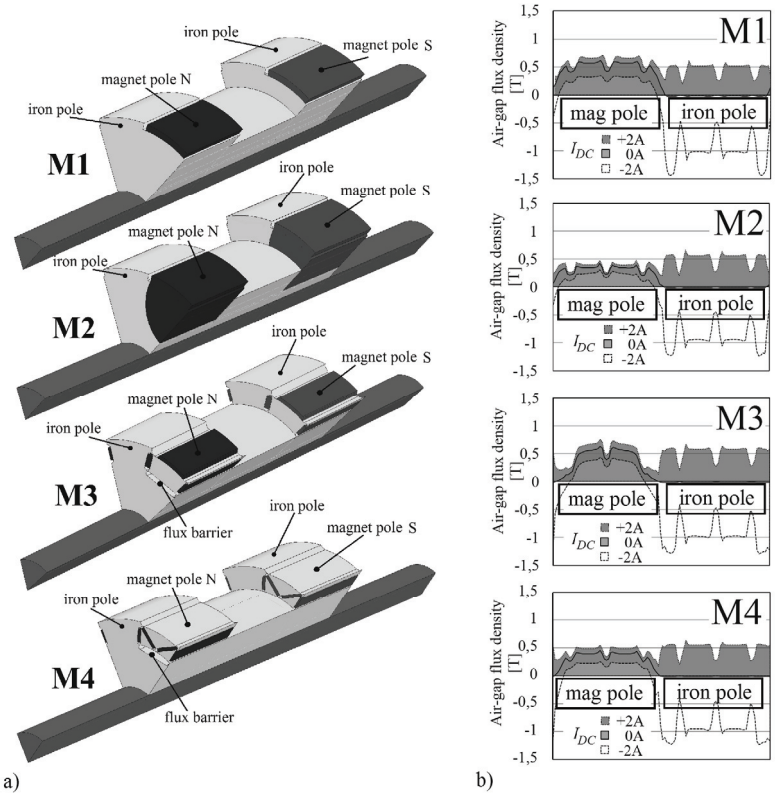

Fig. 3. Rotor design concepts for the ECPMS-machine (a); 2-D air-gap flux density distribution in the M1-M4 models at three field excitation levels (b), in comparison

3. Influence of the arrangement of magnets and flux barriers on ECPMS-machine flux control

In order to examine the influence of magnet type, shape, orientation, grouping and flux barrier arrangement for an ECPMS-machine on the field control capability, a 3-D FEA was carried out. The main goal of this investigation was to determine the field-weakening capability of the machine and to verify the equations that had been developed previously. This time, the nonlinear magnetization curve (B-H curve) was taken into account.

During the design and analysis of the saturation effect on the field control of the machine, it was assumed that an NdFeB-type permanent magnet (N38SH-type) would be used in the M1, M3 and M4 models. In the M2 model, a ferrite magnet (F30) has been used in order to avoid the saturation effects caused by the considerable size of the quadrant-cylinder magnet.

Fig. 3b shows the 2-D air-gap flux density distribution in all models at three different field excitation levels: field-weakening at $I_{DC} = 2.0$A, a field without additional excitation at $I_{DC} = 0$, and, additionally, field-strengthening at $I_{DC} = -2.0$ A. As seen in Fig. 3(b), the air-gap

flux density waveforms and their changes are different for all models. Moreover, it can be observed that a particularly effective increase of the flux $\Phi_{IP/I_{DC}}$ crossing the air-gap over the iron pole is noticeable in the M2 and M4 models. In order to clearly determine the effect of flux changes of the machine, a PM pole growth flux ratio $\Delta\Phi_{PM}$ and an iron pole growth flux ratio $\Delta\Phi_{IP}$ were determined. In this case, the growth flux ratio means a ratio of fluxes passed through the magnet pole/iron pole at $I_{DC} = 2.0$ A (field-weakening) to fluxes passed through the magnet pole/iron pole without the additional excitation (at $I_{DC} = 0$). 3D-FEA results of the mean values of the air-gap flux density over the PM pole (B_{PM}) and the iron pole (B_{IP}) with fluxes Φ_{PM} and Φ_{IP} of the ECPMS-machine for all models were listed in Table 1.

Table 1. 3D-FEA results of the ECPMS-machine for the models M1-M4

Model	**M1**		**M2**		**M3**		**M4**	
I_{DC} (A)	0	2	0	2	0	2	0	2
B_{IP} (T)	−0.02	0.46	−0.01	0.5	−0.02	0.53	−0.01	0.5
B_{PM} (T)	0.49	0.59	0.3	0.38	0.36	0.49	0.31	0.43
Φ_{IP} (mWb)	−0.05	1.6	−0.03	1.7	−0.05	1.8	−0.05	1.7
Φ_{PM} (mWb)	1.6	2.0	0.98	1.2	1.2	1.7	1.1	1.5

Moreover, the simulation results in Fig. 4 show an assessment of the effectiveness of field weakening and the values of determinants of the growth flux ratio $\Delta\Phi_{PM}$, $\Delta\Phi_{IP}$, as well as the control coil axial flux leakage $\Phi_{\text{leak}/I_{DC}}$, in comparison.

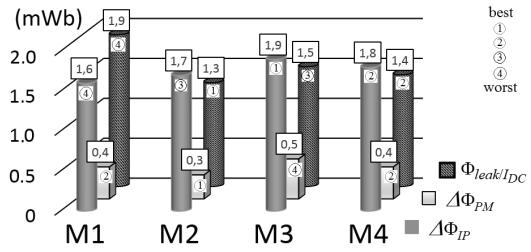

Fig. 4. Flux ratios: $\Delta\Phi_{PM}$, $\Delta\Phi_{IP}$, and the control coil axial flux leakage $\Phi_{\text{leak}/I_{DC}}$ for the M1-M4 models

Fig. 5 shows the 3D-FEA results of a no-load output voltage E_0 (Vrms) versus the control coil current for the load current I_{DC} in the range of 0-2.0 A, which has been determined for the models M1-M4. These characteristics show that the excellent field-weakening capability of the machine is achieved in the rotor based on the M2 model. However, in this case, a low power density ratio occurs. Simulation results demonstrate that a good field-weakening feature is also obtained in the M4 model. Taking into account the technical feasibility of the rotor, it has been decided that the next work will focus on experimental validation of the ECPMS-machine with a rotor prototype based on the M4 model.

In this case, in order to perform an FEA, a three-dimensional meshed model of M4 (Fig. 6), containing approximately 395 000 nodes, was developed, using the commercial Flux3D v.10.4.2 software package by Cedrat Ltd.

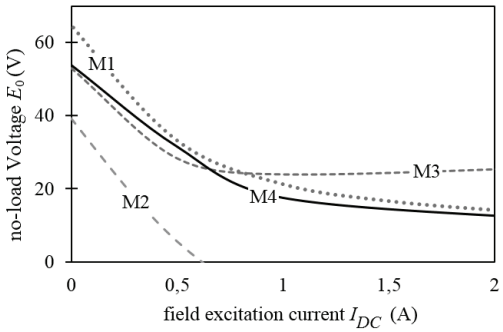

Fig. 5. No-load output terminal voltage E_0 versus the control coil current I_{DC} characteristic

It should be noted that, due to the complexity of the machines' geometry, and its lack of symmetry, FEA computing time is long and costly. For instance, a single step to compute the half-period of the back-EMF waveform might take anywhere between 20 and 60 hours using a standard PC computer platform based on an Intel Core i7 processor. FEA computing time strongly depends on the saturation level of the machine and it is rapidly increased while the control coil current is increasing. For this reason, the research on the development of a simplified reluctance equivalent circuit of the machine for design purposes was independently conducted by the author in [14].

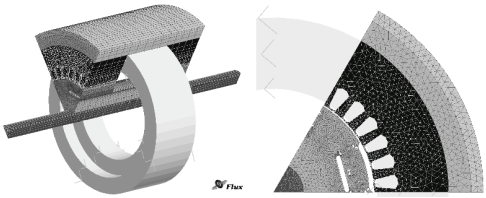

Fig. 6. Meshed 3-D model of M4

Furthermore, in order to showcase the complexity of the problem, Fig. 7 shows the 3-D distribution of the magnetic field in the active magnetic parts of the model without the control coil current I_{DC} at no-load conditions (Fig. 7a), and at a nominal stator current I_{sN} (Fig. 7b).

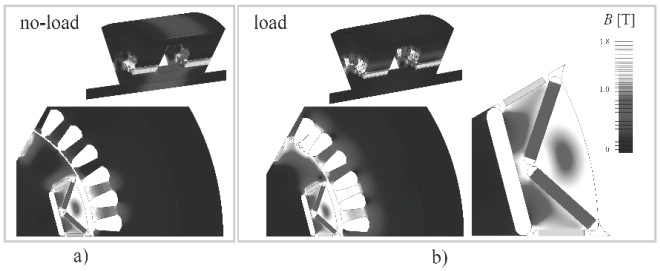

Fig. 7. Magnetic field distribution of the M4 model at $I_{DC} = 0$; no-load $I_s = 0$ (a) and nominal $I_s = I_{sN}$ (b) stator current conditions

Table 2 lists FEA predictions of a PM flux linked Ψ_{PM} and inductances of the M4 model.

Table 2. Magnetic parameters of the M4 model

	Value	**Unit**
PM flux linkage, Ψ_m,	122.6	mWb
d-axes inductance, L_d	4.4	mH
q-axes inductance L_q	5.5	mH

The parameters are performed to analyze and predict the electromagnetic torque-position characteristic of the machine. The electromagnetic torque T_e based on voltage and flux equations of the ECPMS-machine [6] is written as:

$$T_e = \frac{3}{2} p\left[\Psi_{PM} i_q + M_{DC} i_{DC} i_q + (L_d - L_q) i_d i_q\right], \tag{5}$$

where: i_q, i_d *are the* q-axis and d-axis currents respectively, M_{DC} is the DC control coil mutual inductance.

Fig. 8 presents the results of analytical and FEA predictions of static torque-position characteristics obtained at nominal current of stator winding condition $I_{sN} = 30$ A DC for phase A and 15 A DC for phase B and C, and without the control coil current $I_{DC} = 0$.

The characteristics reveal that a relatively small reluctance torque (T_{rel}) is achieved, as the product of the difference of inductances ($L_d - L_q$) and i_d and i_q currents, in comparison with a PM torque (T_{PM}), as the product of the flux linkage Ψ_m by the PMs and i_q current. In this case, the PM torque remains the main torque of the machine. However, this causes that, in the low/high-operation range, the effectiveness of increasing/decreasing the air-gap flux linkage Ψ_m will be closely linked to the DC field strengthening/weakening capabilities of the machine.

Moreover, Fig. 8 shows that the electromagnetic torque $T_{e\,\text{FEA}}$ obtained by FEA predictions and the electromagnetic torque T_e insignificantly differ from each other due to a cogging torque characteristic (Fig. 9), which is neglected in the analytical model.

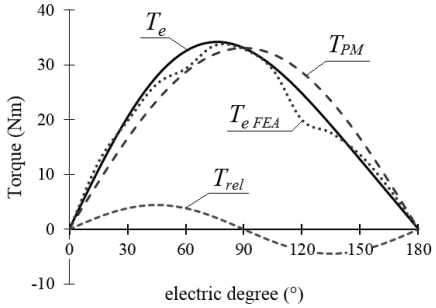

Fig. 8. Torque characteristics at nominal armature current $I_{sN} = 30$ A, $I_{DC} = 0$

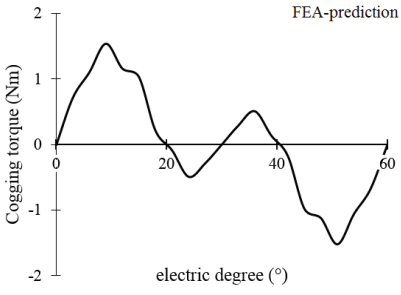

Fig. 9. Cogging torques vs. rotor position for 10 mech. deg. (60 el. deg.) at no-load condition $I_s = 0$, $I_{DC} = 0$

Fig. 10 shows FEA predictions of the torque-position characteristics at full-load conditions, while Fig. 11 shows the predicted performance (range of speed and torque) of the machine, estimated based on the FEA and analytical model results. In these studies, a maximum power supply voltage of 300 V, a stator current I_s up to 30 A, and a maximal control coil current I_{DC} up to ±5 A were assumed.

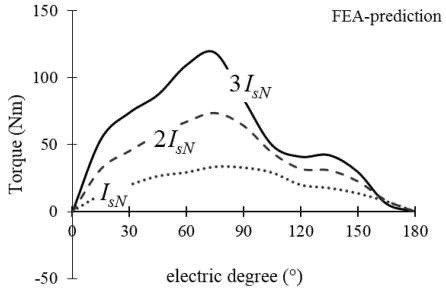

Fig. 10. Torques vs. rotor position at full-load armature current 1-3·I_{sN} without the control coil current $I_{DC} = 0$

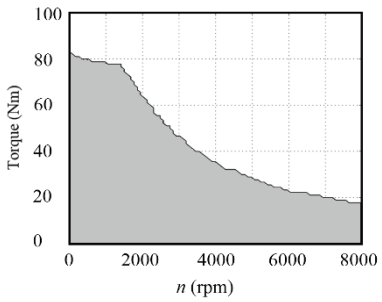

Fig. 11. The predicted operation region of the ECPMS-machine

4. Experimental results

Fig. 12(a) shows a sketch of a rotor magnetic structure based on the M4 model with a distinctive multiple flux barrier arrangement. Three types of flux barriers have been developed. The first one is a single flux barrier (SFB), located at the air-gap over the magnet pole section. The second type is an embedded flux barrier (EFB), located inside the rotor laminations. The third one is a radial flux barrier (RFB), which is radially formed and located inside the rotor magnetic structure.

The primary design data and guidelines for a machine prototype are presented in Table 3.

Table 3. Machine design requirements and assumption

Parameter	Value	Unit
Rotor outer diameter, D_r	163.0	mm
Stator stack length, l_s	2 × 80.0	mm
Air-gap length, l_g	0.5	mm
Maximal speed, n_{max}	8000	min^{-1}
Maximal control coil current, I_{DC}	± 5.0	A
Voltage reduction ratio, ΔU_0	1:4 at least	–
Nominal stator current, I_{sN}	30.0	A (rms)
Stator phase resistance, R_s	0.2	Ω
Pair-poles, p	6	–

The assembled rotor prototype for the ECPMS-machine and its one part of laminations with the view of PMs are illustrated in Fig. 12(b). The lamination material used in the rotor prototype was a 0.5 mm-thick steel sheet of M400-50A-C3. The PMs (N38SH) have a remanent flux density of 1.23 T and coercive force of 907 kA/m. The PMs are inserted into two EFB and two RFB barriers. One open EFB barrier (without PM) is located closest to the axis of the machine.

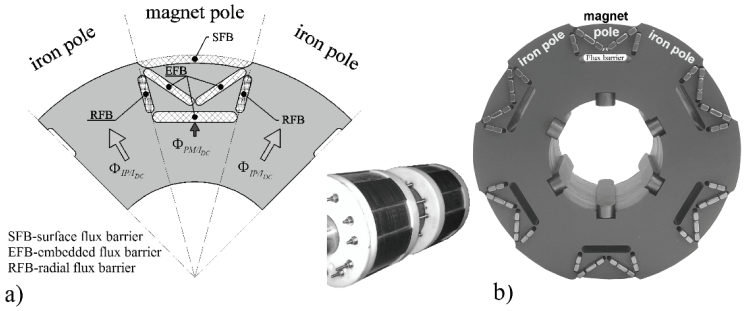

Fig. 12. A sketch of the rotor magnetic structure (a) and the assembled rotor (b)

In order to ensure the effectiveness of the flux Φ_{IP} crossing the air-gap under the limitation of the iron pole section, experiments testing the back-EMF waveforms at different values of the control coil current I_{DC} have been carried out. Fig. 13 shows the back-EMF waveforms obtained at a constant speed of 1000 rpm and at I_{DC} in the range from −5 to 6 A. Moreover, based on these results, a no-load output terminal voltage E_0 (V_{rms}) versus I_{DC} characteristic has been presented in Fig. 14.

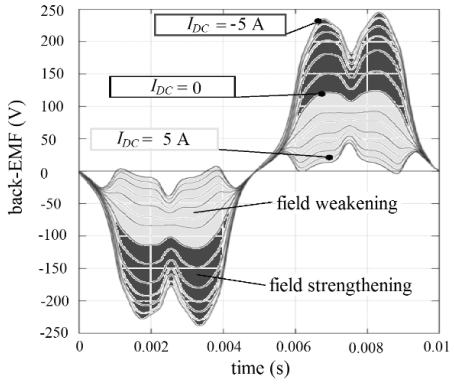

Fig. 13. Back-EMF waveforms under different control coil current I_{DC} at 1000 rpm constant speed

The presented results show an effective capability of magnetic field control for the ECPMS-machine based on the new rotor design. As presented, the voltage E_0 is effectively decreased from 53.0 to 12.0 V_{rms} for the loading control coil current range from 0 to 5.0 A. Moreover, Fig. 14 shows a no-load output voltage reduction ratio ΔE_0 that is determined by the ratio between the no-load output voltage without the additional excitation and the voltage

induced at the field-weakening region. In this case, $\Delta E_0 = 4$ is successfully obtained at $I_{DC} = 4.8$ A. This result is similar to the FEA predictions (for the M4 model) shown in Fig. 5.

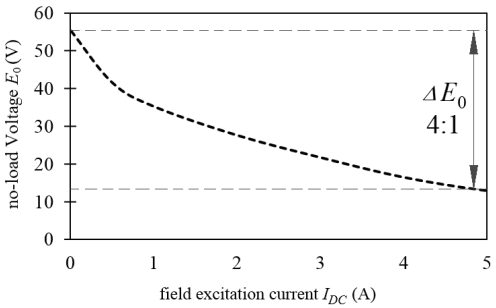

Fig. 14. No-load output terminal voltage E_0 vs. the control coil current I_{DC} characteristic at 1000 rpm

5. Conclusions

The purpose of the paper was to explore the magnetic structure of the modified ECPMS-machine and indicate novel rotor designs for the machine with high field weakening capability. Four different rotor designs have been discussed, including three new rotor concepts for the machine. Based on the 3-D FEA results, field-weakening features for all topologies have been presented. Moreover, the analysis has demonstrated that the proposed rotor machine configurations allow to control the flux in the air-gap without significantly affecting the magnetization characteristics of PMs. Particular attention has been paid to a rotor design concept based on the M4 model with flux barriers in the rotor magnetic structure. Furthermore, a prototype of the ECPMS-machine with a new rotor concept has been successfully tested. For this rotor design, the influence of magnets and flux barriers arrangement on controlling field excitation has been examined. The experiment results have shown that the field-weakening ratio equal to 4:1 is effectively obtained in the prototype of the machine, which implies its great application potential in the development of new BEV technology.

Acknowledgements

This work has been supported with the grant of the National Science Centre, Poland 2015/17/B/ST8/03251

References

[1] Amara Y., Hlioui S., Belfkira R. et al., *Comparison of Open Circuit Flux Control Capability of a Series Double Excitation Machine and a Parallel Double Excitation Machine*, IEEE, IEEE Transactions on Vehicular Technology, vol. 60, no. 9, pp. 4194-4207 (2011).

[2] Wang Y., Deng Z., *Hybrid Excitation Topologies and Control Strategies of Stator Permanent Magnet Machines for DC Power System*, IEEE Transactions on Industrial Electronics, vol. 59, no. 12, pp. 4601-4616 (2012).

[3] Amara Y., Vido L., Gabsi M. et al., *Hybrid excitation synchronous machines: energy-efficient solution for vehicles propulsion*, IEEE Transactions on Vehicular Technology, vol. 58, no. 5, pp. 2137-2149 (2009).
[4] Paplicki P., *Modified concept of axial-flux permanent magnet machine with field weakening capability*, Archives of Electrical Engineering, vol. 63, no. 2, pp. 177-185 (2014).
[5] Mingming H., Xinjun G., Ping J. et al., *Flux-weakening control methods for hybrid excitation synchronous motor*, Archives of Electrical Engineering, vol. 64, no. 3, pp. 427-439 (2015).
[6] Paplicki P., Wardach M., Bonislawski M., Palka R., *Simulation and experimental results of hybrid electric machine with a novel flux control strategy*, Archives of Electrical Engineering, vol. 64, no. 1, pp. 37-51 (2015).
[7] Putek P., Paplicki P., Palka R., *Topology Optimization of rotor poles in a Permanent-Magnet machine using Level Set method and Continuum Design Sensitivity Analysis*, COMPEL, vol. 33, no. 3, pp. 711-728 (2014).
[8] Putek P., Paplicki P., Palka R., *Low cogging torque design of Permanent-Magnet machine using modified multi-level set method with total variation regularization,* IEEE Transactions on Magnetics. vol. 50, no. 2, article no. 7016204 (2014).
[9] Paplicki P., *Optimization of Electrically Controlled Permanent Magnet Synchronous Machine to Improve Flux Control Range*, Elektronika ir Elektrotechnika, vol. 20, no. 10, pp. 17-22 (2014).
[10] Di Barba P., Bonislawski M., Palka R. et al., *Design of Hybrid Excited Synchronous Machine for Electrical Vehicles*, IEEE Transactions on Magnetics, vol. 51, no. 8, article no. 8107206 (2015).
[11] Paplicki P., *Effect of rotor structure on flux weakening characteristics of ECPM synchronous machine*, Zeszyty Problemowe – Maszyny Elektryczne, vol. 107, no. 3, pp. 183-187 (2015).
[12] Paplicki P., *ECPMSM synchronous machine – selected simulations and designing results*, Zeszyty Problemowe – Maszyny Elektryczne, vol. 103, no. 3, pp. 109-114 (2014).
[13] Gieras J., *PM synchronous generators with hybrid excitation systems and voltage control Capabilities, A review*, XX International Conference on Electrical Machines (ICEM), Marseille, pp. 2573-2579 (2012).
[14] Paplicki P., *Simplified Reluctance Equivalent Circuit for Hybrid Excited ECPMS-Machine Modelling*, Proceedings of the 21th International Conference on Methods and Models in Automation an and Robotics (MMAR), pp. 241-244 (2016).

ARCHIVES OF ELECTRICAL ENGINEERING VOL. 66(1), pp. 41-54 (2017)

DOI 10.1515/aee-2017-0004

Simulation of the remanence influence on the transient states in a single-phase multiwinding transformer

ANDRZEJ WILK, MICHAŁ MICHNA

Gdansk University of Technology
Faculty of Electrical and Control Engineering
Narutowicza 11/12, 80-233 Gdańsk, Poland
e-mail:{andrzej.wilk / michal.michna}@pg.gda.pl

(Received: 22.09.2016, revised: 18.10.2016)

Abstract: This paper presents the mathematical model of a single-phase multi-winding core type transformer taking into account magnetic hysteresis phenomenon based on the feedback Preisach model (FPM). The set of loop differential equations was developed for a *K*-th winding transformer model where the flux linkages of each winding includes flux Φ common to all windings as a function of magneto motive force Θ of all windings. The first purpose of this paper is to implement a hysteresis nonlinearity involved in the Φ(Θ) function which also accounts residual magnetic flux. The second purpose of this paper is experimental validation of the developed transformer model in a capacitor discharge test and several different values of residual magnetic flux.

Key words: single-phase transformer, magnetic flux common, magneto motive force, magnetic hysteresis, residual magnetic flux, capacitor discharge test

1. Introduction

One of many consequences of the magnetic hysteresis is the possibility of occurrence of residual magnetic flux density in the core of the transformer, whose value depends on several factors [1]: the magnetic properties of the core, the power factor at the time of shutdown of the transformer, the winding connections, etc. The existence of residual flux may be significant to the maximum value of the inrush current of the transformer and contribute to the undesirable effects of protection systems installed in the power system [2-4]. Effects of inrush currents are somewhat limited by the use of appropriate reactors and protection systems with time-lag characteristics. However, studies are carried out on the use of active control systems of the moment of a switching transformer, including the residual flux in the core [2, 5] to limit the inrush current. Accurate determination of the residual flux is a relatively difficult issue because it requires consideration of the hysteresis phenomenon and the eddy currents in the core. The accurate methods to prediction of the residual flux and inrush current of transformer

circuits are therefore needed. It is expected that in this prediction method accurate mathematical circuit models of the transformers can be useful.

In this paper a single-phase multi-winding transformer with core type of construction is studied taking into account the hysteresis phenomenon of magnetic material and residual magnetic flux. Multi-winding transformers are used in central stations, power trains, and electronic devices. They enable to supply several circuits with different voltage and power level from a single source through a single physical device.

An arrangement of windings and iron core geometry of the considered transformer in cross section is shown in Fig. 1. This transformer has the tape wound core made by wrapping thin long grain oriented silicon steel strip around an appropriate path. The number of windings and arrangement of particular coils corresponds to a transformer used frequently in electric traction [6]. The coils denoted P2 and P4 are two sections of the primary traction winding. The coils denoted P1 and P3, connected in series inside the transformer, form a single section referred to as the primary auxiliary winding. The coils labeled T1 and T2, not connected inside the transformer, form two sections of the traction secondary windings. The coils S1 and S2, connected in series inside the transformer, are the auxiliary secondary winding.

Modeling of traction transformers is very important for simulations and analysis of transient states in power trains. The exact circuit parameters are needed for proper control strategy of drive systems [7] and for diagnosis purposes [8]. The key point of the transformer modeling is the representation of nonlinear magnetization and hysteresis of the iron core.

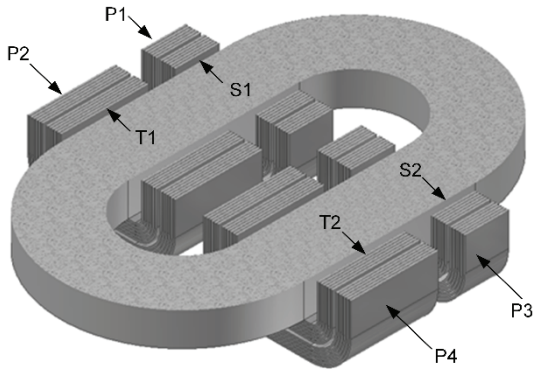

Fig. 1. Isometric view of cross section of the considered transformer and arrangement of its primary P1, P2, P3, P4 windings and secondary S1, S2, T1, T2 windings

2. Macroscopic models of magnetic hysteresis

Several efforts to model magnetic hysteresis have been reported until now. Among many models proposed so far, the hysteresis model based on Preisach's theory [9] and the Jiles-Atherton model [11] are proposed for accurate modeling and prediction of the magnetic characteristics. The Preisach model (PM) and Jiles-Atherton (J-A) model are classified into so-called macroscopic models of hysteresis [12].

In the J-A model the total magnetization in the magnetic material has two components – reversible and irreversible. The J-A model can be used in analysis of coupled electromagnetic and thermal phenomena in the transformers [13]. It was reported in [14] that the J-M model has been successfully utilized to simulate of coupled electromagnetic, fluid dynamic and motion phenomena. This model can be used in FEM calculations [15] and recently, an algorithm and computer code was presented [16] to effectively determine several parameters of the J-A model.

In the PM the double integral of the Preisach distribution function $\mu(\alpha, \beta)$ is involved to find usually magnetic flux density B as the function of the magnetic field intensity H. The induction B depends not only on the magnetic field but also on the history of magnetization of the material. The PM had been initially utilized in the field of magnetism but its mathematical generality suggested implementation of this model in many areas of science. A pure mathematical form of the PM separated from its physical meaning was proposed by Krasnosel'skii [17]. This approach was further developed by Mayergoyz [18] for determining the conditions for the representations of the hysteresis nonlinearities and generalization of the PM.

Nowadays there are several generalizations of the original classical PM in other to improve its ability to represent complex experimental results. One possible solution to gain more accuracy for the representation of hysteresis nonlinearity is to use the so-called feedback Preisach model [19, 20]. Description of most modifications of classical PM (generalized PM, moving PM, dynamic PM, vector PM) can be find in paper [21]. Many recent enhancements to the classical PM also allow simulation of coupled electromagnetic and thermal phenomena in magnetic materials. The PM has been used in this paper to simulate hysteresis effects in a single-phase transformer.

Experimental and simulation studies of the influence of the residual magnetic flux on the value of inrush current are rarely published and selected results are given in [3, 4, 22, 23]. In [3] and [4] lack a comparison of simulation results with experimental results, which do not allow to validate the models of hysteresis. In [22] the simplified model of the transformer was used, which does not take into account classical eddy current losses and anomalous losses. In [23] the components of classical and anomalous losses are included and show relatively good agreement between the results of simulation and experiment. However, in this hysteresis model, the shape of the small loops is deduced from the relevant geometric transformation of the rising and falling curve of the main hysteresis loop, which cannot be proven on the basis of the macroscopic model.

Two main objectives were formulated in this paper. The first objective concerned the development of a circuit model of the single-phase multi-winding transformer coupled with a generalized scalar Preisach hysteresis model. Equivalent circuit model of the transformer is developed in terms of the common magnetic flux Φ_c as function of ampere-turns Θ of all coils. In this paper hysteresis nonlinearity is involved in $\Phi_c(\Theta)$ expression. The new Preisach distribution function $\mu(\alpha,\beta)$ is proposed [24] as an analytical formula approximated by functional series. A hysteresis model with a feedback function as the third order polynomial is assumed in order to gain accuracy of the transformer model. The model also takes into account the equivalent circuit representing the classical and anomalous eddy current losses.

The second objective concerned the simulations of the inrush current at different values of residual magnetic flux. The study of the transient state was based on the capacitor discharge through the primary windings at a predetermined value and sign of the residual magnetic flux in the core. This approach has provided a very good repeatability of the transient states, independent of the switch actuation time and physical phenomena on its contacts. Finally the simulation results predicted by the model have been successfully verified by experiments.

3. Transformer equivalent circuit

A schematic representation of the considered transformer with K-windings and their associated terminal voltages and the assumed current directions is shown in Fig. 2. For the transformer with $K = 8$ windings operating in a power train, primary traction P1, P2, P3, and P4 coils (in parallel connection) are energized from a single AC voltage source. Secondary T1, T2, S1, and S2 coils are connected to power converters.

The set of loop differential equations of K – winding transformer model is expressed in matrix form as:

$$\boldsymbol{u} = \boldsymbol{R}\,\boldsymbol{i} + \frac{\mathrm{d}}{\mathrm{d}t}\boldsymbol{\Psi}(\boldsymbol{i})\,, \tag{1}$$

where: $\boldsymbol{u} = [u_1, u_2,..., u_K,]^{\mathrm{T}}$ is the vector of terminal voltages, $\boldsymbol{i} = [i_1, i_2,..., i_K,]^{\mathrm{T}}$ is the vector of winding currents and $\boldsymbol{\Psi}(\boldsymbol{i}) = [\Psi_1(\boldsymbol{i}), \Psi_2(\boldsymbol{i}),..., \Psi_K(\boldsymbol{i})]^{\mathrm{T}}$ is the vector including the flux linkages in each winding.

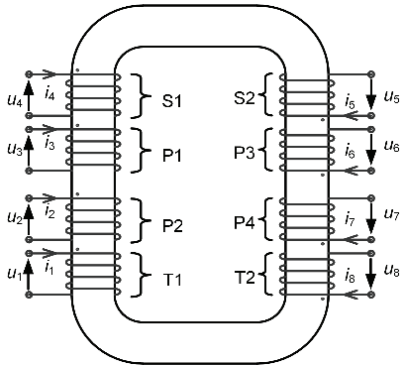

Fig. 2. Schematic representation of a single-phase and eight winding transformer: P1, P2, P3, and P4 – coils of primary winding (connected in parallel), T1, T2, S1, S2 – secondary windings

The time rate of change of $\boldsymbol{\Psi}$ can be represented as:

$$\frac{\mathrm{d}}{\mathrm{d}t}\boldsymbol{\Psi}(\boldsymbol{i}(t)) = \begin{bmatrix} \dfrac{\partial \Psi_1(\boldsymbol{i})}{\partial i_1} & \cdots & \dfrac{\partial \Psi_1(\boldsymbol{i})}{\partial i_K} \\ \vdots & & \vdots \\ \dfrac{\partial \Psi_K(\boldsymbol{i})}{\partial i_1} & \cdots & \dfrac{\partial \Psi_K(\boldsymbol{i})}{\partial i_K} \end{bmatrix} \frac{\mathrm{d}}{\mathrm{d}t}\begin{bmatrix} i_1 \\ \vdots \\ i_K \end{bmatrix} = \boldsymbol{L_d}(\boldsymbol{i})\frac{\mathrm{d}}{\mathrm{d}t}\boldsymbol{i}\,, \tag{2}$$

where $\boldsymbol{L_d(i)}$ is the matrix of self and mutual dynamic inductances.

Recognizing that there is a flux common to all windings, the flux linkages of the k-th winding can be expressed by [25, 26]:

$$\Psi_k(\boldsymbol{i}) = N_k \Phi_c(\Theta(\boldsymbol{i})) + \sum_{n=1}^{K} L_{\sigma,k,n} i_n, \quad k,n = 1,2,...,K, \tag{3}$$

where Φ_c is the flux common to all windings, N_k is the number of turns of the k-th winding, $L_{\sigma,k,n}$ is the leakage inductance resulting from the existence of the leakage flux in the coil k due to the flux generated by the current in the coil n, Θ is the total ampere turns of all windings defined by:

$$\Theta(\boldsymbol{i}) = N_1 i_1 + N_2 i_2 +,...+ N_K i_K. \tag{4}$$

In this paper the relationship $\Phi_c(\Theta)$ accounts for nonlinear magnetic properties of the iron core and hysteresis effect.

4. The feedback hysteresis model

In the classical Preisach model a ferromagnetic material is made up of infinite set of magnetic dipoles (hysteresis operator), each having magnetic characteristics with two separate, randomly distributed properties α, β as shown in Fig. 3. Each operator has a rectangular hysteresis loop and is defined as mathematical operator $\gamma_{\alpha\beta}(H)$ that can assume only two values, +1 (positively switched) and –1 (negatively switched).

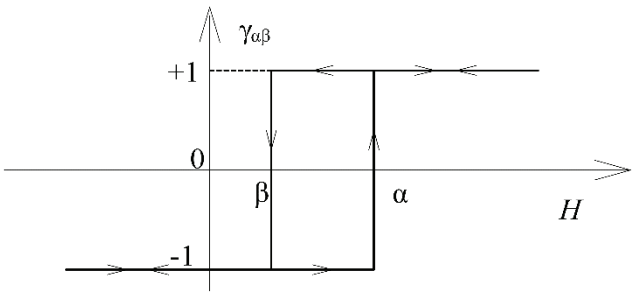

Fig. 3. Rectangular loop of elementary hysteresis operator

The relationship between magnetic field intensity H and flux density B in the classical Preisach model is expressed in the integral form as:

$$B = \iint_{\alpha \geq \beta} \mu(\alpha,\beta)\gamma_{\alpha\beta}(H)\,\mathrm{d}\alpha\,\mathrm{d}\beta, \tag{5}$$

where μ(α,β) is a finite weight function having nonzero values within the limits of a major hysteresis loop. The term μ(α, β) is also called the Preisach distribution function and can be regarded as a material constant. The weight function μ(α, β) can be also treated as a probability density function where μ(α, β)dαdβ equals the probability that a randomly selected operator has a rectangular loop (α, β). In the feedback Preisach model (FPM) the positive switching field α is replaced by $\alpha + H_f(B)$ and the negative switching field β is replaced by $\beta + H_f(B)$ in Eq. (5).

In this paper the hysteresis nonlinearity is proposed to be involved in $\Phi_c(\Theta)$ expression. Hence, a block diagram representing the proposed hysteresis model taking into account $\Phi_c(\Theta)$ term is shown in Fig. 4.

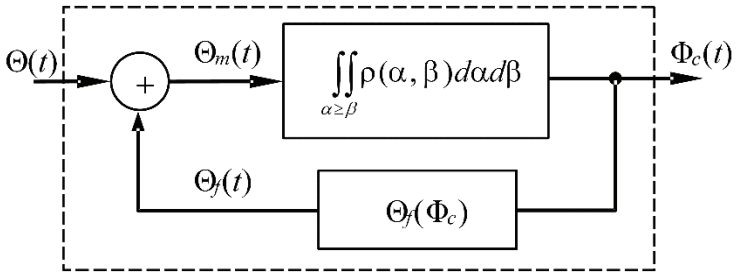

Fig. 4. Block diagram of the feedback hysteresis model

The upper rectangle shown in Fig. 4 represents the classical Preisach transducer [18]. The lower rectangle in feedback loop represents the contribution term $\Theta_f(\Phi_c)$ to the effective magnetomotive force $\Theta_m(t) = \Theta(t) + \Theta_f(\Phi_c)$ acting on elementary hysteresis operators. Hence, the scalar feedback Preisach model (FPM) is formulated by the following formula:

$$\Phi_c(t) = \iint_{\alpha \geq \beta} \rho[\alpha + \Theta_f(\Phi), \beta + \Theta_f(\Phi))]\, \gamma_{\alpha,\beta}[\Theta_m(t)]\, \mathrm{d}\alpha\, \mathrm{d}\beta,$$
$$\Theta_m = \Theta + \Theta_f(\Phi_c), \tag{6}$$

where the $\rho(\alpha, \beta, \Theta(\Phi_c))$ is the so called Preisach distribution function (PDF), which in this model also depends on the common flux Φ_c by a feedback relationship, $\gamma_{\alpha,\beta}(\Theta)$ describes the rectangular loop of elementary hysteresis operators.

Application of the FPM in a circuit simulation requires determination of $\rho(\alpha, \beta, \Theta(\Phi_c))$ and $\Theta_f(\Phi_c)$ functions. An analytical approach for determination of feedback field contribution for $H_f(B)$ function is proposed in [27]. However this approach is applicable only for relatively small feedback factors. A complete parameter identification procedure of FPM is proposed in [28]. In this procedure however a linear feedback function is assumed and it may be applicable to some materials only. In [29] the nonlinear feedback function $H_f(B)$ is taken into account and the factorisation property of the function $\mu(\alpha, \beta)$ is assumed. However this is simplifying assumption and can be usable for a given class of magnetic materials.

In this paper a functional series of two-dimensional Gauss expressions to approximate the PDF is proposed [24] as:

$$\rho(\alpha,\beta)=\frac{1}{2\pi}\sum_{n=1}^{N}\frac{A_n}{S_{x,n}S_{y,n}}\exp\left(\frac{-(\alpha+\beta)^2}{2S_{x,n}^2}\right)\exp\left(\frac{-(\alpha-\beta)^2}{2S_{y,n}^2}\right), \tag{7}$$

where A_n, $S_{x,n}$, and $S_{y,n}$ are constant parameters.

A feedback function is proposed to be the third order polynomial:

$$\theta_f(\Phi_c)=K_1\Phi_c+K_3\Phi_c^{\,3}, \tag{8}$$

where K_1 and K_3 are constant parameters.

5. Parameter identification of the feedback Preisach model

Identification of the FPM requires determination of A_n, $S_{x,n}$, $S_{y,n}$, K_1, and K_3 parameters by means of a convenient set of measured data. Measurements were carried out on a single-phase and eight-winding transformer (Fig. 5). The apparent power of P2, P4, T1, and T2 coils is 6.4 kVA, with a rated voltage of 230 V. The apparent power of P1, P3, S1, and S2 coils is 3.2 kVA, with a rated voltage of 115 V. Rated currents of all coils are the same – 28 A. The iron core of the tested transformer is made with a grain oriented silicon steel strip of ET114-27 type. Thickness of the strip is equal to 0.27 mm.

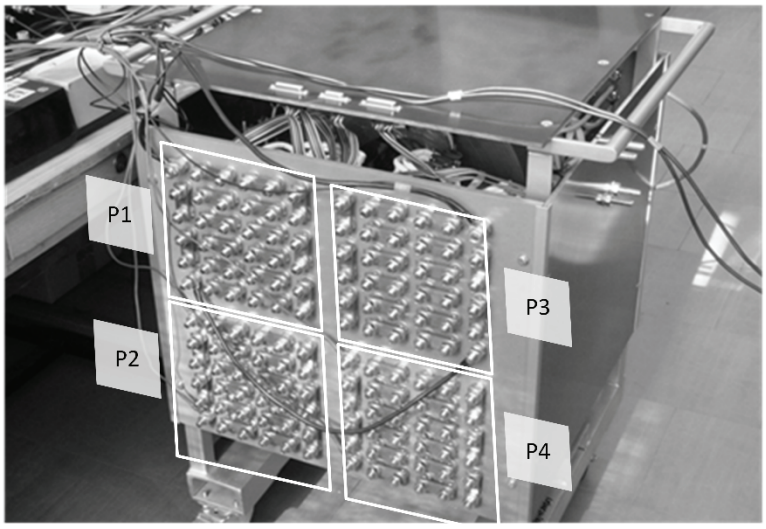

Fig. 5. Single-phase tested transformer with eight windings as part of experimental setup for measurements of hysteresis loops

The magnetizing windings were energized by laboratory power supply of PS 8000 DT type (*Elektro-Automatik GmbH*) controlled by a function generator of AFG3011 type (*Tektronix, Inc.*). The hysteresis $\Phi_c(\Theta)$ characteristics of the tested transformer are calculated from the set

of measured voltages and currents [30, 31]. The flux density is obtained by numerical integration of the voltage induced in the measurement coil. The core was demagnetized before measurements. Measurements have been done under slow time varying excitation current. The frequency equal to 0.020 Hz for the major loop was applied in order to reduce the dynamic effects in magnetic material.

For determinations of A_n, $S_{x,n}$, $S_{y,n}$, K_1, and K_3 parameters the Levenberg-Marquardt optimization algorithm [32] was used. Only initial and limiting descending $\Phi_c(\Theta)$ curves were utilized for calculation of these parameters. Parameter values of the FPM obtained from the identification procedure are shown in Table 1.

Table 1. Parameter values of the FPM – unit of S_x, and S_y is ampere

$S_{x,1}$	$S_{x,2}$	$S_{x,3}$	$S_{y,1}$	$S_{y,2}$	$S_{y,3}$	A_1	A_2	A_3
14.3	99.8	1770	29.3	34.5	16.74	0.024	0.013	0.030

The value of $K_1 = 720$ and $K_3 = -25.9\text{E}{+}06$. A surface plot of the PDF of the tested transformer core is shown in Fig. 6.

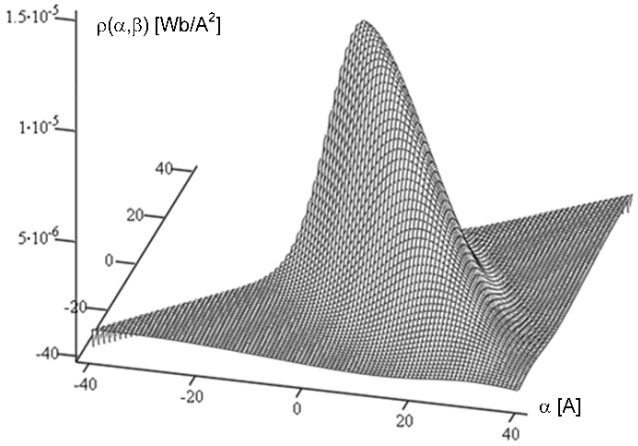

Fig. 6. Surface plot of the PDF of the tested transformer core

6. Experimental and simulation results of magnetic hysteresis

As an example, the FPM has been applied for representation of some symmetrical major loops at different total ampere-turns Θ. Fig. 7 shows the simulated symmetrical major loop compared with the experimental one at the range of ampere turns from 0 to 2600 A. In Fig. 8 the same simulated and measured downward and upward trajectories are shown at the range of ampere turns from 0 to 250 A. Differences between measured and simulated hysteresis loops are relatively small.

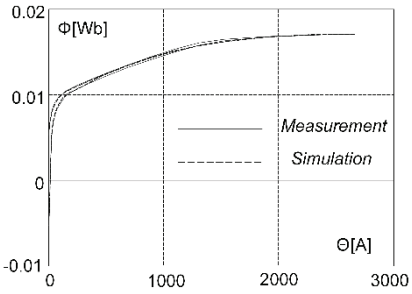

Fig. 7. Simulated and measured trajectories of symmetrical major hysteresis loops – verification of applied model

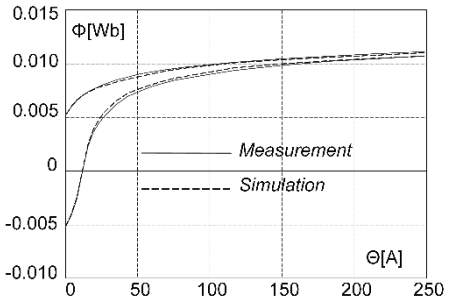

Fig. 8. Simulated and measured parts of symmetrical major hysteresis loops – verification of applied model at the range of ampere turns from 0 to 250 A

7. Circuit simulations of transformer coupled with the feedback hysteresis model

In this chapter, simulations taking into account the hysteresis model are performed for the tested transformer, described in chapter 4 (Fig. 5). In order to demonstrate the hysteresis effect in inrush current the capacitor discharge test at no-load transformer operation is assumed. An equivalent circuit of the transformer at considered test is shown in Fig. 9. The schematic arrangement of core and primary windings for this test is shown in Fig. 1.

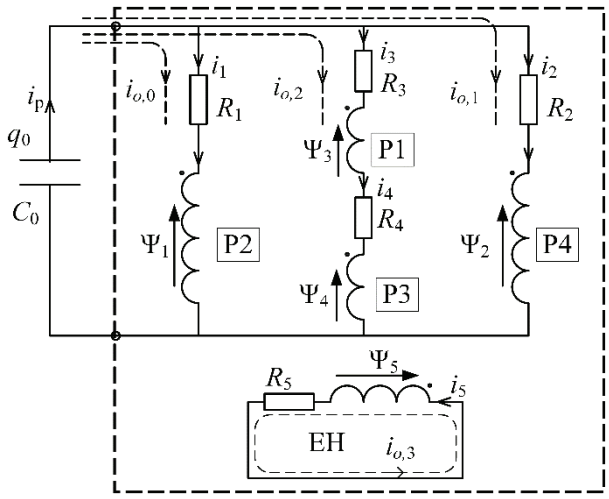

Fig. 9. Equivalent circuit of the considered transformer supplied from voltage source at no load operation

The primary windings (P1 + P3, P2, P4) are energized from the capacitor having capacitance C_0 with the initial charge q_0. A single equivalent circuit EH for modeling eddy current losses and an additional loss component (excess loss) is assumed. The rest of particular sym-

bols are as follows: Ψ_1 is the flux linkage of P2 winding; Ψ_2 is the flux linkage of P4 winding; Ψ_3 is the flux linkage of P1 winding; Ψ_4 is the flux linkage of P3 winning; Ψ_5 is the flux linkage of the equivalent loop representing eddy currents and excess losses; R_1 is the resistance of P2 winding; R_2 is the resistance of P4 winding; R_3 is the resistance of P1 winding; R_4 is the resistance of P3 winding; R_5 is the resistance of equivalent loop representing eddy currents and excess losses.

Mathematical description of the equivalent circuit shown in Fig. 9 that takes into account all magnetic couplings between the transformer windings has the following general form:

$$\left(\boldsymbol{C}_{\boldsymbol{u}}^{\boldsymbol{T}}\boldsymbol{L}_{\boldsymbol{d}}(\boldsymbol{i}_{\boldsymbol{o}})\boldsymbol{C}_{\boldsymbol{u}}\right)\frac{\mathrm{d}}{\mathrm{d}t}\boldsymbol{i}_{\boldsymbol{o}}+\left(\boldsymbol{C}_{\boldsymbol{u}}^{\boldsymbol{T}}\boldsymbol{R}\boldsymbol{C}_{\boldsymbol{u}}\right)\boldsymbol{i}_{\boldsymbol{o}}=\frac{-q_0}{C_0}[1\quad 1\quad 1\quad 0]^{\boldsymbol{T}}, \tag{9}$$

where the matrix of dynamic inductances $\boldsymbol{L_d}$, the matrix of resistances $\boldsymbol{R}$, and the matrix of constraints $\boldsymbol{C_u}$ are defined as follows:

$$\boldsymbol{L_d}=\begin{bmatrix}\frac{\partial\Psi_1}{\partial i_1} & \frac{\partial\Psi_1}{\partial i_2} & \frac{\partial\Psi_1}{\partial i_3} & \frac{\partial\Psi_1}{\partial i_4} & \frac{\partial\Psi_1}{\partial i_5}\\ \frac{\partial\Psi_2}{\partial i_1} & \frac{\partial\Psi_2}{\partial i_2} & \frac{\partial\Psi_2}{\partial i_3} & \frac{\partial\Psi_2}{\partial i_4} & \frac{\partial\Psi_2}{\partial i_5}\\ \frac{\partial\Psi_3}{\partial i_1} & \frac{\partial\Psi_3}{\partial i_2} & \frac{\partial\Psi_3}{\partial i_3} & \frac{\partial\Psi_3}{\partial i_4} & \frac{\partial\Psi_3}{\partial i_5}\\ \frac{\partial\Psi_4}{\partial i_1} & \frac{\partial\Psi_4}{\partial i_2} & \frac{\partial\Psi_4}{\partial i_3} & \frac{\partial\Psi_4}{\partial i_4} & \frac{\partial\Psi_4}{\partial i_5}\\ \frac{\partial\Psi_5}{\partial i_1} & \frac{\partial\Psi_5}{\partial i_2} & \frac{\partial\Psi_5}{\partial i_3} & \frac{\partial\Psi_5}{\partial i_4} & \frac{\partial\Psi_5}{\partial i_5}\end{bmatrix},\quad \boldsymbol{R}=\begin{bmatrix}R_1 & 0 & 0 & 0 & 0\\ 0 & R_2 & 0 & 0 & 0\\ 0 & 0 & R_3 & 0 & 0\\ 0 & 0 & 0 & R_4 & 0\\ 0 & 0 & 0 & 0 & R_5\end{bmatrix},\quad \boldsymbol{C_u}=\begin{bmatrix}1 & 0 & 0 & 0\\ 0 & 1 & 0 & 0\\ 0 & 0 & 1 & 0\\ 0 & 0 & 1 & 0\\ 0 & 0 & 0 & 1\end{bmatrix}. \tag{10}$$

The matrix of constraints establishes a relation between the so called non-generalized coordinates (set of currents – i_1, i_2, i_3, i_4, i_5) and generalized coordinates (set of loop currents – $i_{o,1}$, $i_{o,2}$, $i_{o,3}$, $i_{o,4}$) included in vector $\boldsymbol{i_o}$. The relation between these coordinates is given by:

$$[i_1\quad i_2\quad i_3\quad i_4\quad i_5]^T=\boldsymbol{C_u}[i_{o,0}\quad i_{o,1}\quad i_{o,2}\quad i_{o,3}]^T. \tag{11}$$

Assuming that there is a flux common to all P2, P4, P1, and P3 windings, the matrix of dynamic inductances is expressed by:

$$\boldsymbol{L_d}=\frac{\partial\Phi_c}{\partial\Theta}\begin{bmatrix}N_1N_1 & N_1N_2 & N_1N_3 & N_1N_4 & N_1N_5\\ N_2N_1 & N_2N_2 & N_2N_3 & N_2N_4 & N_2N_5\\ N_3N_1 & N_3N_2 & N_3N_3 & N_3N_4 & N_3N_5\\ N_4N_1 & N_4N_2 & N_4N_3 & N_4N_4 & N_4N_5\\ N_5N_1 & N_5N_2 & N_5N_3 & N_5N_4 & N_5N_5\end{bmatrix}+\begin{bmatrix}L_{\sigma,1,1} & L_{\sigma,1,2} & L_{\sigma,1,3} & L_{\sigma,1,4} & L_{\sigma,1,5}\\ L_{\sigma,2,1} & L_{\sigma,2,2} & L_{\sigma,2,3} & L_{\sigma,2,4} & L_{\sigma,2,5}\\ L_{\sigma,3,1} & L_{\sigma,3,2} & L_{\sigma,3,3} & L_{\sigma,3,4} & L_{\sigma,3,5}\\ L_{\sigma,4,1} & L_{\sigma,4,2} & L_{\sigma,4,3} & L_{\sigma,4,4} & L_{\sigma,4,5}\\ L_{\sigma,5,1} & L_{\sigma,5,2} & L_{\sigma,5,3} & L_{\sigma,5,4} & L_{\sigma,5,5}\end{bmatrix}, \tag{12}$$

where $N_1 = 190$ is the number of turns of P2 winding, $N_2 = 190$ is the number of turns of P4 winding, $N_3 = 95$ is the number of turns of P1 winding, and $N_4 = 95$ is the number of turns of P3 winding.

The matrix of leakage inductances of the considered transformer was defined by Wilk [26] for which the numerical values given in Henrys are:

$$\begin{bmatrix} L_{\sigma,1,1} & L_{\sigma,1,2} & L_{\sigma,1,3} & L_{\sigma,1,4} & L_{\sigma,1,5} \\ L_{\sigma,2,1} & L_{\sigma,2,2} & L_{\sigma,2,3} & L_{\sigma,2,4} & L_{\sigma,2,5} \\ L_{\sigma,3,1} & L_{\sigma,3,2} & L_{\sigma,3,3} & L_{\sigma,3,4} & L_{\sigma,3,5} \\ L_{\sigma,4,1} & L_{\sigma,4,2} & L_{\sigma,4,3} & L_{\sigma,4,4} & L_{\sigma,4,5} \\ L_{\sigma,5,1} & L_{\sigma,5,2} & L_{\sigma,5,3} & L_{\sigma,5,4} & L_{\sigma,5,5} \end{bmatrix} = 10^{-3} \begin{bmatrix} 13.7 & 1.23 & 3.05 & 0.1 & 0 \\ 1.23 & 13.7 & 0.1 & 3.05 & 0 \\ 3.05 & 0.1 & 4.26 & 0.4 & 0 \\ 0.1 & 3.05 & 0.4 & 4.26 & 0 \\ 0 & 0 & 0 & 0 & 0 \end{bmatrix}.$$

The resistances of the considered transformer are as follows (given in Ohms): $R_1 = 0.347$; $R_2 = 0.347$; $R_3 = 0.201$; $R_4 = 0.201$; $R_5 = 5490$. The procedure for the determination of the value of R_5 was reported in [33].

In this model the relationship $\Phi_c(\Theta)$ that accounts for nonlinear magnetic properties of the iron core and hysteresis effect given by Eqs. (6), (7), and (8) is implemented.

8. Measurements and simulation results

Experimental studies consisted of the discharge of the capacitor through the primary winding at several different values of the residual magnetic flux. The use of a capacitor as a power source has provided a relatively high repeatability of the measured transient states independent of the moment of switching and the phenomena at the terminals of the connector [33]. The measurement results of inrush currents are shown in Fig. 10 and the simulation results of inrush currents are shown in Fig. 11. All measurements and simulations were performed at the capacitor C_0 charged to a voltage of 200 V.

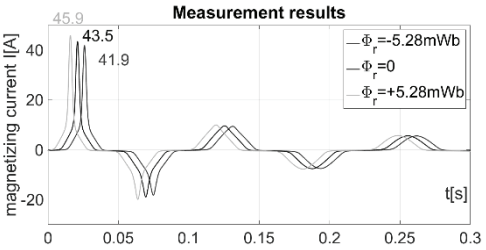

Fig. 10. The results of measurements of the transient state of the magnetizing current i_p, at the different values of residual magnetic flux

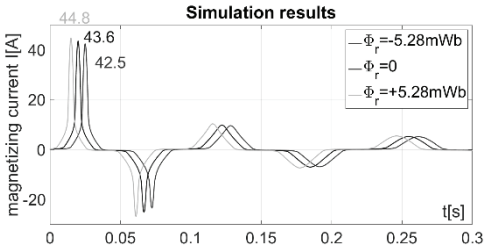

Fig. 11. The results of simulation of the transient state of the magnetizing current i_p, at the different values of residual magnetic flux

The results are given for three different residual magnetic flux values Φ_r = 5.28 mWb, Φ_r = 0 mWb, and Φ_r = –5.28 mWb. A positive value of Φ_r means that the initial magnetic field direction excited by current i_p is consistent with the direction of residual magnetic flux density

B_r. In the case of negative values of Φ_r, the initial direction of the magnetic field excited by current i_p is opposite.

The differences between measurements and simulations are relatively small. The differences between the waveforms of the exciting currents can be reduced by using nonlinear resistance R_5 in the equivalent loop.

9. Conclusions

In this paper the ability of the scalar feedback Preisach model to predict hysteretic behaviour between the common flux Φ_c and the total ampere turns Θ in the singe-phase and multi-winding transformer was implemented. The numerical implementation of the applied model is based on the new analytical distribution function $\rho(\alpha, \beta)$ defined as the functional series of two-dimensional Gauss expressions. The feedback function is represented by the third order polynomial. Hysteresis model is coupled with circuit model of the transformer.

Simulation of the free oscillation waveform in a capacitor discharge test is a relatively critical test of the model. The amplitude of the subsequent oscillations are properly modelled and correspond to the value obtained in the measurements. Good agreement between the phase relationship of simulation and measurement results is also important. This proves the correct approach of classical and anomalous losses in the transformer model. The simulation results indicate the usefulness of the applied circuit modeling methodology for the simulation of the transformer systems in a transient state, taking into account magnetic hysteresis and remanence.

References

[1] Ling P.C.Y., Basak A., *Investigation of magnetizing inrush current in a single-phase transformer*, IEEE Transactions on Magnetics, vol. 24, no. 6, pp. 3217-3222 (1988).

[2] Brunke J.H., Frölich K.J., *Eliminations of transformer inrush currents by controlled switching – Part II: Application and performance considerations*, IEEE Transactions on Power Delivery, vol. 16, no. 2, pp. 281-285 (2001).

[3] Lin C.E., Cheng C.L., Huang C.L., Yeh J.C., *Investigation of magnetizing inrush current in transformers. Part I – Numerical simulation*, IEEE Transactions on Power Delivery, vol. 8, no. 1, pp. 246-253 (1993).

[4] Teape J.W., Slater R.D., Simpson R.R., Wood W.S., *Hysteresis effects in transformers, including ferroresonance*, Proceedings of IEE, vol. 123, no. 2, pp. 153-158 (1976).

[5] Abdulsalam S.G., Xu W., *A sequential phase energization method for transformer inrush current reduction – Transient performance and practical considerations*, IEEE Transactions on Power Delivery, vol. 22, no. 1, pp. 208-216 (2007).

[6] Hayek J.E., *Transformer design as a key for efficiency optimization*, XIX Inter. Conf. on Electrical Machines (ICEM-2010), Rome, Italy, pp. 1-4 (2010).

[7] Jager W.A.G., and Tubbing G.H., *A vector oriented control strategy for a 4-quadrant line side converter*, Fifth European Conference on Power Electronics and Applications (1993), Brighton, pp. 213-218 (1993).

[8] Wilk A., *Internal winding fault detection in a traction transformer using a real-time reference model*, Electromotion, vol. 17, no. 1, pp. 37-46 (2010).

[9] Preisach F., *Über die magnetische Nachwirkung*, Zeitschrift für Physik, Bd.94, 1935, pp. 274-302 (1935).
[11] Jiles D.C., Atherton D.L., *Ferromagnetic hysteresis*, IEEE Transactions on Magnetics, vol. 19 no. 5, pp. 2183-2185 (1983).
[12] Liorzu F., Phelps B., Atherton D.L., *Macroscopic models of magnetization*, IEEE Transactions On Magnetics, vol. 36, no. 2, pp. 418-428 (2000).
[13] Łyskawiński W., Sujka P., Szeląg W., Barański M., *Numerical analysis of hysteresis loss in pulse transformer*, Archives of Electrical Engineering, vol. 60, no. 2, pp. 187-195 (2011).
[14] Jędryczka C., Sujka P., Szeląg W., *The influence of magnetic hysteresis on magnetorheological fluid clutch operation*, COMPEL: The International Journal for Computation and Mathematics in Electrical and Electronic Engineering, vol. 26 no. 2, pp. 711-721 (2009).
[15] Gyselinck J., Dular P., Sadowski N., Leite J., Bastos J., *Incorporation of a Jiles-Atherton vector hysteresis model in 2D FE magnetic field computations*, COMPEL: The International Journal for Computation and Mathematics in Electrical and Electronic Engineering, vol. 23 no. 3, pp. 685-93 (2004).
[16] Knypiński Ł., Nowak L., Sujka P., Radziuk K., *Application of a PSO algorithm for identification of the parameters of Jiles-Atherton hysteresis model*, Archives of Electrical Engineering, vol. 61, no 2, pp. 139-148 (2012).
[17] Krasnosel'skii M.A., Pokrovskii A.V., *Sistemy s gisterezisom (Systems with Hysteresis)*, Nauka, Moskow (1983).
[18] Mayergoyz I.D., *Mathematical models of hysteresis*, IEEE Transactions on Magnetics, vol. MAG-22, no. 5, pp. 603-608 (1986).
[19] Brokate M., Della Tore E., *The wiping-out property of the moving model*, IEEE Transactions on Magnetics, vol. 27 no. 5, pp. 3811-3814 (1991).
[20] Kadar G., Della Torre E., *Hysteresis modeling I: Noncongruency*, IEEE Transactions on Magnetics, vol. 23, no. 5, pp. 2820-2822 (1987).
[21] Iványi A., Füzi J., Szabó Z., *Preisach models of ferromagnetic hysteresis*, Electrical Review (Poland), R. LXXIX 3/2003, pp. 145-150 (2003).
[22] Adly A.A., Hanafy H.H., Abu-Shady S.E., *Utilizing Preisach models of hysteresis in the computation of three-phase transformer inrush currents*, Electric Power System Research, vol. 65, pp. 233-238 (2003).
[23] Faiz J., Saffari S., *Inrush current modeling in a single-phase transformer*, IEEE Transactions on Magnetics, vol. 46, no. 2, pp. 578-581 (2010).
[24] Wilk A., *Representation of magnetic hysteresis in a circuit model of a single-phase transformer*, COMPEL: The International Journal for Computation and Mathematics in Electrical and Electronic Engineering, vol. 34, no. 3, pp. 778-791 (2015).
[25] Wilk A., Nieznanski J., Moson I., *Nonlinear model of a wound iron core traction transformer with the account of magnetic hysteresis*, XIX International Conference on Electrical Machines (ICEM-2010), Rome, Italy, pp. 1-7 (2010).
[26] Wilk A., Pokonski R., *Determination of leakage inductances of multi-winding and single-phase transformer*, The Scientific Papers of Faculty And Control Engineering, Gdansk University of Technology, no. 31, Gdansk, Poland 2011, pp. 145-150 (2011).
[27] Mayergoyz I.D., Adly A.A., *Numerical Implementation of the feedback Preisach model*, IEEE Transactions on Magnetics, vol. 28, no. 5, pp. 2605-2607 (1992).
[28] Della Torre E., Vajda F., *Parameter identification of the complete-moving-hysteresis model using major loop data*, IEEE Transactions on Magnetics, vol. 30 no. 6, pp. 3811-3814 (1994).
[29] Ragusa C., *An analytical method for the identification of the Preisach distribution function*, Journal of Magnetism and Magnetic Materials, vol. 254-255, pp. 259-261 (2003).
[30] Dolinar M., Dolinar D., Štumberger G., Polajžer B., Ritonja J., *A three-phase core-type transformer iron core model with included magnetic cross saturation*, IEEE Transactions on Magnetics, vol. 42, no. 10, pp. 2849-2851 (2006).

[31] Fuchs E.F., You Y., *Measurement of λ-i characteristics of asymmetric three-phase transformers and their applications*, Proc. Ninth International conference on Harmonics and Quality of Power, Orlando, Florida, USA, pp. 91-96 (2000).
[32] More J.J., *The Levenberg-Marquardt algorithm: Implementation and theory*. Lecture Notes in Mathematics, Numerical Analysis, vol. 630, pp. 105-116 (1978).
[33] Wilk A., Michna M., Cichowski A., *Simulation of the remanence influence on the transient states of the single-phase transformer including feedback Preisach model*, 40th Annual Conference of the IEEE Industrial Electronics Society (IECON-2014), Dallas, TX, USA, pp. 875-880 (2014).

ARCHIVES OF ELECTRICAL ENGINEERING VOL. 66(1), pp. 55-75 (2017)

DOI 10.1515/aee-2017-0005

A new algebraic LQR weight selection algorithm for tracking control of 2 DoF torsion system

VINODH KUMAR ELUMALAI[1], RAAJA GANAPATHY SUBRAMANIAN[2]

[1]*School of Electrical Engineering, VIT University*
Vellore, Tamilnadu, 632014, India
e-mail: vinothmepsg@gmail.com

[2]*Eindhoven University of Technology*
5612 AZ Eindhoven, the Netherlands
e-mail: raaja1393@gmail.com

(Received: 30.12.2015, revised: 19.07.2016)

Abstract: This paper proposes a novel linear quadratic regulator (LQR) weight selection algorithm by synthesizing the algebraic Riccati equation (ARE) with the Lagrange multiplier method for command following applications of a 2 degree of freedom (DoF) torsion system. The optimal performance of LQR greatly depends on the elements of weighting matrices ***Q*** and ***R***. However, normally these weighting matrices are chosen by a trial and error approach which is not only time consuming but cumbersome. Hence, to address this issue, blending the design criteria in time domain with the ARE, we put forward an algebraic weight selection algorithm, which makes the LQR design both simple and modular. Moreover, to estimate the velocity of a servo angle, a high gain observer (HGO) is designed and integrated with the LQR control scheme. The efficacy of the proposed control scheme is tested on a benchmark 2 DoF torsion system for a trajectory tracking application. Both the steady state and dynamic characteristics of the proposed controller are assessed. The experimental results accentuate that the proposed HGO based LQR scheme can guarantee the system to attain the design requirements with minimal vibrations and tracking errors.

Key words: ARE, high gain observer, LQR, ***Q*** and ***R*** matrices, 2 DoF torsion system, trajectory tacking

1. Introduction

Due to their inherent stability and robustness characteristics, Linear Quadratic Regulator, a cornerstone of Model Predictive Control and Linear Quadratic Guassian/Loop Transfer Re-

covery (LQG/LTR) Control, finds its applications in many of the engineering and scientific domains [1-2]. The LQR technique is a structured control technique, which can be easily extended to a multi variable system. Moreover, minimizing the quadratic cost function which integrates both states and inputs of the system via penalty matrices, LQR offers an optimal response between speed of response and amount of control input. In the last few decades, several results on LQR: hybrid LQR [3], fuzzy LQR [4], switched LQR [5], to name a few, have been reported in the literature. Moreover, LQR has been successfully applied for a large number of complex systems namely, a double inverted pendulum [6], fuel cell systems [6], and aircraft [7].

However, two major challenges of the LQR design have been the subject of investigation in the last five decades: the choice of $\boldsymbol{Q}$ and $\boldsymbol{R}$ weighting matrices, and the solution of ARE. Both the tasks are known to be highly dependent on the dynamic order of the system and certain operational condition. Since the optimal performance of LQR largely depends on weighting matrices, several results have been reported on optimal selection of $\boldsymbol{Q}$ and $\boldsymbol{R}$ matrices. Sunar and Rao [9], initializing the design variable as diagonal entries of $\boldsymbol{Q}$ and $\boldsymbol{R}$ matrices, proposed a methodology for selecting the state and input matrices of LQR applied to integrated structure design. To save the computational cost with minimal loss in accuracy, they used a substructure decomposition technique. Ohta et al. [10], as an alternate approach, investigated the inverse problem of the LQR controller for a single input system. As a simulation study on a roll autopilot system, they proved that the performance of LQR could be improved if negative diagonal state weights were used in the performance index. Ochi and Kani [11] put forward a new way of placing the LQR poles by solving the differential equations obtained from the Hamilton matrix. Even though this method guarantees that the poles can be located exactly at the desired positions, it does not assure the positive definiteness of the weighting matrix. Moreover, the method does not consider the eigen vector assignment problem and is computationally expensive. Based on the asymptotic modal properties of multivariable LQ regulators, Hiroe et al. [12] proposed a zero addition decoupling (ZED) method, to select the weights of the LQ regulator. The validity of the ZED method was demonstrated on a decoupleing control of an industrial turbine. Choi and Seo [13] presented a new LQR design technique which has the capability to assign not only the eigen values to the desired location but eigen vectors in the least square sense. Moreover, this method can also guarantee the frequency domain characteristics of conventional LQR. Ang et al. [14], using modal control analysis to assess the effect of energy weights on damping ratios, put forward a finite element LQR control technique and applied to vibration control of piezoelectric composite plates. As an alternate approach, several authors have also assessed the efficacy of evolutionary computation techniques like GA and PSO to solve the LQR optimization problem. For instance, Robanti et al. [15] investigated the efficacy of GA to solve the weight optimization problem of LQR on a multi-machine power system. Comparing the performance of GA optimized LQR with those of Bryson's method and a trial and error based method, they reported that the weights optimized via GA yield the best response of all three methods. However, high computational cost and large number of parameter tuning make GA less competitive than particle swarm optimization (PSO). Panda and Pathy [16], comparing the performance of both GA and

PSO based controller designs for a flexible AC transmission system, reported that the PSO based controller yields better performance than that of GA. Similarly, Tasi et al. [17] employed PSO to optimize the gains of a state feedback controller and proved that the tracking performance of PSO optimized LQR is better than that of the linear matrix inequality (LMI) based LQR for automatic fighter tracking problems. Kumar and Jerome [18], utilizing adaptive PSO(APSO) to solve the LQR weight optimization problem and validating the performance of APSO optimized LQR on a benchmark inverted pendulum, reported that the performance of APSO based LQR is better than those of PSO and GA based LQRs.

Nevertheless, high dependency on the parameters of the optimization problem and high computation time limit the use of evolutionary computation technique to solve many of the real world optimization problem. Hence, in this paper, we make an attempt to solve the weight selection problem of LQR by exploring the fundamental relation between the ARE and the Lagrange optimization technique. Computing the solution of ARE, the transformation matrix, as a function of design requirement in time domain and state model, the proposed algebraic approach yields simple mathematical relations for $\boldsymbol{Q}$ and $\boldsymbol{R}$ matrices. The proposed algebraic weight selection algorithm is tested on a benchmark Quanser 2 DoF torsion system for reference following applications. 2 DoF torsion system, which consists of torsional load attached to the shaft of the DC motor via flexible coupling, emulates the dynamics of high gear ratio harmonic drives and light weight transmission shafts. The control objective is to position the torsion module to the desired angle by manipulating the control input given to the DC servo. The system also consists of, along with the optical encoders attached to the shaft and torsion module measure the angular positions, an HGO to estimate the angular velocities. The weights of the LQR are optimized using the proposed algebraic approach and the dynamic and steady state characteristics of the LQR controller framework to follow the reference input is assessed for two test cases namely: sine and square inputs.

The remainder of the paper is structured as follows: Section 2 gives the problem definition and Section 3 describes the algebraic approach for choosing the elements of $\boldsymbol{Q}$ and $\boldsymbol{R}$ matrices based on ARE. Section 4 presents the modeling of the 2-DoF torsion system and the HGO based LQR design control scheme. Section 5 explains the experimental results of the 2 DoF torsion system for tracking applications, and the paper ends with the concluding remarks in Section 6.

2. Problem definition

Consider a linear time invariant (LTI) multivariable system:

$$\dot{\mathbf{X}} = \mathbf{A}\boldsymbol{X}(t) + \mathbf{B}\mathbf{u}(t), \quad t \geq 0, \quad \boldsymbol{X}(0) = \boldsymbol{X}_0, \tag{1}$$

$$\boldsymbol{Y} = \boldsymbol{C}\boldsymbol{X}(t) + \boldsymbol{D}\boldsymbol{u}(t), \quad t \geq 0, \tag{2}$$

where $\boldsymbol{A} \in R^{n\times n}$, $\boldsymbol{B} \in R^{n\times m}$, $\boldsymbol{C} \in R^{p\times n}$, $\boldsymbol{D} \in R^{p\times m}$ are system matrix, input matrix, output matrix and feed-forward matrix, respectively. $\boldsymbol{X}$ is the state vector, $\boldsymbol{u}$ is the control input vector, and $\boldsymbol{Y}$ is the output vector. The objective of the conventional LQR design is to take the states to the desired trajectory by minimizing the following cost function.

$$J(\boldsymbol{u}) = \int_0^{\infty} \left[\boldsymbol{X}^T(t)\boldsymbol{Q}\boldsymbol{X}(t) + \boldsymbol{u}^T(t)\boldsymbol{R}\boldsymbol{u}(t)\right] \mathrm{d}t \,, \tag{3}$$

where $\boldsymbol{Q}$ and $\boldsymbol{R}$ are state and input weighting matrices. The compositions of $\boldsymbol{Q}$ and $\boldsymbol{R}$ elements have large influence on system performance. If the weighting matrices are selected as diagonal matrices, the quadratic performance index is simply a weighted integral of the states and inputs [19]. These weighting matrices are considered as the tuning parameters of LQR by observing $\boldsymbol{Q}$ as state error penalty and $\boldsymbol{R}$ as penalty on control input. The elements of $\boldsymbol{Q}$ and $\boldsymbol{R}$ matrices depend on the number of state and input variables respectively. For the LQR to yield stable response, $\boldsymbol{Q}$ should be a positive semi definite matrix and $\boldsymbol{R}$ should be a positive definite matrix. The solution of following ARE, transformation matrix $\boldsymbol{P}$, can be used to obtain the state feedback gain of LQR.

$$\boldsymbol{A}^T\boldsymbol{P} + \boldsymbol{P}\boldsymbol{A} + \boldsymbol{Q} - \boldsymbol{P}\boldsymbol{B}\boldsymbol{R}^{-1}\boldsymbol{B}^T\boldsymbol{P} = 0 \,. \tag{4}$$

LQR computes the optimal control input given in (5).

$$\boldsymbol{u} = -\boldsymbol{K}\boldsymbol{X} \,, \tag{5}$$

where $\boldsymbol{K}$ is the state feedback gain matrix determined using the following Lagrange multiplier optimization technique.

$$\boldsymbol{K} = \boldsymbol{R}^{-1}\boldsymbol{B}^T\boldsymbol{P} \,. \tag{6}$$

Since the choice of $\boldsymbol{Q}$ and $\boldsymbol{R}$ weighting matrices affect convergence of a quadratic function, it is important to select these matrices by ensuring that both the state and input constraints are met in addition to the stability criteria [20]. However, normally, a trial and error method is used to choose the values of $\boldsymbol{Q}$ and $\boldsymbol{R}$ matrices, which is laborious and time consuming. Hence, to address this weight selection problem in the following section, we formulate an algebraic approach to arrive at simple mathematical relations for these weighting matrices.

3. Algebraic approach for *Q* and *R* matrices selection

Consider an LTI system represented in controllable canonical form as given below.

$$\dot{\mathbf{X}} = \begin{bmatrix} 0 & 1 & 0 & 0 & 0 & 0 \\ 0 & 0 & 1 & 0 & 0 & 0 \\ 0 & 0 & 0 & 1 & 0 & 0 \\ 0 & 0 & 0 & 0 & 1 & 0 \\ 0 & 0 & 0 & 0 & 0 & 1 \\ A_{61} & A_{62} & A_{63} & A_{64} & A_{65} & A_{66} \end{bmatrix} \begin{bmatrix} x_1 \\ x_2 \\ x_3 \\ x_4 \\ x_5 \\ x_6 \end{bmatrix} + \begin{bmatrix} 0 \\ 0 \\ 0 \\ 0 \\ 0 \\ B_{61} \end{bmatrix} \mathbf{u} . \tag{7}$$

We formulate the methodology with the assumption that the system (A, B, C) is both controllable and observable. Selecting the penalty matrices $\boldsymbol{Q}$ and $\boldsymbol{R}$ as diagonal matrices reduces the cost function to a quadratic term and simplifies the optimization problem. Hence, the penalty matrices are assumed to be:

$$\boldsymbol{Q} = \begin{bmatrix} q_1 & 0 & 0 & 0 & 0 & 0 \\ 0 & q_2 & 0 & 0 & 0 & 0 \\ 0 & 0 & q_3 & 0 & 0 & 0 \\ 0 & 0 & 0 & q_4 & 0 & 0 \\ 0 & 0 & 0 & 0 & q_5 & 0 \\ 0 & 0 & 0 & 0 & 0 & q_6 \end{bmatrix}, \quad \boldsymbol{R} = [r] . \tag{8}$$

The solution of ARE, transformation matrix $\boldsymbol{P}$, is a symmetric matrix, which can be represented as:

$$\boldsymbol{P} = \begin{bmatrix} p_{11} & p_{12} & p_{13} & p_{14} & p_{15} & p_{16} \\ p_{12} & p_{22} & p_{23} & p_{24} & p_{25} & p_{26} \\ p_{13} & p_{23} & p_{33} & p_{34} & p_{35} & p_{36} \\ p_{14} & p_{24} & p_{34} & p_{44} & p_{45} & p_{46} \\ p_{15} & p_{25} & p_{35} & p_{45} & p_{55} & p_{56} \\ p_{16} & p_{26} & p_{36} & p_{46} & p_{56} & p_{66} \end{bmatrix} . \tag{9}$$

Substituting the weighting matrices and a transformation matrix in (6) yields

$$\boldsymbol{K} = \boldsymbol{R}^{-1}\boldsymbol{B}^T \quad \boldsymbol{P} = \frac{B_{61}}{r}\begin{bmatrix} p_{16} & p_{26} & p_{36} & p_{46} & p_{56} & p_{66} \end{bmatrix}. \tag{10}$$

The coefficients of $\boldsymbol{P}$ matrix, namely p_{16}, p_{26}, p_{36}, p_{46}, p_{56} and p_{66}, can be obtained using the ARE given in (11).

$$\left\{\begin{bmatrix}
2(p_{16}A_{61})+q_1-\frac{B_{61}^2}{r}p_{16}^2 & A_{61}p_{26}+p_{11}+p_{16}A_{62}-\frac{B_{61}^2}{r}p_{26}p_{16} & A_{61}p_{36}+p_{12}+p_{16}A_{63}-\frac{B_{61}^2}{r}p_{36}p_{16} & A_{61}p_{46}+p_{13}+p_{16}A_{64}-\frac{B_{61}^2}{r}p_{46}p_{16} & A_{61}p_{56}+p_{14}+p_{16}A_{65}-\frac{B_{61}^2}{r}p_{56}p_{16} & A_{61}p_{66}+p_{15}+p_{16}A_{66}-\frac{B_{61}^2}{r}p_{66}p_{16} \\
A_{61}p_{26}+p_{11}+p_{16}A_{62}-\frac{B_{61}^2}{r}p_{26}p_{16} & 2(p_{26}A_{62}+p_{12})+q_2-\frac{B_{61}^2}{r}p_{26}^2 & A_{62}p_{36}+p_{13}+p_{26}A_{63}+p_{22}-\frac{B_{61}^2}{r}p_{36}p_{26} & A_{62}p_{46}+p_{14}+p_{26}A_{64}+p_{23}-\frac{B_{61}^2}{r}p_{46}p_{26} & A_{62}p_{56}+p_{15}+p_{26}A_{65}+p_{24}-\frac{B_{61}^2}{r}p_{56}p_{26} & A_{62}p_{66}+p_{16}+p_{26}A_{66}+p_{25}-\frac{B_{61}^2}{r}p_{66}p_{26} \\
A_{61}p_{36}+p_{12}+p_{16}A_{63}-\frac{B_{61}^2}{r}p_{36}p_{16} & A_{62}p_{36}+p_{13}+p_{26}A_{63}+p_{22}-\frac{B_{61}^2}{r}p_{36}p_{26} & 2(p_{36}A_{63}+p_{23})+q_3-\frac{B_{61}^2}{r}p_{36}^2 & A_{63}p_{46}+p_{24}+p_{36}A_{64}+p_{33}-\frac{B_{61}^2}{r}p_{46}p_{36} & A_{63}p_{56}+p_{25}+p_{36}A_{65}+p_{34}-\frac{B_{61}^2}{r}p_{56}p_{36} & A_{63}p_{66}+p_{26}+p_{36}A_{65}+p_{36}-\frac{B_{61}^2}{r}p_{66}p_{36} \\
A_{61}p_{46}+p_{13}+p_{16}A_{64}-\frac{B_{61}^2}{r}p_{46}p_{16} & A_{62}p_{46}+p_{14}+p_{26}A_{64}+p_{23}-\frac{B_{61}^2}{r}p_{46}p_{26} & A_{63}p_{46}+p_{24}+p_{36}A_{64}+p_{33}-\frac{B_{61}^2}{r}p_{46}p_{36} & 2(p_{46}A_{64}+p_{34})+q_4-\frac{B_{61}^2}{r}p_{46}^2 & A_{64}p_{56}+p_{35}+p_{46}A_{65}+p_{44}-\frac{B_{61}^2}{r}p_{56}p_{46} & A_{64}p_{66}+p_{36}+p_{46}A_{66}+p_{45}-\frac{B_{61}^2}{r}p_{66}p_{46} \\
A_{61}p_{56}+p_{14}+p_{16}A_{65}-\frac{B_{61}^2}{r}p_{56}p_{16} & A_{62}p_{56}+p_{15}+p_{26}A_{65}+p_{24}-\frac{B_{61}^2}{r}p_{56}p_{26} & A_{63}p_{56}+p_{25}+p_{36}A_{65}+p_{34}-\frac{B_{61}^2}{r}p_{56}p_{36} & A_{64}p_{56}+p_{35}+p_{46}A_{65}+p_{44}-\frac{B_{61}^2}{r}p_{56}p_{46} & 2(p_{56}A_{65}+p_{45})+q_5-\frac{B_{61}^2}{r}p_{56}^2 & A_{65}p_{66}+p_{46}+p_{56}A_{66}+p_{55}-\frac{B_{61}^2}{r}p_{66}p_{56} \\
A_{61}p_{66}+p_{15}+p_{16}A_{66}-\frac{B_{61}^2}{r}p_{66}p_{16} & A_{62}p_{66}+p_{16}+p_{26}A_{66}+p_{25}-\frac{B_{61}^2}{r}p_{66}p_{26} & A_{63}p_{66}+p_{26}+p_{36}A_{66}+p_{35}-\frac{B_{61}^2}{r}p_{66}p_{36} & A_{64}p_{66}+p_{36}+p_{46}A_{66}+p_{45}-\frac{B_{61}^2}{r}p_{66}p_{46} & A_{65}p_{66}+p_{46}+p_{56}A_{66}+p_{55}-\frac{B_{61}^2}{r}p_{66}p_{56} & 2(p_{66}A_{66}+p_{56})+q_6-\frac{B_{61}^2}{r}p_{66}^2
\end{bmatrix}\right\}=0. \tag{11}$$

According to LQR control law, the closed loop state equation of the system can be represented as

$$\dot{\boldsymbol{X}}(t)=[\boldsymbol{A}-\boldsymbol{BK}]\boldsymbol{X}(t)=\left[\boldsymbol{A}-\boldsymbol{B}\boldsymbol{R}^{-1}\boldsymbol{B}^T\boldsymbol{P}\right]\boldsymbol{X}(t). \tag{12}$$

The actual characteristic equation of the system can be written as:

$$\left|sI-\boldsymbol{A}+\boldsymbol{BK}\right|=0, \tag{13}$$

$$\left|\begin{bmatrix} s & 0 & 0 & 0 & 0 & 0 \\ 0 & s & 0 & 0 & 0 & 0 \\ 0 & 0 & s & 0 & 0 & 0 \\ 0 & 0 & 0 & s & 0 & 0 \\ 0 & 0 & 0 & 0 & s & 0 \\ 0 & 0 & 0 & 0 & 0 & s \end{bmatrix}-\begin{bmatrix} 0 & 1 & 0 & 0 & 0 & 0 \\ 0 & 0 & 1 & 0 & 0 & 0 \\ 0 & 0 & 0 & 1 & 0 & 0 \\ 0 & 0 & 0 & 0 & 1 & 0 \\ 0 & 0 & 0 & 0 & 0 & 1 \\ A_{61} & A_{62} & A_{63} & A_{64} & A_{65} & A_{66} \end{bmatrix}+\begin{bmatrix} 0 & 0 & 0 & 0 & 0 & B_{61} \end{bmatrix}^T\frac{B_{61}}{r}\begin{bmatrix} p_{16} & p_{26} & p_{36} & p_{46} & p_{56} & p_{66} \end{bmatrix}\right|=0, \tag{14}$$

$$s^6+\left(\frac{B_{61}^2}{r}p_{66}-A_{66}\right)s^5+\left(\frac{B_{61}^2}{r}p_{56}-A_{65}\right)s^4+\left(\frac{B_{61}^2}{r}p_{46}-A_{64}\right)s^3+\left(\frac{B_{61}^2}{r}p_{36}-A_{63}\right)s^2 +\left(\frac{B_{61}^2}{r}p_{26}-A_{62}\right)s+\left(\frac{B_{61}^2}{r}p_{16}-A_{61}\right)=0. \tag{15}$$

Since the system considered here has two identical torsion modules, the desired characteristic equation of the sixth order system is assumed as

$$\left(s^2+2\zeta\omega_n s+\omega_n^2\right)^3=0\,, \tag{16}$$

where ζ and ω_n are the desired damping ratio and natural frequency of the system.

$$s^6+6\zeta\omega_n s^5+\left(\omega_n^2+8\omega_n^2\zeta^2+2\omega_n^2\left(1+2\zeta^2\right)\right)s^4+\left(8\zeta\omega_n^3+2\zeta\omega_n^3\left(1+2\zeta^2\right)\right)s^3 +\left(\omega_n^4+8\omega_n^4\zeta^2+2\omega_n^4\left(1+2\zeta^2\right)\right)s^2+\left(\omega_n^4+8\omega_n^4\zeta^2+2\omega_n^4\left(1+2\zeta^2\right)\right)s^2+6\zeta\omega_n^5 s+\omega_n^6=0. \tag{17}$$

Comparing Equations (15) and (17), the expressions for p_{16}, p_{26}, p_{36}, p_{46}, p_{56}, and p_{66} can be written as:

$$p_{16}=\frac{r}{B_{61}^2}\left[A_{61}+\omega_n^6\right], \tag{18}$$

$$p_{26}=\frac{r}{B_{61}^2}\left[A_{62}+6\zeta\omega_n^5\right], \tag{19}$$

$$p_{36}=\frac{r}{B_{61}^2}\left[A_{63}+\omega_n^4+8\omega_n^4\zeta^2+2\omega_n^4\left(1+2\zeta^2\right)\right], \tag{20}$$

$$p_{46}=\frac{r}{B_{61}^2}\left[A_{64}+8\zeta\omega_n^3+2\zeta\omega_n^3\left(1+2\zeta^2\right)\right], \tag{21}$$

$$p_{56}=\frac{r}{B_{61}^2}\left[A_{65}+\omega_n^2+8\omega_n^2\zeta^2+2\omega_n^2\left(1+2\zeta^2\right)\right], \tag{22}$$

$$p_{66}=\frac{r}{B_{61}^2}\left[A_{66}+6\zeta\omega_n\right]. \tag{23}$$

From the 1st row and 1st column of ARE given in (11)

$$2\left(p_{16}A_{61}\right)+q_1-\frac{B_{61}^2}{r}p_{16}^2=0\,. \tag{24}$$

By rearranging (24), the expression for $\frac{q_1}{r}$ can be obtained as:

$$\frac{q_1}{r}=\frac{1}{B_{61}^2}\left[p_{16}^2-2\left(p_{16}A_{61}\right)\right]. \tag{25}$$

Similarly, p_{12} is obtained using the element available in 1st row 3rd column of (11).

$$p_{12} = \frac{B_{61}^2}{r} p_{36} p_{16} - p_{16} A_{63} - A_{61} p_{36} . \tag{26}$$

The element in 2nd row and 2nd column of (11) is:

$$2(p_{26} A_{62} + p_{12}) + q_2 - \frac{B_{61}^2}{r} p_{26}^2 = 0 . \tag{27}$$

Substituting (26) into (27) and rearranging the expression yields

$$\frac{q_2}{r} = \frac{1}{B_{61}^2} \left[p_{26}^2 - 2\left(p_{26} A_{62} + p_{36} p_{16} - p_{16} A_{63} - A_{61} p_{36} \right) \right]. \tag{28}$$

Likewise, the element available in 3rd row and 3rd column of (11) can be written as:

$$2(p_{36} A_{63} + p_{23}) + q_3 - \frac{B_{61}^2}{r} p_{36}^2 = 0 . \tag{29}$$

Expressions for p_{23} and p_{14} are obtained from 2nd row and 4th column and 1st row and 5th column of (11) respectively.

$$p_{23} = \frac{B_{61}^2}{r} p_{46} p_{26} - A_{62} p_{46} - p_{14} - p_{26} A_{64} , \tag{30}$$

$$p_{14} = \frac{B_{61}^2}{r} p_{56} p_{16} - A_{61} p_{56} - p_{16} A_{65} . \tag{31}$$

Substituting (30) and (31) into Equation (29) and rearranging

$$\frac{q_3}{r} = \frac{1}{B_{61}^2} \left[p_{36}^2 - 2\left(p_{36} A_{63} + p_{46} p_{26} - A_{62} p_{46} - p_{56} p_{16} + A_{61} p_{56} + p_{16} A_{65} - p_{26} A_{64} \right) \right]. \tag{32}$$

Similarly, the element available in 4th row and 4th column of (11) can be written as:

$$2(p_{46} A_{64} + p_{34}) + q_4 - \frac{B_{61}^2}{r} p_{46}^2 = 0 . \tag{33}$$

The terms p_{34}, p_{25} are obtained from 3rd row 5th column and 2nd row 6th column respectively from (11).

$$p_{34} = \frac{B_{61}^2}{r} p_{56} p_{36} - A_{63} p_{56} - p_{25} - p_{36} A_{65} , \tag{34}$$

$$p_{25} = \frac{B_{61}^2}{r} p_{66} p_{26} - A_{62} p_{66} - p_{16} - p_{26} A_{66} . \tag{35}$$

Substituting (34) and (35) into equation (33) and rearranging,

$$\frac{q_4}{r}=\frac{1}{B_{61}^2}\left[p_{46}^2-2\left(p_{46}A_{64}+p_{56}p_{36}-A_{63}p_{56}-p_{66}p_{26}+A_{62}p_{66}+p_{16}+p_{26}A_{66}-p_{36}A_{65}\right)\right]. \quad (36)$$

The element available in 5th row and 5th column of (11) is

$$2(p_{56}A_{65}+p_{45})+q_5-\frac{B_{61}^2}{r}p_{56}^2=0. \quad (37)$$

The term p_{45} is obtained from 4th row 6th column from (11).

$$p_{45}=\frac{B_{61}^2}{r}p_{66}p_{46}-A_{64}p_{66}-p_{36}-p_{46}A_{66}. \quad (38)$$

Substituting (38) into (37) and rearranging,

$$\frac{q_5}{r}=\frac{1}{B_{61}^2}\left[p_{56}^2-2\left(p_{56}A_{65}+p_{66}p_{46}-A_{64}p_{66}-p_{36}-p_{46}A_{66}\right)\right]. \quad (39)$$

Similarly, from the element available in 6th row and 6th column of (11),

$$2(p_{66}A_{66}+p_{56})+q_6-\frac{B_{61}^2}{r}p_{66}^2=0. \quad (40)$$

Upon rearranging,

$$\frac{q_6}{r}=\frac{1}{B_{61}^2}\left[p_{66}^2-2\left(p_{66}A_{66}+p_{56}\right)\right]. \quad (41)$$

The expressions (25), (28), (32), (36), (39) and (41) exhibit the relation between $\boldsymbol{Q}$ and $\boldsymbol{R}$ weighting matrices of LQR and the design requirements in time domain and state model. Equation (42) summarizes the expressions for weighting matrices.

$$\begin{aligned}
\frac{q_1}{r}&=\frac{1}{B_{61}^2}\left[p_{16}^2-2\left(p_{16}A_{61}\right)\right],\\
\frac{q_2}{r}&=\frac{1}{B_{61}^2}\left[p_{26}^2-2\left(p_{26}A_{62}+p_{36}p_{16}-p_{16}A_{63}-A_{61}p_{36}\right)\right],\\
\frac{q_3}{r}&=\frac{1}{B_{61}^2}\left[p_{36}^2-2\left(p_{36}A_{63}+p_{46}p_{26}-A_{62}p_{46}-p_{56}p_{16}+A_{61}p_{56}+p_{16}A_{65}-p_{26}A_{64}\right)\right],\\
\frac{q_4}{r}&=\frac{1}{B_{61}^2}\left[p_{46}^2-2\left(p_{46}A_{64}+p_{56}p_{36}-A_{63}p_{56}-p_{66}p_{26}+A_{62}p_{66}+p_{16}+p_{26}A_{66}-p_{36}A_{65}\right)\right],\\
\frac{q_5}{r}&=\frac{1}{B_{61}^2}\left[p_{56}^2-2\left(p_{56}A_{65}+p_{66}p_{46}-A_{64}p_{66}-p_{36}-p_{46}A_{66}\right)\right],\\
\frac{q_6}{r}&=\frac{1}{B_{61}^2}\left[p_{66}^2-2\left(p_{66}A_{66}+p_{56}\right)\right].
\end{aligned} \quad (42)$$

The elements of $\boldsymbol{Q}$ matrix can be obtained using the desired specifications by fixing the

value of ***R*** matrix which is taken as scalar in the present example because the plant taken for experimentation is a single input multi output system. It can be observed that the expression (42) yields a simple relation to select the elements of penalty matrices according to the design criteria given in time domain. Hence, from the design perspective, knowing the desired damping ratio, natural frequency of the system and the state space matrices of the plant, one can determine the elements of weighting matrices and in turn the optimal controller gain (***K***) can be obtained using (6) by solving the ARE. In the next section, the validation of the proposed algebraic weight selection algorithm on a 2 DoF torsion system for tracking application is presented.

4. LQR tracking control of 2 DoF torsion system

The 2 DoF torsion system, as shown in Fig. 1, consists of a DC motor whose shaft is attached to a series of torsion modules via flexible linkage. Table 1 gives the nominal plant parameters of the 2 DoF torsion system. When the voltage given to the motor is varied, the corresponding shaft position varies, which in turn alters the position of the torsion modules.

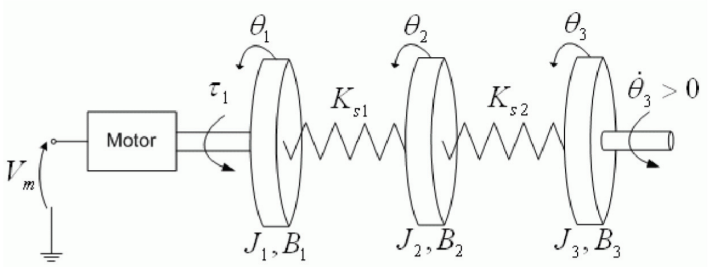

Fig. 1. Schematic diagram of 2-DoF torsion system

Applying Newton's second law to the schematic diagram shown in Fig. 1, and assuming the states $\boldsymbol{X} = \begin{bmatrix}\theta_1 & \theta_2 & \theta_3 & \dot{\theta}_1 & \dot{\theta}_2 & \dot{\theta}_3\end{bmatrix}^T$ and the input $U = V_m$, we obtain the following state space model:

$$\begin{bmatrix}\dot{\theta}_1\\ \dot{\theta}_2\\ \dot{\theta}_3\\ \ddot{\theta}_1\\ \ddot{\theta}_2\\ \ddot{\theta}_3\end{bmatrix} = \begin{bmatrix} 0 & 0 & 0 & 1 & 0 & 0\\ 0 & 0 & 0 & 0 & 1 & 0\\ 0 & 0 & 0 & 0 & 0 & 1\\ \dfrac{-K_{s1}}{J_1} & \dfrac{K_{s1}}{J_1} & 0 & \dfrac{-B_1}{J_1} & 0 & 0\\ \dfrac{K_{s1}}{J_2} & \dfrac{-(K_{s1}+K_{s2})}{J_2} & \dfrac{K_{s2}}{J_2} & 0 & \dfrac{-B_2}{J_2} & 0\\ 0 & \dfrac{K_{s2}}{J_3} & \dfrac{-K_{s2}}{J_3} & 0 & 0 & \dfrac{-B_3}{J_3}\end{bmatrix}\begin{bmatrix}\theta_1\\ \theta_2\\ \theta_3\\ \dot{\theta}_1\\ \dot{\theta}_2\\ \dot{\theta}_3\end{bmatrix} + \begin{bmatrix}0\\ 0\\ 0\\ \dfrac{1}{J_1}\\ 0\\ 0\end{bmatrix} V_m, \qquad (43)$$

$$\boldsymbol{Y} = \begin{bmatrix} 1 & 0 & 0 & 0 & 0 & 0 \\ 0 & 1 & 0 & 0 & 0 & 0 \\ 0 & 0 & 1 & 0 & 0 & 0 \end{bmatrix} \begin{bmatrix} \theta_1 \\ \theta_2 \\ \theta_3 \\ \dot{\theta}_1 \\ \dot{\theta}_2 \\ \dot{\theta}_3 \end{bmatrix}. \tag{44}$$

Table 1. List of parameters of 2-DoF torsion system

Symbol	Description	Value	Unit
J_1	Equivalent moment of inertia as seen at SRV02 load shaft	0.0022	Kg · m^2
B_1	Equivalent viscous damping coefficient as seen at SRV02 load shaft	0.0150	N.m.s/rad
J_2	Equivalent moment of inertia from the torsion module-1	$5.46 \cdot 10^{-4}$	Kg · m^2
B_2	Equivalent viscous damping coefficient as seen at SRV02 load shaft	0.0010	N · m · s/rad
J_3	Equivalent moment of inertia from torsion module-2	$5.45 \cdot 10^{-4}$	Kg · m^2
B_3	Equivalent viscous damping coefficient as seen at SRV02 load shaft	0.0030	N · m · s/rad
K_{s1}	First flexible coupling stiffness	1.0000	N · m/rad
K_{s2}	Second flexible coupling stiffness	1.0000	N · m/rad

Figure 2 depicts the proposed LQR controller framework for tracking control of torsion system. The system consists of an LQR controller whose weights are determined using the algebraic approach and an HGO which estimates the unmeasured angular velocities. The following section explains the need and design of HGO in torsion system.

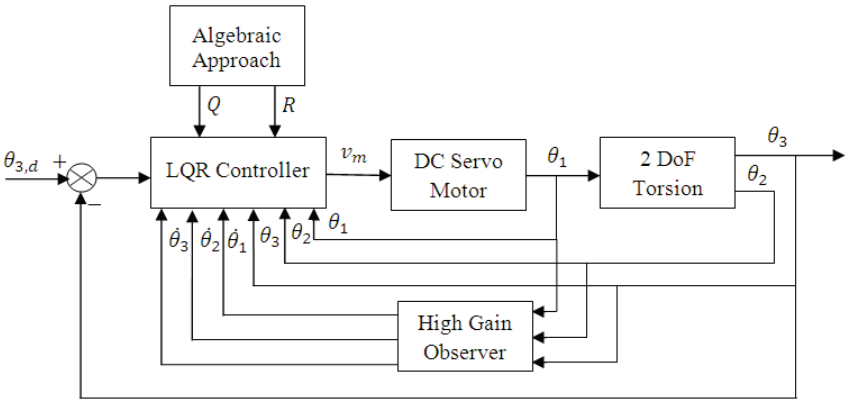

Fig. 2. Proposed controller strategy for tracking control of 2 DoF torsion

4.1. High gain observer

To implement LQR control, full state vector information must be available for feedback. The 2 DoF torsion system has six state variables, namely three angular positions and three angular velocities. The torsion angular positions can be measured accurately using the position encoders. However, the angular velocities are normally determined either by differentiating the measured angular position or through tachometers in practical cases. In both the cases, the velocity signal is contaminated by noise, and this degrades the performance of the closed loop torsion system [21]. Hence, an HGO is included in the feedback path to estimate the angular velocities of torsional loads.

The state variables of the system can be grouped as position and velocity vectors, namely $\boldsymbol{X}_p$ and $\boldsymbol{X}_v$.

$$\boldsymbol{X}_p = \theta = \begin{bmatrix} \theta_1 \\ \theta_2 \\ \theta_3 \end{bmatrix}, \tag{45}$$

$$\boldsymbol{X}_v = \dot{\theta} = \begin{bmatrix} \dot{\theta}_1 \\ \dot{\theta}_2 \\ \dot{\theta}_3 \end{bmatrix}. \tag{46}$$

The output vector is:

$$\boldsymbol{Y} = \boldsymbol{X}_p = \begin{bmatrix} \theta_1 \\ \theta_2 \\ \theta_3 \end{bmatrix}. \tag{47}$$

The equation of motion of torsion system can be expressed in state space form as:

$$\boldsymbol{X}_v = \dot{\boldsymbol{X}}_p, \tag{48}$$

$$\dot{\boldsymbol{X}}_v = \Phi(\boldsymbol{X}_p, \boldsymbol{X}_v, \boldsymbol{u}), \tag{49}$$

$$\boldsymbol{Y} = \boldsymbol{X}_p. \tag{50}$$

The structure of the HGO is:

$$\dot{\hat{\boldsymbol{X}}}_p = \hat{\boldsymbol{X}}_v + \boldsymbol{H}_p\left(\boldsymbol{Y} - \hat{\boldsymbol{X}}_p\right), \tag{51}$$

$$\dot{\hat{\boldsymbol{X}}}_v = \boldsymbol{H}_v\left(\boldsymbol{Y} - \hat{\boldsymbol{X}}_p\right) + \Phi(\boldsymbol{X}_p, \boldsymbol{X}_v, t), \tag{52}$$

where $\dot{\hat{\boldsymbol{X}}}_p$ and $\dot{\hat{\boldsymbol{X}}}_v$

represent the dynamic estimates of the angular positions and angular velocities, respectively. The HGO consists of two constant gain matrices, $\boldsymbol{H}_p$ and $\boldsymbol{H}_v$. which are assumed to be a diagonal matrix as given below.

$$\boldsymbol{H}_p = \begin{bmatrix} h_{p1} & 0 & 0 \\ 0 & h_{p2} & 0 \\ 0 & 0 & h_{p3} \end{bmatrix}; \quad H_v = \begin{bmatrix} h_{v1} & 0 & 0 \\ 0 & h_{v2} & 0 \\ 0 & 0 & h_{v3} \end{bmatrix}. \tag{53}$$

The convergence rate of the HGO can be varied by adjusting the gain matrices $\boldsymbol{H}_p$ and $\boldsymbol{H}_v$. The error between the actual states and estimated states via HGO is given as:

$$\dot{\tilde{\boldsymbol{X}}}_p = -\boldsymbol{H}_p \tilde{\boldsymbol{X}}_p + \tilde{\boldsymbol{X}}_v, \tag{54}$$

$$\dot{\tilde{\boldsymbol{X}}}_v = -\boldsymbol{H}_v \tilde{\boldsymbol{X}}_p + \delta(\boldsymbol{X}, \hat{\boldsymbol{X}}), \tag{55}$$

where:

$$\delta(\boldsymbol{X}, \hat{\boldsymbol{X}}) = \Phi(\boldsymbol{X}_p, \boldsymbol{X}_v, \boldsymbol{u}) - \Phi_0(\hat{\boldsymbol{X}}_p, \hat{\boldsymbol{X}}_v, \boldsymbol{u}) \text{ and } \tilde{\boldsymbol{X}}_i = \boldsymbol{X}_i - \hat{\boldsymbol{X}}_i,\ i = 1, 2, 3.$$

In the absence of disturbance signal, the asymptotic error convergence can be achieved by selecting the observer gain matrix given in (56) as Hurwitz [22]. Moreover, to guarantee the convergence of the error dynamic equation, the eigenvalues of matrix $\boldsymbol{F}$ should be located on the left half of s-plane.

$$\boldsymbol{F} = \begin{bmatrix} -\boldsymbol{H}_p & I_{3\times3} \\ -\boldsymbol{H}_v & 0_{3\times3} \end{bmatrix}. \tag{56}$$

5. Experimental results and discussion

The test bed consists of a Quanser SRV02 rotary servo base unit, Q8 data acquisition board, power amplifier and two torsion modules. Fig. 3 illustrates the connection diagram of experimental setup. The rotary servo base unit contains a 10 V DC motor equipped with the internal gearbox. The torsional load consists of two inertial disc masses which are located at different anchor points along the support bar. To measure the angular positions, both the DC motor and the torsion modules have optical encoders, which offer a resolution of 4096 counts per revolution. The Q8 USB hardware-in-loop (HIL) data acquisition board has 8 digital inputs and 8 pulse width modulated (PWM) digital outputs, and it is capable of reaching 4 kHz sampling rate. The control algorithm implemented in SIMULINK communicates with the hardware using QUARC interfacing software. In addition, the system contains a Volt-PAQ power amplifier, which provides a regulated ±10 V at 1 A, to amplify the control signal given to the DC motor.

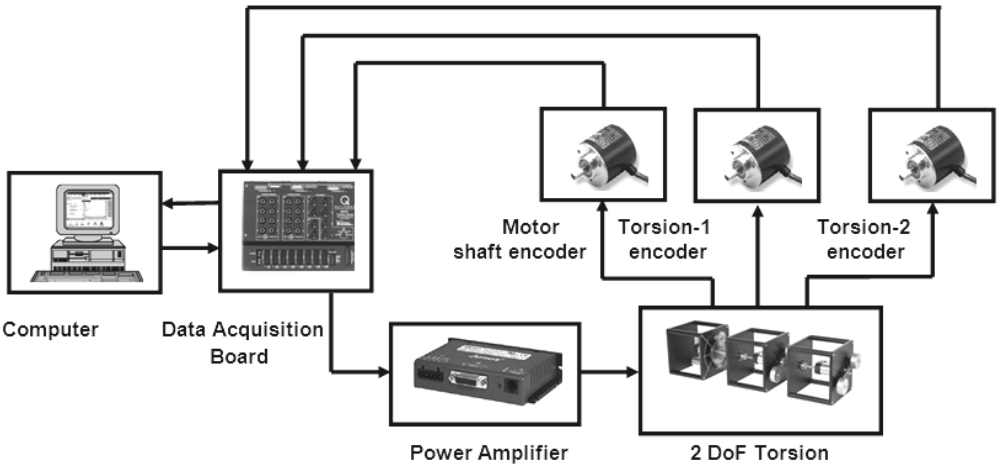

Fig. 3. Connection Diagram of 2-DoF torsion system

By substituting the plant parameters given in Table 1 into the state space model given in (45) and (46), the following state space matrices are obtained.

$$\boldsymbol{A}=\begin{bmatrix} 0 & 0 & 0 & 1 & 0 & 0 \\ 0 & 0 & 0 & 0 & 1 & 0 \\ 0 & 0 & 0 & 0 & 0 & 1 \\ -457.8 & 457.8 & 0 & -6.9 & 0 & 0 \\ 1831.1 & -3662.2 & 1831.1 & 0 & -1.8 & 0 \\ 0 & 1883.6 & -1883.6 & 0 & 0 & -5.5 \end{bmatrix},\quad \boldsymbol{B}=\begin{bmatrix} 0 \\ 0 \\ 0 \\ 457.84 \\ 0 \\ 0 \end{bmatrix},$$

$$\boldsymbol{C}=\begin{bmatrix} 1 & 0 & 0 & 0 & 0 & 0 \\ 0 & 1 & 0 & 0 & 0 & 0 \\ 0 & 0 & 1 & 0 & 0 & 0 \end{bmatrix}.$$

Then, the above model is transformed into following controllable canonical form:

$$\boldsymbol{A}=\begin{bmatrix} 0 & 1 & 0 & 0 & 0 & 0 \\ 0 & 0 & 1 & 0 & 0 & 0 \\ 0 & 0 & 0 & 1 & 0 & 0 \\ 0 & 0 & 0 & 0 & 1 & 0 \\ 0 & 0 & 0 & 0 & 0 & 1 \\ -1.4\times10^{-7} & -2.9\times10^{7} & -5.2\times10^{6} & -6.4\times10^{4} & 6014 & -14.2 \end{bmatrix},\quad \boldsymbol{B}=\begin{bmatrix} 0 \\ 0 \\ 0 \\ 0 \\ 0 \\ 1.5\times10^{9} \end{bmatrix},$$

$$\boldsymbol{C} = \begin{bmatrix} 1 & 0 & 0 & 0 & 0 & 0 \\ 0 & 1 & 0 & 0 & 0 & 0 \\ 0 & 0 & 1 & 0 & 0 & 0 \end{bmatrix}.$$

The design requirement of the control scheme is that it should provide a tracking response, which has an overshoot of less than 10% and a settling time of 0.6 sec. Moreover, the tracking error should be less than 5 deg (2% criterion of the torsion load angle), and the control effort should not reach the saturation level when the above criteria are met. To compute the state feedback gain for the above design requirement, first, the damping ratio of the system is determined using the 2% criterion of settling time, and it is calculated as 0.1. Then, using the corresponding damping ratio and natural frequency, the desired characteristic equation is formulated, and with the aid of the proposed algebraic approach the following $\boldsymbol{Q}$ and $\boldsymbol{R}$ weighing matrices are obtained.

$$\boldsymbol{Q} = \begin{bmatrix} 5.04 & 0 & 0 & 0 & 0 & 0 \\ 0 & 6.08 & 0 & 0 & 0 & 0 \\ 0 & 0 & 2.49 & 0 & 0 & 0 \\ 0 & 0 & 0 & 0.33 & 0 & 0 \\ 0 & 0 & 0 & 0 & 6\times10^{-6} & 0 \\ 0 & 0 & 0 & 0 & 0 & 4\times10^{-10} \end{bmatrix}, \quad \boldsymbol{R} = [200],$$

Using the above weighing matrices and the state space model of the system, the solution of ARE ($\boldsymbol{P}$) and the state feedback gain matrix ($\boldsymbol{K}$) are calculated and given below.

$$\boldsymbol{P} = 10^5 \times \begin{bmatrix} 2441.4 & 0 & 0 & 0 & 0 & 0 \\ 0 & 4.3 & 0 & 0 & 0 & 0 \\ 0 & 0 & 2959.7 & 0 & 0 & 0 \\ 0 & 0 & 0 & 65.4 & 0 & 0 \\ 0 & 0 & 0 & 0 & 4.7 & 0 \\ 0 & 0 & 0 & 0 & 0 & 0.01 \end{bmatrix},$$

$$\boldsymbol{K} = [0.15 \quad 0.29 \quad 0.19 \quad 0.04 \quad 0.0003 \quad 7.7\times10^{-6}].$$

Gain matrices of the HGO to estimate the velocity component of the system are found to be:

$$\boldsymbol{H}_p = \begin{bmatrix} 10 & 0 & 0 \\ 0 & 16 & 0 \\ 0 & 0 & 23 \end{bmatrix}, \quad \boldsymbol{H}_v = \begin{bmatrix} 12 & 0 & 0 \\ 0 & 27 & 0 \\ 0 & 0 & 34 \end{bmatrix}.$$

The corresponding eigenvalues of the closed loop system are:

$$\lambda_{cl} = \begin{bmatrix} -398.76 & -398.26+0.29i & -398.26-0.29i & -1.6+0.05i & -1.6-0.05i & -1.5 \end{bmatrix}.$$

It is worth to note that the first three eigenvalues are placed far away from the imaginary axis of s-plane. Hence, it will assist in improving the speed of response of the system. Similarly, three eigenvalues which are placed sufficiently close to imaginary axis will aid in reducing the amount of control input given to the system. Before implementing the proposed control framework in real time, the simulation was carried out in MATLAB. On verifying that the design meets the specification, we also have implemented it on a real time 2 DoF torsion system.

5.1. Trajectory tracking

To test the tracking response of the controller, a square trajectory with amplitude of 300 deg at a frequency of 0.1 Hz is given as a reference signal. Fig. 4 shows both the simulated and experimental tracking response of the controller for the square wave trajectory. Simulated angular position response has an overshoot of 4.16% with a settling time of 0.88 sec, whereas the overshoot of the experimental output is 9.6% with a settling time is 0.92 sec. It is worth to note that the experimental results meet the design requirements both interms of steady state error and overshoot. However, there is a small deviation in real time output from the simulated one due to the presence of noise in measurement. To assess the reference following performance of the control scheme, the integral square error (ISE) is calculated and given in Table 2. Fig. 5 illustrates the estimated velocities of the torsion system using HGO and Table 3 gives the tracking error of HGO for all three velocities. Minimum value of IAE suggests that the estimated output is very close to the actual output.

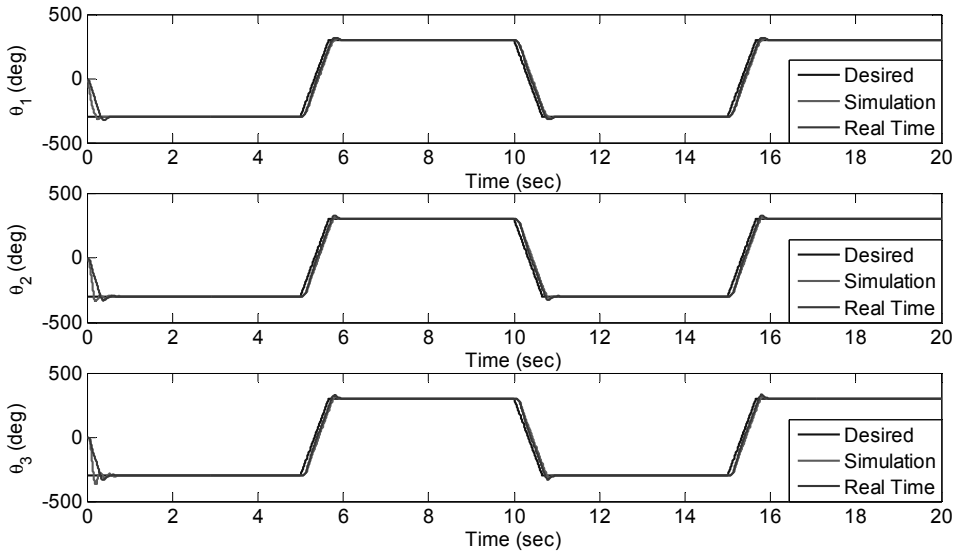

Fig. 4. Square trajectory tracking response

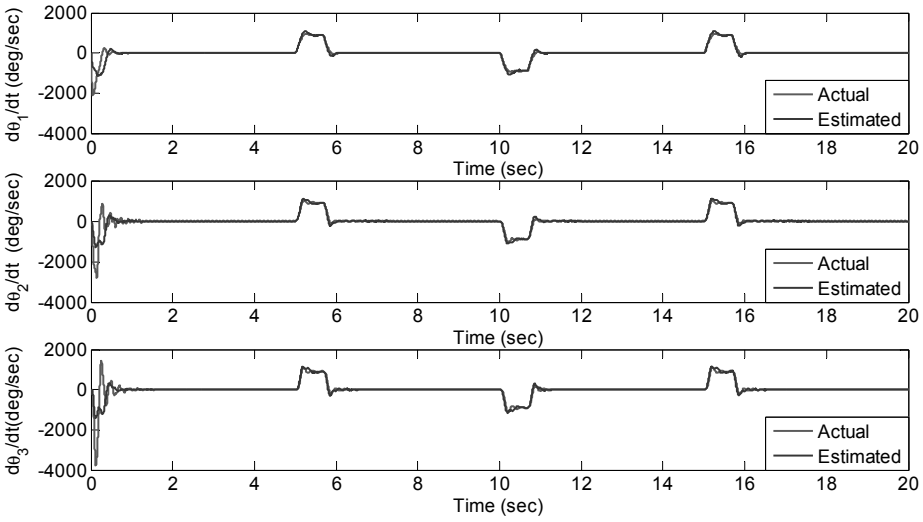

Fig. 5. Estimated velocities of HGO for square trajectory

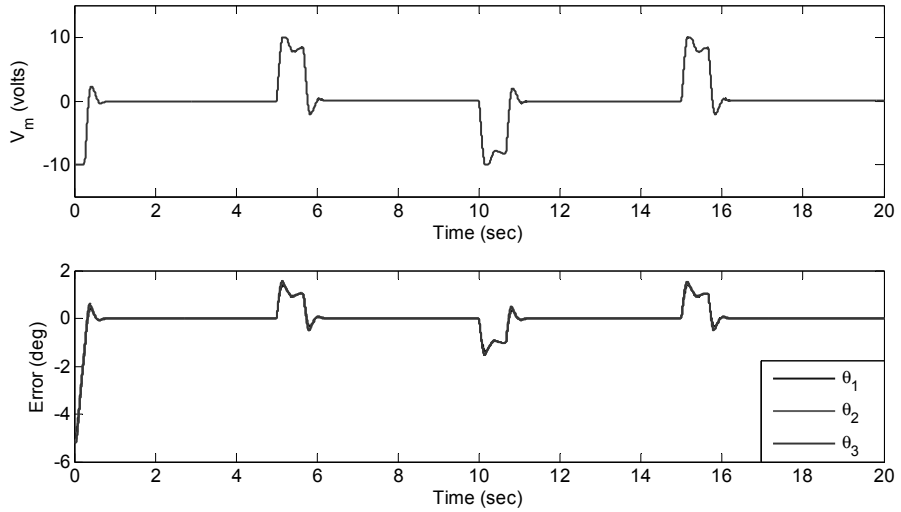

Fig. 6. Control signal and tracking error of square trajectory

The control input applied to motor for tracking the desired tracjectory and the error between the reference trajectory and actual trajectory signal are shown in Fig. 6. The maximun tracking error is found to be less than 1.5 deg, which accentuates that the controller effectively follows the given trajectory.

5.2. Sinusoidal trajectory

The performance of the controller framework to track the continuously changing reference signal is validated using a sinusoidal signal of amplitude 300 deg at a frequency of 0.1 Hz.

Fig. 7, which shows the sinusoidal tracking response, highlights that the LQR controller closely tracks the reference trajectory. The estimated velocities of HGO and the control signal applied to DC servo along with the tracking error are shown in Figs. 8 and 9, respectively. It can be seen that the rate of convergence of the system is faster with the maximum tracking error of 0.3 deg, which is negligible in case of torsional position control applications. Moreover, the error converges exactly to desired trajectory variations with very minimal spikes occuring concurrently at random intervals due to the presence of noise in real time.

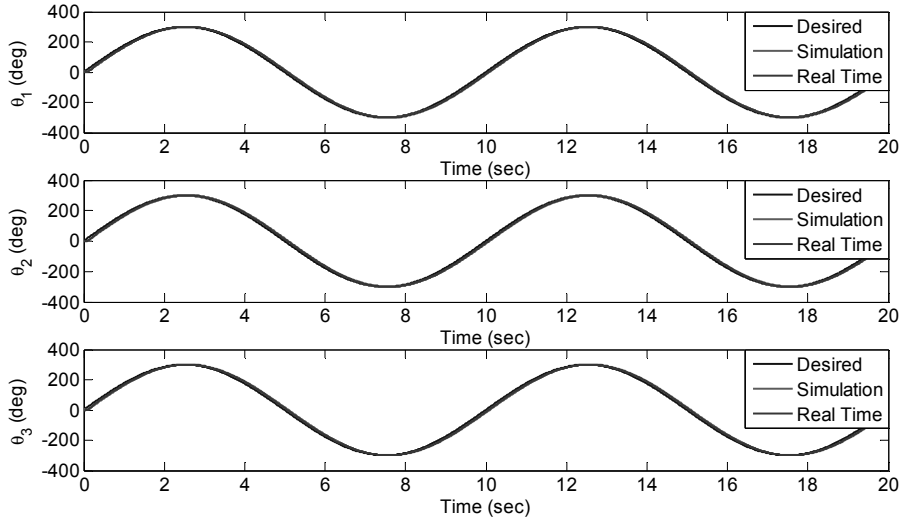

Fig. 7. Sinusoidal tracking response

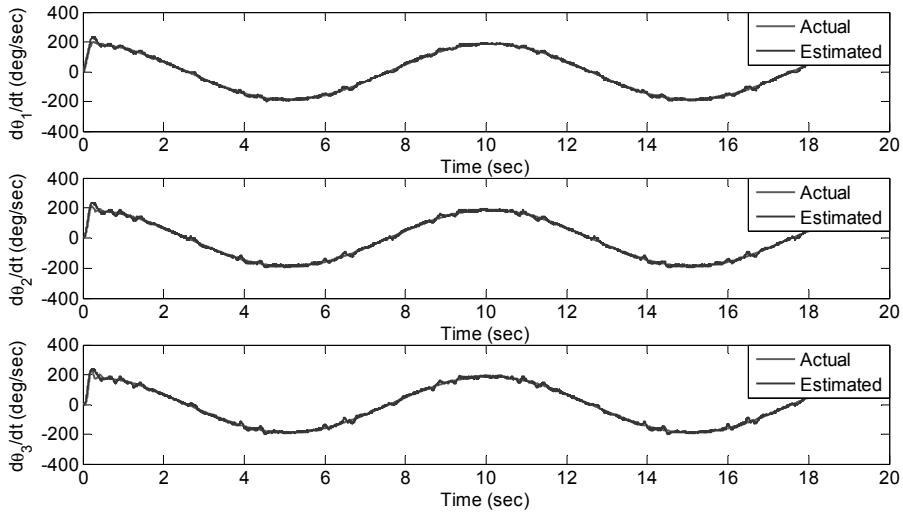

Fig. 8. HGO response for sinusoidal trajectory

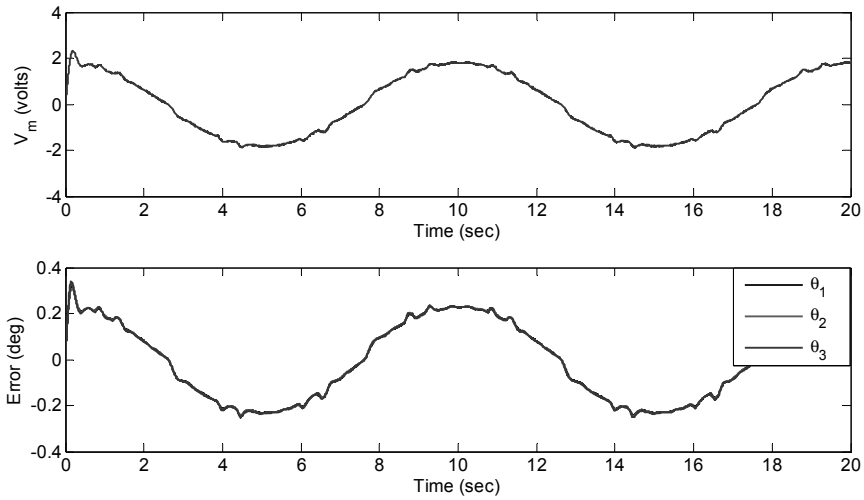

Fig. 9. Control signal and tracking error of sine trajectory

Table 2. ISE of LQR control scheme for test trajectories

Test signal	**Simulation**	**Real Time**
Square	0.0007	0.0029
Sine	0.0015	0.0022

Table 3. IAE of HGO for test trajectories

Test signal	θ_1	θ_2	θ_3
Square	0.0312	0.0215	0.0351
Sine	0.0231	0.0226	0.0218

6. Conclusion

Even though the optimal performance of LQR is highly dependent on weighting matrices Q and R, normally, these weighting matrices are chosen based on the trial and error approach, which is not only tedious but also time consuming. Hence, in this paper, to address the weight selection problem of LQR, we have put forward an algebraic weight selection algorithm, by synthesizing the ARE with the Lagrange optimization technique. Simple mathematical expressions for weighting matrices have been obtained as a function of the design criteria and state model. The efficacy of the proposed methodology has been tested on a benchmark 2 DoF torsion system for tracking applications. To estimate the angular velocities of servo and torsional loads, an HGO has been integrated with the LQR design. Two test cases namely sine and square trajectories have been given as a reference signal and the efficacy of the control scheme to follow the input with minimal vibration and error has been assessed. The experi-

mental results accentuate that the proposed control scheme can make the torsional load meet the design criteria with minimal vibrations and reduced tracking error.

References

[1] da Fonseca Neto J.V., Abreu I.S., da Silva F.N., *Neural-Genetic Synthesis for State-Space Controllers Based on Linear Quadratic Regulator Design for Eigenstructure Assignment*, IEEE Transactions on Systems, Man, and Cybernetics–Part B: Cybernetics, vol. 40, no. 2, pp. 266-285 (2010).

[2] Das S., Pan I., Halder K., Das S., Gupta A., *LQR based improved discrete PID controller design via optimum selection of weighting matrices using fractional order integral performance index*, Applied Mathematical Modelling, vol. 37, no. 6, pp. 4253-4268 (2013).

[3] Bevilacqua R., Lehmann T., Romano M., *Development and experimentation of LQR/APF guidance and control for autonomous proximity maneuvers of multiple spacecraft*, Acta Astronautica, vol. 68, no. 8, pp. 1260-1275 (2011).

[4] Tao C., Taur J., Chen Y., *Design of a parallel distributed fuzzy LQR controller for the twin rotor multi-input multi-output system,* Fuzzy Sets and Systems, vol. 161, no. 15, pp. 2081-2103 (2010).

[5] Balandat M., Zhang W., Abate A., *On infinite horizon switched LQR problems with state and control constraints,* Systems & Control Letters, vol. 61, no. 4, pp. 464-471 (2012).

[6] Wang L., Ni H., Zhou W., Pardalos P.M., Fang J., Fei M., *MBPOA-based LQR controller and its application to the double-parallel inverted pendulum system,* Engineering Applications of Artificial Intelligence, vol. 36, pp. 262-268 (2014).

[7] Niknezhadi A., Allué-Fantova M., Kunusch C., Ocampo-Martínez C., *Design and implementation of LQR/LQG strategies for oxygen stoichiometry control in PEM fuel cells based systems*, Journal of Power Sources, vol. 196, no. 9, pp. 4277-4282 (2011).

[8] Liu H., Lu G., Zhong Y., *Robust LQR Attitude Control of a 3-DoF Laboratory Helicopter for Aggressive Maneuvers*, IEEE Transactions on Industrial Electronics, vol. 60, no. 10, pp. 4627-4636 (2013).

[9] Sunar M., Rao S.S., *Optimal Selection of Weighting Matrices in Integrated Design of Structures/Controls*, AIAA Journal, vol. 31, no. 4, pp. 714-720 (1993).

[10] Ohta H., Kakinuma M., Nikiforuk P.N., *Use of Negative Weights in Linear Quadratic Regulator Synthesis*, Journal of Guidance, Control and Dynamics, vol. 14, no. 4, pp. 791-796 (1991).

[11] Ochi Y., Kanai K., *A New Way of Pole Placement in LQR and its Application to Flight Control*, Proc. Conf. AIAA Guidance, Navigation and Control, pp. 1295-1301 (1993).

[12] Hiroe T., Morimoto T., Inoue S.I., Takamatsu H., *A New Method for Selecting Weighting Matrices of LQ Regulators and its Application to an Industrial Turbine*, Proc. 32nd Conf. on Decision and Control, pp. 3333-3334 (1993).

[13] Choi J.W., Seo Y.B., *LQR Design with Eigenstructure Assignment Capability*, IEEE Transactions on Aerospace and Electronic System, vol. 35, no. 2, pp. 700-708 (1999).

[14] Ang K.K., Wang S.Y., Quek S.T., *Weighted Energy Linear Quadratic Regulator Vibration Control of Piezoelectric Composite Plates*, Smart Materials and Structures, vol. 11, no. 1, pp. 98-106 (2002).

[15] Robandia I., Nishimori K., Nishimura R., Ishihara N., *Optimal feedback control design using genetic algorithm in multimachine power system*, Electrical Power and Energy Systems, vol. 23, no. 4, pp. 263-271 (2001).

[16] Panda S., Padhy N.P., *Comparison of particle swarm optimization and genetic algorithm for FACTS-based controller design*, Applied Soft Computing, vol. 8, no. 4, pp. 1418-1427 (2008).

[17] Tsai S.J., Huo C.L., Yang Y.K., Sun T.Y., *Variable feedback gain control design based on particle swarm optimizer for automatic fighter tracking problems*, Applied Soft Computing, vol. 13, no. 1, pp. 58-75 (2013).

[18] Vinodh K.E., Jerome J., *An Adaptive Particle Swarm Optimization Algorithm for Robust Trajectory Tracking of a Class of Under Actuated System*, Archives of Electrical Engineering, vol. 63, no. 3, pp. 345-365 (2014).

[19] Desineni S.N., *Optimal Control Systems*, CRC press (2003).
[20] Oral O., Çetin L., Uyar E., *A novel method on selection of Q And R matrices in the theory of optimal control*, International Journal of Systems Control, vol. 1, no. 2, pp. 84-92 (2010).
[21] Wang G., *Observer based feedback control methods for an under actuated robot system. M.S Thesis*, Simon Fraser University, Canada, November (2003).
[22] Khalil H.K., Praly L., *High gain observers in nonlinear feedback control*, International Journal of Robust and Nonlinear Control, vol. 24, no. 6, pp. 993-1015 (2014).

ARCHIVES OF ELECTRICAL ENGINEERING VOL. 66(1), pp. 77-87 (2017)

DOI 10.1515/aee-2017-0006

Optimal load distribution estimation for fault location in electric power distribution systems

YOUSSEF MENCHAFOU[1], MUSTAPHA ZAHRI[2], MOHAMED HABIBI[2], HASSANE EL MARKHI[1]

[1]*Laboratory of Signals, Systems and Components*
Sidi Mohamed Ben Abdellah University, Fez, Morocco
e-mail: {youssef.menchafou/hassane.elmarkhi}@usmba.ac.ma

[2]*Laboratory of Electrical Engineering and Energy Systems*
Ibn Tofail University, Kenitra, Morocco
e-mail: mustapha.zahri@gmail.com, mohamed.habibi@hotmail.com

(Received: 19.04.2016, revised: 19.07.2016)

Abstract: Accurate fault location in an electric power distribution system (EPDS) is important in maintaining system reliability. Diverse methods have been proposed in the past. These methods whither require measurements at each load point or use single-step loads compensation, which is hardly available in practical uses. In this paper, a simple technique to bypass the load problems is proposed. The method requires calculating an optimal load distribution using the total load seen from the substation (The rated power of distribution transformers) and the network topology. The optimal load distribution is used as a fictive distribution to replace the real unknown one in fault location (FL) algorithms. The effectiveness of the proposed technique is demonstrated using a mathematical formulation first, and next, by several simulations with a classic iterative fault location algorithm. The test results are obtained from the numerical simulation using the data of a distribution line recognized in the literature.

Key words: electric power distribution systems, fault location, fictive load distribution, load variation

1. Introduction

Power distribution systems play important roles in modern society. When distribution system outages occur, speedy and precise fault location is crucial in accelerating system restoration, reducing outage time and significantly improving system reliability. This allows consequently improving the quality of services and customer satisfaction. Nevertheless, Owing to the expansion of distribution networks, their radial topology, and the existence of short and heterogeneous lines and intermediate loads, it is very difficult and complicated to locate the fault in these networks.

In the past, various fault location algorithms have been developed. Novosel et al. (1998) make use of apparent impedance, defined as the ratio of selected voltage to current based on

fault type and faulted phases, to locate faults in [1]. In [2], Das (1998) locates the faulted section and next the distance to the fault in this section is calculated. Yang and Springs (1998) propose a fault location method which corrects the fault resistance effects in [3]. The method proposed by Das et al. (2000) in [4] used the fundamental frequency voltages and currents measured at a line terminal before and during the fault. In [5] the method proposed by Saha and Rosolowski (2002) estimates the fault location by comparing the measured impedance with the calculate feeder impedance assuming faults each section line. Choi et al. (2004) locating faults by solving a quadratic equation resulting from the direct circuit analysis in [6]. Senger et al. (2005) in [7] proposed a method that was based on measurement provided by intelligent electronics Devices (IEDs). In [8] Kim et al. (2007) estimated fault location on distribution feeders using Power Quality monitoring data. An extended fault location method for generalized distribution systems is presented in [9] by Salim et al. (2009). A way to optimally place faulted circuit indicators along the feeder is developed in [10] by Almeida et al. (2011). Methods to reduce and eliminate the uncertainty about the fault location are discussed by authors of [11, 12] (2012). In [13], Sadeh et al. (2013) suggested a new algorithm for radial distribution systems using modal analysis. Wanjing et al. presented a novel method based on two types of fault location approaches using line to neutral or line to line measurement at substation in [14] (2014). In [15], Zahri et al. (2014) proposed a new hybrid method based on ANN and Apparent impedance calculation to determinate the faulty section of line. A reduced algorithm for fault location in EPDS is suggested by Zahri et al, in [16] (2015), utilizing voltages and currents measurement only at the sub-station as input data to calculate the fault current, and therefore, avoid the iterative aspect of the classic algorithm for single line to ground fault location and reduce its computational charge.

However, fault location approaches for transmission lines are generally not applicable to distribution systems, because of their inherent characteristic, such as unbalance and lack of measuring meters in each load point.

According to literature review, it's shown that existing fault location methods require iterative short circuit analysis or iteratively calculating voltages and currents at different segments. Nevertheless, individually these methods do not fully consider the characteristics of distribution systems (unbalanced operation, presence of intermediate loads, laterals, and time-varying load profile), which significantly affect their performance. Except for [6] and [9], the previously cited methods do not account for the time-varying load profile. This intrinsic characteristic of EPDS has a detrimental effect on the fault locators' accuracy, since the load data during the fault period is a required input for any impedance-based method. The approach described in [6, 9] uses a single-step compensation of loads, which requires measurements at each load point. However, these measurements are hardly available in practical EPDS.

Considering the limitations mentioned previously. In this paper, a mathematical development is presented to determinate the optimal load distribution. It is considered as an imaginary distribution, calculated using the total load seen from the substation and the network topology. To show the technique performances, a comparison is performed between different load distributions using a fault location algorithm recognized in literature.

The remainder of this paper is organized as follows: the optimal load distribution formulation and the iterative fault location algorithm are presented in Sections 2 and 3 respectively, the test results are shown in Section 4, whereas the conclusion of this work is presented in Section 5.

2. Optimal load distribution formulation

The load demand in EPDS depends on the consumer type (residential, industrial or commercial) and may vary with many factors. Also, impedance-based fault-location methodlogies are dependent on the system loading during the fault. If the system has a different load profile during the algorithm execution, this will lead to errors [9]. The minimum errors correspond to the optimal load profile (distribution).

In order to determinate the optimal load distribution, the following mathematical development is done using a simplified modeling of a distribution network illustrated in Figs. 1 and 2. The fault location is calculated using the sending-end voltages and currents, line parameters and load current. Consequently, the errors on the fault location are computed as a function of load distribution variation.

2.1. Pre-fault mathematical development

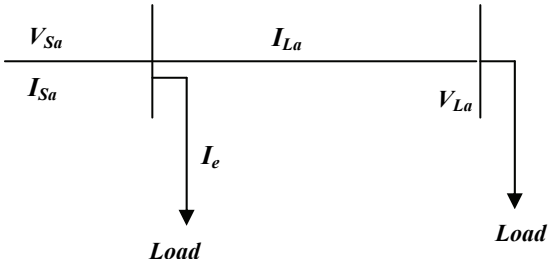

Fig. 1. Pre-fault simplified distribution network modeling

where: I_{Sa} is the phase a pre-fault sending-end current; V_{Sa} is the phase a pre-fault sending-end voltage; I_e is the first pre-fault load current; Z_a is the line impedance; V_{La} is the phase a pre-fault voltage at the end of the line section.

Considering the system illustrated in Fig. 1, the following equations can be obtained:

$$V_{Sa} = Z_a \cdot l \cdot I_{La} + V_{La}\,, \tag{1}$$

$$V_{Sa} - V_{La} = Z_a \cdot l \cdot I_{La}\,, \tag{2}$$

$$V_{Sa} - V_{La} = Z_a \cdot l \cdot \left(I_{Sa} - I_e\right). \tag{3}$$

Since all the loads after the section illustrated in Fig. 1 are represented as one equivalent load Z_e, and the total current dispatched to it is I_{La}, Z_e is then computed by Equation (4):

$$Z_e = \frac{V_{Sa}}{I_{Sa} - I_e} - \left(Z_a \cdot l\right). \tag{4}$$

2.2. Mathematical development during the fault

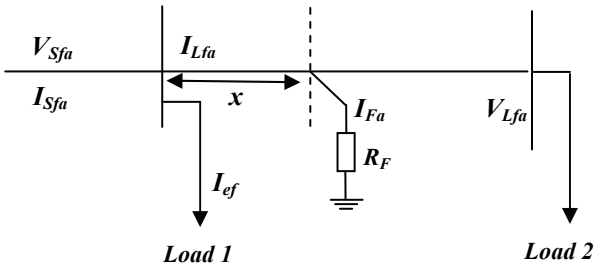

Fig. 2. During-fault simplified distribution network modeling

where: I_{Sfa} is the phase a sending-end current during the fault; V_{Sfa} is the phase a sending-end voltage during the fault; I_{ef} is the first load current during the fault; Z_a is the line impedance; V_{Lfa} is the phase a voltage at the end of the line during the fault; I_{Fa} is the phase a fault current.

Referring to Fig. 2, the following equations can be obtained:

$$\begin{cases} V_{Sfa} = Z_a \cdot x \cdot I_{Lfa} + R_F \cdot I_{Fa}, \\ R_F \cdot I_{Fa} = V_{Lfa} + Z_a \cdot (l - x) \cdot \left(I_{Lfa} - I_{Fa}\right), \end{cases} \tag{5}$$

$$\begin{cases} V_{Sfa} - R_F \cdot I_{Fa} = Z_a \cdot x \cdot \left(I_{Sfa} - I_{ef}\right), \\ R_F \cdot I_{Fa} - V_{Lfa} = Z_a \cdot (l - x) \cdot \left(I_{Sfa} - I_{ef} - I_{Fa}\right), \end{cases} \tag{6}$$

$$\begin{cases} R_F = \dfrac{V_{Sfa} - Z_a \cdot x \cdot \left(I_{Sfa} - I_{ef}\right)}{I_{Fa}}, \\ x = \dfrac{V_{Sfa} - V_{Lfa}}{Z_a \cdot I_{Fa}} - \dfrac{I_{Sfa} - I_{ef} - I_{Fa}}{I_{Fa}} \cdot l. \end{cases} \tag{7}$$

Furthermore, the load voltage during fault can be obtained by (8):

$$V_{Lfa} = Z_e \cdot \left(I_{Sfa} - I_{ef} - I_{Fa}\right),$$

$$V_{Lfa} = \left(\frac{V_{Sa}}{I_{Sa} - I_e} - Z_a \cdot l\right) \cdot \left(I_{Sfa} - I_{ef} - I_{Fa}\right). \tag{8}$$

Using Equations (7) and (8), the fault distance can be estimated by (9):

$$x = \frac{1}{Z_a \cdot I_{Fa}} \cdot \left(V_{Sfa} - \left(I_{Sfa} - I_{ef} - I_{Fa}\right) \cdot \left(\frac{V_{Sa}}{I_{Sa} - I_e}\right)\right). \tag{9}$$

From (9) it is possible to obtain the fault distance from the parameters of the system: the fault current, the sending-end pre-fault voltage and the sending-end during-fault voltage. However, the important parameter is the load current since its variation allows to determinate the optimal errors, and therefore, estimates the optimal load distribution.

3. Iterative fault location algorithm

After determination of the optimal load distribution using the mathematical development, it's necessary to test the reliability of the technique by simulations. To reach that, the iterative fault location algorithm presented next is used [15, 17]:

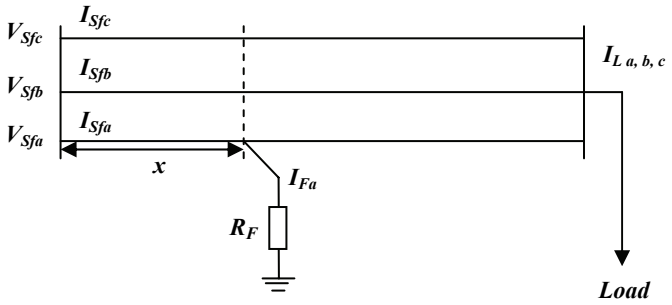

Fig. 3. Single-phase-to-ground fault modeling

Referring to the single line-to-ground fault illustrated in Fig. 3, the sending-end voltage during the disturbance is given by (10):

$$V_{Sfa} = V_{Fa} + x \cdot \left(Z_{aa} \cdot I_{Sfa} + Z_{ab} \cdot I_{Sfb} + Z_{ac} \cdot I_{Sfc} \right). \tag{10}$$

Supposing the fault impedance strictly resistive and constant, (10) may be expanded into its real and imaginary parts:

$$\begin{bmatrix} V_{Sfar} \\ V_{Sfai} \end{bmatrix} = \begin{bmatrix} M_{1a} & I_{Fmr} \\ M_{2a} & I_{Fmi} \end{bmatrix} \begin{bmatrix} x \\ R_{Fa} \end{bmatrix}. \tag{11}$$

From (11), the fault distance may be calculated as a function of the sending-end voltages and currents, as well as the line parameters:

$$\begin{bmatrix} x \\ R_F \end{bmatrix} = \frac{1}{M_{1a} \cdot I_{Fai} - M_{2a} \cdot I_{Far}} \begin{bmatrix} I_{Fai} & -I_{Far} \\ -M_{2a} & M_{1a} \end{bmatrix} \begin{bmatrix} V_{Sfar} \\ V_{Sfai} \end{bmatrix}, \tag{12}$$

where the subscript indices *r* and *i* represent, respectively, the variables real and imaginary parts, the variables are as follows: V_{Sfa} is the phase a sending-end voltages (in volts); x is the fault point to local bus distance (in kilometers); I_{Fa} is the fault current (in amperes).

Also, M_{1m} and M_{2m} are defined in (13) and (14)

$$M_{1m} = \sum_{k} (Z_{mkr} \cdot I_{Skr} - Z_{mki} \cdot I_{Ski}) , \tag{13}$$

$$M_{2m} = \sum_{k} (Z_{mkr} \cdot I_{Ski} - Z_{mki} \cdot I_{Skr}) , \tag{14}$$

where k indicates the phases a, b and c; Z_{mk} is the impedance between phase m and k [Ω/km]; I_{Sk} is the phase k sending-end current (in amperes).

The fault distance is then estimated by (15):

$$x = \frac{I_{Fai} \cdot V_{Sfar} - I_{Far} \cdot V_{Sfai}}{M_{1a} \cdot I_{Fai} - M_{2a} \cdot I_{Far}} . \tag{15}$$

4. Tests and results

4.1. Optimal load distribution formulation test

First, the optimal load distribution formulation test is done for determining the optimal load distribution. The test's system is constituted by two sections of a 20 kV distribution line. Their lengths are 2 km and 1 km, respectively. The currents of the first load I_{ef} and the second load ($I_{af} - I_{ef}$) are varied, since they are complementary. Based on this variation the errors on the fault distance are calculated and the minimum errors correspond to an optimal load pair (load 1, load 2).

On the Fig. 4, the errors on fault distance varies according to the current of the first load I_{ef} between "I_{af} /100" and "I_{af}" (with I_{af} is the total current during the fault), since I_{af} = 239.1857, I_{ef} varies between [2.3919-239, 1857].

To determinate the optimal load distribution, or in other words the value of I_{ef} which gives the minimum errors, the module of the errors in Fig. 4 is computed, the results are illustrated in Fig. 5.

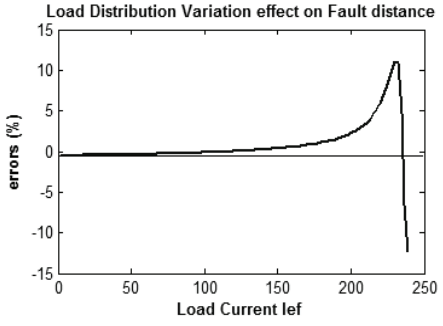

Fig. 4. Errors on the fault distance according to the current of the first load

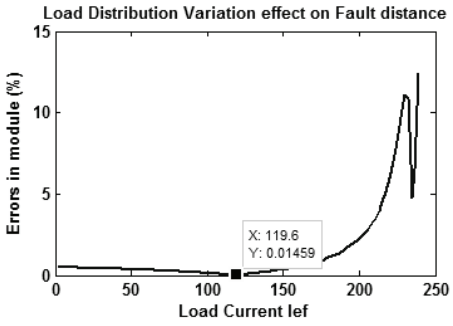

Fig. 5. Module of errors on the fault distance according to the current of the first load

On the Fig. 5, it can easily be seen that the error is null for the value "I_{ef} = 119.6" which represents 50% of the current I_{ef}, since I_{ef} /2 = 239.1857 / 2 = 119.59285.

Therefore, from the figures below, we can conclude that:

– The Load distribution variation influences the accuracy of the fault location methods.

– The optimal load distribution which gives the minimum errors is around 50% of the total load. Thus, the optimal load distribution is the pair (50%, 50%) this pair can be called "the balanced loads distribution".

4.2. Application for the iterative fault location algorithm

To verify performances of this method, we have conducted several simulations using data from a distribution system recognized in literature [18].

The system that we have studied is a part of the underground distribution network. It is a line from 20 KV distribution network of total length 22.5 km, composed of 6 sections of different lengths and simulated using distributed parameter line model as shown in Table 1.

Table 1. Studied sections of lines parameters

Input voltages [KV]	$Vs = 11.547,\ U = 20$
R_F [ohms]	10
line impedance [ohms/km]	$Z_1 = 0.56 + j0.831,\ \ Z_0 = 0.845 + j\ 2.742$
line section length[km]	$l_1 = 2.4;\ l_2 = 4;\ l_3 = .4;\ l_4 = 4;\ l_5 = 4.1;\ l_6 = 4$

Using Matlab [19] as simulation tool, 26 fault cases are simulated at different FL between 0-100%, for fault resistance $R_F = 10\ \Omega$ and for different load distributions as explained in Table 2:

– balanced loads distribution,
– increasing loads distribution,
– decreasing loads distribution,
– total load at the first load point,
– total load at the last load point.

Table 2. Different load distributions

Load distribution (KVA) for each bus	**1**	**2**	**3**	**4**	**5**	**6**
Balanced loads distribution	15	15	15	15	15	15
Increasing loads distribution	0.1	5	10	20	25	29.9
Decreasing loads distribution	29.5	25	20	10	5	0.1
Total load at the first load point	89.5	0.1	0.1	0.1	0.1	0.1
Total load at last load point	0.1	0.1	0.1	0.1	0.1	89.5

The fault distance is calculated for each case using the currents and voltages at the input of the line. The sending-end currents and voltages are computed considering a real load distribution. The errors on fault location obtained using the real load distribution are compared with

those obtained using the others as imaginary load distributions in order to determinate the optimal load distribution.

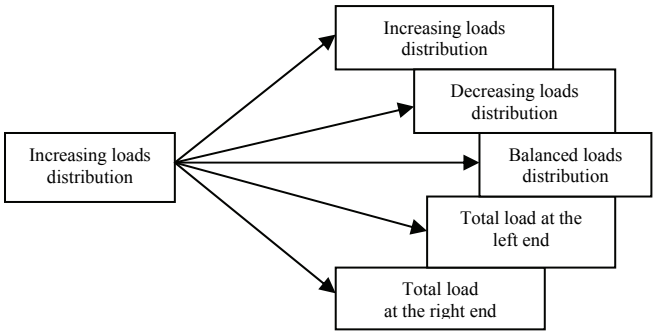

Fig. 6. Example of simulation procedure

The Fig. 6 above illustrates an example of this comparison, the increasing loads distribution is the real distribution, and the others are considered fictive.

To analyze the load distribution variation effect on the fault location, and to confirm the results of the optimal load distribution formulation, the cross distributions in Figs. 7(a-d) are classified according to their errors.

Fig. 7(a) illustrates some obtained test results, for the simulation system presented above, with the balanced loads distribution as real distribution during the fault, compared with the five other distributions used to compute the fault location as fictive distributions.

The increasing loads distribution is used as real distribution in Fig. 7(b), from the comparison of the real distribution with the other fictive distributions used as input of the fault location algorithm. The simulation of the decreasing loads distribution in comparison with the other distributions is plotted in Fig. 7(c).

To confirm the previous results, a random distribution is simulated in Fig. 7(d). The classification obtained from these simulations is presented in Table 3.

Table 3. Load distributions classification

Fictive load distribution	**Real load distribution**			
	Balanced loads distribution	Increasing loads distribution	Decreasing loads distribution	Random distribution
Balanced loads distribution	+	+	+	+
Increasing loads distribution	+	+	–	–
Decreasing loads distribution	–	–	+	+
Total load at the first point	–	-	+	–
Total load at the last point	+	+	–	–
Random distribution	–	–	–	+

From load distribution classification below, it can be concluded that the best results are, always, obtained using the real distribution to compute the fault location. Nevertheless, the

real distribution is not available in practical networks, because it requires knowledge about measurements at each load point which is hardly available in practical EPDS.

However, it can be seen that the maximum errors for the balanced loads distribution are less than 0.04% for all the distributions. Thus, this distribution is the optimal load distribution which proves the result of the optimal load distribution formulation.

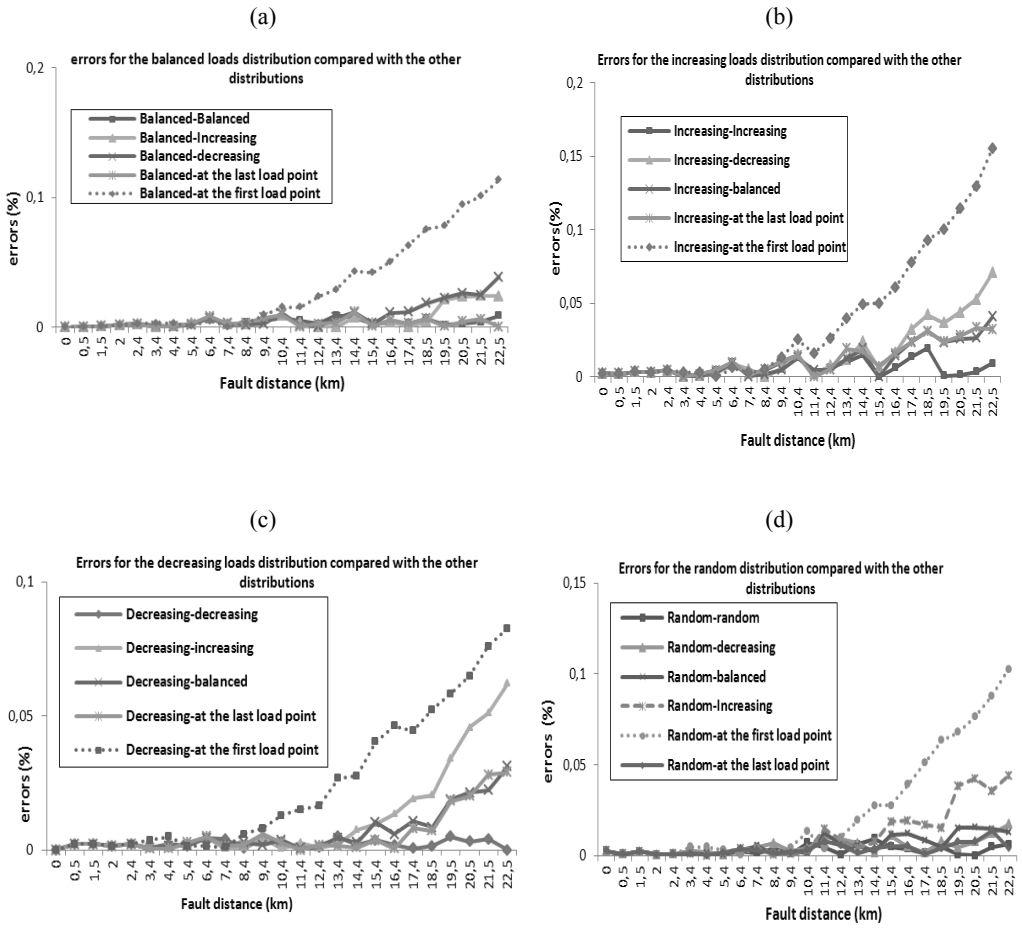

Fig. 7. Errors for each real load distribution compared with the other fictive load distributions.

6. Conclusions

A novel technique to estimate the optimal load distribution in fault location algorithms for Electrical Power Distribution Systems has been presented in this paper. Voltage and current measurements at substation are utilized to estimate the total load during the fault. The total

load is divided fairly on all load points considering network topology. Most of the techniques found in the literature are focused on measurement at each load point or based on load compensation which is hardly available in practical EPDS. The difficulties that arise when considering a load distribution known to locate faults on practical EPDS were highlighted in this paper.

The performances of this technique are verified by several tests simulating 26 cases of single phase to ground faults for different cross load distributions.

Simulation results and mathematical formulation show that the balanced loads distribution can be considered as a fictive optimal distribution in fault location algorithms thanks to its estimation simplicity and its robust effectiveness.

References

[1] Novosel D., Hart D., Myllymaki J., S*ystem for locating faults and estimat-ing fault resistance in distribution networks with tapped loads*, U.S. Patent 5839093 (1998).

[2]Das R., *Determining the locations of faults in distribution systems*, Doctoral thesis. University of Saskatchewan, Saskatoon, Canada (1998).

[3] Yang L., Springs C., *One terminal fault location system that corrects for fault resistance effects*, US Patent number 5,773,980 (1998).

[4] Das R., Sachdev M.S., Sidhu T.S., *A fault locator for radial sub-transmission and distribution lines*, IEEE Power Engineering Society Summer Meeting, Seattle, WA, USA, July 16-20 (2000).

[5] Saha M., Rosolowski E., M*ethod and device of fault location for distribution networks*, US Patent number 6,483,435 (2002).

[6] Choi M.S., Lee S., Lee D., Jin B., *A new fault location algorithm using direct circuit analysis for distribution systems*, IEEE Trans. Power Syst., vol. 19, no. 1, pp. 35-41 (2004).

[7] Senger E., Manassero J., Goldemberg C., Pellini E., *Automated fault location system for primary distribution networks*, IEEE Trans. Power Del., vol. 20, no. 2, pp. 1332-1340 (2005).

[8] Kim J., Baran M., Lampley G., *Estimation of fault location on distribution feeders using PQ monitoring data*, IEEE Power Engineering Society General Meeting, Tampa, FL (2007).

[9] Salim R.H., Resener M., Filomena A.D., Rezende Caino d'Oliveira K., Bretas A.S., *Extended Fault-Location Formulation for Power Distribution Systems*", IEEE Transactions on Power Delivery, vol. 24, no. 2 (2009).

[10] d'Almeida M.C., Costa F.F., Xavier-de-Souza S., Santana F., *Optimal placement of faulted circuit indicators in power distribution systems*, Electr. Power Syst. Res., vol. 81, no. 2, pp. 699-706 (2011).

[11] Krishnathevar R., Ngu E.E., *Generalized impedance-based fault location for distribution systems*, IEEE Transactions on Power Delivery, vol. 27, no. 1, pp. 449-451 (2012).

[12] Avendano-Mora M., Milanovic J.V., *Generalized formulation of the optimal monitor placement problem for fault location*, Electr. Power Syst. Res., vol. 93, no 12, pp. 120-126 (2012).

[13] Sadeh J., Bakhshizadeh E., Kazemzadeh R., *New fault location algorithm for radial distribution systems using modal analysis*, Int. J. Electr. Power Energ. Syst., vol. 45, no. 1, pp. 271-278 (2013).

[14] Wanjing X., Yuan L., *Novel fault location methods for ungrounded radial distribution systems using measurements at substation*, Electric Power Systems Research, vol. 106, pp. 95-100 (2014).

[15] Zahri M., Menchafou Y., El Markhi H., Habibi M., *ANN and Impedance Combined method for Fault Location in Electrical Power Distribution Systems*, International Journal of Electrical Engineering and Technology, vol. 5, no. 9, pp. 29-38 (2014).

[16] Zahri M., Menchafou Y., El Markhi H., Habibi M., *Simplified method for single line to ground-fault location in electrical power distribution systems*, International Journal of Electrical and Computer Engineering, vol. 5, no. 2, pp. 246-255 (2015).

[17] Filomena A.D., Resener M., Salim R.H., Bretas A.S., *Fault location for underground distribution feeders: An extended impedance-based formulation with capacitive current compensation*, Electr. Power and Energy Syst., vol. 31, pp. 489-496 (2009).
[18] Filomena A.D., Resener M., Salim R.H., Bretas A.S., *Distribution systems fault analysis considering fault resistance estimation*, Electr Power and Energy Syst., vol. 33, pp. 1326-1335 (2011).
[19] Matlab Help Manual, The Mathworks Inc. (2009).

ARCHIVES OF ELECTRICAL ENGINEERING VOL. 66(1), pp. 89-104 (2017)

DOI 10.1515/aee-2017-0007

Detection of single and multiple IGBTs open-circuit faults in a field-oriented controlled induction motor drive

PIOTR SOBAŃSKI, TERESA ORŁOWSKA-KOWALSKA

Department of Electrical Machines, Drives and Measurements
Wrocław University of Science and Technology
Wybrzeże Wyspiańskiego 27, 50-370 Wrocław
e-mail: {piotr.sobanski/teresa.orlowska-kowalska}@pwr.edu.pl

(Received: 23.01.2016, revised: 01.10.2017)

Abstract: In this paper a transistor open-circuit fault diagnosis method in a rotor field oriented controlled induction motor drive, fed by a two-level voltage inverter has been proposed. The diagnostic procedure ensures detection and localization of single or multiple power switch failures in time shorter than one period of a stator current fundamental harmonic, without regard to a drive operation point. A new simple scheme of the diagnostic system is proposed. In order to validate the proposed transistor fault diagnostic method, a detailed simulation as well as experimental tests of the field-oriented control drive system were carried out and some of them are shown in this paper.

Key words: induction motor; field-oriented control; condition monitoring; open-circuit fault; fault diagnosis

1. Introduction

Induction motors (IM) are the most popular electrical machines in industry nowadays because of their robust construction and relatively low manufacturing cost. They are practically maintenance-free and they assure very good dynamic performance if appropriate control structure is applied. The aforementioned qualities have been researched and improved by using intelligent and sophisticated control methods based on the field oriented control (FOC) or the direct torque control (DTC) because these control concepts enable both the amplitude and phase control of ac-excitation. In general, these adjustable IM drives are composed of advanced structures that include the static inverter, induction motor, control blocks, electrical and mechanical connections, sensors, etc. Thus, the total reliability of the drive system can be improved by increasing the reliability of each single component or by decreasing the number of the structure components of a drive through the development of sensorless drives [1, 2].

Faults of power electronics, an electrical motor or sensors in adjustable-speed electrical motor drives can significantly disturb the control process, resulting in a drive availability

decrease. As a result, in the last decades, the interest of many members of the drives community and marketplace has been focused on new control techniques, that allow simultaneous electric drive operation after faults occurrence [3]. These techniques, known as fault-tolerant control (FTC) methods, integrate failure diagnosis algorithms and hardware or software redundancy that allow correct drive operation under its faulty condition. In [4] motor speed sensor fault-tolerant control technique based on the drive angular speed estimation is presented. The speed sensor failure is detected by analysing the error between the measured and estimated motor speed. According to this method, if a sensor is faulty, the drive operates using the estimated signal for the speed control. In [5] the hardware redundancy is utilized for the current sensor fault-tolerant control. The faulty sensor is replaced with the healthy ones. In the case of transistor failures the redundant converter topologies are required [6, 7]. First, the faulty transistor is isolated and then, thanks to the converter circuit reconfigurations, the post-fault control is implemented. The effectiveness of faults diagnostic techniques, namely correct failure detection and its localization, robustness against false alarms as well as fast diagnosis have an important influence on the possibility of an appropriate remedial action.

Among various types of faults, power converter faults, related to semiconductor or control circuit damages, are the most frequent ones and are estimated to make up to 60% of power device failures [8]. Thus recently quite a lot of different fault detection and localization methods and techniques devoted to power converters have been reported in technical literature. Surveys of diagnostic methods dedicated to transistor failures are presented in many works, e.g. [9]. In fact, they are hardware- and software-based transistor faults diagnostic techniques. The most frequently used approaches are based on the analysis of easily accessible signals, such as measured current or estimated voltage, thus these methods are usually classified as current- or voltage-based ones. It is important that, in accordance with these techniques, no additional measurement systems are utilized, in most cases. Many transistor failure monitoring techniques are based on the analysis of standardized errors between the reference estimated, predicted or measured variables [10-15]. For this purpose, the average values of these errors, which are additionally normalized by dividing them by the module of the variable vector, are calculated. Thanks to signal normalization the constant fault threshold can be assumed. The effectiveness of some of these techniques depends on the accuracy of the used estimation or prediction algorithms. Moreover, they require a relatively high computational effort so the industrial application of these algorithms is limited.

The second group of the transistor fault diagnostic methods consists of techniques based on the analysis of vector hodographs of the fault diagnostic variables [16-19]. A vast majority of these algorithms use the current vector whose amplitude is load-dependent. To overcome this disadvantage the flux vector, whose amplitude is stabilized for speed control, is utilized [16].

Unfortunately, some of the diagnostic methods are applied by using sophisticated algorithms, such as fuzzy-logic techniques [16] or neural networks [20, 21], that require a relatively high computational effort, so their applications are limited.

In this paper, an open-circuit fault diagnostic method for transistors with a two-level voltage inverter is developed and extensively tested. The technique is dedicated to vector-controlled AC-drives fed by a two-level inverter with the voltage Space Vector Modulation

(SVM). The diagnostic procedure ensures the detection and localization of single power switch failures as well as single-phase transistor faults, in time shorter than one period of the stator current fundamental harmonic, without regard to a drive operation point. In order to reduce an implementation effort of the solution, a scheme of the diagnostic system was simplified compared to the solution presented by the authors in previous work [17, 18]. In comparison to the methods described in the introduction, the developed algorithm is simpler to implement, which improves its applicability, in particular in the case of the low cost motor drive systems. Additionally, the method was validated by simulation and experimental tests, in different operation conditions of the drive system. The tests were carried out in the direct rotor field oriented controlled (DRFOC) induction motor drive under single and multiple switch open-circuit failures. To prove the diagnostic method robustness against false alarms simulation as well as experimental tests under various healthy motor drive operations have been carried out. The presented method was validated not only during constant speed and load of the drive but also under the drive acceleration and deceleration as well as rapid load changes.

2. Description of the fault diagnosis method

In Fig. 1a, the basic scheme of two-level voltage source inverter topology, whose faults are considered in this paper, is presented. For this inverter only eight switch-status combinations are possible, so that eight voltage vectors described as $\boldsymbol{U0}$, ..., $\boldsymbol{U7}$ can be generated, according to Fig. 1b. In accordance with the diagnostic algorithm, detection and localization of transistor faults can be carried out by processing signals related to reference inverter voltages, generated in the control structure of the drive system, based on the rotor-field-oriented control (DRFOC), as it is presented in Fig. 1c.

These voltages can be produced by using eight combinations of the switch status. In order to achieve a reference voltage vector $\boldsymbol{U}_\mathrm{r}$, whose position in the α–β plane is defined by an angle γ, that is referred to the α axis, six active voltage vectors ($\boldsymbol{U1}$,...,$\boldsymbol{U6}$) and two zero ones ($\boldsymbol{U0}$ and $\boldsymbol{U7}$) are used. These vectors divide the α–β plane into six sectors: I, ... ,VI, in accordance with (1):

$$SN = \mathrm{int}\left(\frac{\gamma}{\pi/3}\right)+1, \tag{1}$$

where int means the operation that returns the integer value.

Extraction of fault information is based on monitoring the voltage vector presence time t_M in the specific sectors of the complex α–β plane. Depending on motor speed direction and fault location, in a drive steady state, the reference voltage vector is forced in one characteristic sector during a much longer time-period than in the case of some other ones [16]. The direction of the voltage vector rotation is related to the angular motor speed direction. In further considerations it was assumed that under the motor mode of the machine, which rotates in the positive speed direction, the voltage space vector rotates in the positive direction as well. This means that the numbers of the sectors are increasingly changed.

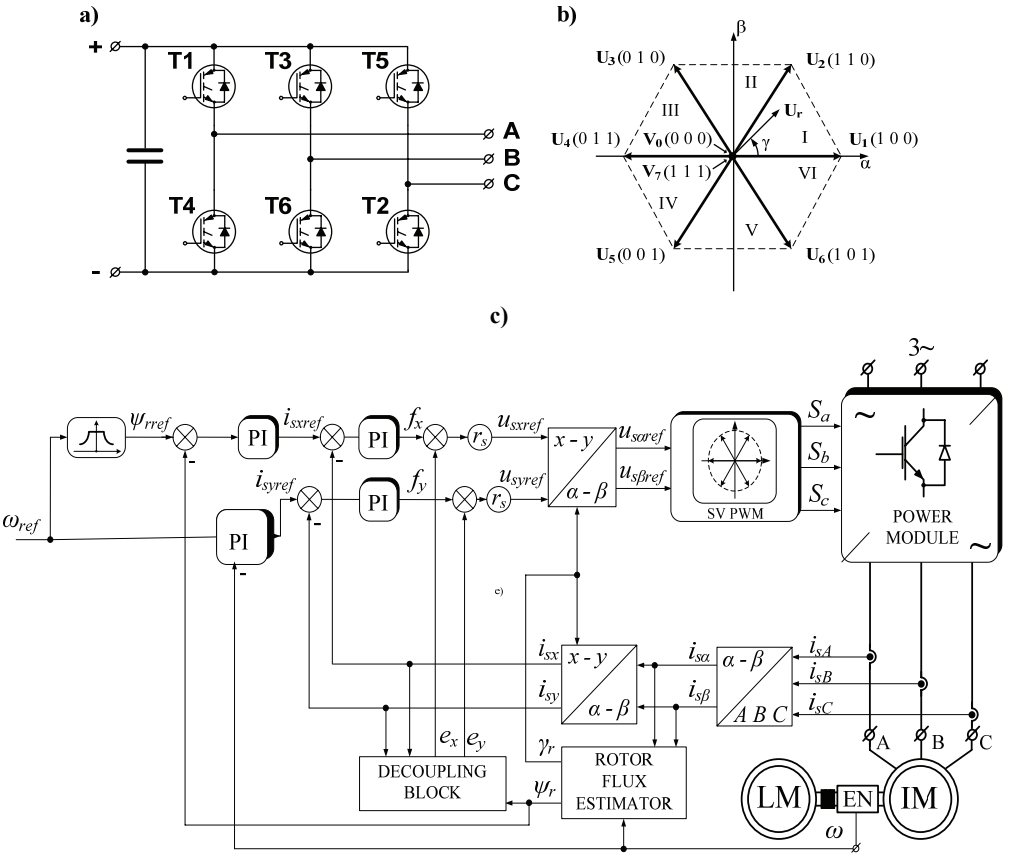

Fig. 1. A standard three-phase voltage source inverter: topology (a), voltage space vectors (b), DRFOC structure (c)

In this paper, a new simple implementation scheme of the diagnostic method described in detail in [17] is proposed, namely a number of counters used to realize the diagnostic system has been decreased from six to one. Additionally, to localize the faulted transistor, the signal *SN* is considered in the rule base. The block diagram of the analysed transistor fault diagnostic system is shown in Fig. 2.

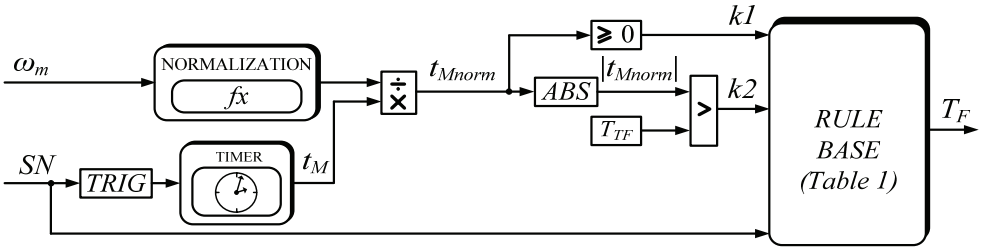

Fig. 2. A block diagram of the transistor faults diagnostic system

In this system, the counter whose frequency is equal to 5 kHz is activated by a triggering event, which consists in a change of the sector *SN* that describes the position of the reference voltage vector on the α–β plane. The value of the output counter signal t_M is proportional to the duration when the reference voltage vector is located in particular sectors. Due to the fact that the voltage frequency changes depending on the required motor speed, the diagnostic variable t_M is normalized by assuming the linear relationship between the speed and the reference voltage resulting in (2):

$$t_{M\,\mathrm{norm}} = 6nt_M /(f_{\mathrm{Timer}} T_N n_N)\,, \tag{2}$$

where n is the drive speed, f_{Timer} means the timer frequency, T_N is the period of the nominal voltage and n_N means the nominal speed, number 6 appears in the nominator of (2), because the α–β plane is divided into 6 sectors. Thanks to the normalization, for the healthy motor drive operations, a constant maximum value of the diagnostic signal $|t_{M\,\mathrm{norm}}| = 1$ is obtained. If the signal $|t_{M\,\mathrm{norm}}|$ reaches the fault threshold T_{TF}, then the transistor fault is detected. In order to localize a faulty switch, the rule base which considers the motor speed direction is utilized in accordance with Table 1. Logical variables $k1$ and $k2$ are related to the comparators of the diagnostic system (see Fig. 2).

Table 1. Open-switch fault symptoms patterns

Faulted switch T_F	$k1$	$k2$	SN
$T1$	1	1	1
	0	1	6
$T2$	1	1	2
	0	1	1
$T3$	1	1	3
	0	1	2
$T4$	1	1	4
	0	1	3
$T5$	1	1	5
	0	1	4
$T6$	1	1	6
	0	1	5

3. Simulation results of the IGBT fault detection method in a DRFOC-based induction motor drive

3.1. A short presentation of the simulation model and research scenario

This section presents selected simulation results which prove the effectiveness of the transistor fault diagnostic method. The presented results were obtained using a simulation model of the DRFOC induction motor drive system, which was using Matlab/Simulink and the specialized Sim Power Systems toolbox. In order to simulate open-switch faults, transistor gate control signals were removed, which results in non-conduction mode of the transistors. An assumed voltage modulation period is equal to 100 μs similarly to the experimental research described in Section 4. The nominal parameters of the induction machine are shown in Table 2 in the Appendix.

The simulation results are presented according to the following scenario. First, the diagnostic method robustness against the false alarms during the healthy motor drive operations is validated. Then, the open-circuit transistor failures are studied under a constant reference angular speed ω_m and a different load torque m_l of the motor drive system, namely the algorithm was tested for the almost fully-loaded motor ($m_l = 0.8m_N$) under the fault of $T1$ then the load was rapidly decreased to $m_l = 0.2m_N$ and the switch failure of $T4$ was simulated. Moreover, the diagnostic algorithm was validated for the transistor faults occurring during motor speed accelerations and rapid (step) load changes. In figures, a magenta dotted line indicates the fault occurrence, but a moment of the fault detection is depicted as a blue or yellow dotted line. In order to rate the speed of the transistor failures diagnosis procedure, the normalized fault localization time t_{TF} is defined in accordance with (3):

$$t_{TF} = \frac{t_{\text{fault}}}{T_i}, \tag{3}$$

where t_{fault} means the time period between two instants: the fault occurrence and the fault localization, but T_i means the period of the current waveform which is measured shortly before the failure occurrence.

To prove the effectiveness of the considered transistor fault diagnostic method, transients of the diagnostic variable $|t_{M\,\text{norm}}|$ that are compared with the failure threshold T_{TF}, are presented. As proved in the next section of this paper, this threshold could be equal to 1.15, nevertheless in order to present the method more clearly, for the simulations it is assumed that $T_{TF} = 1.5$. Additionally, relevant transients of the signal SN referred to the number of the sector, which describe the position of the reference voltage vector in the α–β stationary coordinates system, are shown. Moreover, phase currents $i_{sA,\,B,\,C}$, reference speed $\omega_{m\,\text{ref}}$ and the measured angular motor speed ω_m, are presented. The following results have a representative character and they are related to the transistor failures in phase A of the inverter. The observations for the faults in the phase B or C are analogical.

3.2. Validation of the diagnostic method robustness against false alarms

Taking into account healthy motor drive operations, the values of the diagnostic signal $|t_{M\,\text{norm}}|$ are less than one, so the fault threshold should be greater than one. To assume the appropriate value of this threshold, namely to avoid false alarms, the diagnostic system was tested during rapid (step) load changes from the nominal value to zero. Fig. 3 shows the time domain waveforms of the angular speed, currents, electromagnetic torque and diagnostic signal for healthy motor drive operations.

First, at the instant $t = 0.2$ s the motor was loaded when the drive was operating at a low speed. Then, at $t = 0.4$ s the load was changed from the nominal value to zero. Then, at $t = 0.5$ s the nominal load torque $m_l = m_N$ was applied (step change) once again and the speed was increased up to the nominal value. After that, at $t = 0.9$ s the load was suddenly reduced to zero. In Fig. 3e it is visible that the diagnostic signal does not exceed the assumed fault threshold not only during sudden load torque step changes but also during fast acceleration of the drive.

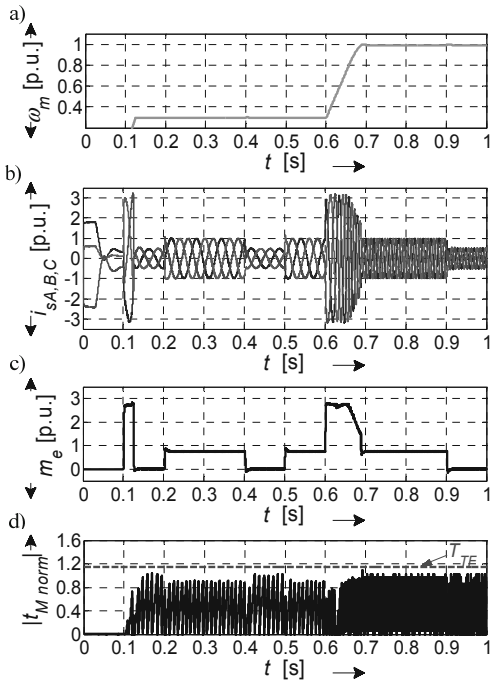

Fig. 3. Time domain waveforms achieved during the test of the diagnostic method robustness against false alarms ($T_{TF} = 1.15$) during a healthy mode

3.3. Validation of the diagnostic method under constant speed operation of the DRFOC drive

The LHS column of Fig. 4 presents simulation results achieved for the $T1$ failure, which occurred at the instant $t = 0.3$ s, under the transistor conducting mode.

In the LHS of Fig. 4 (c, d), it is visible that, for the $SN = 1$ at $t = 0.303$ s, the diagnostic signal achieved the fault threshold $T_{TF} = 1.5$, which is indicated by the green dotted line. For this case, the speed diagnosis takes 0.15 of the current fundamental period T_i. After that, at $t = 0.35$ s, the motor was loaded ($m_l = m_N$) and at the instant $t = 0.45$ s the fault of the lower transistor in phase A was simulated. As it can be seen in LHS of Fig. 4 (c, d) the failure of $T4$ was detected at $t = 0.47$ s, so the duration of the fault diagnosis was also shorter than one current fundamental period ($t_{TF} = 0.77$). Compared to the previously considered case, which illustrates the faulty drive operation under nominal motor speed, in the RHS of Fig. 4 faults of the inverter were simulated at the low velocity of the drive ($\omega_m = 0.4\omega_N$). When the $T1$ failure occurred the load torque was $m_l = 0.8m_N$, next, at the instant $t = 0.35$ s, the load was rapidly decreased to $m_l = 0.2m_N$. Then at $t = 0.45$ s the fault of $T4$ was simulated. The $T1$ failure was detected within the time that is equal to 0.35 of the current fundamental period but, in the case of $T4$ open-circuit failure the detection time was $t_{TF} = 0.98$ of T_i.

The simulation results show the effectiveness of the single and multiple transistor fault diagnostic method under various motor drive conditions, namely the changeable load and various motor speed that was referred as a constant values.

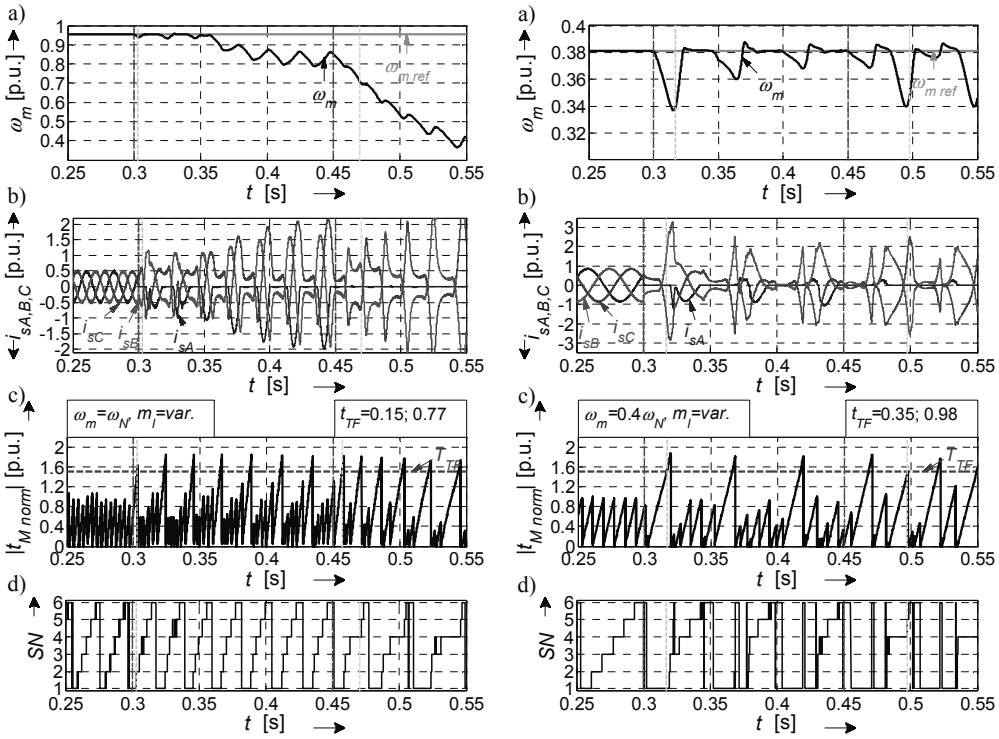

Fig. 4. Reference $\omega_{m\,\mathrm{ref}}$ and measured ω_m angular motor speed (a), phase currents $i_{sA,\,B,\,C}$ (b), the diagnostic variable $|t_{M\,\mathrm{norm}}|$ (c) and *SN* signal (d) for the motor drive operation under: LHS – nominal reference angular speed $\omega_{m\,\mathrm{ref}} = \omega_N$, variable load torque and the fault of *T*1 and next *T*4; RHS – reference angular speed $\omega_{m\,\mathrm{ref}} = 0.4\omega_N$, variable load torque and the fault of *T*1 and next *T*4

3.4. Evaluation of the diagnostic method under DRFOC drive operation with linear speed changes

Many electrical drives operate with frequent motor speed changes so it is necessary to validate also the effectiveness of the analysed fault diagnostic technique during speed acceleration and deceleration. The following part of the article shows simulation results that confirm the correctness of the diagnostic algorithm for the single as well as multiple transistor open-circuit faults occurring in the inverter phase (see Fig. 5).

In accordance with the presented tests, the fault of *T*1 transistor was simulated at $t = 0.30$ s, but the failure of *T*4 switch occurred at $t = 0.45$ s. Until $t = 0.35$ s the drive operated with the load $m_l = 0.8m_N$ and then was rapidly (step) changed to the value $m_l = 0.2m_N$. As shown in Fig. 5, the transistor fault diagnosis took less time than one current fundamental period. In accordance with the presented simulation results the transistor open-circuit fault diagnostic method is effective even when the drive operates at a linear speed and the rapid load changes as well. From Fig. 4 and Fig. 5 results, that the fault threshold can be taken lower than the assumed value in all operation condition of the drive system (see a remark in section 3.1), thus in the experimental tests this value was taken $T_{TF} = 1.15$.

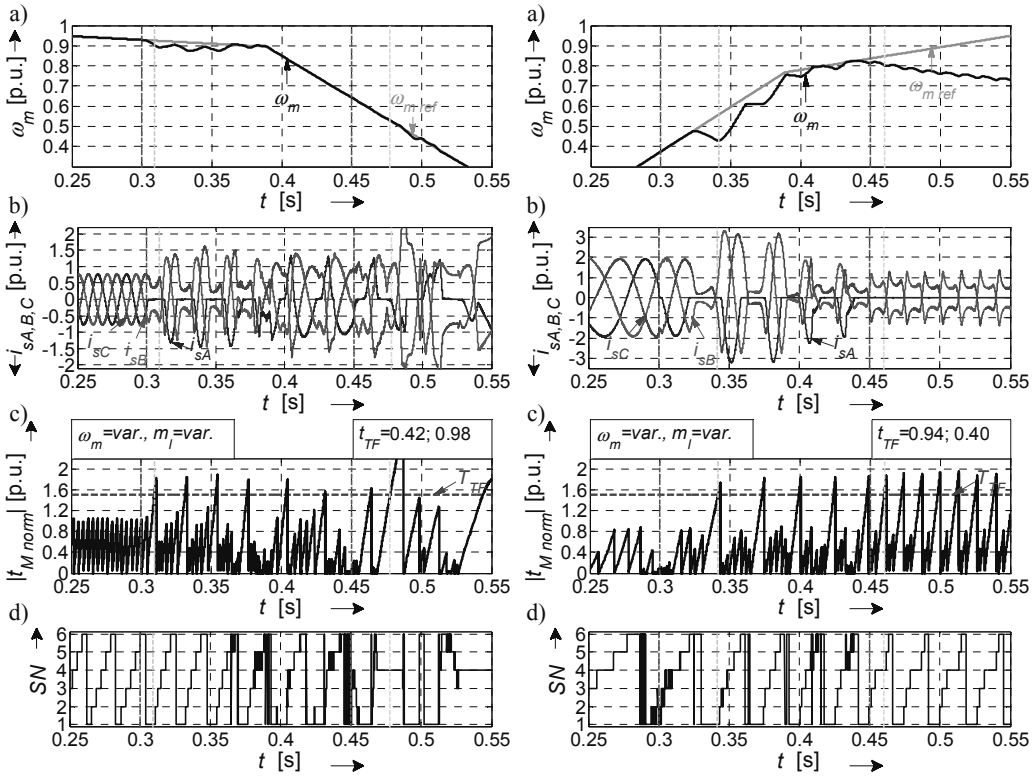

Fig. 5. Reference $\omega_{m\,ref}$ and measured ω_m angular motor speed (a), phase currents $i_{sA,\,B,\,C}$ (b), the diagnostic variable $|t_{M\,norm}|$ (c) and *SN* signal (d) for the motor drive operation under: LHS – speed acceleration; RHS – speed deceleration; variable load torque and the faults of *T*1 and next *T*4

4. Experimental validation of the IGBT fault detection method in a DRFOC-based induction motor drive

4.1. A short presentation of the experimental set-up and research scenario

In this section, selected experimental results, that confirm the effectiveness of the proposed open-switch fault diagnostic method, are presented. The research was carried out using a laboratory set-up whose schematic diagram and a picture are shown in Fig. 6 (for the same IM that was used in simulation tests). The experimental results, that are presented in this section, are organized in accordance with the following scenario. First, the diagnostic method robustness against the false alarms is tested. For this purpose the diagnostic signal $|t_{M\,norm}|$ is analysed during the speed acceleration or its deceleration as well as rapid load changes. Then, the open-switch faults are obtained under a constant angular speed ω_m of the drive system. Next, the diagnostic method is tested for the failures that occur during motor speed acceleration. The results of the research have been presented similarly to the previously discussed simulations.

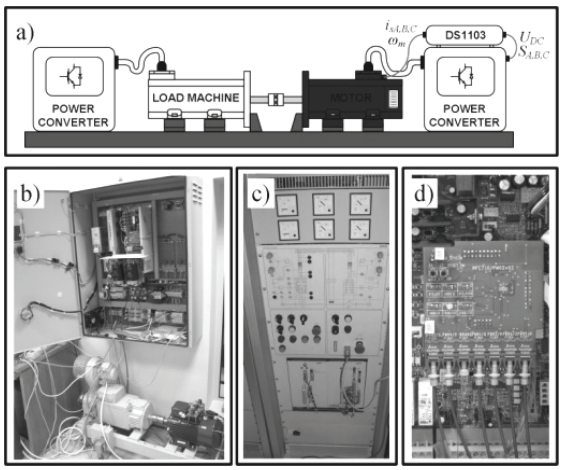

Fig. 6. The laboratory motor drive system: schematic diagram (a), photo of the induction motor drive (b) the power converter that supplies the DC motor (c) the fibre-optic modules of the inverter (d)

4.2. Validation of the diagnostic method robustness against false alarms

Figure 7 shows the time domain waveforms of the angular speed, currents, electromagnetic torque and diagnostic signal for the healthy motor drive operations that take into account various speed and load variations.

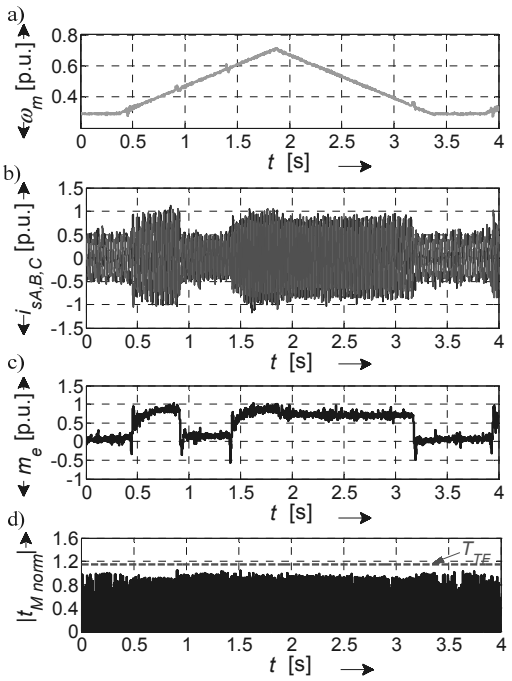

Fig. 7. Time domain waveforms achieved during the test of the diagnostic method robustness against false alarms

At the instant $t = 0.45$ s the motor was loaded when the speed of the drive was increasing. Then, at $t = 0.9$ s the load was changed from the nominal value to zero. At $t = 1.4$ s the load torque was applied $m_l = m_N$ and then at $t = 3.2$ s the load was reduced under the motor speed deceleration. In Figure 6e it is visible that the diagnostic signal does not exceed the fault threshold $T_{TF} = 1.15$ (similarly like in the simulation tests – Fig. 3), so it is justified to assume that this threshold is reached only for the faulty mode of the inverter.

4.3. Evaluation of the diagnostic method under constant speed operation of the DRFOC drive

In the LHS column of Fig. 8 experimental results obtained for the $T1$ fault, which occurred at the instant $t = 0.506$ s, under the transistor conducting mode, when the current of the faulty inverter phase i_{sA} achieved the peak value, are presented.

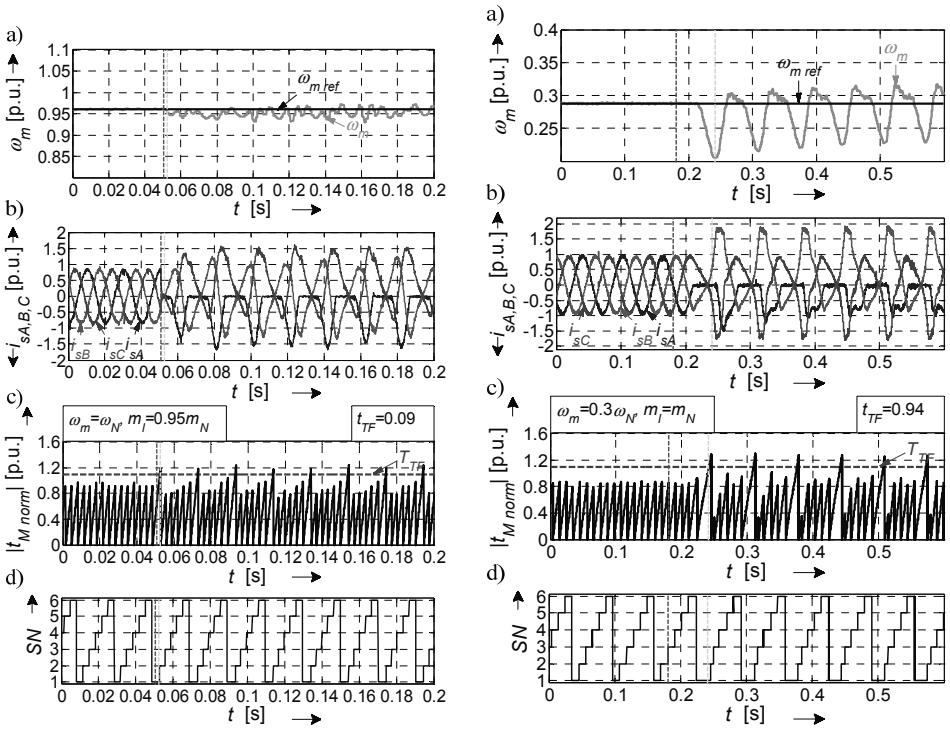

Fig. 8. Reference $\omega_{m\,ref}$ and measured ω_m angular motor speed (a), phase currents $i_{sA,\,B,\,C}$ (b), the diagnostic variable $|t_{M\,norm}|$ (c) and SN signal (d) during $T1$ open-circuit fault, for the motor drive operation under: LHS – nominal reference angular speed $\omega_{m\,ref} = \omega_N$ and the load torque $m_l = 0.95m_N$; RHS – reference angular speed $\omega_{m\,ref} = 0.3\omega_N$ and the load torque $m_l = m_N$

As can be seen in the LHS of Fig. 8(c, d), for the $SN = 1$, at $t = 0.524$ s the diagnostic signal achieved the fault threshold, so the fault localization time comprises 0.09 of the current fundamental period. Compared to the previously considered case, in the RHS of Fig. 8 results achieved for the $T1$ failure, which occurred at the instant $t = 0.181$ s, under the transistor non-

conducting mode, when the current of the faulty inverter phase i_{sA} crosses the zero-level, are shown. As is clearly seen in the RHS of Fig. 8(c, d), for the $SN = 1$, at $t = 0.241$ s the diagnostic signal reached the fault threshold, so the fault localization time comprises 0.94 of the current fundamental period.

The second considered group of transistor faults are single phase open-circuit failures. Fig. 9 presents the results which concern $T1$ and $T4$ faults, that occurred at $t = 0.162$ s, when the no-loaded motor operated at a nominal speed. At $t = 0.191$ s the diagnostic signal reached the fault threshold (Fig. 9c) when the reference voltage vector was located in the 4th sector of the α–β plane (see Fig. 9d), so the failure of $T4$ was recognized. After that, at $t = 0.234$ s the fault of $T1$ was detected. As it is visible in Fig. 9c, the failure diagnostic time is shorter than one period of the stator current fundamental harmonic, in both cases.

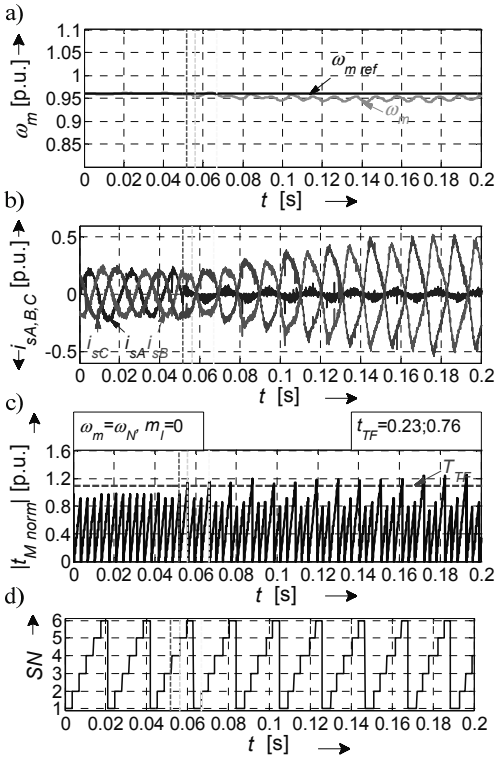

Fig. 9. Reference $\omega_{m\,\mathrm{ref}}$ and measured ω_m angular motor speed (a), phase currents $i_{sA,\,B,\,C}$ (b), the diagnostic variable $|t_{M\,\mathrm{norm}}|$ (c) and SN signal (d) during $T1$ and $T4$ open-circuit faults, for the no-loaded motor drive operation with nominal reference angular speed $\omega_{m\,\mathrm{ref}} = \omega_N$

The presented results proved the effectiveness of the proposed transistor fault diagnostic method in various motor drive conditions. Without regard to the fault instant, the transistor failure is localized faster than one period of the stator current fundamental harmonic. Additionally, thanks to diagnostic signal normalization, false alarms or a false diagnosis are avoided.

4.4. Evaluation of the diagnostic method under DRFOC drive operation at linear speed changes

In this subsection, the experimental results related to the transistor failures which occurred during linear changes of the drive speed are presented. In the LHS of the Fig. 10, the behaviour of the drive system under a single transistor fault is presented. In Fig. 10a (LHS) it is visible that at the instant $t = 0.042$ s the fault of $T1$ was introduced, when the speed of the no-loaded motor was decreased. Shortly after the fault occurrence, the diagnostic variable obtained the failure threshold at $t = 0.045$ s (see Fig. 10c). In this case, the normalized fault localization time $t_{TF} = 0.2$ is also shorter than one current fundamental period.

Next in the RHS of Fig. 10, the experimental results that concern the transistor faults in phase A of the inverter during speed increasing at 80% of nominal load torque are demonstrated. At $t = 0.146$ s the transistors $T4$ and $T1$ (phase A) failures were introduced, while the speed of the drive was increased. First, at $t = 0.157$s the failure of $T4$ was detected and after that, at the instant $t = 0.173$ s, the $T1$ failure was localized. Similarly to the previously described experimental tests, the normalized fault localization time is shorter than one current fundamental period, in both cases $(t_{TF}(\mathrm{T4}) = 0.35,\ t_{TF}(\mathrm{T1}) = 0.86)$.

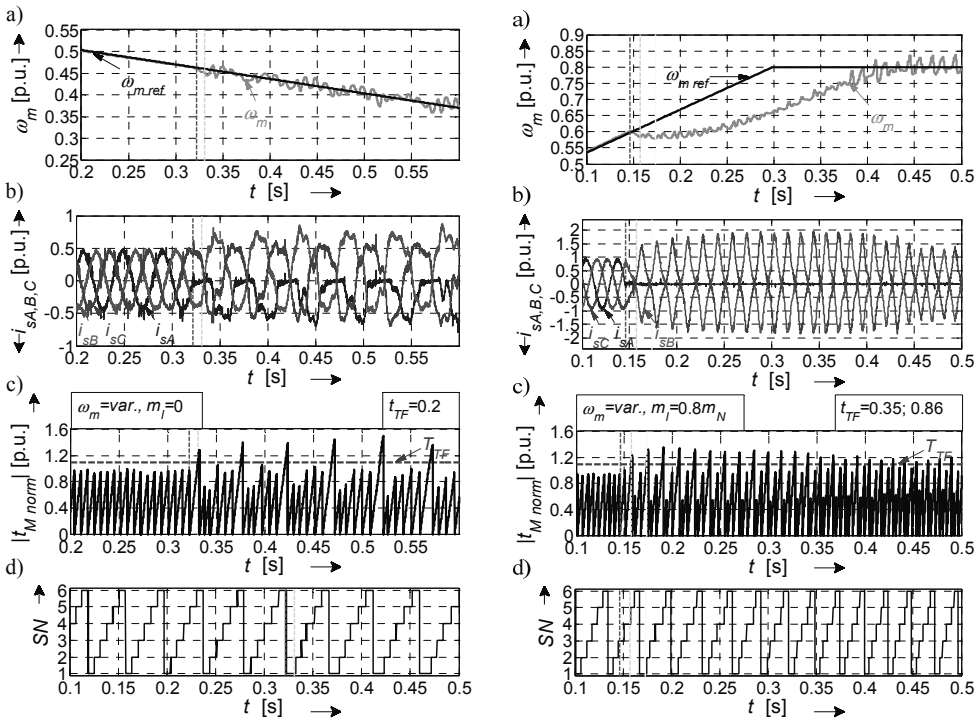

Fig. 10. Reference $\omega_{m\,\mathrm{ref}}$ and measured ω_m angular motor speed (a), phase currents $i_{sA,\,B,\,C}$ (b), the diagnostic variable $|t_{M\,\mathrm{norm}}|$ (c) and SN signal (d): LHS – during $T1$ open-circuit fault, for no-loaded motor drive operation with decreasing rotor speed; RHS – during $T1$ and $T4$ open-circuit faults, for the motor drive operation with increasing speed and the load torque $m_l = 0.8m_N$

The obtained results proved the high effectiveness of the proposed diagnostic system under various load and speed operation conditions of the motor drive. The system ensures the correct failure localization within time shorter than one period of the stator current fundamental harmonic, without regard to an instant of the fault occurrence. Additionally, this method is not limited to the detection and localization of single switch open-circuit faults only, but also ensures the detection and localization of single-phase failures.

5. Conclusions

The low-computational diagnostic method of the single switch or single phase open-circuit faults in the two-level inverter fed IM drive system is proposed in this paper. The authors have already verified the diagnostic algorithm by some simulations in the previous work, but in this paper not only new simulation research results but also the detail experimental validation of the method was presented. Additionally, the scheme of the diagnostic system was significantly simplified, which makes the approach more applicable. The proposed diagnostic technique ensures the correct single-switch open-circuit faults diagnosis as well as single-phase failures detection in a time shorter than one period of the stator current fundamental harmonic without regard to an instant of the fault occurrence and the drive operation point. The presented method gives very good results as well for constant speed operation as for variable speed of the drive system, under constant and variable load torque (including its step changes). It has been proved in simulations and laboratory experiments that the proposed method does not produce false alarms. The proposed method can be applied in all control structures of IM drives, where the information on the reference stator voltage position is known, like in DRFOC or DTC methods with SV-PWM. It is possible to extend this technique to other control strategies such as vector control with hysteresis current controllers and sinusoidal PWM, however in the case of these techniques the stator voltage vector magnitude and position have to be estimated based on the measured DC-bus voltage of the inverter.

The presented solution requires a low-computational effort and is easy applicable in modern electrical drives. The hardware implementation of the proposed transistor fault diagnostic technique can be based on a simple microprocessor system or FPGA.

Appendix

Table 2. Data of the tested induction motor drive

Quantity	Symbol	Physical units	Per unit system
power	P_N	2.2 kW	0.71
torque	m_N	14.6 Nm	0.74
speed	n_N	1440 rpm	0.96
voltage	u_N	400 V	0.71
current	i_N	4.5 A	0.71

Per unit system values have been calculated according to [2].

Acknowledgements
This work was supported by the National Science Centre (Poland) under Project 2013/09/B/ST7/04199 (2014-2017) and partially by the statutory founds of the Department of Electrical Machines, Drives and Measurements, Wroclaw University of Science and Technology (2015-2016).

References

[1] Holtz J., *Sensorless control of induction motors*, Proceedings IEEE, vol. 90, no. 8, pp. 1358-1394 (2002).
[2] Orlowska-Kowalska T., *Sensorless induction motor drives*, Wroclaw University of Technology Press (2003).
[3] Isermann R., *Fault-Diagnosis Applications: An Introduction from Fault Detection to Fault Tolerance*, Springer Science & Business Media (2006).
[4] Dybkowski M., Klimkowski K., Orlowska-Kowalska T., *Speed sensor fault tolerant direct torque control of induction motor drive*, 16th Inter. Power Electronics and Motion Control Conference and Exposition, PEMC 2014, Antalya, Turkey, pp. 810-815 (2014).
[5] Romero M.E., Seron M.M., De Dona J.A., *Sensor fault-tolerant vector control of induction motors*, IET Control Theory Applications, vol. 4, no. 9, pp. 1707-1724 (2010).
[6] Welchko B.A., Lipo T.A., Jahns T.M., Schulz S.E., *Fault tolerant three-phase ac motor drive topologies: a comparison of features, cost, and limitations* IEEE Trans. Power Electronics, vol. 19, no. 4, pp. 1108-1116 (2004).
[7] Zhang W., Xu D., Enjeti P.N. et al., *Survey on Fault-Tolerant Techniques for Power Electronic Converters*, IEEE Trans. Power Electronics, vol. 29, no. 12, pp. 6319-6331 (2014).
[8] Yeh C.C., Demerdash N.A.O., *Induction Motor-Drive Systems with Fault Tolerant Inverter-Motor Capabilities*, IEEE International Electric Machines and Drives Conference, IEMDC 2007, Antalya, Turkey, pp. 1451-1458 (2007).
[9] Lu B., Sharma S.K., *A literature review of IGBT fault Diagnostic and protection methods for power inverters,* IEEE Trans. Industry Applications, vol. 45, no. 5, pp. 1770-1777 (2009).
[10] Estima J.O. and Cardoso A.J.M., *Fast fault detection, isolation and reconfiguration in fault-tolerant permanent magnet synchronous motor drives*, Energy Convers. Congress and Exposition, Raleigh, North Carolina, USA, pp. 3617-3624 (2012).
[11] Choi U., Lee K.B., Blaabjerg F., *Diagnosis and Tolerant Strategy of an Open-Switch Fault for T-Type Three-Level Inverter Systems*, IEEE Trans. Industry Applic., vol. 50, no. 1, pp. 495-508 (2014).
[12] Tabbache B., Kheloui A., Benbouzid M.E.H. et al., *Research on fault analysis and fault-tolerant control of EV/HEV powertrain*, Int. Conf. on Green Energy, Sfax, Tunisia, pp. 284-289 (2014).
[13] Sleszynski W., Nieznanski J., Cichowski A., *Open-Transistor Fault Diagnostics in Voltage-Source Inverters by Analysing the Load Currents*, IEEE Trans. Industrial Electronics, vol. 56, no. 11, pp. 4681-4688 (2009).
[14] An Q-T., Sun L., Sun L-Z., *Current Residual Vector-Based Open-Switch Fault Diagnosis of Inverters in PMSM Drive Systems*, IEEE Trans. Power Electronics, vol. 30, no. 5, pp. 2814-2827 (2015).
[15] Estima J.O., Marques Cardoso A.J., *A New Algorithm for Real-Time Multiple Open-Circuit Fault Diagnosis in Voltage-Fed PWM Motor Drives by the Reference Current Errors*, IEEE Trans. Industrial Electronics, vol. 60, no. 8, pp. 3496-3505 (2013).
[16] Sobanski P., *Fuzzy-logic-based approach to voltage inverter fault diagnosis in induction motor drive*, Przegląd Elektrotechniczny, vol. 90, no. 6, pp. 149-153 (2014).
[17] Orlowska-Kowalska T., Sobanski P., *Simple Sensorless Diagnosis Method for Open-Switch Faults in SVM-VSI-fed Induction Motor Drive*, IEEE 39th Ann. Conf. Industrial Electronics Society IECON'2013, Vienna, Austria, pp. 8210-8215 (2013).
[18] Sobanski P., Orlowska-Kowalska T., Kowalski C.T., *Multiple transistor open-circuit faults diagnosis in a vector-controlled induction motor drive,* IEEE Intern. Conf. on Industrial Technology ICIT'2015, Seville, Spain, pp. 3238-3242 (2015).

[19] Espinoza-Trejo D.R., Campos-Delgado D.U., Bossio G. et al., *Fault diagnosis scheme for open-circuit faults in field-oriented control induction motor drives,* IET Power Electronics, vol. 6, no. 5, pp. 869-877 (2013).
[20] Alavi M., Wang D., Luo M., *Short-Circuit Fault Diagnosis for Three-Phase Inverters Based on Voltage-Space Patterns*, IEEE Trans. on Industrial Electronics, vol. 61, no. 5, pp. 5558-5569 (2014).
[21] Alavi M., Luo M., Wang D., Bai H., *IGBT fault detection for three phase motor drives using neural networks*, 17th Conf. on Emerging Technol. and Factory Automation, Krakow, Poland, pp. 1-8 (2012).

ARCHIVES OF ELECTRICAL ENGINEERING VOL. 66(1), pp. 105-119 (2017)

DOI 10.1515/aee-2017-0008

Condition monitoring of induction motor bearing based on bearing damage index

R.K. PATEL, V.K. GIRI

Department of Electrical Engineering,
Madan Mohan Malaviya University of Technology
Gorakhpur-273 010, India
e-mail: rajkp007@gmail.com

(Received: 07.07.2015, revised: 19.10.2016)

Abstract: The rolling element bearings are used broadly in many machinery applications. It is used to support the load and preserve the clearance between stationary and rotating machinery elements. Unfortunately, rolling element bearings are exceedingly prone to premature failures. Vibration signal analysis has been widely used in the faults detection of rotating machinery and can be broadly classified as being a stationary or non-stationary signal. In the case of the faulty rolling element bearing the vibration signal is not strictly phase locked to the rotational speed of the shaft and become "transient" in nature. The purpose of this paper is to briefly discuss the identification of an Inner Raceway Fault (IRF) and an Outer Raceway Fault (ORF) with the different fault severity levels. The conventional statistical analysis was only able to detect the existence of a fault but unable to discriminate between IRF and ORF. In the present work, a detection technique named as bearing damage index (BDI) has been proposed. The proposed BDI technique uses wavelet packet node energy coefficient analysis method. The well-known combination of Hilbert transform (HT) and Fast Fourier Transform (FFT) has been carried out in order to identify the IRF and ORF faults. The results show that wavelet packet node energy coefficients are not only sensitive to detect the faults in bearing but at the same time they are able to detect the severity level of the fault. The proposed bearing damage index method for fault identification may be considered as an 'index' representing the health condition of rotating machines.

Keywords: bearing damage index (BDI), inner raceway fault (IRF), outer raceway fault (ORF), fault severity, vibration signal

1. Introduction

Rotating machinery is an essential component in most of today's manufacturing and production industries. Fault detection techniques for rotating machinery were studied by numerous researchers with an objective of reducing operational and maintenance costs besides preventing unscheduled downtimes [1-2]. Bearing failure can take place because of many reasons such as wear, contamination, and improper installation. One of the common modes of failure

in a rolling element bearing is a point defect on the inner or outer raceway of the bearing [3]. Such defects produce a series of impacts in a vibration signal. When a running roller passes over the surface of the defects, a fault of a different impact will appear, with different frequencies. The magnitude of frequencies is often lost in the general background noise when the degree of damage is small, but because of their precise nature, they present an effective route for monitoring of progressive bearing degradation. To detect such faults in bearings, many kinds of methods have been developed so far [4-6]. One of the widely used methods for failure detection and diagnosis of the rotating machines is vibration analysis. This recorded vibrational signal is usually non-stationary, non-linear, and with strong noise interference. The feature extraction of these vibration signals is a very important and difficult research task [7-8].

A machine in standard condition has certain vibration signatures. These signatures are modulated by a number of high-frequency harmonic components resulting from structural response to individual impacts. Fault development changes these signatures in a way which may be related to these faults. This has given rise to the term 'mechanical signature analysis' [9]. To make a proper maintenance decision for rotating machinery it is helpful to know the health condition and severity (size) of the fault during operation [10]. S. Wadhwani et al., E. Cabal-Yepez, and Choudary et al., suggested that as the fault increases in severity, the magnitude of the broadband changes in the machine vibration increases accordingly [11-13].

Any recorded signal may be analyzed in a time domain, frequency domain, and time-frequency domain. The selection of a proper signal processing technique is important for extracting the fault- related information. The time domain analysis mainly uses the parameters like RMS value, a peak factor, a crest factor, a skewness and kurtosis [14]. Among these, the kurtosis has been found to be very effective. Time domain information, however, is mostly rich in content with little useful information. In the frequency domain approach, major frequency components of the vibration signals and their amplitude are used for trending purposes. The frequency characteristics of the vibration for a defective bearing subjected to various load condition have been investigated [15]. Time-frequency domain techniques have been proposed including Short-Time Fourier Transform (STFT), the Wigner-Ville Distribution (WVD), and the Wavelet Transform (WT) [16-17].

However, most of such methods only identify the fault type and location, lacking a quantitative index to describe the fault severity which is the basis of the condition base maintenance [18]. A quantitative method for a fault diagnosis method is required to describe the evolution of fault location and identifying the fault size. Hong and Liang studied the damage degree of the rolling bearing in the single damage cases under the experimental simulation based on continuous wavelet and Lempel-Ziv indicators [19].

The bearings in rotating machinery should be periodically checked with a frequency spectrum and time signal in order to detect and study the emergent defects on the outer and inner races. An accurate method for the calculation of bearing defect length is needed to allow the quantitative determination of the defect severity. The remaining bearing life may be estimated based on the defect size and progression of development of the fault.

In the present work, the bearing vibration signal is taken only to diagnose the faults in the bearing part and develop an improved method to identify the bearing fault for rotating ma-

chinery based on a calculation of a bearing damage index (BDI) in the time-frequency domain. In this method, the energy of the decomposed and reconstructed signal is calculated by using the Wavelet Packet Transform (WPT) on different fault severity level. Then we have calculated the percentage variation of wavelet energy which is termed as a bearing damage index (BDI). In the further section of the paper details of measured data, specification, the analysis in time, frequency and time-frequency domain analysis have been presented. The results obtained have been analyzed for different severity level using envelope spectra analysis.

2. Machinery specification and vibration data

In the present study, bearing vibration records have been selected from the Case Western Reserve University Lab data center for analysis and faults recognition [20]. The analysis is applied to a 6205 SKF deep-groove ball bearing and this bearing is used as motor shaft support at the drive end of a 2 HP, three-phase induction motor. The accelerometer was mounted on the motor housing at the drive end of the motor. The samples have been taken at 12000 per second for each of a 16-channel digital audio tape (DAT) recorder. The speed of the shaft is measured as 1797 and 1752 rpm from no load to full load respectively. The specifications of the bearing are: numbers of balls are 9, the ball diameter is 7.94 mm, the pitch diameter is 39.04 mm and a contact angle is 0°. Single point faults were introduced to the test bearings using electro-discharge machining. The seeded fault sizes in the bearing are 0.007 inches and 0.021 inches in diameter with the depth of 0.011 inches each.

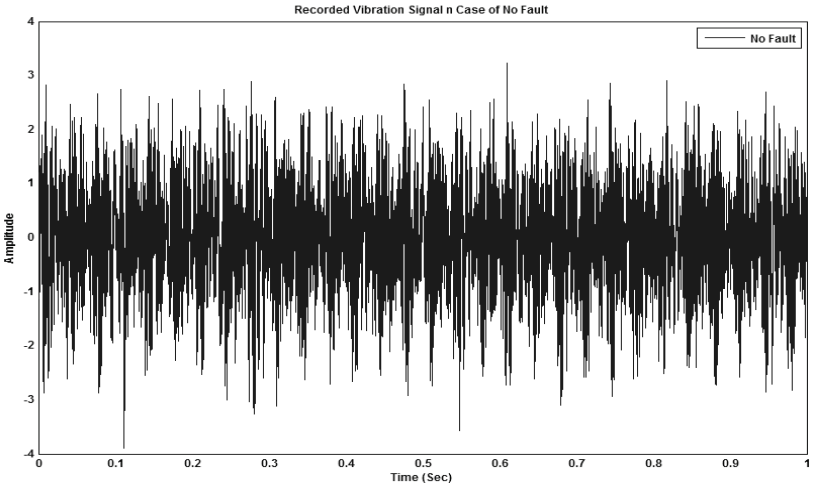

Fig. 1. Vibration signal for normal bearing

The vibration signature of a normal bearing is shown in Fig. 1. The vibration signature for faulty bearings with the located fault in the inner raceway and outer raceway are shown in Figs. 2 and 3 with the superimposed fault level of 0.007 inches and 0.021 inches diameter

[20]. From the visual image of the vibration, repetitive impacts may be observed corresponding to the rotation of the rolling elements past the race damage.

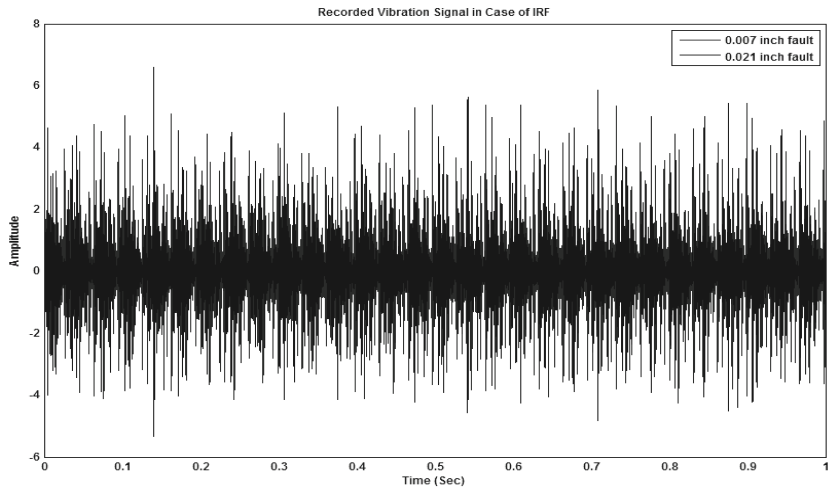

Fig. 2. Vibration signal for inner race fault

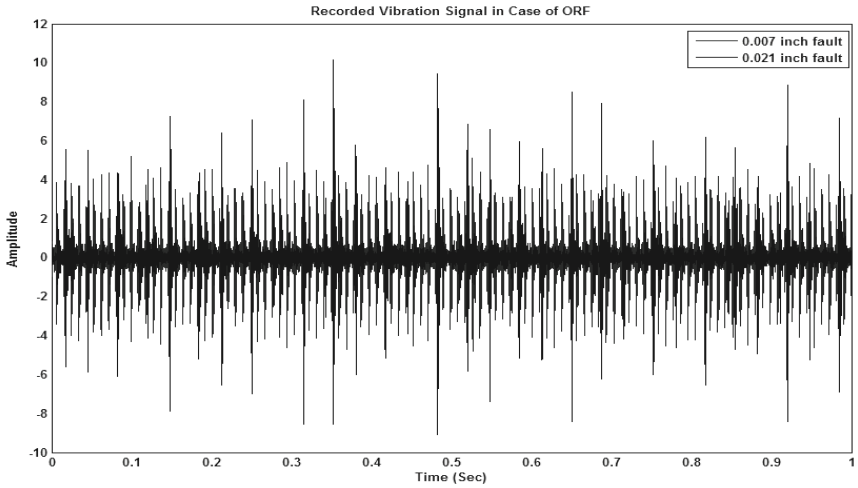

Fig. 3. Vibration signals for outer race fault

3. Statistical analysis

One of the simpler detection and diagnosis approaches is to analyze the measured vibration signal in the time domain.The simplest, though not the most reliable way to detect faults in machines, is to compare their vibration levels with standard criteria for the vibration severity.

In the time domain analysis, first, we use the probability density distribution function $p(x)$ of the vibration signal. The probability density of the distribution of a data sample is defined as:

$$prob[x \le x(t) \le x + dx] = p(x)dx \,. \tag{1}$$

Since, the vibration of a normal bearing consists of the combination of numbers of separate independent effects, the central limit theorem indicates that its probability density will tend towards a Gaussian curve (bell shaped).

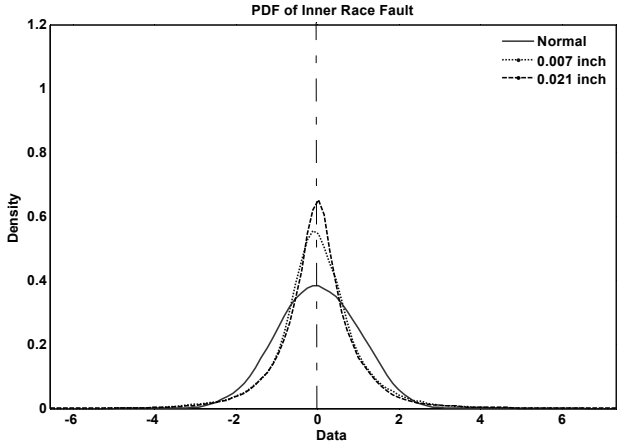

Fig. 4. Probability density distribution of IRF

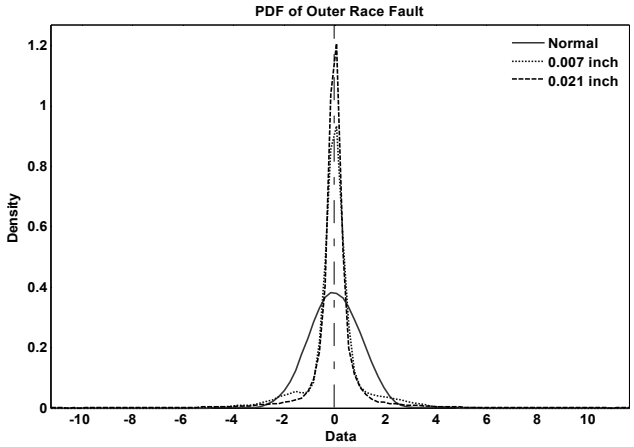

Fig. 5. Probability Density Distribution of ORF

The probability density of acceleration of a bearing in good condition has a Gaussian distribution, whereas a deterioration and damaged bearing lead to non-Gaussian distribution with dominant tails because of a relative increase in the number of high levels of acceleration [21]. This theoretical prediction is confirmed in practice. Figs. 4 and 5 show the probability density

distribution of a bearing in normal condition and with a case of a fault in IRF, ORF conditions. The taken fault sizes are 0.007 and 0.021 inches in diameter, the figure also exhibits that when the fault severity increases the probability density distribution become more non-Gaussian with the dominating tail. Mathew and Alfredson [22] reported similarity after obtaining a near-Gaussian distribution for some damaged bearings and the same is observed in the case of the probability density distribution of IRF shown in Fig. 4, which, some times, may be taken as a healthy bearing.

Hence, instead of studying the probability density distribution curves, it is often more informative to examine the statistical parameters. Time domain numerical parameters have been used as a trend to detect the presence of incipient bearing damage. In this paper, the stated statistical parameters have been categorized as follows:

- measure of moments and
- dimensionless quantity of the data.

Mathematically the above may be calculated or expressed as follows:

First moment
$$\mu_{\text{mean}} = \frac{1}{N}\sum_{i=1}^{N}|x_i| . \tag{2}$$

Second moment
$$\sigma^2{}_{\text{varience}} = \frac{1}{N}\sum_{i=1}^{N}(x_i - \bar{x})^2 . \tag{3}$$

Third moment
$$\gamma_{\text{skewness}} = \frac{\frac{1}{N}\sum_{i=1}^{N}(x_i - \bar{x})^2}{\sigma^3} . \tag{4}$$

Fourth moment
$$\gamma_{\text{kurtosis}} = \frac{\frac{1}{N}\sum_{i=1}^{N}(x_i - \bar{x})^4}{\sigma^4} - 3 . \tag{5}$$

Crest factor
$$X_{cf} = \frac{\max\left(\left|x_1^2\right|\right)}{\left(\frac{1}{N}\sum_{i=1}^{N}x_1^2\right)^{1/2}} . \tag{6}$$

Impuls factor
$$X_{if} = \frac{\max\left(\left|x_i\right|\right)}{\frac{1}{N}\sum_{i=1}^{N}|x|} . \tag{7}$$

Margin factor
$$X_{mf} = \frac{\max\left(\left|x_i\right|\right)}{\left(\frac{1}{N}\sum_{i=1}^{N}\sqrt{x_1}\right)^2} . \tag{8}$$

Shape factor
$$X_{cf} = \frac{\left(\frac{1}{N}\sum_{i=1}^{N} x_1^2\right)}{\frac{1}{N}\sum_{i=1}^{N}|x_1|}, \tag{9}$$

where X_i is the data set and N is the total number of samples.

A Measure of moments as; first and second moments are well known, being the mean value and the variance respectively. The third moment normalized with respect to the cube of standard deviation is known as the coefficient of 'skewness'. The fourth moment, normalized with respect to the fourth power of standard deviation is known as 'kurtosis'[23]. The equation (2) to (5) belongs to the measure of moments. The dimensionless quantities which include a crest factor, impulse factor, margin factor and shape factor have been calculated using Equation (6) to (9). These statistical parameters may be used to perform a quick check of the changes in the statistical behavior of the signal [24].

Figs. 6 and 7 show a three-dimensional (3D) graph of IRF and ORF at two different stages of the fault. In the 3D figure, the amplitude of measures is compared with increasing fault severity for IRF and ORF. The graph shows that the dimensionless quantity and the kurtosis (fourth moment) are more effective to investigate the fault severity level because of a significant improvement in amplitude with the increasing fault diameter. However, numerical parameters can only be used for estimating the fault severity but are unable to differentiate between the IRF and ORF because the measures of the amplitude are display increasing nature in both types of the fault.

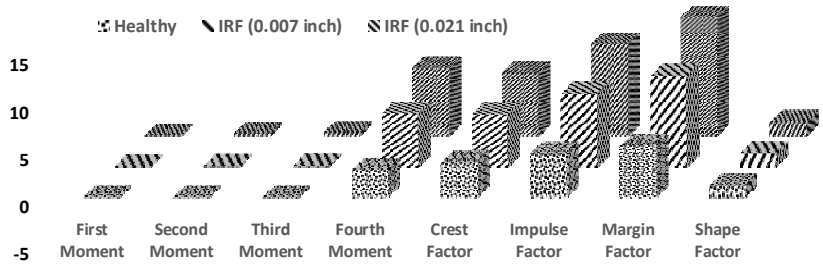

Fig. 6. A 3D plot showing the behavior of statistical parameters for healthy and inner race fault (IRF)

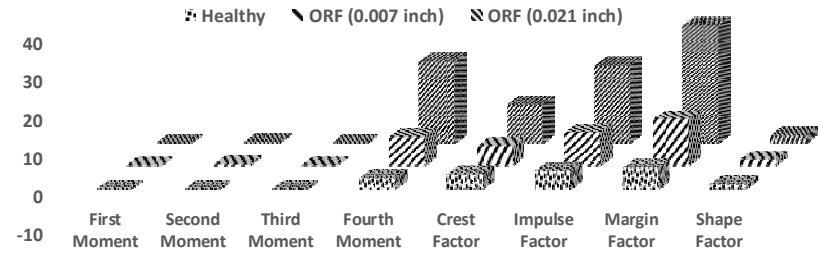

Fig. 7. A 3D plot showing the behavior of statistical parameters for healthy and outer race fault (ORF)

4. Bearing damage index based envelope power spectrum

The main drawback of the time domain analysis is an inability to identify the location of faults. In the frequency domain, these faults are characterized by significant peaks at periodic intervals but they are of low energy. These signals are modulated by a number of high-frequency harmonic components, subsequently from the structural response to individual impacts. Due to this, the characteristics frequencies are missing in the noise. The characteristics frequencies are shown in Table 1. How to extract the fault features and identify the condition from vibration signals are the key steps in the fault diagnosis of rotating machinery. Signal processing is an approach broadly used in diagnostics since it allows directly characterizing the state of the system. Several types of advanced technique have a different theoretical basis, the results obtained are usually different. Some techniques may be more suitable than others for a specific system component, depending on the environmental conditions. Therefore, it is important to choose techniques that are the most effective for the case and situation under testing for a reliable diagnosis.

The limitation of the FFT led to the development of the joint time-frequency analysis technique, in which a wavelet transform is giving information in both time and frequency domains. The wavelet transform can be considered as a mathematical tool which is further extended as Wavelet Packet Transform (WPT). The WPT is a development of wavelet decomposition that offers a richer range of possibilities for the signal analysis [25]. This analysis is obtained as a result of successive time localization of frequency sub-bands generated by a tree of low pass and high pass filter operations. The enhanced signal decomposition capability in the high-frequency region makes WPT an attractive tool for detecting and differentiating transient components with high- frequency characteristics. Wang and Zhang [26] extensively studied on the Wavelet Packet Transform (WPT) and envelope analysis for rolling bearing fault diagnosis. However, the demodulation property of these methods is limited by the degree of damage of the bearing.

In order to explore fault feature information, WPT may be used to divide finer frequency ranges. The finer frequencies ranges are known as sub-bands. Each sub-band covers one eight of the frequency information successfully. Therefore, a WPT-based method is proposed for the damage assessment of a bearing in the present study. The Daubechies family db10 has been used as a mother wavelet for wavelet packet analysis. The further energy of each sub-band has been calculated using Parsvel's theorem. The objective of the proposed method is to estimate a quantity based on WPT energy called bearing damage index (BDI) as well as to identify the WPT sub-band which contains maximum fault information.

One of the most prominent vibration signal processing techniques for the detection and diagnosis of early faults in the rolling element is envelope analysis, originally called the high-frequency resonance technique. For instance, when a rolling element contacts a defect on the inner or outer raceway, it produces an impact which in turn excites the structural modes of the bearing and its support. If a bearing has a spall type of defect on the raceway, every time a rolling passes through the spall, it would generate an impact with relatively large amplitude and decay exponentially according to the damping characteristics of the structure [27].

Therefore, the overall vibration signal measured on the bearing shows a pattern consisting of a succession of oscillating bursts dominated by the major resonance frequency of the structure. The process of demodulating the vibration signals of the resonance condition is known as envelope analysis which finally results in the excitation of an impulse. This impulse not only detects the presence of a fault but also localizes the component of the fault. It provides a mechanism for extracting out the periodic excitation of the resonance from vibration signals.

The procedure of envelope analysis is as follows: first, calculate the envelope signal $y(t)$ by applying Hilbert transform (HT) to vibration signal $x(t)$;

$$y(t) = \sqrt{x^2(t) + H^2[x(t)]} \,. \tag{10}$$

The envelope signal of $x(t)$ is simply the absolute value of the analytic signal $|y(t)|$.

The Hilbert transform can be said to be the relationship between the real and imaginary parts of the FFT of a one-sided function. Assume a piece of signal $x(t)$ its Hilbert transform $H[x(t)]$ which is defined as:

$$H[x(t)] = \frac{1}{\pi} \int_{-\infty}^{+\infty} \frac{x(\tau)}{t-\tau} \mathrm{d}\tau \,, \tag{11}$$

where, t and τ are time and translation parameters, respectively.

The next step is to go for Fourier Transform of the envelope signal in order to get the frequency domain information and calculate the spectrum.

Step for calculating BDI based enveloped power spectrum demonstrated as follows:

1) Take the measured healthy and faulty signals of IRF and ORF at 0.007 and 0.021 inches for each diameter of a fault.
2) Decompose all five signals using WPT up to level three.
3) Reconstruct each node using Db10 coefficients.
4) Calculate node energy E_i (I = 1, 2, 3….8) for one healthy and four faulty signals.

The energy of each node reconstructed signal can be obtained by

$$E_i = \sum_{i=1}^{N} |x_1|^2 \,, \tag{12}$$

where, N is the number of the sample in the reconstructed signal.

5) Calculate the percentage of the damage with the help of the bearing damage index (BDI) as shown in the flow chart.
6) Select a higher index node for identification of bearing characteristic frequency. Because the resonant vibration existing in a higher node energy,
7) Perform Hilbert transform to obtain analytical signal $y(t)$.
8) Perform spectrum analysis of signal $y(t)$.
9) Identify theoretical characteristic frequency of the bearing.

Table 1 shows the theoretical characteristic frequencies at rated load based on the geometric structure of the bearing used in this work. These frequencies are Fundamental Train

Frequency (FTF), Ball Spin Frequency (BSF), Outer Raceway Fault (ORF), and Inner Raceway Fault (IRF) frequencies and have been calculated as follows: [28-29].

Fundamental train frequency,

$$FTF = \frac{f_r}{2}\left[-\left(\frac{B_d}{P_d}\right)\cos\theta\right]. \tag{13}$$

Ball spin frequency,

$$BSF = \frac{f_r}{2}\left(\frac{P_d}{B_d}\right)\left[1-\left(\frac{B_d}{P_d}\right)\cos\theta\right]. \tag{14}$$

Outer raceway frequency,

$$ORF = N \times (FTF). \tag{15}$$

Inner raceway frequency,

$$IRF = N \times (f_r - (FTF)). \tag{16}$$

where, f_r, B_d, P_d, θ are the running speed frequency, the ball diameter, pitch diameter and contact angle respectively. Manufacturers often provide these defect frequencies in the bearing data sheet.

Table 1. The theoretical characteristics frequencies

Characteristics frequency	Value (Hz)
Running speed frequency, (Fr)	29.23 Hz
Fundamental train frequency, (FTF)	11.64 Hz
Ball spin frequency, (BSF)	68.89 Hz
Outer race fault frequency, (RFF),	104.76 Hz
Inner race fault frequency, (FTF)	158.34 Hz

5. Results and discussions

In this paper, we have studied a bearing fault diagnosis method of an induction motor rolling bearing for its inner race and outer race. The proposed method is based on BDI and enveloped power spectrum using Hilbert transform, which, overcome the limitations of enveloped power spectrum. Fig. 8 shows the flow chart of calculation of BDI and enveloped power spectrum. Figs. 9 and 10 shows the calculated BDI for IRF and ORF up to three levels i.e. eight sub-bands or wavelet order. Further, a higher value of wavelet order is chosen to perform Hilbert transform and the spectral analysis. It is observed that the wavelet order 7 gives a higher value for both the cases IRF and ORF. These wavelet orders primarily may consist of

the fault information. Based on this investigation the wavelet order 7 has been chosen for the enveloped power spectrum.

After performing Hilbert transform and the spectral analysis on the wavelet order 7, theoretical frequencies have been observed. The calculated characteristic frequencies are 158.34 Hz for the inner race fault and 104.76 Hz for the outer race fault as shown in Table 1. The BDI based enveloped power spectrum for the vibration data shows spectrum peaks values at 161.1 Hz for the inner race fault in Fig. 11 with a fault size equal to 0.007 and 0.021 inches. Frequency 323.7 Hz is the multiple of 161.1 Hz which also confirms the existence of the inner race fault in the rolling bearing. Similarly, frequency 107 Hz observed for the outer race fault in Fig. 12 with fault sizes of 0.007 inches and 0.021 inches and frequency 215.3 Hz multiple of 107 Hz which ensure the existence of the outer race fault in the rolling bearing. The obtained frequencies are near to the calculated frequency as per Table 2. Frequency peak 30.03 Hz is the running speed frequency which is also present in both Figs. 11, 12 and represents the rotational speed of the induction motor. The above analysis shows that energy of the wavelet orders is sensitive to the faults identification in bearings.

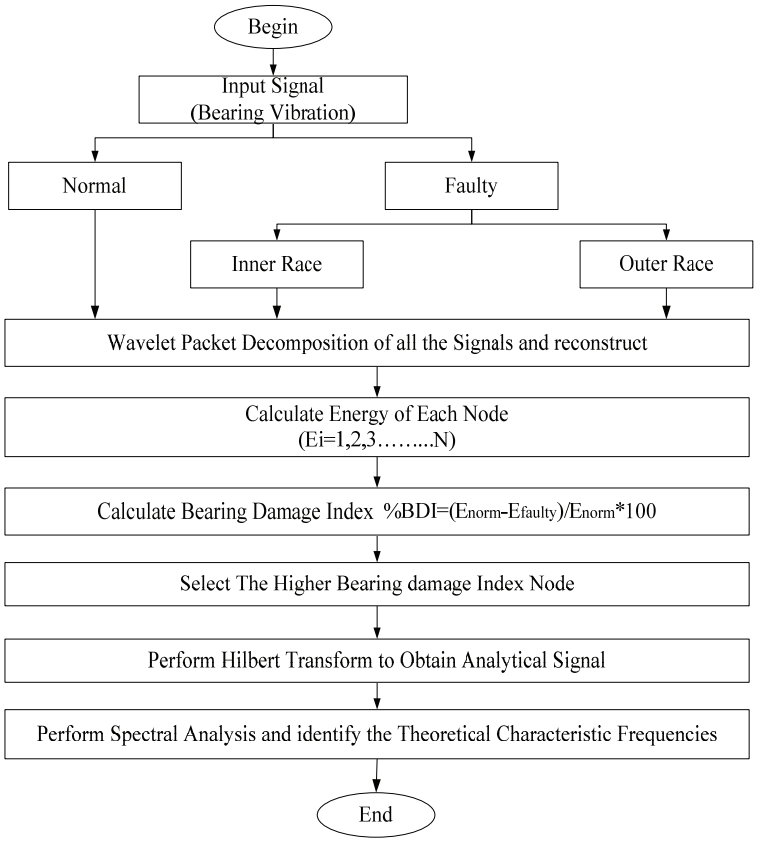

Fig. 8. Flow chart for calculation of bearing damage index

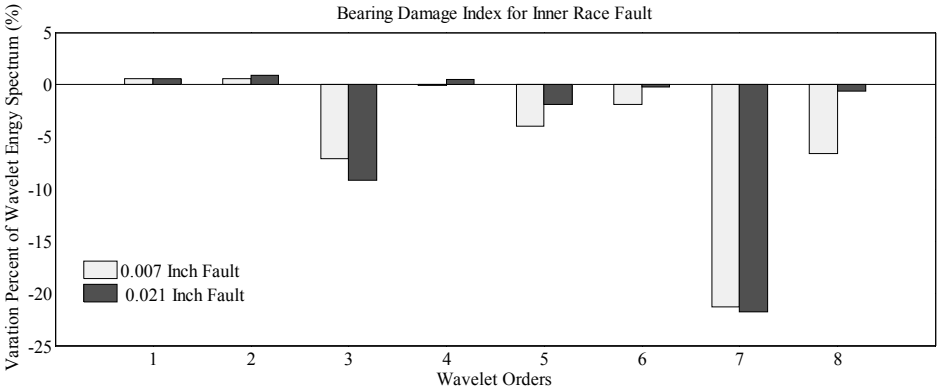

Fig. 9. Bearing damage index of inner race fault

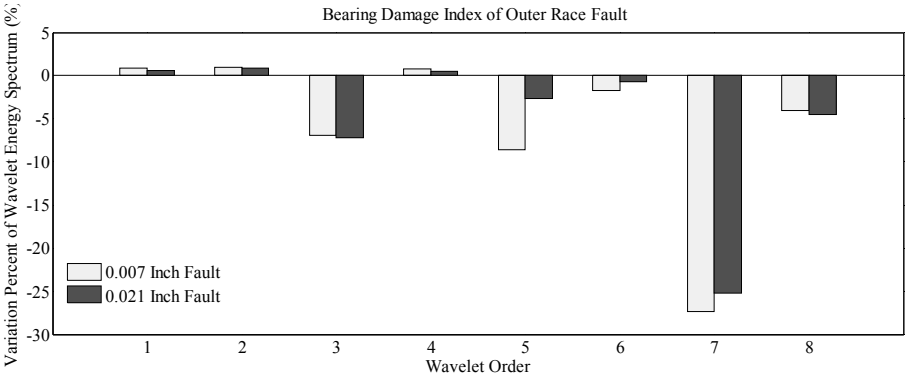

Fig. 10. Bearing damage index of outer race fault

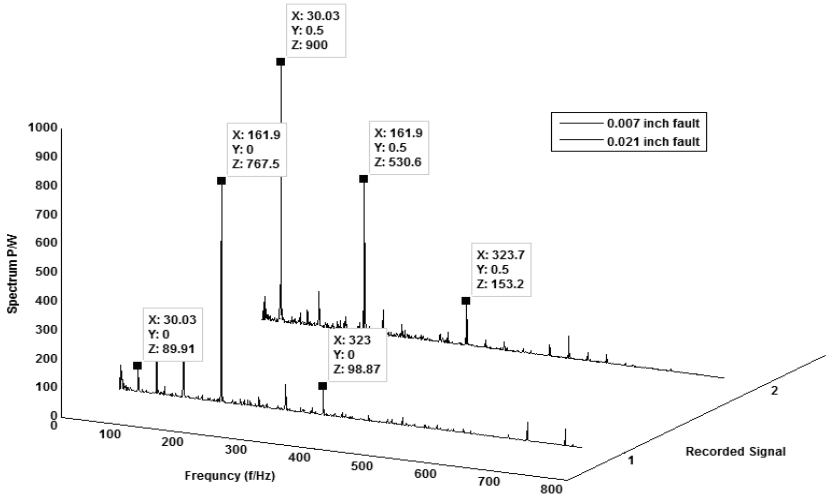

Fig. 11. Power spectrum of inner race fault

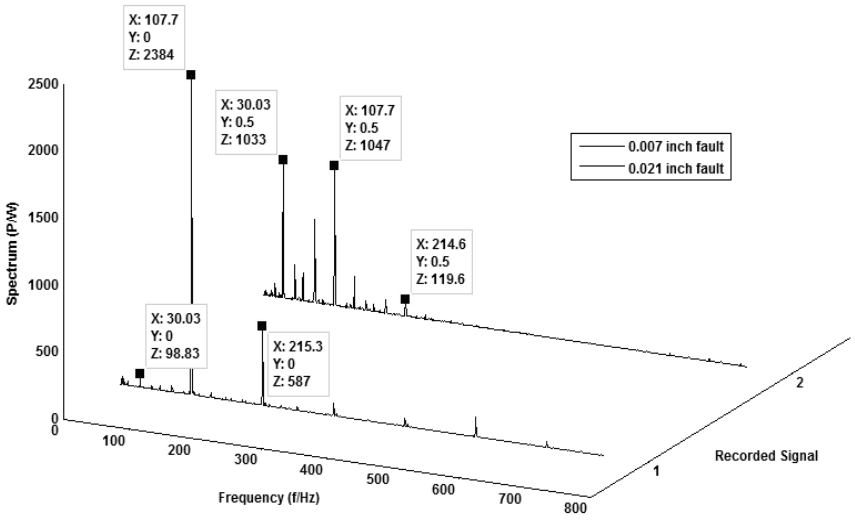

Fig. 12. Power spectrum of outer race fault

Table 2. Comparison of observed and theoretical frequency

	Theoretical calculated frequency (Hz)	**Observed frequency (Hz)**
IRF	158.3 Hz	161.9 Hz
ORF	104.7 Hz	107.7 Hz

6. Conclusions

The parameters calculated from time domain are not capable of identifying the fault in the bearing. Results show that kurtosis and dimensionless quantities are more sensitive towards the fault severity but fail to find the location of the fault. A new approach based on BDI enveloped power spectrum is proposed. In order to calculate BDI, Wavelet Packet Transform (WPT) is used which is a time-frequency analysis and has great advantages in dealing with the vibration signature of the bearing health monitoring system. The BDI has been used as selection criteria of the wavelet order for enveloped power spectrum to find out the theoretical characteristic frequency for outer and inner race defective bearings from noisy vibration signals.

References

[1] Mehrjou M.R., Mariun N., Marhaban M.H., *Rotor fault condition monitoring techniques for squirrel-cage induction machine - A review,* Mech. Syst. Signal Process, no. 25, pp. 2827-2848 (2011).

[2] Wadhwani S., Gupta S.P., Kumar V., *Wavelet based vibration monitoring for detection of faults in ball bearings of rotating machines*, Journal Inst. Eng. (India)-EL, no. 86, pp. 77-81 (2005).

[3] Purushotham V., Narayanan S., Prasad S.A.N., *Multi-fault diagnosis of rolling bearing elements using wavelet analysis and hidden Markov model based fault recognition*, NDT E Int., no. 38, pp. 654-664 (2005).
[4] Chandel A.K., Patel R.K., *Bearing Fault Classification Based on Wavelet Transform and Artificial Neural Network*, IETE Journal of Research, vol. 59, no. 3, pp. 219-225 (2013).
[5] Qin Y., Mao Y., Tang B., *Vibration signal component separation by iteratively using basis pursuit and its application in mechanical fault detection*, J. Sound Vib., no. 332, pp. 5217-5235 (2013).
[6] Djebala A., Ouelaa N., *Detection of rolling bearing defects using discrete wavelet analysis*, pp. 339-348 (2008).
[7] Gao R.X., Yan R., *Non-stationary signal processing for bearing health monitoring,* Int. J. of Manufacturing Research, vol. 1, no. 1, pp. 18-40 (2006).
[8] Gouda Kareem M., Joshua Tarbutton A., Hassan M.A. et al., *A wavelet-based index for fault detection and its application in condition monitoring of helicopter drive-train components*, Int. J. of Manufacturing Research, vol. 10, no.1, pp. 87-106 (2015).
[9] Randall R., Antoni J., *Rolling element bearing diagnostics–A tutorial*, Mech. Syst. Signal Process, no. 25, pp. 485-520 (2011).
[10] Changting W., Gao R.X., Ruqiang Y., Malhi A., *Rolling bearing defect severity assessment under varying operating conditions*, Int. J. of Manufacturing Research, vol. 4, no. 1, pp. 37-56 (2009).
[11] Wadhwani S., Gupta S.P., Kumar V., *Fault Classification for Rolling Element Bearing in Electric Machines*, IETE J. Res. 54 (2011).
[12] Cabal-Yepez E., Romero-Troncoso R.J., Garcia-Perez A., Osornio-Rios R.A., *Single-parameter fault identification through information entropy analysis at the startup-transient current in induction motors*, Electr. Pow. Syst. Res, vol. 89, pp. 64-69 (2012).
[13] Choudary A., Tondon N., *Vibration response of rolling element bearings in a rotor bearing system to a local defect under radial load*, Transactions of ASME, vol. 128, pp. 252-61(2006).
[14] Sreejith B., Verma A.K., Srividya A., *Fault diagnosis of rolling element bearing using time-domain features and neural networks*, IEEE Region 10 Colloquium and the Third ICIIS, Kharagpur, India, pp. 6-11 (2008).
[15] Miao Q., Wang D., Huang H.Z., *Identification of characteristic components in frequency domain from signal singularities*, Rev. Sci. Instrum, 81: 035113 (2010).
[16] Nikolaou N.G., Antoniadis I.A., *Rolling element bearing fault diagnosis using wavelet packets*, NDT & E International, vol. 35, pp. 197-205 (2002).
[17] Yen G.G., Lin K.-C., *Wavelet Packet Feature Extraction for Vibration monitoring*, Proceedings of the IEEE Conference on Control Applications, pp. 1573-1578 (1999).
[18] Powalka B., Dhupia J.S., Ulsoy A.G., Katz R., *Identification of machining force model parameters from acceleration measurements*, Int. J. of Manufacturing Research, vol. 3, no. 3, pp. 265-284 (2008).
[19] Hong H., Liang M., *Fault severity assessment for rolling element bearings using the Lempel-Ziv complexity and continuous wavelet transform*, Journal of Sound and Vibration, vol. 320, pp. 452-468 (2009).
[20] Case Western Reserve University, Bearing data center [online]: URL:http://www.eecs.cwru.edu/laboratory/bearing/download.htm, accessed 2011.
[21] Collacott R.A., *Mechanical fault diagnosis and condition monitoring*, London, Chapman and Hall (1977).
[22] Mathew J., Alfredson R.J., *The condition monitoring of rolling element bearings using vibration analysis*, Journal of Vibration, Acoustics Stress and Reliability in Design, vol. 106, pp. 447-53 (1984).
[23] Pachaud C., Salvetat R., Fray C., *Crest factor and kurtosis contributions to identify defects inducing periodical impulsive forces,* Mechanical Systems and Signal Processing, vol. 11, pp. 903-916 (1997).
[24] Heng R.B.W., Nor M.J.M., *Statistical Analysis of Sound and Vibration Signals for Monitoring Rolling Element Bearing Condition*, Applied Acoustics, vol. 53, pp. 211-226 (1998).

[25] McFadden P. ., Smith J.D., *Vibration monitoring of rolling element bearings by the high frequency resonance technique-a review*, Tribology International, vol. 17, pp. 3-10 (1984).
[26] Wowk V., *Machinery Vibration Measurement and Analysis*, McGraw-Hill, New York (1991).
[27] Liu Q., Chen F., Zhou Z., Wei Q., *Fault Diagnosis of Rolling Bearing Based on Wavelet Package Transform and Ensemble Empirical Mode Decomposition*, (2013).
[28] Wang D., Zhang W., *Fault diagnosis study of ball bearing based on wavelet packet transform*, China Mechanical Engineering, vol. 23, no. 3, pp. 295-298 (2012).
[29] Jiang F., Li W., Wang Z., Zhu Z., *Fault Severity Estimation of Rotating Machinery Based on Residual Signals*, Adv. Mech. Eng., vol. 2012, pp. 1-8 (2012).

ARCHIVES OF ELECTRICAL ENGINEERING VOL. 66(1), pp. 121-139 (2017)

DOI 10.1515/aee-2017-0009

Comparison of higher harmonic contents in salient pole synchronous generator with different rotor construction

KRZYSZTOF LUDWINEK, ROMAN NADOLSKI, JAN STASZAK

Kielce University of Technology, Department of Automatic Control and Computer Science
Tysiąclecia P. P. 7, 25-314 Kielce, Poland
tel. +48 41 342 46 82
e-mail: {k.ludwinek / r.nadolski / j.staszak}@tu.kielce.pl

(Received: 05.02.2016, revised: 13.09.2016)

Abstract: The paper presents a comparison of higher harmonics in induced phase voltages of a stator winding in the no-load state of a three-phase 5.5 kVA salient pole synchronous generator. The comparison is carried out for the synchronous generator with different salient pole rotor constructions: a non-skewed solid rotor, a non-skewed solid rotor with radial incisions, and a laminated electrotechnical steel rotor with skewed slots and damping bars. The calculations of higher harmonics are based on the magnetic field distributions in the air gap, which are carried out in a 2D model in a FEMM program and on the induced voltage waveforms in the stator windings registered during experimental investigations of the 5.5 kVA salient pole synchronous generator in the no-load state.

Key words: salient pole synchronous generator, higher harmonics, solid rotor, rotor with radial incisions, laminated rotor

1. Introduction

The distribution of the magnetic flux density in the air gap of a salient pole synchronous generator has an influence on the occurrence of higher harmonics in voltage induced in the stator windings [1-8]. The shape of the stator and rotor magnetic surfaces has an influence on the distribution of the magnetic flux density along the air gap circumference, and the magnetic flux density:

– decreases at the stator and rotor slot opening,

– increases if the length of the air gap decreases.

Knowledge about the effective air gap length allows, for example, an analytically more precise specification of: self- and mutual inductances, the distribution of flux density in the air gap, voltages induced in the stator windings etc. [9-14]. The effective air gap length is calculated from the initial length of the air gap by taking into account the total Carter Factor, which is the sum of two factors [4, 14, 15]. The first factor is calculated by assuming a smooth rotor

surface and taking into account stator slots. The second factor is calculated by assuming a smooth stator surface and with rotor slots. In electrical machines the problem of variations in the distribution of the magnetic flux density due to stator and rotor slot openings was first solved by F.W. Carter in 1901 [16]. Generally, the variations in the distribution of magnetic flux density are taken into account in increases of the initial length of the air gap by means of the Carter factor [4, 14-16]. Variations in the distribution of the magnetic flux density in a one sided uniform air gap (including the slots on the stator or on the rotor side) can be determined:

– by the quotient of minimum to maximum magnetic flux density [14, 15]

$$\frac{B_{\min}}{B_{\max}} = \frac{2u}{1+u^2}, \tag{1}$$

– in relation to the quotient of average to maximum magnetic flux density [4]

$$\frac{B_0}{B_{\max}} = \frac{(u-1)^2}{2(1+u^2)}, \tag{2}$$

where: $B_{\min}$ is the minimum magnetic flux density, $B_{\max}$ is the maximum magnetic flux density, u is the coefficient

$$u = b_s / 2\delta_0 + \sqrt{1+(b_s / 2\delta_0)^2},$$

δ_0 is the initial length of the air gap, b_s is the length of the stator slot opening, B_0 is the average magnetic flux density,

As shown in [4] when assuming no eddy currents and the same length of the air gap, if the relation between the length of the stator slot opening and the stator tooth pitch is $b_s/\tau_s < 0.625$, then an analytical expression of the flux density variations in an air gap can be described as:

– if $0 < \alpha < 0.8\alpha$

$$B(\alpha) = \left(1-\beta-\beta\cos\frac{\pi}{0.8\alpha_0}\alpha\right)B_{\max}, \tag{3}$$

– if $0.8\alpha < \alpha < 0.5\alpha_d$

$$B(\alpha) = B_{\max}, \tag{4}$$

where: $\beta = B_0/B_{\max}$, α is the angle of the stator slot opening in relation to the rotor circumference [4], $\alpha_0 = 2b_s/d = b_s/r_s$, d is the inner stator diameter, r_s is the inner stator radius.

In a salient pole synchronous generator the magnetic rotor asymmetry (in the direct and quadrature axes) and the shape of a pole shoe with various lengths of an air gap and with the bars of the damping cage (placed inside the pole shoes) mean that the air gap is more complex than in cylindrical or asynchronous generators. The air gap length has a significant influence on the magnetic flux density distribution and on the induced stator voltage waveforms [1-13, 17, 18].

Most frequently, the pole shoes in a salient pole synchronous generator are made of solid iron or with electrotechnical sheets (up to 2.5 mm in thickness) [14].

The presence of a rotor damping cage during the cooperation of a synchronous generator with a power grid allows the shortening of many transient processes [19-21] and the presence of a damping cage is not a subject of discussion. But in the case of the synchronous generator set (working as a back-up power system), the presence of a damping cage is debatable particularly in the no-load state. The damping cage can be made of solid iron [14].

Apart from the stator and rotor slotting and the type of stator and rotor windings and damping cage, the inner eccentricity of the stator and rotor has an influence on the distribution of the magnetic flux density in the air gap of a salient pole synchronous generator. This problem is widely discussed in many papers [22-25].

Because of the small initial length of the air gap, the influence of the air gap length on the eddy currents and power loss in the solid elements in low-power synchronous generators is more visible than in high-power ones. The depth of eddy current penetration λ is determined as [14, 15]:

$$\lambda = \frac{5 \cdot 10^5}{\sqrt{f \gamma \mu_r}}, \tag{5}$$

where: f is the frequency, γ is the electrical conductivity, μ_r is the relative magnetic permeability.

Frequently, electrotechnical sheets are used as a method of eddy current reduction in pole shoes [14]. The other method of reducing the eddy currents shown in this paper is by making radial incisions across the width of the pole shoe [18]. According to expression (5), the depth of an incision across the width of the pole shoe depends on the frequency of the magnetic field and the type of rotor material (its electrical conductivity and magnetic permeability).

This paper presents the influence of the pole shoe radial incision across the width of the pole shoe:

– on the distribution of the normal magnetic flux density in the air gap of a 5.5 kVA salient pole synchronous generator,

– on the waveform of voltages induced in the stator windings.

The air gap length δ between the stator and solid pole shoe in relation to the initial length of the air gap in the longitudinal axis of the examined 5.5 kVA salient pole synchronous generator is expressed as [18]:

$$\delta = \frac{\delta_0}{\cos\alpha}, \tag{6}$$

where: δ is the air gap length between the stator and solid pole shoe, δ_0 is the initial length of the air gap in the longitudinal axis, α is the electrical angle of the pole shoe which is calculated in relation to the longitudinal axis.

The visualization of air gap length δ between the stator and solid pole shoe and the depth of incision δ_i across the width of the pole shoe in relation to the initial length of air gap δ_0 and inner stator radius r_s are shown in Fig. 1.

Fig. 2 shows the relative influence of the air gap length δ (6) and of radial incision of a pole shoe on the effective air gap length in relation to inner stator radius r_s and diameter d vs. the electrical angle of the pole shoe α in relation to the longitudinal axis.

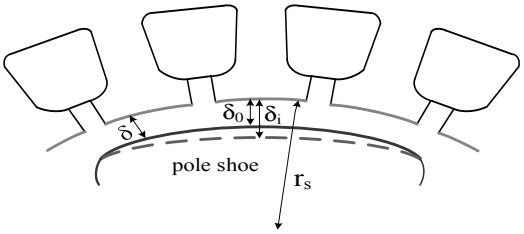

Fig. 1. Visualization of the air gap length δ and the depth of incision δ_i across the width of a pole shoe in relation to the initial length of the air gap δ_0 and inner stator radius r_s

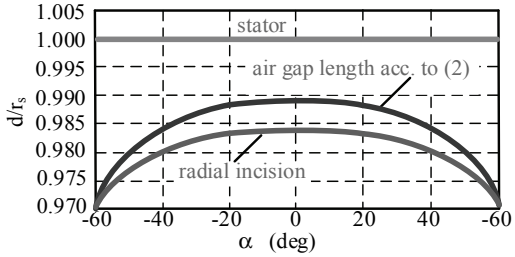

Fig. 2. Relative influence of the air gap length δ and the radial incision δ_i of a pole shoe in relation to inner stator radius r_s and diameter d vs. electrical angle α of the pole shoe

The introduction of the radial incisions on the pole shoe surface results in even loss of the steel (Figs. 1 and 2) and has the effect of flattening the resultant magnetic flux density in the air gap [14, 18]. The effect of flattening the resultant magnetic flux density due to the radial incisions on the pole shoe surface has a similar effect to the case of the pole shoe saturation [14, 18]. The advantage of radial incisions on the solid rotor on the pole shoe surface is that the incisions can be done by utilising a simple lathe. The depth of the radial incisions on the examined rotor circumference is equal to $2\delta_0$ (Fig. 2).

Due to the complex air gap, more detailed results are obtained using Finite Element Method (FEM) software for 2D or 3D models [12, 26]. Simulations of the magnetic flux density distribution and induced voltages with the FEM software are very similar to the results of experimental investigations due to the fact that the FEM models include many construction details [11, 12]. But the FEM calculations also have many disadvantages, for example [11, 12, 27, 28]:

– the length of time required for the calculations in FEM programs is longer than in an analytical way,
– commercial FEM programs are very expensive and require detailed knowledge about the construction of the electrical machine,
– FEM models require a large number of constructional details,
– for a beginner or even a person with intermediate skills, considering which electromagnetic parameters have a direct influence on the final results is difficult.

Therefore, simulations of the magnetic flux density distribution and induced voltages in electrical machines are often carried out by means of both analytical expressions, circuital models and/or FEM software [3, 5-12, 27-29].

In this paper the simulation of the magnetic flux density distribution and experimental investigations of induced voltages are carried out for the salient pole synchronous generator rated: $S_N = 5.5$ kVA, $U_N = 400$ V (Y), $I_N = 7.9$ A, $\cos\varphi_N = 0.8$, $n_N = 3000$ rpm, the number of pole pairs $p_b = 1$, the number of stator slots $Q_s = 24$ with a single-layer winding, rotor: with and without the skew angle $\alpha_q = 15°$ (the skew angle is equal to a single stator tooth pitch). Moreover, magnetic flux density distributions are determined in the air gap of the examined 5.5 kVA salient pole synchronous generator after creating the geometry of the 2D field model in the FEMM program [9, 11-13, 26]. In calculations of the distribution of the magnetic flux density the presence of eddy currents is omitted in the 2D field model due to the powering of the field winding by DC nominal current at no-load $I_{f0N} = \text{const}$.

2. Distributions of magnetic flux density

The distribution of the magnetic flux density lines is obtained taking into account the non-linear material properties. Fig. 3 shows two no-load magnetisation characteristics obtained from the measurement set for the 5.5 kVA salient pole synchronous generator with two rotor structures. One of the no-load characteristics is for a salient pole synchronous generator with a factory rotor made of insulated electrotechnical sheets and the second one is for a generator with a solid rotor with radial incisions.

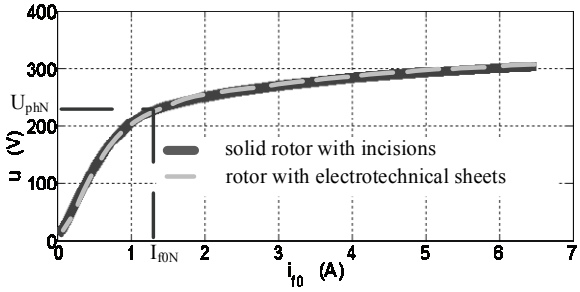

Fig. 3. Comparison of the two no-load magnetisation characteristics of the 5.5 kVA salient pole synchronous generator with two rotor structures obtained from the measurement set

Figure 3 shows that the presented no-load characteristics are very similar.

Figures 4 and 5 show the distribution of the magnetic flux density lines of the examined 5.5 kVA nonlinear salient pole synchronous generator in the no-load steady state in the Finite Element Method Magnetics (FEMM) freeware program [26]. The magnetic flux density lines are obtained from DC current I_{f0N} flowing in the field winding. In the FEMM 2D software, the skew effect in the normal component of magnetic flux density distributions is obtained by subdividing the active rotor length into 79 skewed axial slides along the axial length (39 radial

incisions and 40 without radial incisions – detailed in Fig. 9b). The normal component of magnetic flux density B_{ns} with the rotor skewed slots is calculated as [7]:

$$B_{ns} = \frac{1}{\alpha_q} \int_{\theta-\frac{\alpha_q}{2}}^{\theta+\frac{\alpha_q}{2}} B_n \partial\theta \,, \tag{7}$$

where: α_q is the electrical skew angle, B_{ns}, B_n are the normal component of magnetic flux density in a non-skewed and skewed rotor, respectively.

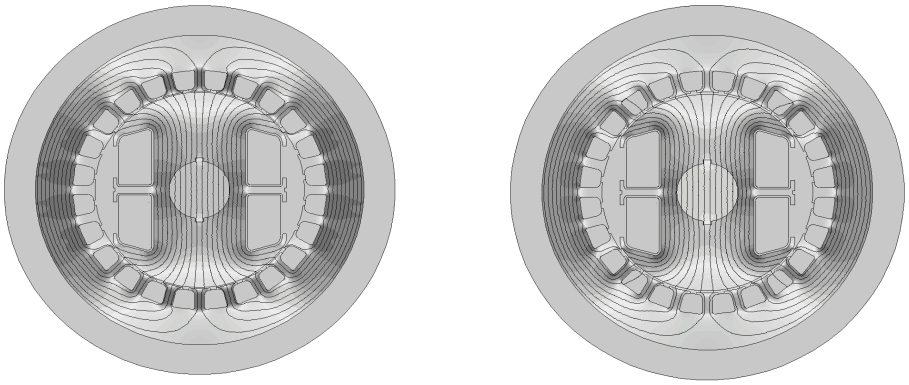

(a) (b)

Fig. 3. General view of the distribution of the magnetic flux density lines in the no-load steady state in the examined 5.5 kVA salient pole synchronous generator: with solid rotor without radial incisions (a), with solid rotor with radial incisions (b)

The distribution of the magnetic flux density lines of the examined 5.5 kVA nonlinear salient pole synchronous generator with the rotor made of 0.5 mm insulated electrotechnical sheets (with an air gap as in the case of the solid rotor without radial incisions) is the same as shown in Fig. 4a.

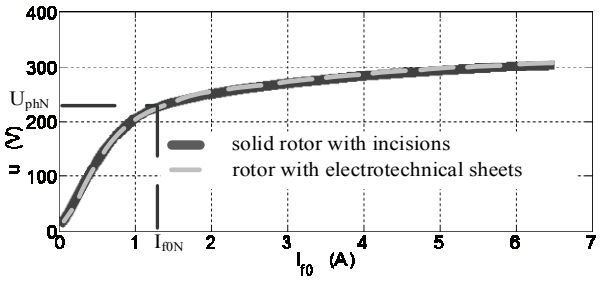

Fig. 4. Comparison of the two no-load magnetisation characteristics of the 5.5 kVA salient pole synchronous generator with two rotor structures obtained in the measurement set

Differences in the distribution of the magnetic flux density are more evident in Fig. 5 (detailed view of the air gaps) and in Fig. 6, where the comparison of the distribution of the normal component of magnetic flux density in the air gap vs. the circumference of the two rotor types is shown.

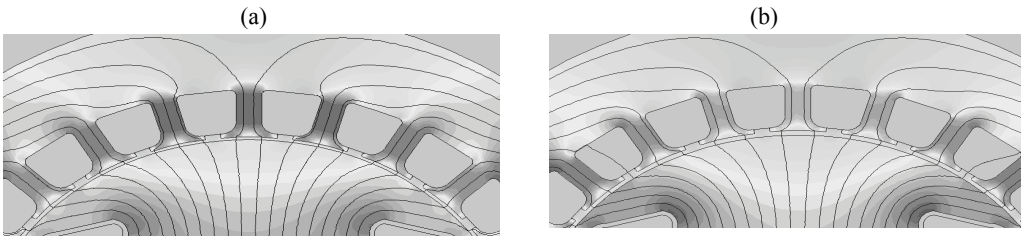

Fig. 5. Detailed view of the distribution of the normal component of magnetic flux density lines in the no-load steady state in the air gap with rotor: without radial incisions (a), with radial incisions (b)

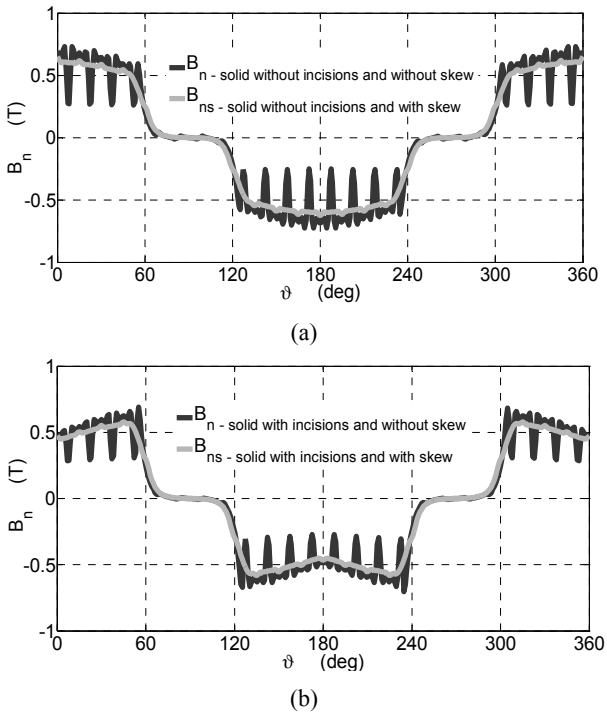

Fig. 6. Comparison of normal component of magnetic flux density distributions for the examined synchronous generator with: a non-skewed and skewed solid rotor (a), a non-skewed and skewed solid rotor with the radial incision (b)

Fig. 6 shows a comparison of the distribution of the normal component of magnetic flux density in the air gap for the synchronous generator with and without the radial incisions and with and without the skew angle. The distribution of the normal component of magnetic flux

density in the air gap for the 5.5 kVA synchronous generator with a rotor made of insulated 0.5 mm electrotechnical sheets gives the same result as in the case of the solid rotor without radial incisions.

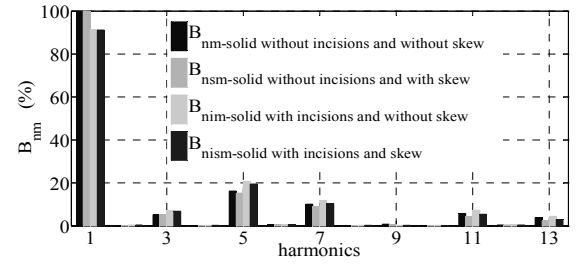

(a)

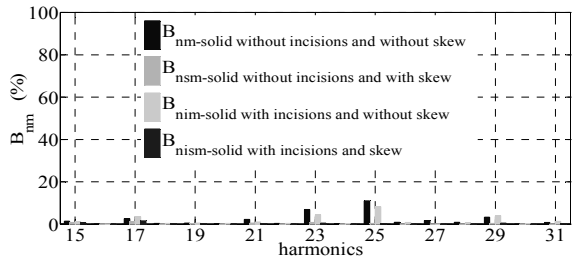

(b)

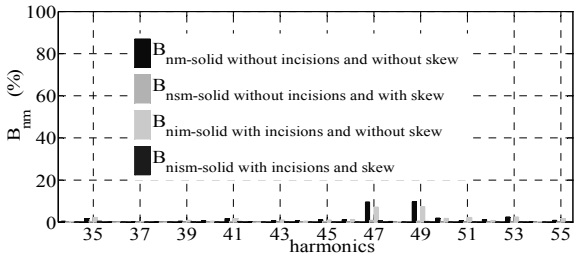

(c)

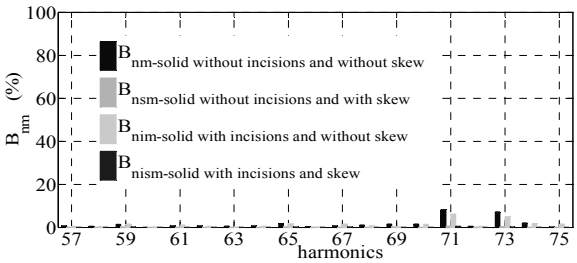

(d)

Fig. 7. Comparison of harmonic contents in the normal component of magnetic flux density distributions: from 1st to 13th order (a), from 15th to 31st order (b), from 35th to 55th order (c), from 57th to 75th order (d)

The distribution results presented in Fig. 6 show that in the areas with a longer air gap the flux density distributions decrease but in the areas with a smaller air gap they increase (Fig. 5b). The variations in the distribution of the normal component of the magnetic flux density shown in Fig. 6 are caused by a permeance change between the stator teeth and slots on the circumference of the stator and rotor (Fig. 5).

Figure 7 shows the comparison of the magnitude of harmonic contents in the magnetic flux density distributions (Fig. 6) due to the Fourier analysis.

The comparisons shown in Fig. 7 are determined in relation to the amplitude of the fundamental component of the magnetic flux density distribution in the air gap for the synchronous generator with a solid rotor without incisions and without skewed poles. The results in Fig. 7 reveal that the $2\delta_0$ radial incision causes:

– 10% reduction of the magnetic flux density fundamental component (Fig. 7a),

– an increase of the odd harmonics up to the 17th order by a few percent,

– a reduction of the $kQ_s \pm 1$ higher harmonic amplitudes by a few percent (k is integer number).

The number of radial incisions has an influence on the increase of the odd harmonics up to the 17th order (Fig. 7). The radial incisions, which are the percentage loss of steel along the length of the pole shoe, changed the v-th harmonics of the magnetic flux density from B_{nv} (for the non-skewed rotor without incisions) to B_{niv} (for the non-skewed rotor with incisions) and from B_{nsv} (for the skewed rotor without incisions) to B_{nisv} (for the skewed rotor with incisions).

The effect of flattening the equivalent air gap between the stator and the pole shoe (with the radial incision) can be reduced by incisions defined according to the relation (6). But such incision must be made with numerically controlled machine tools instead of a typical lathe. The normal component of the magnetic flux density distributions for the examined 5.5 kVA synchronous generator, as presented in Fig. 6, has an impact on the content of higher harmonics in the induced stator phase voltages. As was shown in [9, 18], the wave-shape of the induced stator phase voltages is influenced not only by the magnetic flux density distributions (Fig. 5) but also by the winding coefficient (which for a single-layer winding depends on the winding distribution, slot opening and rotor skew coefficients).

3. Voltages induced in the stator windings

In the no-load state of the salient pole synchronous generator (currents i_a, i_b and i_c are equal to zero) without the power grid and a damping cage, voltages: u_a, u_b, u_c induced in the stator windings and u_f in the field winding, taking into account the electrical angle of the rotor position θ, can be derived for the stator windings (in stator coordinates) and for the field winding in rotor coordinates [11, 12]

$$\frac{\mathrm{d}\Psi_a(\theta, i_f)}{\mathrm{d}t} = u_a\,, \quad \frac{\mathrm{d}\Psi_b(\theta, i_f)}{\mathrm{d}t} = u_b\,, \quad \frac{\mathrm{d}\Psi_c(\theta, i_f)}{\mathrm{d}t} = u_c\,, \tag{8}$$

$$\frac{\mathrm{d}\Psi_f(\theta, i_f)}{\mathrm{d}t} + R_f i_f = u_f\,, \tag{9}$$

$$\frac{\mathrm{d}\theta}{\mathrm{d}t} = \omega\,, \tag{10}$$

where: a, b, c and f are the indexes of stator windings and field winding, u_a, u_b, u_c and u_f are the stator phase voltages and field voltage, Ψ_a, Ψ_b, Ψ_c and Ψ_f are the stator and field linkage fluxes, θ is the electrical angle of the rotor position, $\theta = \theta_m p$, θ_m is the mechanical angle of the rotor position, $\omega = \mathrm{d}\theta/\mathrm{d}t$ is the electrical angular velocity, R_f is the resistance of the field winding, i_f is the field current, p is the number of pole pairs.

Based on expressions (8)-(10) and the relations between the magnetic fluxes and magnetic flux densities and taking into account ω = const and $i_f = I_{f0N}$ = const (I_{f0N} – nominal field current at no-load), the induced phase stator voltages u_a, u_b, u_c and u_f can be expressed as:

$$\left.\begin{aligned} 2N_s k_w \frac{r_s l_s}{p}\frac{\partial B_a(\theta)}{\partial\theta}\frac{\mathrm{d}\theta}{\mathrm{d}t} &= u_a\,,\\ 2N_s k_w \frac{r_s l_s}{p}\frac{\partial B_b(\theta)}{\partial\theta}\frac{\mathrm{d}\theta}{\mathrm{d}t} &= u_b\,,\\ 2N_s k_w \frac{r_s l_s}{p}\frac{\partial B_c(\theta)}{\partial\theta}\frac{\mathrm{d}\theta}{\mathrm{d}t} &= u_c\,, \end{aligned}\right\} \tag{11}$$

$$2N_f k_{wf} \frac{r_r l_r}{p}\frac{\partial B_f(\theta)}{\partial\theta}\frac{\mathrm{d}\theta}{\mathrm{d}t} + R_f i_f = u_f\,, \tag{12}$$

where: B_a, B_b, B_c and B_f are the stator and field density of magnetic fluxes with and without the rotor skew (eg. Fig. 6), N_s, N_f are the number of stator and field windings, r_s, r_r are the inner stator and outer rotor radius, l_s, l_r are the length of stator and rotor, k_w is the winding factor: $k_w = k_d\, k_p\, k_b\, k_q$ [9, 14], k_d is the distribution factor, k_p is the pitch factor, k_{bv} is the slot opening factor, k_{qv} is the skew factor, k_{wf} is the field winding factor.

The problem of the influence of the pitch- and winding distribution, and slot-opening and slot-skewing winding factors (of the 5.5 kVA salient pole synchronous generator) on the reduction of the harmonic contents in induced stator voltages in the most frequently used windings: single-layer, double-layer and triangular, is widely discussed in [9].

Fig. 8 shows the comparison of the lower order harmonics of magnetic flux density (shown in Fig. 6) and magnetic flux density derivatives for the synchronous generator with a solid rotor without incisions. Lower order harmonics of magnetic flux density for the generator with solid rotor with incisions are very similar to ones presented in Fig. 8 and are omitted. The differences in magnitudes of the harmonics are better visible in Fig. 7. Fig. 8 shows that the ν-harmonic presence in magnetic flux density is enhanced ν-times in magnetic flux density derivatives. The ν-harmonic in magnetic flux density enhanced ν-times by derivatives has significant influence on the increase of the harmonic content in the induced stator voltages-expression (11).

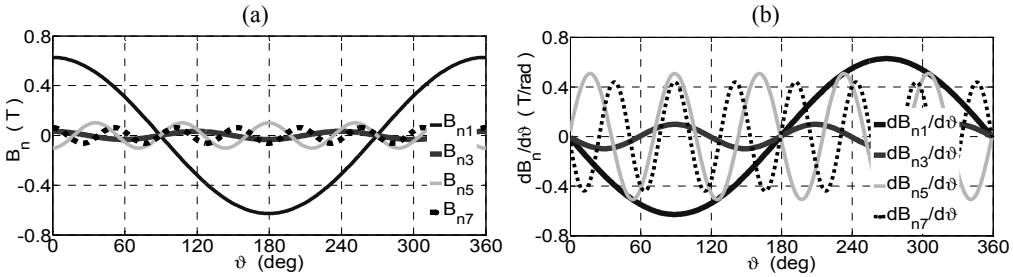

Fig. 8. Comparison of the lower order harmonics: of magnetic flux density (a), magnetic flux density derivatives (b)

Fig. 9 presents winding coefficients for a single layer three-phase winding [9]. The following parameters of the 5.5 kVA synchronous generator are used in calculation of the winding factors of the harmonic v [9]: the number of phases $m = 3$, the number of pole pairs $p_b = 1$, the number of stator slots $Q_s = 24$, the stator slot opening $b_s = 3$ mm, the coil pitch in per unit $y = 1$.

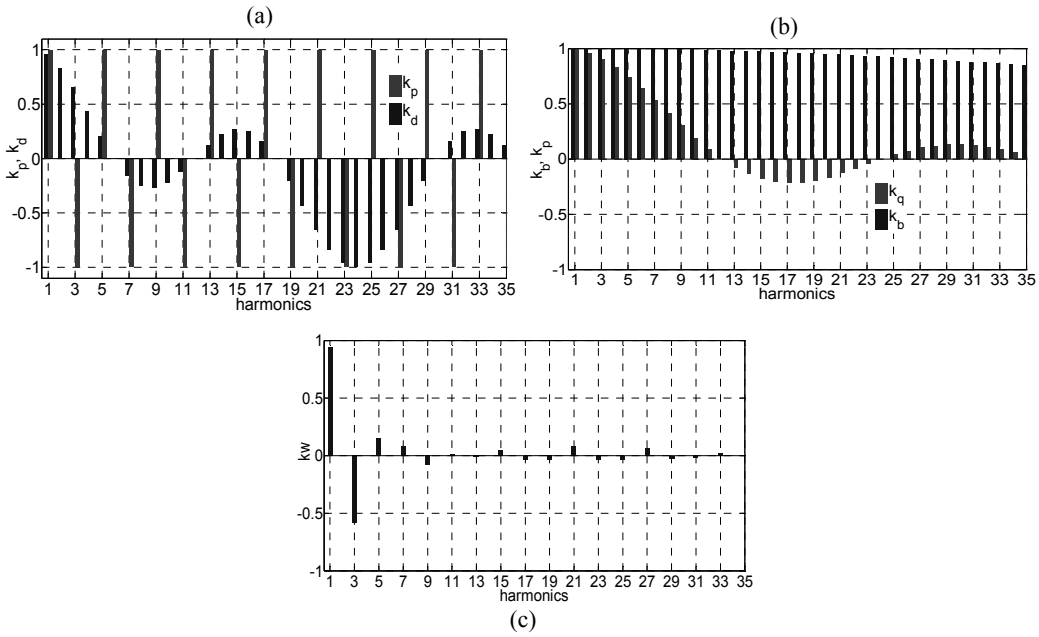

Fig. 9. Winding factors for single layer winding of the 5.5 kVA synchronous generator: k_p and k_d (pitch and distribution factors) (a), k_b and k_q (slot opening and skew factors) (b), $k_w = k_p\,k_d\,k_b\,k_q$ (total factor) (c)

Fig. 10 presents the waveforms of the induced stator voltages of the examined 5.5 kVA salient pole synchronous generator in no-load state calculated in Matlab from expression (11)

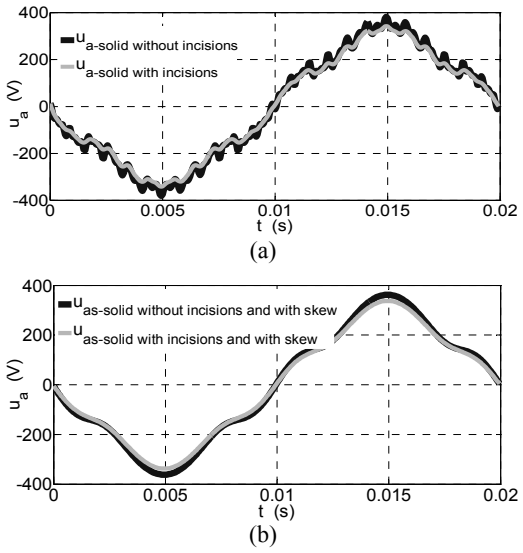

Fig. 10. Waveforms of the induced stator voltages under no-load conditions for the examined 5.5 kVA synchronous generator with the following rotors: solid, skewed and non-skewed (a), solid, skewed and non-skewed with radial incisions (b)

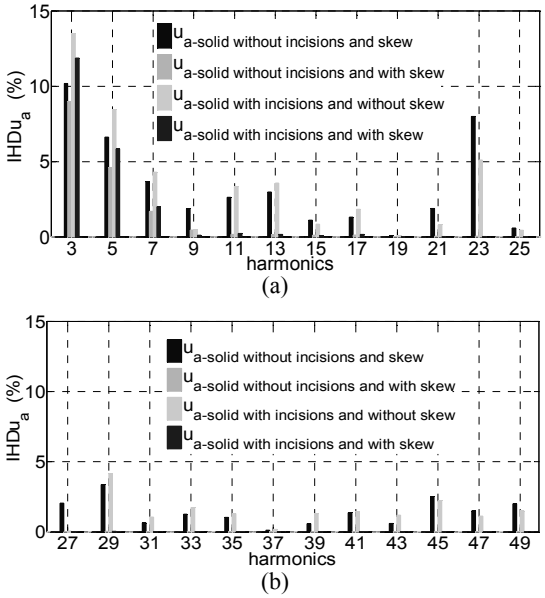

Fig. 11. Individual harmonic distortion of the induced stator voltages under no-load conditions for the examined 5.5 kVA synchronous generator: from 3rd to 25th order (a), from 27th to 49th order (b)

and utilising the normal component of magnetic flux density distributions (presented in Fig. 6 for the synchronous generator with the following rotor structures: solid with and without skew, solid with and without radial incisions). Fig. 10 presents the calculated waveforms of

the induced stator voltages only in phase *a*. Voltages u_b and u_c are very similar to u_a (Fig. 10) and are shifted by the electrical degree of $2\pi/3$. Moreover, Fig. 11 presents the individual harmonic distortion $IHDu_a$ in relation to the fundamental component of the induced stator voltages of the synchronous generator with the non-skewed solid rotor.

Comparing the induced stator voltages (Fig. 10), the magnetic flux density derivatives (Fig. 8) and the winding factors (Fig. 9) it can be concluded that the higher harmonic content is primarily influenced by the product of the electrical angular velocity ω and derivatives of magnetic flux density $\partial B/\partial\theta$. The product $\omega(\partial B/\partial\theta)$ is reduced by the winding factors (Fig. 9). The greatest reduction of the harmonic content in the induced stator voltages is achieved by skewing the rotor (Fig. 10c). The rotor skewness has a very small influence on harmonic reduction of the 3rd and 5th order harmonics (Figs. 9-11).

4. Experimental investigations

Experimental investigation of the influence of the rotor incisions on the waveforms of induced stator voltages of the 5.5 kVA salient pole synchronous generator is carried out by comparison of the induced stator voltages for the three rotor structures shown in Fig. 12. Fig. 12 shows [18]:

– a non-skewed solid rotor,

– a non-skewed solid rotor with 39 radial incisions,

– a skewed rotor with insulated electrotechnical sheets and open (not shorted) damping bars.

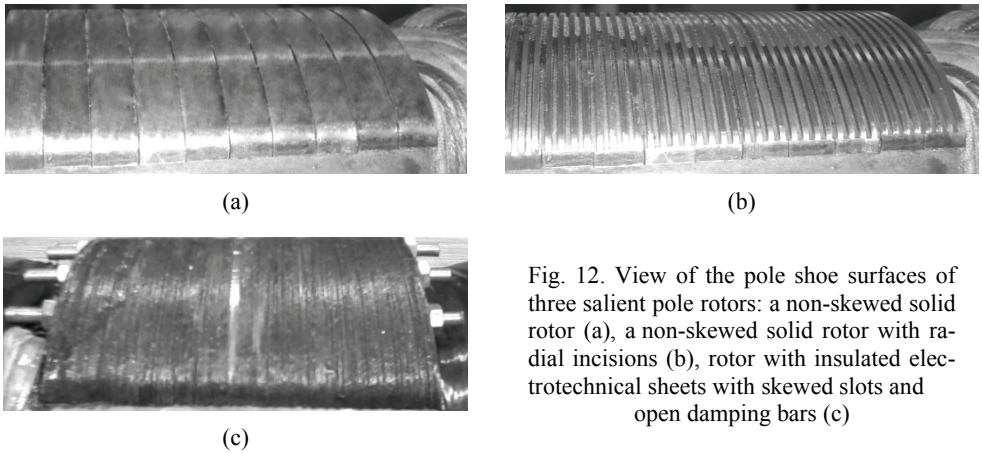

(a) (b) (c)

Fig. 12. View of the pole shoe surfaces of three salient pole rotors: a non-skewed solid rotor (a), a non-skewed solid rotor with radial incisions (b), rotor with insulated electrotechnical sheets with skewed slots and open damping bars (c)

Experimental investigations of the 5.5 kVA salient pole synchronous generator with the three rotor structures are carried out using the measurement set shown in Fig. 13.

Fig. 14 presents a simplified block diagram of the measurement set (shown in Fig. 13).

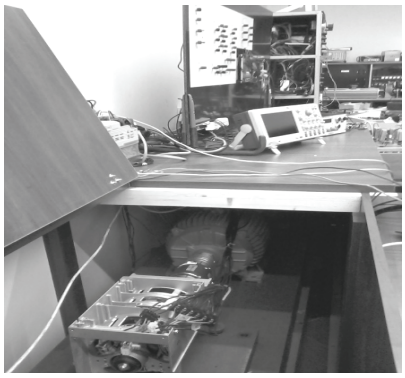

Fig. 13. General view of the measurement set used for the investigation of the 5.5 kVA salient pole synchronous generator with the three rotor structures

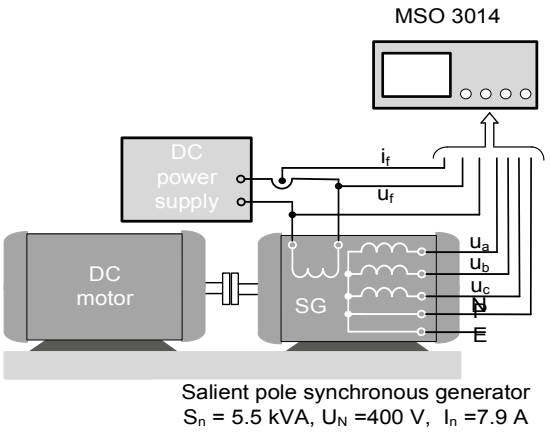

Fig. 14. Simplified block diagram of the measurement set used for the investigation of the 5.5 kVA salient pole synchronous generator

Fig. 15 presents the registered waveforms of the induced stator voltages and the field voltage as well as the current of the examined 5.5 kVA salient pole synchronous generator in no-load state. During the experimental investigations the synchronous generator was running with the following rotor structures: solid, non-skewed, solid, non-skewed with radial incisions, and skewed with insulated electrotechnical sheets. Moreover, the field winding of the examined 5.5 kVA salient pole synchronous generator for all cases was powered by a DC voltage source (U_f = const-shown in Fig. 15c) for the same RMS value of 230 V of the fundamental component phase stator voltages. As shown in [11], when powering the field winding of the 5.5 kVA salient pole synchronous generator, in induced u_a, u_b and u_c voltage waveforms (11) in no-load state, the total harmonic distortion *THDu* is the lowest. So, during the experimental investigations the field winding of the examined 5.5 kVA salient pole synchronous generator is powered using a DC voltage source.

Fig. 16 shows a comparison of the individual harmonic distortion ($IHDu_a$) in the induced stator voltages in phase *a* shown in Fig. 15. $IHDu_a$ is calculated due to the Fourier analysis of voltage u_a with respect to the fundamental component.

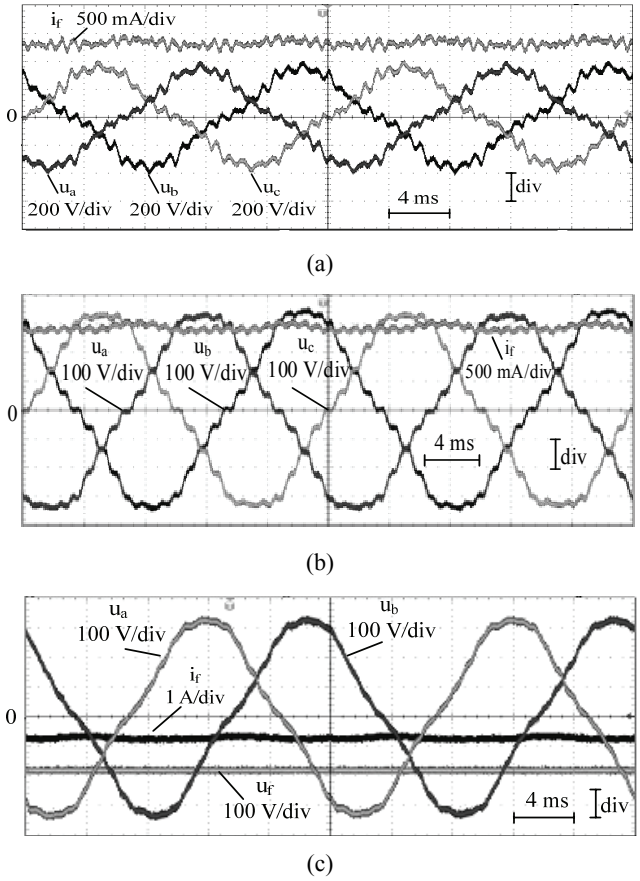

Fig. 15. Waveforms of the induced stator voltages under no-load conditions for the examined 5.5 kVA salient pole synchronous generator with the following rotors: solid, non-skewed (a), solid, non-skewed with radial incisions (b), skewed, made of electrotechnical sheets (c)

Based on the presented waveforms in the induced voltages in the stator winding in no-load state of the examined 5.5 kVA salient pole synchronous generator (Fig. 15) and on individual harmonic distortion (Fig. 16), the total harmonic distortion (THDu_a, THD$u_{a\text{-}ri}$ and THD$u_{a\text{-}e}$) counted up to the 75th harmonic is equal to:

– THDu_a = 16.39% for the generator with a solid, non-skewed rotor without radial incisions (THD$u_{a\text{-}c}$ = 17.23% calculated for generator with the same rotor construction – details Fig. 11),

– THD$u_{a\text{-}ri}$ = 9.58% for the generator with a solid, non-skewed rotor with radial incisions (THD$u_{a\text{-}ri\text{-}c}$ = 18.34% calculated for generator with the same rotor construction – details Fig. 11),

– THD$u_{a\text{-}e\text{-}s}$ = 9.30% for the generator with a skewed rotor made of electrotechnical sheets (THD$u_{a\text{-}s\text{-}c}$ = 10.35% calculated for a generator with the solid, skewed rotor without incisions – details Fig. 11).

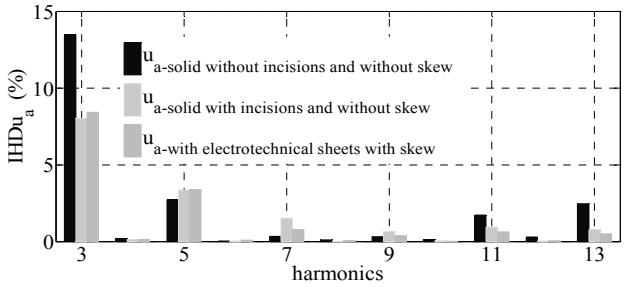

(a)

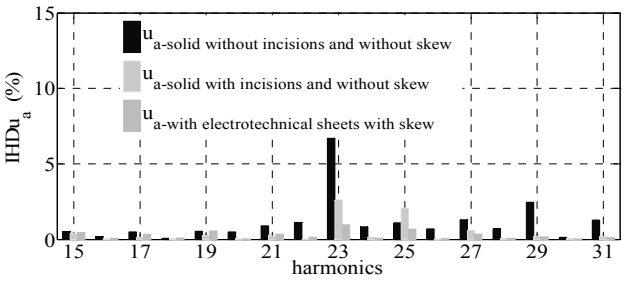

(b)

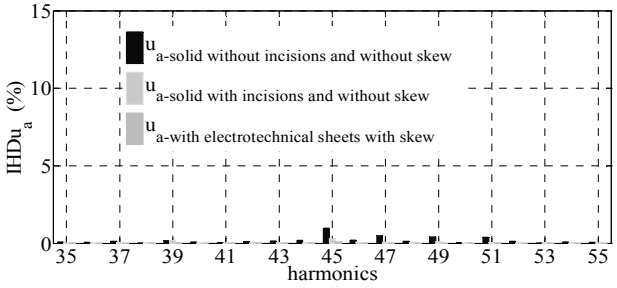

(c)

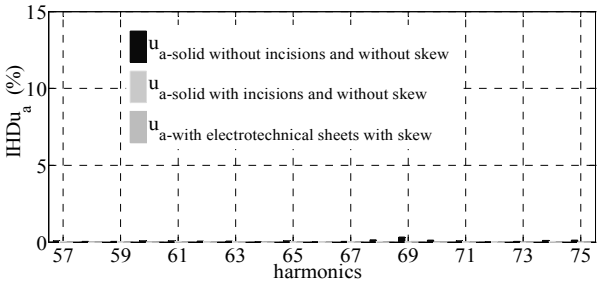

(d)

Fig. 16. Comparison of individual harmonic distortion in the induced voltages in stator winding in no-load state of the 5.5 VA salient pole synchronous generator with three rotor constructions: from 3rd to 13th order (a), from 15th to 31st order (b), from 35th to 55th order (c), from 57th to 75th order (d)

5. Conclusion

The main motivation of this paper is to show the influence of the radial incisions, saliency and the skewness of the rotor and the stator slotting on the higher harmonic contents in the magnetic flux density in the air gap (calculated during simulations in the FEMM program) and in the voltage waveforms induced in the stator winding (registered in a single-layer winding during experimental investigations) in the no-load state of the salient pole synchronous generator. The simulations and experimental investigations were carried out for the low power 5.5 kVA salient pole synchronous generator with a solid, non-skewed rotor, with a solid, non-skewed rotor and radial incisions, and with a skewed rotor made of electrotechnical sheets. Based on the presented comparison of THDu_a and THDu_a for the examined 5.5 kVA synchronous generator, it can be concluded that the introduction of 39 constant depth radial incisions on the rotor solid surface of the pole shoe equal to $2\delta_0$:

– reduces the amplitude of the magnetic flux density by 10% (Figs. 6 and 7),

– increases by 32% the 3rd harmonic in the component of the normal magnetic flux density and reduces by 43% its participation in the induced stator voltages,

– in the induced stator voltages gives a similar higher harmonic spectrum to the case of the generator with the rotor made of electrotechnical sheets.

The higher harmonics that occur in the induced voltages of a single-layer stator winding are v-times lower than in the normal component of the magnetic flux density. This is due to the fact that in the single-layer stator winding the harmonic contents are reduced by pitch, slot opening and skew winding factors.

During the experimental investigation of the three-phase salient pole synchronous generator with a solid, non-skewed rotor with radial incisions, the total harmonic distortion was found to be 9.58%. THD$u_{a\text{-}c}$ obtained from the 2D model in FEMM program (without eddy current) and expression (11) is 18.34%. It means that there are some differences between FEMM's 2D model and the investigated generator that have an influence on the harmonic content. These differences can be explained by:

– different saturation in the 2D model and in the investigated 5.5 kVA synchronous generator,

– omission of eddy currents in rotor poles in the 2D model (eddy currents have a shielding effect on magnetic flux density distribution [30]),

– different shape and nonuniformity of the real air gap along the length of the rotor and stator than in the 2D model.

References

[1] Dajaku G., Gerling D., *Stator slotting effect on the magnetic field distribution of salient pole synchronous permanent-magnet machines*, IEEE Transactions on Magnetics, vol. 46, no. 9, pp. 3676-3683 (2010).

[2] Dajaku G., Gerling D., *Air-gap flux density characteristics of salient pole synchronous permanent-magnet machines*, IEEE Transactions on Magnetics, vol. 48, no. 7, pp. 2196-2204 (2012).

[3] Gaussens B., Saint-Michel J., Lécrivain M., Gabsi M., *Analytical approach for air-gap modeling of field-excited flux-switching machine: No-load operation*, IEEE Transactions on Magnetics, vol. 10, no. 10, pp. 1-13 (2012).
[4] Xiaohua B., Na L., Yong F., Fuying L., *Novel method of evaluation of Carter factor for closed slot submersible motor including fringing effect and magnetic saturation*, Transactions of China Electrotechnical Society, vol. 30, no. 12, pp. 220-227 (2015).
[5] Sobczyk T.J., *Mathematical model of synchronous generators accounting for saturation due to the first and the third MMF harmonic*, 35th International Symposium on Electrical Machines SME'99, 14-16 June, Kazimierz Dolny, Poland, OWPW, Elektryka, no. 111, pp. 43-51 (1999).
[6] Kutt F., Michna M., Ronkowski M., Chrzan P.J., *Non-uniform saturation modelling of synchronous generator pole shoes*, Zeszyty Problemowe Maszyny Elektryczne, no. 103, pp. 121-126 (2014).
[7] Skwarczyński J., Weinreb K., *Method of analysis of slot harmonics in the salient-pole synchronous generators*, International Conference on Electrical Machines (ICEM'1990), Aug. 13-15, Boston MA, USA, pp. 1165-1170 (1990).
[8] Moreira J., Lipo T.A., *Modeling of saturated AC machines including air gap flux harmonic components*, IEEE-IAS Conference Record, 7-12 October, Seattle, Washington, USA, Part 1, pp. 37-44 (1990).
[9] Ludwinek K., *An overview of the most important methods of reducing the harmonic content introduced by discretely distributed armature winding*, Elektro. Info. (in Polish), no. 7-8, pp. 53-57 (2014).
[10] Kutt F., Michna M., Ronkowski M., Chrzan P.J., *Polyharmonic model of synchronous generator for analysis of autonomous power generation systems*, Zeszyty Problemowe Maszyny Elektryczne, no. 92, pp. 109-114 (2011).
[11] Ludwinek K., *Influence of DC voltage and current of field winding on induced stator voltages of a salient pole synchronous generator*, International Review of Electrical Engineering, vol. 9, no. 1, pp. 62-72 (2014).
[12] Ludwinek K., *FEMM utilisation in representation of inductance distributions in a salient pole synchronous generator circuital model in no-load state*, Technical Transactions – Electrical Engineering, vol. 1-E/2015, pp. 325-341 (2015).
[13] Ludwinek K., *Some aspects of inductance distributions modeling in dq0-axes and damping circuits on the rotor of a salient pole synchronous generator*, Technical Transactions – Electrical Engineering, vol. 2-E/2015, pp. 37-52 (2015).
[14] Dąbrowski M., *Design of Alternating Current Electrical Machines*, WNT (in Polish), Warszawa (1994).
[15] Pyrhönen J., Jokinen T., Hrabcová V.P., *Design of Rotating Electrical Machines*, John Wiley & Sons (2014).
[16] Carter F.W., *Note on air gap and interpolar induction*, Journal of Institution of Electrical Engineering, vol. 29, no. 146, pp. 923-933 (1926).
[17] Ludwinek K., *Influence of representation of the stator to rotor mutual inductances on the induced phase voltage waveforms in a salient pole synchronous generator*, Zeszyty Problemowe Maszyny Elektryczne, no. 104, pp. 147-154 (2014).
[18] Ludwinek K., Nadolski R., Staszak J., *Comparison of higher harmonic contents in salient pole synchronous generator with radial incisions on the solid pole surface*, Maszyny Elektryczne – Zeszyty Problemowe, no. 108, pp. 113-119 (2015).
[19] Vicol L., Banyai A., Viorel I.A., Simond J.J., *On the damper cage bars' currents calculation for salient pole large synchronous machines*, 11th International Conference on Optimization of Electrical and Electronic Equipment, May 22-24, Brasov, Romania, pp. 9-14 (2008).
[20] Nadolski R., Staszak J., *Natural hunting pulsations of large power turbogenerators*, Archives of Electrical Engineering, vol. XLV, no. 4, pp. 405-459 (1996).
[21] Bacher J., Maier G., *The shielding effect of the built-in damper cage in a synchronous machine*, International Conference on Renewable Energy and Power Quality (ICREPQ'04), 31 March-02 April, Barcelona, Spain, pp. 250-259 (2004).

[22] Sahoo S.K., Rodriguez P., Sulowicz, M., *Comparative investigation of fault indicators for synchronous machine failures*, International Conference on Electrical Machines (ICEM'2014), September 2-5, Berlin, Germany, pp. 1503-1509 (2014).
[23] Rodriguez P., Sahoo S., Pinto C.T., Sulowicz M., *Field current signature analysis for fault detection in synchronous motors, in diagnostics for electrical machines*, IEEE 10th International Symposium on Electric machines, Power Electronics and Drives (SDEMPED), 1-4 September, Guarda, Portugal, pp. 246-252 (2015).
[24] Raziee S.M., Kelk H.M., Alikhani H.R.R., Omati A., *Air-gap eccentricity effects on harmonic contents of field current in synchronous generators*, International Review of Electrical Engineering, vol. 5, no. 1, pp. 83-89 (2010).
[25] Akbari H., *An improved analytical model for salient pole synchronous machines under general eccentricity fault, Progress in Electromagnetic Research*, no. 49, pp. 389-409 (2013).
[26] http://www.femm.info/wiki/HomePage, accessed November 2015.
[27] Jedryczka C., Szelag W., Demenko A., Wojciechowski R. M., *Description of multiply connected regions with induced currents using T-T method*, Progress in Electromagnetic Research B, no. 43, pp. 279-294 (2012).
[28] Bastos J.P.A., Sadowski N., *Electromagnetic Modeling by Finite Element Methods*, Marcel Dekker, New York (2003).
[29] Gomez E., Roger-Folch J., Gabaldon A., Molina A., *Coupling 2D finite element models and circuit equations using a bottom-up methodology*, ACES Journal, vol. 17, no. 3, pp. 225-231 (2002).
[30] Chung Y., Galyda J., *Effect of Eddy Current in the Laminations on the Magnet Field,* LS Note No. 200, April (1992).

ARCHIVES OF ELECTRICAL ENGINEERING VOL. 66(1), pp. 141-154 (2017)

DOI 10.1515/aee-2017-0010

Multilevel inverter with optimal THD through the firefly algorithm

RIADH EL MEHDI BELKACEM[1, 2], REDHA BENZID[1], NOUREDDINE BOUGUECHAL[1, 2]

[1]*Department of Electronics, Faculty of Technology*
University of Batna, Algeria
[2]*Laboratoire d'Électronique Avancée (LEA), Département d'Électronique*
Faculté de Technologie Université de Batna, Algérie
e-mail: mehdi.belkacem@yahoo.fr

(Received: 28.05.2016, revised: 09.09.2016)

Abstract: Reduction of the Total Harmonic Distortion (THD) in multilevel inverters requires resolution of complex nonlinear transcendental equations; in this paper we propose a combination of one of the best existing optimized hardware structures with the recent firefly algorithm, which was used to optimize the THD, through finding the best switching angles and guaranteeing the minimization of harmonics within a user defined bandwidth. The obtained THD through the simulation of the thirteen-level symmetric inverter has been reduced down to 5% (FFT of 60 harmonics). In order to validate the simulation results, a thirteen-level symmetric inverter prototype has been made, and practically experimented and tested with different loads. Consequently, the measured THD with resistive load was 4.7% on a bandwidth of 3 kHz. The main advantage of the achieved work is the reduction of the THD.

Key words: firefly algorithm (FFA), genetic algorithm (GA), inverter, multilevel, optimized THD

1. Introduction

Through the last few years, there have been extensive researches about substitutes of conventional energies through renewable energies. This new type of energy can be produced by wind turbines and Solar Photovoltaic Energy. Such a solution needs systems to stock and convert the energy. Considered as one of the crucial parts that allow delivering clean Alternating Current (AC), inverters have been one of the important research axes, the main ambition was to increase the quality of the output waveform, in addition to promote and improve friendly environment systems [1, 2].

It is well established that a multilevel inverter (MLI) can produce a high quality signal and low Total Harmonics Distortion (THD) [3, 4, 8, 12]. In fact, during these many years, several applications using multilevel inverters have been proposed and realized.

The most important structures of multilevel inverters can be classified into three types, a diode-clamped, flying capacitors and a cascaded H-bridge [3, 4].

The first diode-clamped inverter and also called neutral-point-clamped was introduced the first time by Nabae in 1981 and was essentially a three-level-clamped inverter, where during the off period of the PWM each output terminal will be clamped to the neutral potential [4, 5], this is shown in Figure 1a.

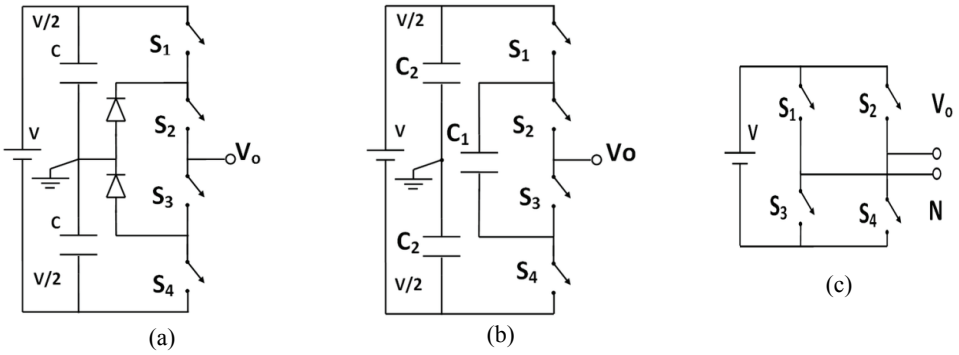

Fig. 1. Three-level-diode-clamped inverter: (a) three-level flying capacitor inverter; (b), three-level H-bridge inverter (c)

The first flying capacitor inverter has been introduced by Meynard in 1992, a 3 level topology single phase of this inverter is illustrated in Figure 1b, it is similar to the first type but the clamping diodes are replaced by a capacitor [4, 6].

The third type is the cascaded H-bridge multilevel inverter, which offers a design with less power devices. This design offers a higher number of levels, but requires an isolated and separated DC source for each H-bridge [3].

This structure has been introduced the first time by Hammond in 1997, Figure 1c [3, 7]. The cascaded multilevel inverter has been previously designed for Static VAR compensator and motor drives, but the topology has been also used to interface with renewable energy sources, because it uses separated dc sources. [3, 4, 7], accordingly, the produced AC voltage is generated by connecting multiple Cells in series. Each cell will generate three levels $+V_{dc}$, 0 and $-V_{dc}$. Consequently, connecting n cells will generate $2n + 1$ levels.

In addition to the three types described above, other Hybrid topologies have been developed, a diode-clamped or flying capacitor with a cascaded H-bridge. [4].

Resolving the inverters problem does not depend only on the hardware, it depends also on the sequence and the timing of controlling each switch in the structure, this can become complicated when the number of switches increases, the goal is to get a smooth clean signal at the output of the inverter, choosing the best switching time for each switch will significantly reduce the THD.

Usually solving the switching time problem, or finding the best switching angles requires resolving complicated nonlinear transcendental equations, the number of variables will in-

crease when the number of switches increases, therefore new methods have been introduced such as Particle Swarm Optimization (PSO), Genetic Algorithms (GA) and biogeographical based optimization (BBO) [9, 10, 11]. In our proposed solution, the reduction of the THD is accomplished by using the recent firefly algorithm (FFA).

The rest of the paper is organized as follows: in Section 2, the necessary theory background, signal synthesis, optimization problem definition, in Section 3, introduction of the firefly algorithm and proposition of solving the optimization problematic presented in Section 2, Section 4, contains the used hardware, application of the simulation results to build the 13-level inverters, Section 6, presentation of the experimental results and finally, the last section is a conclusion, reporting the benefits and features of the proposed method.

2. Background and problem statement

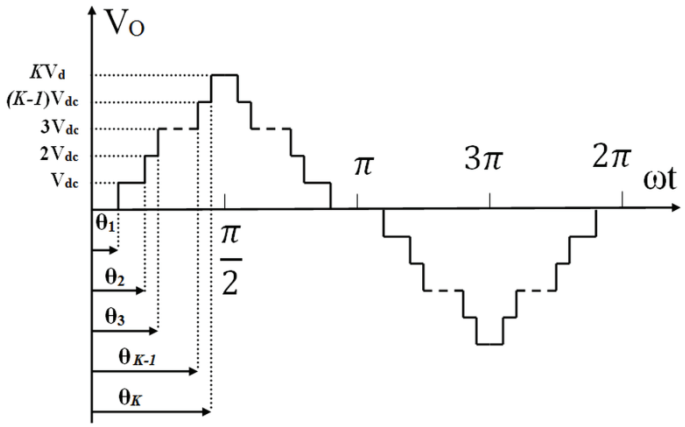

Fig. 2. Typical *K* Multilevel inverter output waveform

A typical *K* multilevel inverter voltage waveform will look like the waveform in Figure 2, where θ_1, θ_2,…, θ_K are the switching angles, $\theta_1 < \theta_2 <$,…, $< \theta_K < \pi/2$ [10].

Since this function is periodic, as per the Fourier theory the function can be expressed by a sum of sines and cosines.

The output voltage function can be expressed by:

$$f(t) = a_0 + \sum_{n=1}^{\infty} A_n \cos(n\omega t) + B_n \sin(n\omega t), \tag{1}$$

where $\omega = 2\pi/T$ and T is the period of the function.

The reference signal is half wave symmetry and odd at the same time, therefore we can write it as:

$$f(t) = \sum_{n=1}^{\infty} B_n \sin(n\omega t), \tag{2}$$

$$B_n = \frac{8}{T}\int_0^{T/4} f(t)\sin(n\omega t)\mathrm{d}t\,. \tag{3}$$

For odd *n*s, zero for the others.

$$B_n = \frac{4Vdc}{n\pi}\sum_{i=1}^{K}\cos(n\theta_i)\,. \tag{4}$$

For odd *n*s, and zero for even *n*s [9, 10], *K* is the number of switching angles.

$$f(\omega t) = \sum_{n=1,3,5}^{\infty}\frac{4Vdc}{n\pi}\left[\cos(n\theta_1)+\cos(n\theta_2)+.....+\cos(n\theta_K)\right]\sin(n\omega t)\,. \tag{5}$$

Our objective is to have a pure sine wave at the output. Therefore, it is possible to find the angles $\theta_1 < \theta_2 <, \ldots, < \theta_K < \pi/2$ in order to illuminate the lower order harmonics and have the THD at minimum (ideally zero). The desired output signal is in Equation (6).

$$f(\omega t) = V_1 \sin\omega t\,, \tag{6}$$

where V_1 is the fundamental.

Actually, this will be achieved by targeting a maximum value of V_1, and minimizing the amplitude of the other harmonics. In order to solve our problem we have gathered all the parameters in the system of Equations (7) [9, 10].

One solution set is found by zeroing the *K*-1 equations, in (7).

As an example, for $K = 6$ the target solution will eliminate all the harmonics up to the 11th one.

The methods used to find solution include but are not limited to iterative approaches and optimization methods [9].

$$\left.\begin{aligned}
B_1 &= \frac{4V_{dc}}{\pi}\sum_{i=1}^{k}\cos\theta_i = V_1,\\
B_3 &= \frac{4V_{dc}}{3\pi}\sum_{i=1}^{k}\cos 3\theta_i = V_3,\\
B_5 &= \frac{4V_{dc}}{5\pi}\sum_{i=1}^{k}\cos 5\theta_i = V_5,\\
&\ldots\\
&\ldots\\
B_n &= \frac{4V_{dc}}{n\pi}\sum_{i=1}^{k}\cos n\theta_i = V_n.
\end{aligned}\right\} \tag{7}$$

For $n = 1, 3, 5\ldots\ldots\infty$ (for odd *n*s) zero for the others. Where in this equations: θ_1, θ_2, ..., θ_K are the switching angles.

In order to process the optimization and find the best angles, we need to define an objective function, this one will need to maintain the fundamental harmonic at maximum, and

minimize the effects of the other harmonics up to a predefined range, under the constraint $\theta_1 < \theta_2 <,\ldots,< \theta_K < \pi/2$.

One possible objective function is described in (8):

$$F(\theta_1,\theta_2,...,\theta_K) = (\sum_{i=1}^{k}\cos\theta_i - m)^2 + (\sum_{i=1}^{k}\cos 3\theta_i)^2 + (\sum_{i=1}^{k}\cos 5\theta_i)^2 .... + (\sum_{i=1}^{k}\cos n\theta_i)^2, \quad (8)$$

where:

$$m = V_1/(4V_{dc}/\pi) \quad (9)$$

and n is the highest rank of harmonics we want to reduce and is an odd number.

The best solution for $(\theta_1, \theta_2,\ldots, \theta_K)$ will be found by reducing $F(\theta_1, \theta_2,\ldots, \theta_K)$ under the constraint $\theta_1 < \theta_2 <,\ldots,< \theta_K < \pi/2$ [9, 10].

Another frequently used equivalent cost function is the Total Harmonic Distortion (THD). By reducing the THD we ensure that our signal strongest contributor is coming from the first harmonic.

$$F(\theta_1,\theta_2,...,\theta_K) = THD(\theta_1,\theta_2,...,\theta_K) = \sqrt{\frac{V_3^2 + V_5^2 + V_7^2 + ...V_n^2}{V_1^2}} \times 100, \quad (10)$$

where n is the order of the highest harmonic and needs to be predefined.

Now we have to choose an algorithm for optimization, this later needs to be able to reduce the function THD $(\theta_1, \theta_2,\ldots, \theta_K)$, below a preferred value, once this value is reached, the optimization conditions are satisfied.

We have chosen to use the recent firefly algorithm to find the best solution and reduce the THD $(\theta_1, \theta_2,\ldots, \theta_K)$.

3. Firefly algorithm

Today's world development and growth are calling for more and more resources, with the fact that most of the resources are limited, this reality has called for a new ways to manage the available resources, and optimization is one of these preferred methods. The evolution of computers has influenced the optimization of a wide spectrum of interests, as many new optimization methods are being developed, such as artificial intelligence and nature – inspired metaheuristic algorithms [13].

In the late of 2007 and early 2008, Xin-She Yang has developed a new firefly algorithm (FA), which is one of the metaheuristic algorithms, and is based on social behavior, interaction and communication between fireflies. Fireflies generate bioluminescence flashes to communicate with mates or to attract prey.

Three rules below are defining the firefly algorithm [13]:

a) Fireflies are unisex so that one firefly will be attracted to other fireflies regardless of their sex.

b) The attractiveness is proportional to the brightness, and they both decrease as the distance between fireflies increases. Thus for any two flashing fireflies, the less bright one will move towards the brighter one. If there is no brighter one than a particular firefly, they will move randomly.

c) The brightness of a firefly is determined by the landscape of the objective function.

Fireflies' attractiveness is proportional to the light intensity seen by adjacent fireflies, we can now define the variation of fireflies attractiveness β with the distance *r* by:

$$\beta = \beta_0 e^{-\gamma r^2}, \tag{11}$$

where β_0 is the attractiveness at $r = 0$.

Considering fireflies $\boldsymbol{X}_i$ and $\boldsymbol{X}_j$, r_{ij} is the distance between firefly $\boldsymbol{X}_i$ and $\boldsymbol{X}_j$.

$$r_{ij} = \left\| \boldsymbol{X}_i - \boldsymbol{X}_j \right\|. \tag{12}$$

The attractiveness will be expressed as per Equation (13):

$$\beta = \beta_0 e^{-\gamma r_{ij}^2}. \tag{13}$$

The firefly *i* is attracted to another more attractive (brighter) firefly *j* according to movement equation:

$$\boldsymbol{X}_i^{t+1} = \boldsymbol{X}_i^t + \beta_0 e^{-\gamma r_{ij}^2} (\boldsymbol{X}_j^t - \boldsymbol{X}_i^t) + \alpha_t \varepsilon_i^t. \tag{14}$$

The second term is due to the attraction. The third term is randomization with α_t the randomization parameter, and ε_i^t is a vector of random numbers drawn from a Gaussian distribution or uniform distribution at time *t* [13].

The FFA has been developed and executed through Matlab, the pseudo code of the FFA is given in Figure 5.

The work done in [15] has used more complex hardware structure, cascaded H-bridges, and has used the FFA not to optimize directly the THD, but to resolve the nonlinear transcendental equations. A similar approach has been also used in [16, 17], in our case we have used the THD $(\theta_1, \theta_2, \ldots, \theta_K)$ as the light intensity *I*, the best solution will check $F(\boldsymbol{X}_{\text{best}}) = \text{THD}(\theta_1^*, \theta_2^*, \ldots, \theta_K^*)$ which is the lowest THD.

The optimization of the THD will guarantee the minimization of the harmonics within the selected bandwidth (in our case, 3 kHz bandwidth where the fundamental is 50 Hz, 60 harmonics were involved in the THD minimization), while in [15], the author is targeting the minimization of the 5th, 7th, 11th and 13th harmonics. This will not be efficient for the higher harmonics (from the 15th harmonic and above).

The FA pseudo code presented in Figure 3 has been translated to a Matlab program. In all performed simulations we have used the parameters below:

IT = 40 maximum generation,

P = 50 population size,

$K = 6$	number of variables,
$\beta_0 = 100$	attractiveness at $r = 0$,
$\gamma = 1$	light absorption coefficient,
$\alpha = 100$	randomization parameter.

```
Firefly Algorithm
Objective(Cost) function
f(x), x = (x1, ..., xd)^T
Generate initial population of fireflies xi (i = 1, 2, ..., n)
Light intensity Ii at xi is evaluated as f(xi)
Define light absorption coefficient γ
while (t <MaxGeneration)
for i = 1 : n all n fireflies
for j = 1 : i all n fireflies
if (Ii > Ij) /*in the case of maximization Ii < Ij  */
 Move firefly i towards j in d-dimension;
end if
Attractiveness varies according to the distance r via exp[-γr]
Evaluate new solutions and update light intensity
end for j
end for i
Rank the fireflies and find the current best
end while

  Postprocess results and visualization
```

Fig. 3. Pseudo code of the firefly algorithm (FA) [14]

The best THD has been found to be 5% for $N = 60$, N is the order of the highest harmonic of the spectrum, corresponds to 3 kHz.

The fitness function we have used is the THD ($\theta_1, \theta_2, \ldots, \theta_K$) of the produced signal based on the first N harmonics of the FFT. The order of the highest harmonic N has been chosen as 60 to cover for all the low frequencies, practically we are working up to 3 kHz.

We have built in a program to reduce the THD for a K level inverter. The program entries are the number of switching angles.

It is obvious that more switching angles will generate a better signal and therefore less THD. Below the simulation results for 3 and 6 angles corresponding to 7 and 13-level symmetric inverter.

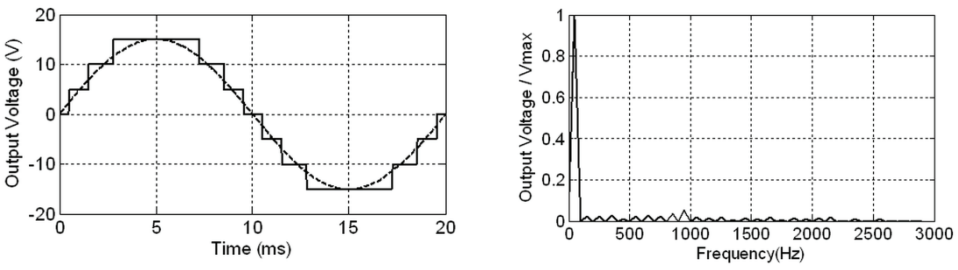

(a) (b)

Fig. 4. Seven-level inverter output: time domain $\theta_1 = 9.1^\circ$, $\theta_2 = 27.5^\circ$, $\theta_3 = 50.4^\circ$ (a); FFT, THD = 11% (b)

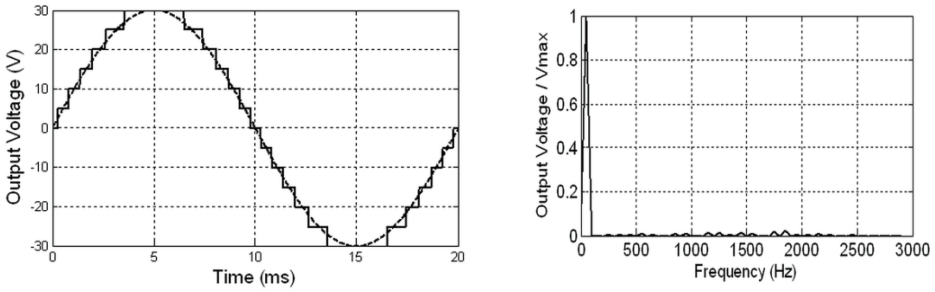

(a) (b)

Fig. 5. Thirteen-level inverter output: time domain $\theta_1 = 5.0^\circ$, $\theta_2 = 14.3^\circ$, $\theta_3 = 24.5^\circ$, $\theta_4 = 35.3^\circ$, $\theta_5 = 46.2^\circ$, $\theta_6 = 63.7^\circ$ (a); FFT, THD = 5% (b)

Figure 4 shows the simulation results and the output of the 7-level inverter, Figure 4a shows the waveform in the time domain, with the perfect waveform, a pure sine wave, Figure 4b shows the FFT of the output signal.

Compared to the work done in [11], where the obtained THD through the simulation was 12.39%, the optimized angles were found through the BBO algorithm, the waveform is similar to the one generated by a symmetrical multilevel inverter, with a step of 100. While in our proposed method we have reached 11% THD, the result obtained in running 10 iterations of the built program which was based on the recent FFA.

In order to reach the 5% THD we had to go up to a 13-level inverter, simulation results are shown in Figure 5.

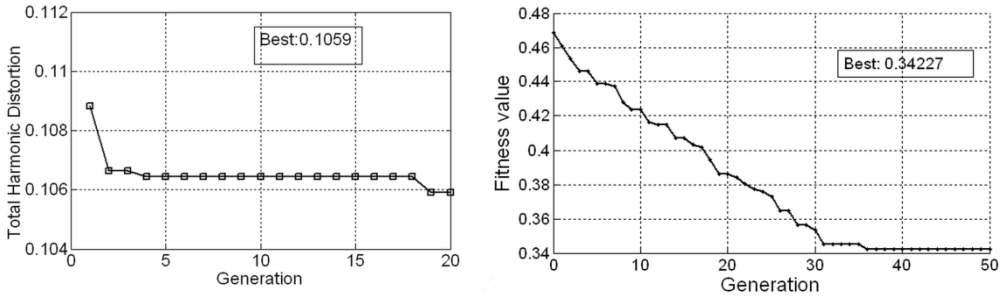

(a) (b)

Fig. 6. Firefly algorithm THD vs. generation: (a) genetic algorithm THD vs. generation (b)

We have also compared the proposed FFA to the GA tool on Matlab, see Figure 6, the proposed FFA with the proposed parameters converges faster, it is 90% close to the optimum solution after the fourth iteration and usually the optimum solution is obtained before the 10^{th} iteration. When using the GA with the same parameters, $IT = 20$, population size = 50, the best obtained fitness value with the GA is 3.9 times the value obtained by the FFA. To obtain similar result with the GA we need 150 generations.

4. Hardware implementation

For the experiment we have chosen an already optimized structure, presented by Ebrahimi et al., in [18].

Figure 7a shows the sub-multilevel inverter topology proposed in [18], the typical output voltage of the sub-multilevel inverter is given in Figure 7b.

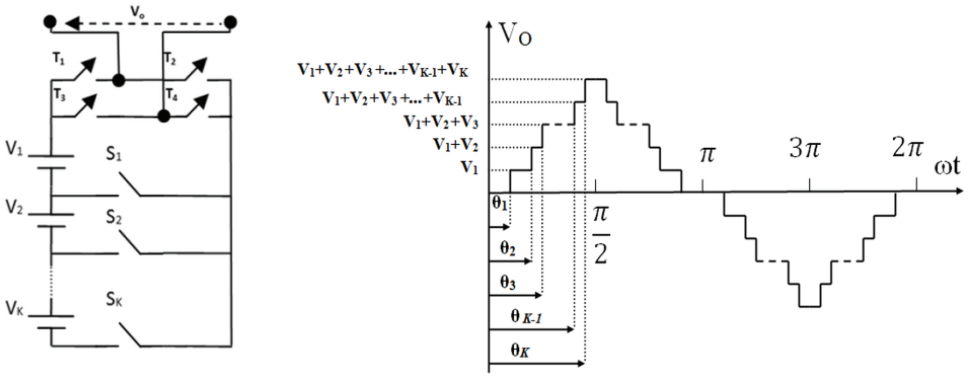

(a) (b)

Fig. 7. Sub-multilevel topology [18] (a); typical output voltage of MLI in [18] (b)

The block diagram of the hardware implementation is shown in Figure 8. The thirteen-level inverter was built around a microchip microcontroller type PIC16F628A.

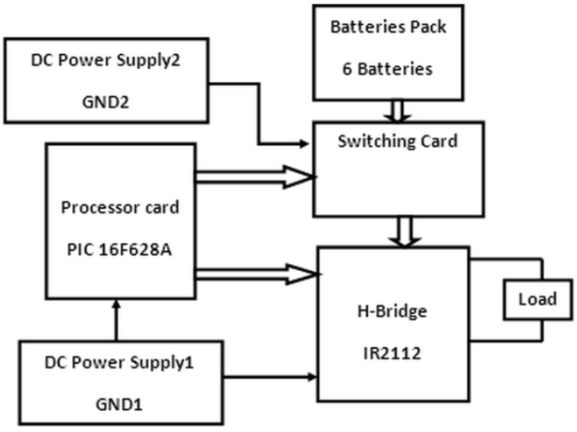

Fig. 8. Block diagram of the multilevel inverter

The multilevel inverter consists of 4 major parts:

1) Processor card: this is the brain of the inverter; it generates all the switching angles to activate the switches, to generate the exact angles, to minimize the THD. The best

values found through the simulation have been programmed on the PIC 16F628A, targeting the 5% THD.

2) Switching card: this card contains the switching devices and isolates the control from the power (photo couplers), it takes controls from the processor card and switches power from the batteries pack to the H-bridge.
3) Batteries pack: directly connected to the switching card and both make the level generator.
4) H-bridge card: the input of the H-bridge is a half wave, the H-bridge will make the full wave at its output, and feeds the load. The H-bridge is also controlled by the microprocessor.

Three prototype cards have been made: a processor card, level generator card and the H-bridge card.

5. Experimental tests and discussion

Tests have been conducted with different loads to check the performance of the MLI. The first set of experiments has been done with a resistive load. Figure 9 shows experimental hardware, the 13-level inverter running with a resistive load, and an ITT OX 710c oscilloscope. Please note that we have also used a USB oscilloscope, type PicoScope 3204, this one was used to view the signal, the spectrum and to measure the frequency and the THD.

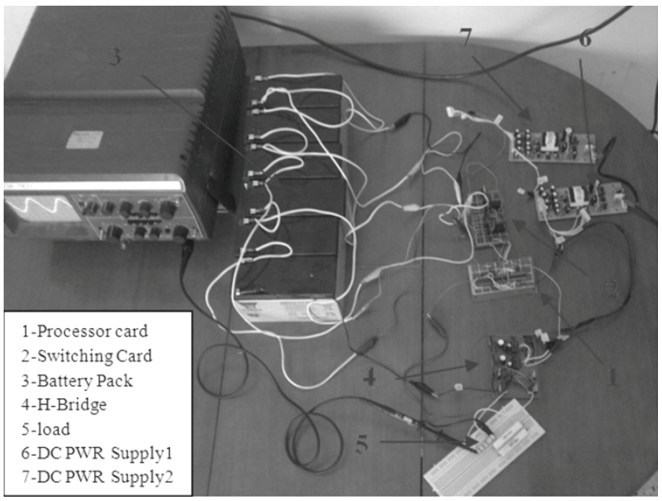

Fig. 9. The 13-level inverter running with resistive load

The experimental results have confirmed the theory, with an R load the THD was 4.6% on a spectrum of 3 kHz. Figure 10 shows the current with a resistive load, on a digital scope, the signal frequency is 50 Hz, while Figure 11 shows the spectrum of the output signal on a 3 kHz bandwidth. The measured value of the THD was 4.6%. This is a satisfactory result as we were targeting 5% THD.

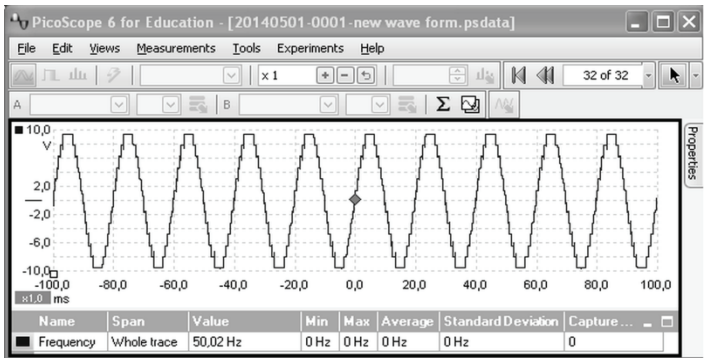

Fig. 10. current waveform of the 13-level inverter with a resistive load

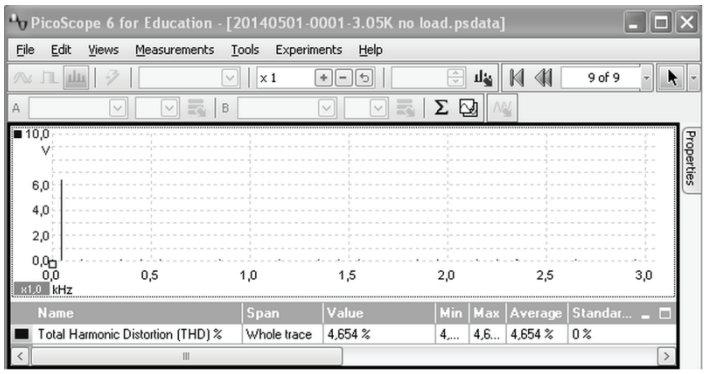

Fig. 11. Current FFT on 3 kHz bandwidth of the 13-level inverter with a resistive load THD = 4.65%

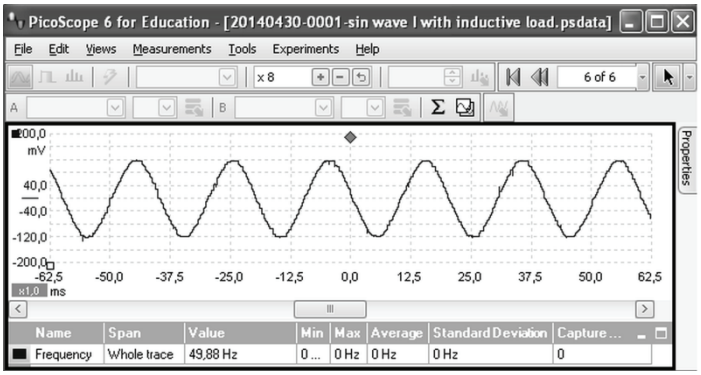

Fig. 12. Current waveform of the 13-level inverter with an inductive load L = 100 mH

The second set of experiments was done with a 100 mH induction load. Figure 12 shows the current waveform through the inductive load. More harmonics have been filtered and we see that the resulting THD is 3.2%, this is shown in Figure 13.

Figure 14a shows the shape of the output voltage of the 13-level inverter on an analogue scope ITT OX 710 C. Figure 14b shows the current through a motor load, current pick is 2.5 A.

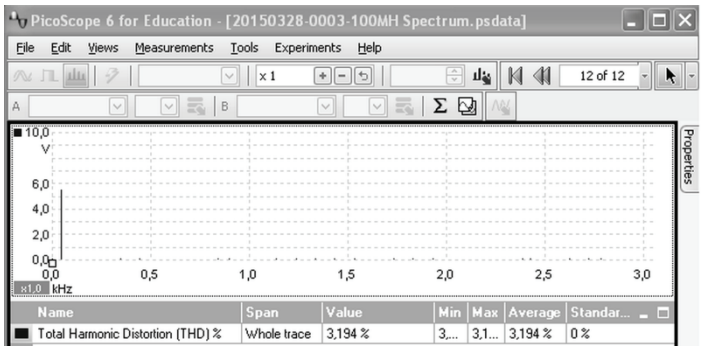

Fig. 13. Current FFT on 3 kHz bandwidth THD = 3.2%. The 13-level inverter with an inductive load, L = 100 mH

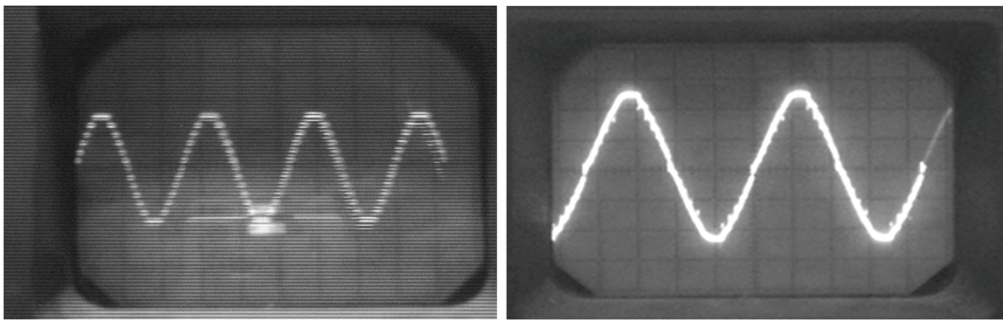

(a) (b)

Fig. 14. 13-level inverter: output voltage on an analogue scope ITT OX 710 C (a), current through motor load on an analogue scope ITT OX 710 C (b)

8. Conclusion

In this paper, the recent firefly algorithm has been used to find the best switching angles in order to minimize the THD on a user defined bandwidth. The method focuses on optimizing directly the THD and not to resolve the equations or minimizes a selected number of harmonics. The THD over the predefined range was minimized. The best THD found through the simulation is 5% on a bandwidth of 3 kHz.

One of the best optimized hardware structures of MLI has been used [18] to verify and validate the simulation results.

The signal generated by 13-level symmetric inverter has a low THD, and the measured THD is 4.8% on a bandwidth of 3 kHz, which is a satisfactory result. Simulation results as well as experimental results have been shared to prove the performance of software solution and the used hardware structure.

Under the same conditions (3 kHz bandwidth and 50 Hz fundamental), we have compared the proposed FFA to the BBO algorithm developed in [11] and the GA implemented in Matlab. Obtained THD by the BBO algorithm [11] was 12.39% while the obtained THD by using the suggested FFA was 11%.

In this specific problem, the FFA, compared to the GA, converged faster.

As for future development, we need to mention that the work performed in [19, 20] is an excellent work, and can be considered as one of the opportunities of expansion and improvement of the actual work, instead of choosing the staircase basic waveform as a target output voltage, we can choose to combine it with the PWM, this will reduce the number of levels, therefore the required hardware, the FFA will allow us to find the optimized switching angles to reduce the THD even further.

References

[1] Ilango G.S., Rao P.S., Karthikeyan A., Nagamani C., *Single-stage sine-wave inverter for an autonomous operation of solar photovoltaic energy conversion system*, Renew. Energ., vol. 35, no. 1, pp. 275-282 (2010).

[2] Carrasco J.M., Franquelo L.G., Bialasiewicz J.T., Galvan E., Guisado R.C.P., Prats M.Á.M., León J.I., Moreno-Alfonso N., *Power-electronic systems for the grid integration of renewable energy sources: a survey,* IEEE Trans. Ind. Electron., vol. 53, no. 4, pp. 1002-1016 (2006).

[3] Rodríguez J., Lai J., Peng F., *Multilevel inverters: a survey of topologies, controls, and application,* IEEE Trans. Ind. Electron., vol. 49, no. 4, pp. 724-738 (2002).

[4] Colak I., Kabalci E., Bayindir R., *Review of multilevel voltage source inverter topologies and control schemes,* Energ. Convers. Manage., vol. 52, no. 2, pp. 1114-1128 (2011).

[5] Nabae A.,Takahashi I., Akagi H., *A new neutral-point-clamped PWM inverter*, IEEE Trans. Ind. Appl., vol. IA-17, no. 5, pp. 518-523 (1981).

[6] Meynard T.A., Foch H., *Multi-level conversion: high voltage choppers and voltage-source inverters*, IEEE Power Electronics Specialists Conf., Toledo, Spain, pp. 397-403 (1992).

[7] Hammond P., *A new approach to enhance power quality for medium voltage AC drives,* IEEE TRANS. IND. APPL., vol. 33, no. 1, pp. 202-208 (1997).

[8] Dixon J., Moran L., *High-level multistep inverter optimization using a minimum number of power transistors*, IEEE Trans. Power Electron., vol. 21, no. 2, pp. 330-337 (2006).

[9] Dahidah M.S.A., Agelidis V.G., *A hybrid genetic algorithm for selective harmonic elimination control of a multilevel inverter with non-equal DC sources,* IEEE International Conf. on Power Electronics and Drives Systems, Kuala Lumpur, Malaysia, pp. 1205-1210 (2005).

[10] Al-Othman A.K., Abdelhamid T.H., *Elimination of harmonics in multilevel inverters with non-equal dc sources using PSO,* Energ. Convers. Manage., vol. 50, no. 3, pp. 756-764 (2009).

[11] Kavitha R., Thottungal R., *WTHD minimisation in hybrid multilevel inverter using biogeographical based optimization*, Arch. Elect. Eng., vol. 63, no. 2, pp. 187-196 (2014).

[12] Malinowski M., Gopakumar K., Rodriguez J., Perez M., *A survey on cascaded multilevel inverters*, IEEE Trans. Ind. Electron., vol. 57, no. 7, pp. 2197-2206 (2010).

[13] Yang X.S., *Studies in Computational Intelligence Cuckoo Search and Firefly Algorithm: Theory and Applications*, Springer International Publishing Switzerland, Chapter 5 (2014).

[14] Yang X.S., *Engineering Optimization, An Introduction with Metaheuristic Applications*, John Wiley & Sons, Inc. Hoboken, New Jersey, Chapter 17 (2010).

[15] Nawaz F., Yaqoob M., Ming Z., Ali M.T., *Low order harmonics minimization in multilevel inverters using firefly algorithm,* Power and Energy Engineering Conf., IEEE PES Asia-Pacific, pp. 1-6 (2013).

[16] Ould Cherchali N., Tlemçani A., Morsli A., Boucherit M.S., Barazane L., *Application of firefly algorithm on the SHEPWM strategy for the multilevel inverters,* International Conf. on Electrical Sciences and Technologies in Maghreb (CISTEM), pp. 1-6 (2014).

[17] Karthik N., Arul R., *Harmonic elimination in cascade multilevel inverters using Firefly algorithm,* Circuit, International Conference on Power and Computing Technologies (ICCPCT), pp. 838-843 (2014).

[18] Ebrahimi J., Babaei E., Gharehpetian G.B., *A new multilevel converter topology with reduced number of power electronic components,* IEEE Trans. Ind. Electron., vol. 59, no. 2, pp. 655-667 (2012).
[19] Sharifzadeh M., Vahedi H., Sheikholeslami A., Labbé P.A., Al-Haddad K., *Hybrid SHM-SHE modulation technique for four-leg NPC inverter with DC capacitors self-voltage-balancing,* IEEE Trans. Ind., vol. 62, no. 8, pp. 4890-4899 (2015).
[20] Sharifzadeh M., Vahedi H., Portillo R., Khenar M., Sheikholeslami A., Franquelo L.G., Al-Haddad K., *Hybrid SHM-SHE pulse amplitude modulation for high power four-leg inverter,* IEEE Trans. Ind. Electron., accepted (2016).

ARCHIVES OF ELECTRICAL ENGINEERING VOL. 66(1), pp. 155-163 (2017)

DOI 10.1515/aee-2017-0011

Fractional derivatives in electrical circuit theory – critical remarks*

RYSZARD SIKORA

Department of Electrical Engineering
West Pomeranian University of Technology
Sikorskiego 37, 70-313 Szczecin, Poland
e-mail:rs@zut.edu.pl

(Received: 07.09.2016, revised: 01.11.2016)

Abstract: A number of critical remarks related to the application of fractional derivatives in electrical circuit theory have been presented in this paper. Few cases have been pointed out that refer to observed in selected publications violations of dimensional uniformity of physical equation rules as well as to a potential impact on the Maxwell equations.

Key words: dimensional uniformity, physical equations, capacity, super capacitor

1. Introduction

One may meaningfully benefit in many fields (also in electrical engineering) from the introduction of new mathematical methods or from the reapplication of already existing ones. A mathematical notation models real phenomena. We often face a problem, how to describe particular phenomenon in a comprehensive and at the same time simple way. On one side new phenomena are surfacing and on the other the already known are being understood better. Newton's physics differs from the Einstein's one. Quantum theory resulted with new formulae. Nevertheless, new equations that model the phenomena shall be always dimensionally uniform. Ampere's and Faraday's laws haven't changed as a result of new scientific findings. The dependence between the voltage at the coil and coupled alternate magnetic flux remains the same for decades. The same applies to Maxwellian distribution laws, although we shall fine-tune them with the Lorentz's transformation for high velocities. The implementation of fractional derivatives shouldn't change this principle. It shouldn't impact basic physical laws, including the Maxwellian distribution laws. The implementation of fractional derivatives shall not contradict the laws of physics [1]. This applies to each mathematical description of any

* At the request of part of the reviewers this article has been considered as a discussion article. Therefore, the Editorial Board of AEE turned to the experts indicated by the people interested in the subject matter, to present their views in papers or messages, which will be published in the subsequent issues of AEE.

phenomenon. A mathematical model of a process must be dimensionally uniform and comply with the valid laws. Each model shall be confirmed with the relevant experiment(s). Unfortunately, the authors who deal with fractional derivatives sometimes don't follow this rule. It's quite common that dimensional uniformity of equations is not followed or misinterpreted by laws of physics that are in use. The papers [2] and [4] as well as many other may serve as an example here. At the same time, many authors notice the dimensional non-uniformity, as to mention [12], page 145, p. 3, where we find: "an auxiliary parameter is introduced in order to preserve the physical dimensionality of the fractional temporal operator". We may find similar references in other works as well.

Till now, the introduction of fractional derivatives has not affected the content of any well-known textbooks in electrical circuit theory or magnetic field theory. Mentioned textbooks don't refer to fractional derivatives at all. Only derivatives of natural order are used in these books. Similar applies to electromagnetic field wave propagation theory, wave-guide theory, nondestructive testing, electrical machine theory and many other fields of applied science.

2. Curie's law

Curie's law presented with the formula below (quoted "as is" from the paper [9]) was applied in the works [9] and [10] to model current in the capacitor:

$$i(t)=\frac{U_0}{h_1 t^n} \quad 0<n<1, \quad t>0\,. \tag{1}$$

The mentioned formula refers both to real (with losses, where $n \neq 1$) and ideal capacitors ($n = 1$). In the case of an ideal capacitor the formula (1) will translate into (2):

$$i(t)=\frac{U_0}{h_1 t}\,. \tag{2}$$

It doesn't matter which power exponent n we take, the formula (1) will not be precisely true. The problem with this formula has been flagged by the authors of the paper [9], who wrote namely: "For instance von Schweidler [2, 3] was of the opinion that the Curie current is abnormal and named it accordingly.

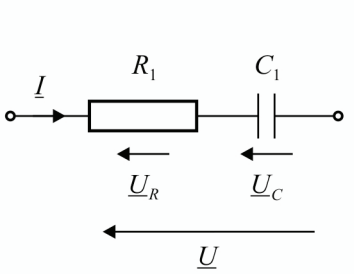

Fig. 1. Serial capacitor scheme

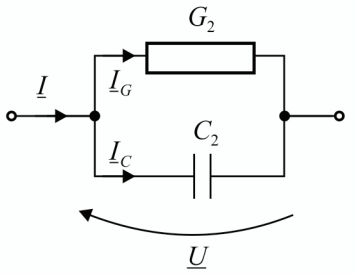

Fig. 2. Parallel capacitor scheme

Many modern workers assent to the ideas of Schweidler, for instance [4]. But there are also a few who disagree, maybe foremost Jonscher, who in 1977 named the Curie response "the universal dielectric response [5]". Without discussing further the paper [9] we can state that the experimental Curie formula is not the universal one. It is widely used that a real capacitor may be modelled with the dual schemes, serial or parallel [13]. These very simple schemes have been presented in Figs. 1 and 2.

In order to obtain a general model of the capacitor we shall apply one of the canonical schemes (Figs. 3 and 4)

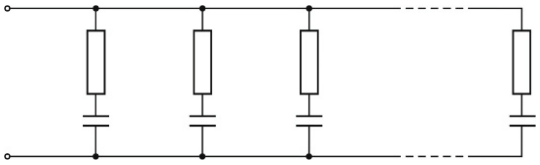

Fig. 3. First canonical scheme

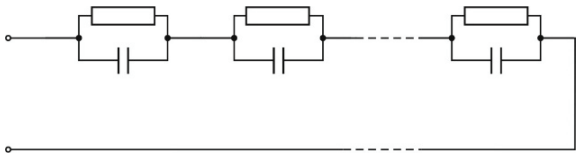

Fig. 4. Second canonical scheme

or Cauer's schemes (Figs. 5 and 6) [13].

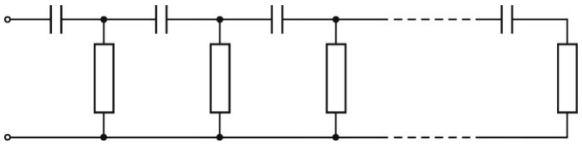

Fig. 5. First Cauer's scheme

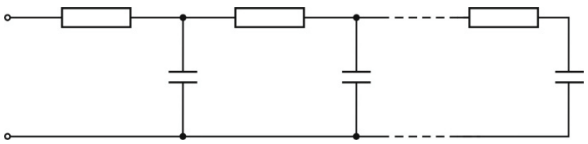

Fig. 6. Second Cauer's scheme

The schemes used may be partial ones. It seems that the scheme presented in Fig. 7 might be feasible.

Resistances R_1 and R_2 take finite values in the case of real capacitor $R_1 = \infty$ and $R_2 = 0$ and for an ideal capacitor. A more general model is represented by one of the long-distance line schemes shown above.

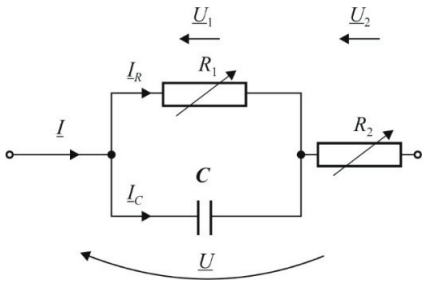

Fig. 7. Serial-parallel scheme

In such a case we don't need to use fractional derivatives that contradict well-established electrical circuit theory, consider how to obtain dimensionally uniform physical equations or reflect whether the dependence between the capacitor's current and voltage shall be described by the well-known formula:

$$i_c(t) = C\frac{\mathrm{d}u_C(t)}{\mathrm{d}t}, \tag{3}$$

or by dimensionally non-uniform and physically questionable one:

$$i_c(t) = C\frac{\mathrm{d}^{\alpha}u_C(t)}{\mathrm{d}t^{\alpha}}. \tag{4}$$

Dimensional uniformity of physical equation is fulfilled by the formula (3). On the left side we have current, which may be described as coulomb to second. On the right side we find farad multiplied by volt and divided by second, what brings us also to coulomb to second in the end. So we face no doubts.

The problem arises in the case of Eq. (4). As in the previous case we have coulomb to second on the left side, while coulomb to second to the power of α on the right side. And everything works well for $\alpha = 1$, but for the case considered by the author of the papers [2, 4] and few other works, when $\alpha \neq 1$ dimensional uniformity is not in place and further discussions aren't correct.

3. Fractional derivatives in electrical circuit theory

Many works have been published recently that refer to fractional derivatives, namely [2, 4-9, 10, 14-16]. They play a significant role in automatics and robotics. They may be also useful in other disciplines, e.g. in electrical engineering. In my opinion, the very interesting, fundamental work of prof. T. Kaczorek "*Standard and Positive Electrical Circuits with Zero Transfer Matrices*" presented at ZKWE'16 and published in Poznan University of Technology Academic Journals Issue 85 2016, which refers to this topic, contains a serious mistake in its crucial part [2, 4]. Unfortunately, a similar problem appears in many other works that discuss frac-

tional derivatives. Namely, Eqs. (43-45) and (46) which we can find in the paper [2] and which are presented below as (5), (6), (7) and (8):

$$i_c(t) = \frac{\mathrm{d}^{\alpha} q(t)}{\mathrm{d}t^{\alpha}}, \tag{5}$$

$$i_c(t) = C\frac{\mathrm{d}^{\alpha} u_C(t)}{\mathrm{d}t^{\alpha}}, \tag{6}$$

$$u_L(t) = \frac{\mathrm{d}^{\alpha} \Psi(t)}{\mathrm{d}t^{\alpha}}, \tag{7}$$

$$u_L(t) = L\frac{\mathrm{d}^{\alpha} i_L(t)}{\mathrm{d}t^{\alpha}}, \tag{8}$$

are simply wrong. If to write them correctly, they look as below:

$$i_c(t) = \frac{\mathrm{d}q(t)}{\mathrm{d}t}, \tag{9}$$

$$i_c(t) = C\frac{\mathrm{d}u_C(t)}{\mathrm{d}t}, \tag{10}$$

$$u_L(t) = \frac{\mathrm{d}\Psi(t)}{\mathrm{d}t}, \tag{11}$$

$$u_L(t) = L\frac{\mathrm{d}i_L(t)}{\mathrm{d}t}. \tag{12}$$

Eqs. (9-11) and (12) have been known for decades. They sometimes appear in the same form as in the works [2, 4], but they are complemented with the factor providing dimensional uniformity in such a case. The Faraday's law as presented with the formula (11) has been known for over 100 years. It appears in this form in handbooks, publications and monographs. It hasn't been stated that the mentioned law was applied in the form proposed in the work [2] in any handbook. E.g., Eqs. (6) and (8) could have fulfilled the dimensional uniformity rule, if capacity and inductivity had been functions of time and not measured in farads or henrys.

Consequently, following equations where fractional derivatives were used are wrong as well. If the equations above had been true, the dimensional uniformity rule wouldn't be valid anymore. The discussed equations don't fulfill the mentioned rule.

Let's look at Eq. (5) first. On the left side we have current that may be expressed with coulomb divided by a second, while on the right side we can see coulomb divided by a second to the power with the exponent different than one. This is not correct. A similar problem concerns remaining equations. They are not true as well, so the whole theory established in [2, 4] is not true as well and it doesn't matter, if we want to use it for the explanation of the pheno-

mena in super or classical capacitors. The dimensional uniformity requirement must be met. Acting modes of circuit elements don't influence this rule.

The impact of using the discussed equations is even more serious. Assuming, the mentioned equations were true, this would have influenced the content of the Maxwell equations [14]. The first two Maxwellian distribution laws [14] that create the base of electromagnetism wouldn't have been valid anymore:

$$\text{rot}\,\boldsymbol{H} = \boldsymbol{J} + \frac{\partial \boldsymbol{D}}{\partial t}, \tag{13}$$

$$\text{rot}\,\boldsymbol{E} = -\frac{\partial \boldsymbol{B}}{\partial t}, \tag{14}$$

$$\text{rot}\,\boldsymbol{H} = \boldsymbol{J} + \frac{\partial^{\alpha} \boldsymbol{D}}{\partial t^{\alpha}}, \tag{15}$$

$$\text{rot}\,\boldsymbol{E} = -\frac{\partial^{\alpha} \boldsymbol{B}}{\partial t^{\alpha}}. \tag{16}$$

With such an approach we face well-established bases of electromagnetism and the rules of physical formula formulation changing. If the theory presented in the works [2, 4] is true, we have to do with the fundamental discovery in the field of electromagnetism. If otherwise, the works [2, 4] contain mistake(s).

We may have similar concerns, when we start looking at the huge energy stored by super capacitors. The application of the new technology increased their capacity in relation to volume significantly. However, the amount of the stored energy is determined not only by the capacitor's capacity, but by voltage as well. We may conclude so based on the following formula:

$$W_e = \frac{CU^2}{2}. \tag{17}$$

The energy stored within the electrical (electrostatic) field is a function of energy's volume density:

$$W_e' = \frac{\boldsymbol{E} \cdot \boldsymbol{D}}{2}, \tag{18}$$

and of inter-electrode volume and may be written as follows:

$$W_e = \int_V W_e' \cdot \mathrm{d}V. \tag{19}$$

The energy density of an electrical field is the function of dielectric strength of inter-electrode dielectric and of its permittivity ε. We may increase the electrodes' surface, but we

won't be able to overcome the limitations resulting from Eq. (18). The maximal stored energy is limited by the finite permittivity ε values and by the defined electrical strength of the inter-electrode dielectric. If we assume that super capacitors don't work basing on the electrostatic rule of energy storing, then we shall define, in what way the energy is stored in such capacitors and then describe this operating mode with relevant formulae.

Is Eq. (47) from the paper [2] correct?

$$\frac{\mathrm{d}^{\alpha}x(t)}{\mathrm{d}t^{\alpha}} = Ax(t) + Bu(t)\,. \tag{20}$$

It's hard to conclude, as we don't know the dimensions of particular elements. Nevertheless Eq. (48) [2]:

$$e = RC_1\frac{\mathrm{d}^{\alpha}u_1}{\mathrm{d}t^{\alpha}} + u_1\,, \tag{21}$$

is just wrong. For α not equal to 1 the statement

$$RC_1\frac{\mathrm{d}^{\alpha}u_1}{\mathrm{d}t^{\alpha}}$$

doesn't represent voltage. The dimensional uniformity has been described briefly in p. 2.4 of [13]. This rule may be sometimes helpful for building formulae that describe various physical phenomena. Independently from the need of obeying the dimensional uniformity, the dependences between voltage and current at particular elements of the electrical circuit are precisely defined by the laws of electrical engineering. Let's consider three passive elements *R*, *L* and *C*. For these elements the dependence between current and voltage are clearly defined. For resistance this dependence is described by Ohm's law:

$$i = \frac{u}{R}\,. \tag{22}$$

Ohm's law has exactly the form as above and not any other, e.g.:

$$i = \frac{u^{\alpha}}{R^{\alpha}}\,. \tag{23}$$

The same applies to inductivity, which connects current and voltage with the following equations:

$$u = L\frac{\mathrm{d}i}{\mathrm{d}t}\,, \tag{24}$$

$$\text{or } i = \frac{1}{L}\int u\mathrm{d}t \text{ and not } u = L\frac{\mathrm{d}^{\alpha}i}{\mathrm{d}t^{\alpha}}\,.$$

Similarly for capacity:

$$u = \frac{1}{C}\int i\mathrm{d}t\,, \tag{25}$$

$$\text{or } i = C\frac{\mathrm{d}u}{\mathrm{d}t} \text{ and not } i = C\frac{\mathrm{d}^{\alpha}u}{\mathrm{d}t^{\alpha}}\,.$$

In other words, current in the capacitor equals capacity C multiplied by derivative of voltage at the capacitor. This expresses the physical law. It hasn't been questioned yet – as well as the dependence between voltage at the coil and the derivative of the flux coupled with the coil.

Special "fractional" *R*, *L*, *C* elements have been introduced in the paper [10]. Consequently, special coefficient, ensuring dimensional uniformity has been incorporated in the equations that describe "fractional circuit".

In the paper [10] the Maxwell equations have been presented in the form of (13) and (14), amended with the continuity laws instead of Eqs. (15) and (16). "Classical Equation" has been benchmarked with "Fractional Equation" there as well and dimensional uniformity has been assured. Many simulations have been included in this work as well.

Calculations have been compared to measurements in the paper [16]. A *RC* circuit has been investigated there. We may conclude from the curves in Fig. 3 in [16] that the transient voltage that has been calculated from the formula

$$e = RC\frac{\mathrm{d}u_C}{\mathrm{d}t} + u_C\,, \tag{26}$$

matches the experimental results and the one calculated from the formula (21) for the values α = 0.998, 0.997, 0.996 only approaches the measurement curve. Another set of calculations has been presented in Fig. 4 in [16]. In this case the results of formula (21) calculations reflect better the measurement curve. Authors explain this fact with non-linearity of circuit elements. However, they don't explain how to take this non-linearity into account, applying fractional derivatives. This may be however realized in the simpler way without fractional derivatives.

4. Conclusions

Implementation of new mathematical methods drives the development of many disciplines, including physics. They simplify the complex form of many formulae. For this reason we shall recognize the works related to fractional derivatives that have been touched in this paper. But on this way one may face various problems related to mathematical reflection of physical phenomena. Let's take the mathematical challenges faced by Albert Einstein [17]. At the begining he was stating that when the mathematicians started to analyze his relativity theory he started to have problems with understanding his theory himself. Later he appreciated the role of mathematics and the work of Herman Minkowski.

Having this in mind, we shall be conscious that even the newest mathematical methods, used for description of physical phenomena shouldn't contradict the physical laws. Complex methods of mathematical modelling may make the understanding of the described phenomenon challenging, but they shouldn't make it completely blurred. I leave it up to audience to opinion, how it is in this particular case.

Future research will aim to recommend the ways of correct application of fractional derivatives in electrical circuit theory and electromagnetic field theory. The topic of local and global solutions for the equations containing fractional derivatives will be in scope of the planned research. Potentially, new types of filters will be designed based on the results of mentioned re-search.

References

[1] Sikora R., *Fractional derivatives in electrical circuits theory – critical remarks*, (in Polish), Electrical Review, no. 10, pp. 274-276 (2016).
[2] Kaczorek T., *Standard and Positive Electrical Circuits with Zero Transfer Matrices*, Poznan University of Technology Academic Journals, no. 85 (2016).
[3] Kaczorek T., *Zeroing of state variables in fractional descriptor electrical circuits by state-feedbacks*. Archives of Electrical Engineering, vol. 63(249), no. 3 (2014).
[4] Kaczorek T., *Positivity and Reachability of Fractional Electrical Circuits*, Acta Mechanica et Automatica, vol. 5, no. 2 (2011).
[5] Domek S., *Application of fractional derivatives calculus in predictive control,* (in Polish), West Pomeranian University of Technology Publishing, Szczecin (2013).
[6] Domek S., Dworak P., *Theoretical Developments and Application of Non-Integer Order Systems*, Springer (2016).
[7] Włodarczyk M., Zawadzki A., *Positive order fractional derivatives in RLC circuits*, (in Polish), Electrics, no. 1(217) (2011).
[8] Zawadzki A., Włodarczyk M., *Modelling of super capacitor's charging and discharging processes*, (in Polish), Measurements, Automatics, Control, vol. 56, no. 12, pp. 1413-1415 (2010).
[9] Westerlund S., Ekstam L., *Capacitor Theory,* IEEE Transaction on Dielectric and Electrical Insulation, vol. 1, no. 5, pp. 826-839 (1994).
[10] Morales M.A., Lainez R., *Mathematical Modelling of Fractional Order Circuits*, arXiv: 1602.03541v1 [physics. class-ph], vol. 21 (2016).
[11] Povstenko Y., *Solutions to time-fractional diffusion-wave equation in spherical coordinates*, Acta Mechanica et Automatica, vol. 5, no. 2, pp. 108-111 (2011).
[12] Gomez-Aguilar J.F., et al., *Electrical circuits described by a fractional derivative with regular Kernel*, Revista Mexicana de Fisica, vol. 62 (2016).
[13] Sikora R., Chady T., Łopato P., Psuj G., *Theoretical Electrical Engineering*, (in Polish), West Pomeranian University of Technology Publishing, Szczecin (2016).
[14] Sikora R., *Electromagnetic field theory*, (in Polish), WNT Warszawa (1997).
[15] Gomez-Aguilar J.F., *Behavior characteristics of a cap-resistor, memcapacitor, and a memristor from the response obtained of RC and RL electrical circuits described by fractional differential equations*, Turkish Journal of Electrical Engineering & Computer Sciences, no. 24, pp. 1421-1433 (2016).
[16] Erti H., Calik A.E., Sirin H., Sen M., Oder B., *Investigation of electrical RC circuit within the framework of fractional calculus*, Revista Mexicana de Fisica, vol. 61, pp. 58-63 (2015).
[17] Kaku M., *Einstein's universe*, (in Polish), Pruszynski & Co (2004).

ARCHIVES OF ELECTRICAL ENGINEERING VOL. 66(1), pp. 165-178 (2017)

DOI 10.1515/aee-2017-0012

Influence of output conductance on characteristic frequencies of switch mode BUCK and BOOST converter

WŁODZIMIERZ JANKE, MARCIN WALCZAK

Department of Electronics, Koszalin Technical University of Technology
Śniadeckich 2, 75-453 Koszalin, Poland
e-mail: wlodzimierz.janke@tu.koszalin.pl

(Received: 13.09.2016, revised: 08.11.2016)

Abstract: Characteristic frequencies corresponding to poles and zeros of small-signal control-to-output transfer functions of popular DC-DC converters (BUCK and BOOST) are analyzed. The main attention is paid to influence of load conductance on the characteristic frequencies for converters working in continuous conduction mode (CCM) as well as in discontinuous conduction mode (DCM). Parasitic resistances of all converter components are included in calculations. In addition the improved description of CCM-DCM boundary is presented. The calculations are verified experimentally and good consistency of the results is observed.

Key words: pulse converters, BUCK, BOOST, small-signal models, control-to-output characteristics, DCM boundary, characteristic frequencies

1. Introduction

Switch-mode DC-DC power converters find great amount of applications. Their circuit solutions and control methods as well as component parameters are steadily improved [1, 2]. The most popular DC-DC converters – step-down (BUCK) and step-up (BOOST) are the objects of this paper. Typical converter contains a power stage and control subcircuit and its operation is based on a PWM principle. The precise knowledge of dynamic characteristics of the power stage is necessary for proper design of control circuit. The description of dynamic properties of the power stage has usually the form of small-signal transmittances in s-domain. These transmittances are obtained after linearization of an averaged model of the power stage [1-5, 9]. The most important small-signal transmittances of DC-DC converters are control-to-output and input-to-output transmittances. The characteristic frequencies corresponding to poles and zeros of transmittances are crucial parameters describing dynamic properties of converter power stage.

The converters may operate in continuous conduction mode (CCM) or discontinuous conduction mode (DCM). Formulas for small-signal transmittances and characteristic frequencies depend on the conduction mode, therefore the conditions for DCM-CCM boundary should be known. Characteristic frequencies in given operation mode depend mainly on the parameters of an induction coil and capacitor used in the power stage. In typical description of these frequencies, their dependence on load current (or load conductance) is not taken into account [1-6] but it is shown in [7] that in some situations, this dependence may be important. The considerations in [7] are only theoretical and restricted to a step-down converter (BUCK). In the present paper, formulas describing the influence of load conductance on characteristic frequencies of BUCK and BOOST converters are presented and theoretical results are verified by measurements. Section 2 of the paper is devoted to a general description of characteristic frequencies of DC-DC converters. In Section 3, new expressions defining a CCM-DCM boundary for nonideal converters are given. Theoretical description of characteristic frequencies of nonideal BUCK and BOOST is presented in Section 4. Examples of numerical calculation and measurement results are shown and compared in Section 5. Some concluding remarks are given in Section 6. The electrical schemes of the power stages of the converter under consideration are shown in Fig. 1. Apart from ideal components of converters – *T* (controlled switch), *D* (diode), *L* (inductor coil), *C* (capacitor), the parasitic resistances of each component are included.

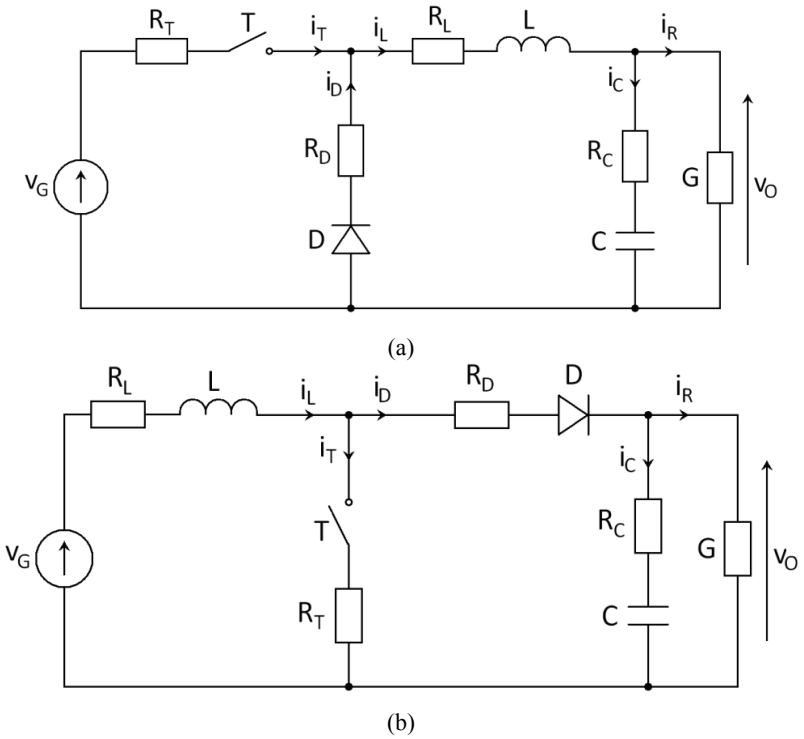

Fig. 1. Power stage of BUCK (a) and BOOST (b) converters including parasitic resistances

2. General description of small-signal transmittances and characteristic angular frequencies

Small-signal control-to-output and input-to-output transmittances of basic DC-DC converters (such as BUCK and BOOST) may be expressed in the form of second-order or first-order function of s variable [1-3]. For continuous conduction mode of operation one usually obtains [1, 2, 7, 8, 10]:

$$H_t = H_0 \frac{1 + s/\omega_Z}{1 + s/(Q \cdot \omega_0) + s^2/\omega_0^2}. \tag{1}$$

In the case of the BOOST converter, a transfer function has additional zero. For the DCM mode, based on separation of variable technique, it is obtained [4, 7]:

$$H_s = H_{s0} \frac{1 + s/\omega_{ZS}}{1 + s/\omega_P}. \tag{2}$$

Transmittance (1), for typical component values of the BUCK or BOOST converter has a pair of complex poles:

$$s_{P1,2} = \sigma \pm j \cdot \omega_R. \tag{3}$$

The resonance frequency f_R correspond to relation:

$$\omega_R = 2\pi \cdot f_R = \omega_0 \sqrt{1 - \frac{1}{4Q^2}}. \tag{4}$$

The maximum value of $|H_s|$ is obtained for frequency f_M, where:

$$\omega_M = 2\pi \cdot f_M = \omega_0 \sqrt{1 - \frac{1}{2Q^2}}. \tag{5}$$

The numerical values of ω_R and ω_M are usually very close to ω_o.

Apart from characteristic frequencies f_o, f_R and f_M involved with the poles of type (1) transmittances, there are frequencies $f_Z = \omega_Z/2\pi$, $f_{ZS} = \omega_{ZS}/2\pi$ corresponding to zeros of transmittances (1) and (2).

For some specific set of converter parameters, one obtains $Q < 1/2$ and corresponding values of poles of expression (1) are real numbers. The characteristic angular frequency in this case is:

$$\omega_{1,2} = \frac{\omega_0}{2Q} \cdot \left(1 \pm \sqrt{\frac{1}{4} - Q^2}\right) \quad \text{for} \quad Q < 0.5. \tag{6}$$

Dependencies of characteristic frequencies of BUCK and BOOST on the parameters of converter components are presented in the further part of the paper.

3. CCM and DCM boundary

Characteristic frequencies of converters working in CCM and in DCM are different. The CCM-DCM boundary are usually defined by threshold value G_C of load conductance. G_C depends on switching period T_S, duty ratio D_A of switching waveform and the inductance L of coil. The expressions for G_C given in the literature (e.g. [1, 2]) refer to ideal converters only. The equations given below describe threshold conductance G_C obtained with parasitic resistances accounted for.

For BUCK converter:

$$G_{C(\mathrm{BUCK})} = \frac{(1-D_A)T_S}{2L-(R_L+R_D)(1-D_A)T_S}. \tag{7}$$

For BOOST converter:

$$G_{C(\mathrm{BOOST})} = \frac{(1-D_A)^2 D_A T_S}{2L-(R_D-R_T)(1-D_A)D_A T_S}. \tag{8}$$

Converter works in DCM for load conductance $G < G_C$. A converter is always designed to work in a specific mode of operation. Due to work of the converters in a wide range of parameters, the worst case scenario should be considered, regarding Eqs. (7) and (8), to ensure that the converter stays in the CCM or DCM mode. Examples of modifications that include the worst case have been presented in [2].

4. Small signal transmittances and characteristic frequencies of BUCK and BOOST converters

In this section, the expressions for control-to-output transmittances H_d and corresponding characteristic angular frequencies derived for BUCK and BOOST converters are presented. Control-to-output transmittance is usually used in the procedure of control subcircuit design [1-3]. In addition, it is known [1-3] that the denominators of expressions describing control-to-output and input-to-output transmittances, as well as output impedance of a given converter type are the same, therefore the same angular frequencies of poles refer to various transmittances.

Control-to-output transmittance H_d is defined as follows:

$$H_d(s) = \left.\frac{V_o}{\theta}\right|_{V_g=0}, \tag{9}$$

where θ, V_g and V_o are small-signal values of duty ratio and input and output voltage.

Control to output transmittances of BUCK and BOOST converters working in CCM with parasitic resistances (see Fig. 1) may be expressed as [7]:

$$H_{d(\mathrm{BUCK})} = \frac{(V_G - I_L(R_T - R_L))(1 + sCR_C)}{s^2 LC_Z + s(GL + R_Z C_Z + CR_C) + 1 + GR_Z}, \tag{10}$$

$$H_{d(\mathrm{BOOST})} = \frac{-s^2 LCR_C I_L + s(V_A CR_C - LI_L - CR_C R_Z I_L) + V_A - I_L R_Z}{s^2 LC_Z + s(GL + R_Z C_Z + (1 - D_A)^2 + CR_C) + (1 - D_A)^2 + GR_Z}. \tag{11}$$

The example of transfer function derivation is given in Appendix A.
By comparison of (10) and (11) with general description in Eq. (1), one obtains:

$$\omega_{Z(\mathrm{BUCK})} = \frac{1}{C \cdot R_C}, \tag{12}$$

$$\omega_{0(\mathrm{BUCK})} = \frac{1}{\sqrt{LC}} \sqrt{\frac{GR_Z + 1}{GR_C + 1}}, \tag{13}$$

$$Q_{(\mathrm{BUCK})} = \frac{\sqrt{LC_Z(G \cdot R_Z + 1)}}{GL + C_Z R_Z + CR_C}, \tag{14}$$

$$\omega_{0(\mathrm{BOOST})} = \frac{1}{\sqrt{LC}} \sqrt{\frac{GR_Z + (1 - D_A)^2}{GR_C + 1}}, \tag{15}$$

$$Q_{(\mathrm{BOOST})} = \frac{\sqrt{LC_Z(GR_Z + (1 - D_A)^2)}}{GL + C_Z R_Z + (1 - D_A)^2 CR_C}. \tag{16}$$

The notation in Eqs. (10) – (16) corresponds to following dependencies:

$$R_Z = R_L + D_A \cdot R_T + (1 - D_A) \cdot R_D, \tag{17}$$

$$C_Z = C \cdot (1 + G \cdot R_C), \tag{18}$$

$$V_X = V_O - I_L(R_T - R_D), \tag{19}$$

$$V_A = (1 - D_A) V_X, \tag{20}$$

$$I_{L(\mathrm{BUCK})} = GV_O, \tag{21}$$

$$I_{L(\mathrm{BOOST})} = \frac{GV_O}{1 - D_A}, \tag{22}$$

$$V_{O(\mathrm{BUCK})} = \frac{D_A V_G}{1 + R_Z G}, \tag{23}$$

$$V_{O(\mathrm{BOOST})} = \frac{(1 - D_A) V_G}{(1 - D_A)^2 + R_Z G}. \tag{24}$$

From Eqs. (4) – (6) and (10) – (24), the following expressions for characteristic angular frequencies ω_R, ω_M, $\omega_{1,2}$ are obtained:

$$\omega_{R\,(\mathrm{BUCK})} = \frac{1}{2LC_Z}\sqrt{4LC_Z(1+GR_Z)-(GL+R_ZC_Z+CR_C)^2}\,, \tag{25}$$

$$\omega_{M\,(\mathrm{BUCK})} = \frac{1}{2LC_Z}\sqrt{4LC_Z(1+GR_Z)-2(GL+R_ZC_Z+CR_C)^2}\,, \tag{26}$$

$$\omega_{1,2\,(\mathrm{BUCK})} = \frac{1}{4LC_Z}\left(2(GL+R_ZC_Z+CR_C)\pm\sqrt{(GL+R_ZC_Z+CR_C)^2-4LC_Z(1+GR_Z)}\right), \tag{27}$$

$$\omega_{R(\mathrm{BOOST})} = \frac{1}{2LC_Z}\sqrt{4LC_Z\left((1-D_A)^2+GR_Z\right)-\left(GL+R_ZC_Z+(1-D_A)^2CR_C\right)^2}\,, \tag{28}$$

$$\omega_{M(\mathrm{BOOST})} = \frac{1}{2LC_Z}\sqrt{4LC_Z\left((1-D_A)^2+GR_Z\right)-2\left(GL+R_ZC_Z+(1-D_A)^2CR_C\right)^2}\,, \tag{29}$$

$$\omega_{1,2\,(\mathrm{BOOST})} = \frac{1}{4LC_Z}2\left(GL+R_ZC_Z+(1-D_A)^2CR_C\right)\pm \\ +\frac{1}{4LC_Z}\sqrt{\left(GL+R_ZC_Z+(1-D_A)^2CR_C\right)^2-4LC_Z\left((1-D_A)^2+GR_Z\right)}\,. \tag{30}$$

Control-to-output conductances of converters working in DCM are following:

$$H_{dD(\mathrm{BUCK})} = \frac{2G_ZV_GD_A(M_{ID}-1)}{sC+G_ZD_A{}^2M_{ID}{}^2+G}\,, \tag{31}$$

$$H_{dD(\mathrm{BOOST})} = \frac{2D_AG_ZV_G(M_{VD}-1)}{sC(M_{VD}-1)^2+G_ZD_A{}^2+(M_{VD}-1)^2G}\,, \tag{32}$$

where:

$$M_{VD(\mathrm{BUCK})} = \frac{G_ZD_A}{2G}\left(\sqrt{D_A^2+4\frac{G}{G_Z}}-D_A\right), \tag{33}$$

$$M_{VD(\mathrm{BOOST})} = \frac{1}{2}\left(1+\sqrt{1+D_A^2G_ZR}\right), \tag{34}$$

$$M_{ID} = \frac{1}{M_{VD}}\,, \tag{35}$$

$$G_Z = \frac{T_S}{2L}\,. \tag{36}$$

The formulas for small-signal transmittances may be derived for averaged models in the form of equivalent circuits shown in Appendix B. The resulting characteristic angular frequencies for BUCK and BOOST in DCM may be expressed as:

$$\omega_{PD(\mathrm{BUCK})} = \frac{1}{C}(G_Z D^2 M_{ID}{}^2 + G)\,, \tag{37}$$

$$\omega_{PD(\mathrm{BOOST})} = \frac{1}{C}\left(\frac{G_Z D^2}{M_{VD} - 1} + G\right). \tag{38}$$

It may be shown that the influence of parasitic resistances on control-to-output transmittances and related characteristic frequencies may be neglected for DCM.

The influence of load conductance on characteristic frequencies of converters in DCM seems to be relatively strong, as it is seen from Eqs. (37), (38). It may be quantitatively evaluated by numerical experiments.

5. Examples of calculations and measurements

The measurements and numerical calculations have been performed for a laboratory model of a BUCK converter with parameters established by auxiliary measurements: $L = 32$ µH; $C = 345$ µF; $R_L = 53$ mΩ; $R_C = 91$ mΩ; $R_T = 20$ mΩ; $R_D = 281$ mΩ. Switching frequency of 100 kHz and 250 kHz was used for the converter working in DCM and CCM respectively. An indirect method of measuring frequency characteristic was used. First a response of output voltage to a step change of a duty cycle was measured with an MSO5104 digital oscilloscope. Next, the digital data were processed and an FFT function was used to find the spectrum of the measured function. Fluctuations appear at higher frequencies due to limited resolution of the oscilloscope. The exemplary frequency characteristics of the control-to-output transmittance magnitude calculated and measured for the BUCK converter are presents in Figs. 2 and 3.

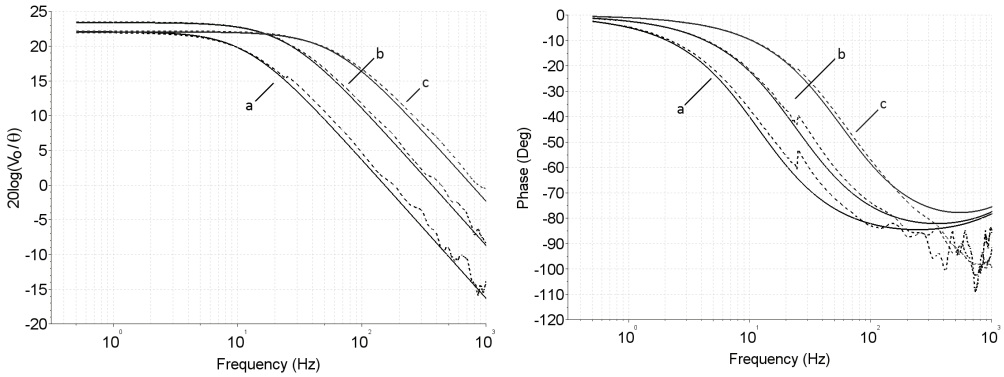

Fig. 2. Magnitude and phase of control-to-output transmittance calculated (solid lines) and measured (dotted lines) for BUCK converter for load resistance values corresponding to operation in DCM

Load resistance values assumed in Fig. 2 are: 198 Ω (curve a), 61.5 Ω (curve b) and 20 Ω (curve c), that corresponds to DCM. Load resistance values in Fig. 3: 4.7 Ω (curve a), 1 Ω (curve b), 0.5 Ω (curve c) and 0.2 Ω (curve d) correspond to the CCM mode. Values of $|H_d|$ in Figs. 2 and 3 are normalized to 1 V. The exemplary frequency characteristics of the control-to-output transmittance magnitude calculated and measured for the BOOST converter are presented in Figs. 4 and 5. Load resistance values assumed in Fig. 2 are: 198 Ω (curve a), 50 Ω (curve b) and 20 Ω (curve c), that corresponds to DCM. Load resistance values in Fig. 3: 4.7 Ω (curve a), 1 Ω (curve b), 0.5 Ω (curve c) and 0.2 Ω (curve d) correspond to the CCM mode. Values of $|H_d|$ in Figs. 4 and 5 are normalized to 1 V.

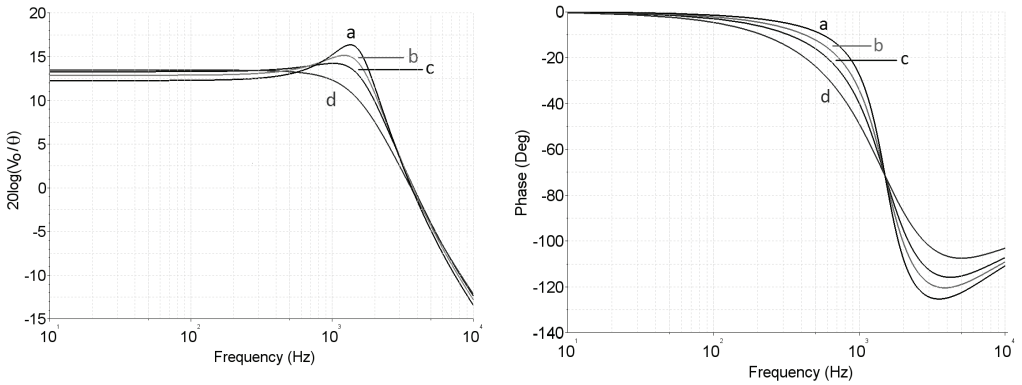

Fig. 3. Magnitude and phase of control-to-output transmittance calculated for BUCK converter for load resistance values corresponding to operation in CCM

Values of characteristic frequencies f_P corresponding to pole frequency ω_P in DCM (Fig. 2) are equal to: 12 Hz (curve a); 25 Hz (curve b) and 60.3 Hz (curve c). The influence of zero (ω_Z) of transmittance for DCM is not visible in Fig. 2 because $\omega_Z \gg \omega_P$.

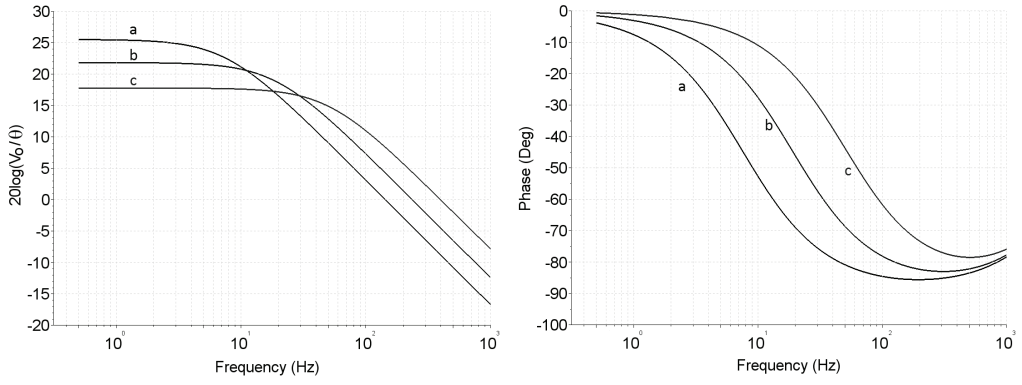

Fig. 4. Magnitude and phase of control-to-output transmittance calculated for BOOST converter for load resistance values corresponding to operation in DCM

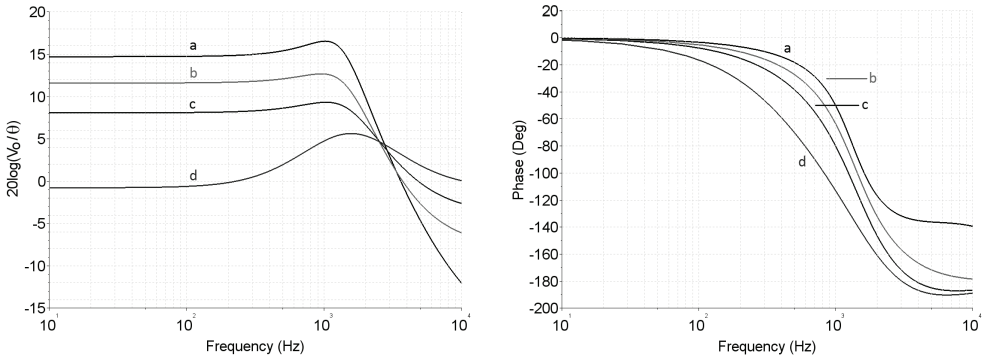

Fig. 5. Magnitude and phase of control-to-output transmittance calculated for BOOST converter for load resistance values corresponding to operation in CCM

6. Conclusions

Characteristic frequencies corresponding to poles and zero of control-to-output transmittance are important parameters, used in the procedure of control subcircuit design of switch-mode power converters. These frequencies are usually assumed to be independent of the load conductance. In some cases, the load conductance of a converter changes considerably and its influence on characteristic frequencies cannot be neglected. Such situations, for popular DC-DC converters BUCK and BOOST are considered in the paper. The expressions describing characteristic frequencies of converters, are derived with the parasitic resistances of converter components included. Calculations based on theoretical formulas are compared with the measurement results and good consistency is obtained. It is observed that the influence of load conductance on characteristic frequencies of converters working in discontinuous conduction mode (DCM) are much stronger than in CCM. Therefore, the precise description of the boundary between CCM and DCM is necessary and such description for converters with parasitic resistances is presented in Section 3.

Appendix A. A derivation of ideal BUCK converter transmittance for DCM

This derivation, presented in [5], is depicted here in brief for readers' convenience. A schematic used for the following derivation has been presented in Fig. A1.

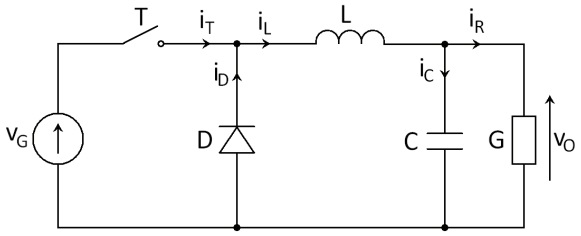

Fig. A.1. Ideal BUCK converter

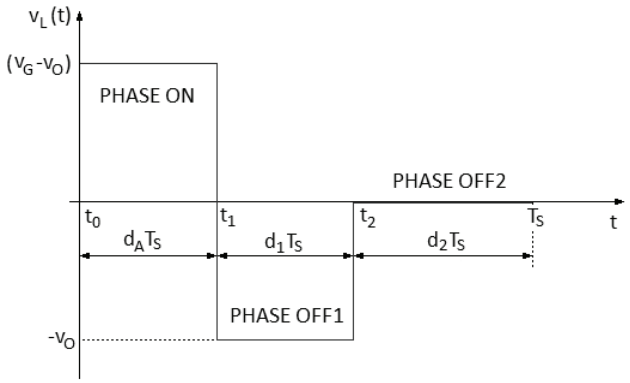

Fig. A.2. Inductor voltage of BUCK converter working in DCM

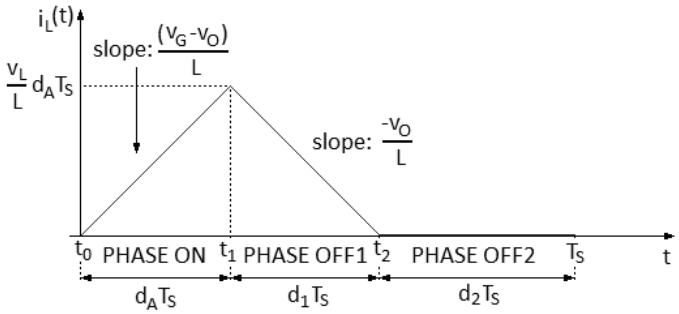

Fig. A.3. Inductor current of BUCK converter working in DCM

The waveform of inductor current in single switching period is shown in Fig. A3. The value of d_1 is:

$$d_1 = \frac{(v_G - v_O)}{v_O} d_A , \tag{A.1}$$

where d_A is the externally forced duty ratio.

Contrary to the situation in CCM the values of the inductor current is identical (and equal to zero) at the beginning and at the end of each period. The average value of inductor voltage v_{LS} is zero in DCM, not only for DC condition but also in transients:

$$v_{LS} = 0 . \tag{A.2}$$

As a consequence, the inductor doesn't exist in the large-signal averaged model of BUCK and BOOST for DCM. This observation agrees with result of deriving the models for DCM based on state-space averaging.

The local average values of inductor current i_L(ON) for the ON phase, i_L(OFF1) for the OFF1 phase (see Fig. A.2) and average over the whole period, i_{LS} obtained from the figure regarding the expression for d_1 are obtained in the form:

$$i_{L(\mathrm{ON})} = \frac{d_A T_S}{2} \frac{v_G - v_O}{L}, \tag{A.3}$$

$$i_{L(\mathrm{OFF1})} = \frac{d_1 T_S}{2} \frac{-v_O}{L}, \tag{A.4}$$

with (42) and (43) One can calculate the average value of inductor current in the whole phase:

$$i_{LS} = \frac{v_G - v_O}{2L} d_A T_S (d_A + d_1). \tag{A.5}$$

From (A.1), (36) and (A.5):

$$i_{LS} = d_A^2 G_Z \frac{v_G}{v_O} (v_G - v_O). \tag{A.6}$$

Small-signal relation based on (A.6) may be presented as:

$$I_l = \alpha_1 V_g + \alpha_2 \theta + \alpha_3 V_o, \tag{A.7}$$

where:

$$\alpha_1 = \frac{\partial f(v_G, d_A, v_O)}{\partial v_G} = D_A^2 G_Z (2\frac{V_G}{V_O} - 1), \tag{A.8}$$

$$\alpha_2 = \frac{\partial f(v_G, d_A, v_O)}{\partial d_A} = 2 D_A G_Z V_G (\frac{V_G}{V_O} - 1), \tag{A.9}$$

$$\alpha_3 = \frac{\partial f(v_G, d_A, v_O)}{\partial v_O} = -D_A^2 G_Z \frac{{V_G}^2}{V_O^2}, \tag{A.10}$$

substituting (A.8)-(A.10) into (A.7):

$$I_l(s) = D_A^2 G_Z (2\frac{V_G}{V_O} - 1) V_g(s) + 2 D_A G_Z V_G (\frac{V_G}{V_O} - 1)\theta(s) - D_A^2 G_Z \frac{{V_G}^2}{V_O^2} V_o(s). \tag{A.11}$$

Small-signal dependence of I_L on V_O resulting from Fig. A.1 is:

$$I_l(s) = V_o(s)(sC + G), \tag{A.12}$$

which leads to:

$$H_d(s) = \frac{2 D_A G_Z V_G (M_{ID} - 1)}{sC + G + D_A^2 G_Z M_{ID}^2} \theta(s), \tag{A.13}$$

where static current transmittance is:

$$M_{ID} = \frac{1}{M_{VD}} \tag{A.14}$$

and

$$M_{VD} = \frac{V_O}{V_G} = \frac{G_Z D_A}{2G}\left(\sqrt{\left(D_A^2 + 4\frac{G}{G_Z}\right)} - D_A\right). \tag{A.15}$$

Appendix B. Equivalent circuit, representing small-signal models of BUCK and BOOST in CCM and DCM

The models have been previously presented in [5] and are shown here for reader's convenience.

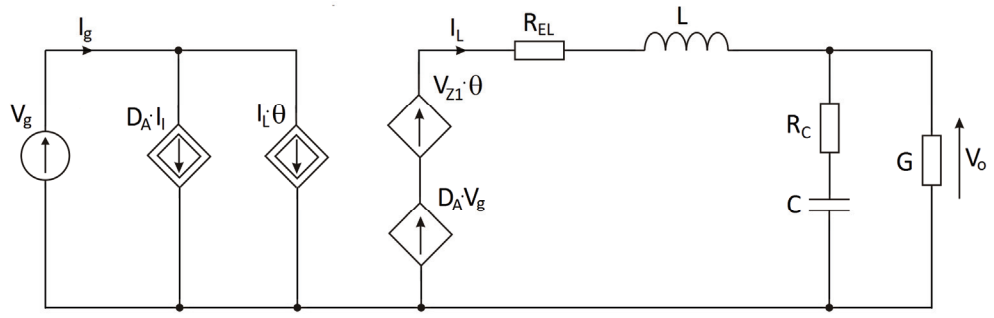

Fig. B.1. Small-signal model of BUCK converter working in CCM

$$R_{EL} = R_E + R_L, \tag{B.1}$$

$$R_E = R_T D_A + R_D(1 - D_A), \tag{B.2}$$

$$V_{Z1} = V_G + (R_D - R_T) I_L. \tag{B.3}$$

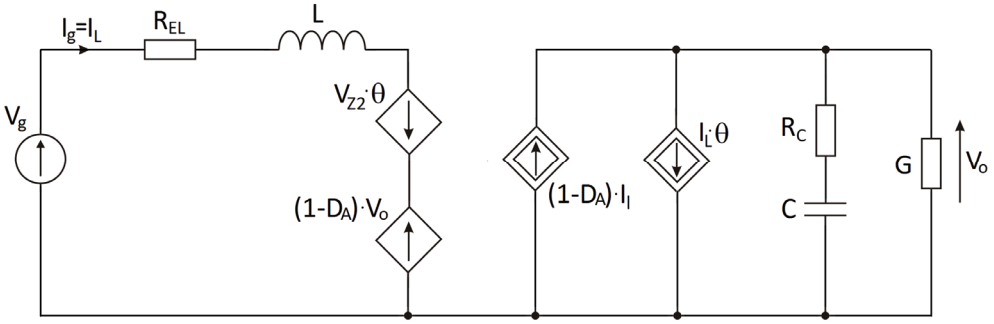

Fig. B.2. Small-signal model of BOOST converter working in CCM

$$V_{Z2} = V_O + (R_D - R_T) I_L. \tag{B.4}$$

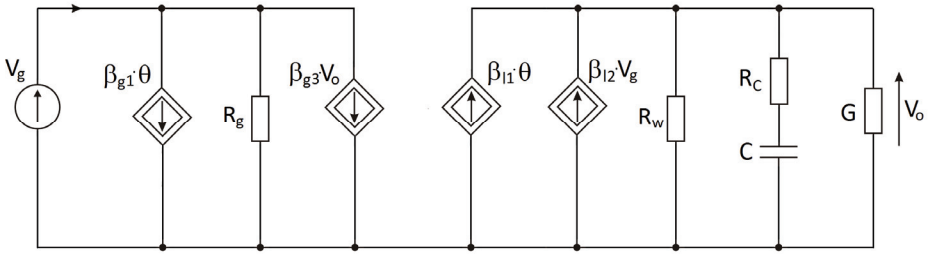

Fig. B.3. Small-signal model of BUCK converter working in DCM

$$\beta_{g1} = 2G_Z D_A (V_G - V_O), \tag{B.5}$$

$$R_g = \frac{1}{G_Z D_A^2}, \tag{B.6}$$

$$\beta_{g3} = -G_Z D_A^2, \tag{B.7}$$

$$\beta_{l1} = 2G_Z V_G D_A \left(\frac{V_G}{V_O} - 1 \right), \tag{B.8}$$

$$\beta_{l2} = G_Z D_A^2 \left(\frac{2V_G}{V_O} - 1 \right), \tag{B.9}$$

$$R_w = \left(G_Z D_A^2 \frac{V_G^2}{V_O^2} \right)^{-1}. \tag{B.10}$$

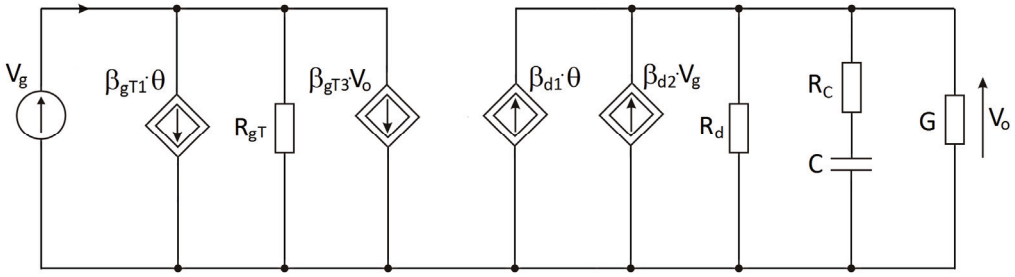

Fig. B.4. Small-signal model of BOOST converter working in DCM

$$\beta_{gT1} = 2G_Z D_A \frac{V_G V_O}{V_O - V_G}, \tag{B.11}$$

$$R_{gT} = \frac{(V_O - V_G)^2}{G_Z D_A^2 V_O^2}, \tag{B.12}$$

$$\beta_{gT3} = -\frac{G_Z D_A^2 V_G^2}{(V_O - V_G)^2}, \tag{B.13}$$

$$\beta_{d1} = 2G_Z D_A \frac{V_G^2}{V_O - V_G}, \tag{B.14}$$

$$\beta_{d2} = G_Z D_A^2 \frac{V_G (2V_O - V_G)}{(V_O - V_G)^2}, \tag{B.15}$$

$$R_w = \left(G_Z D_A^2 \frac{V_G^2}{V_O^2} \right)^{-1}. \tag{B.17}$$

References

[1] Erickson R.W., Maksimovic D., *Fundamentals of Power Electronics*, *2-nd Edition*, Kluwer (2002).

[2] Kazimierczuk M.K., *Pulse-Width Modulated DC-DC Power Converters*, J. Wiley (2008).

[3] Janke W., *Averaged Models of Pulse-Modulated DC-DC Converters, Part I. Discussion of standard methods*, Archives of Electrical Engineering, vol. 61, no. 4, pp. 609-631 (2012).

[4] Janke W., *Averaged Models of Pulse-Modulated DC-DC Converters, Part II. Models Based on the Separation of Variables*, Archives of Electrical Engineering, vol. 61, no. 4, pp. 633-654 (2012).

[5] Janke W., *Equivalent Circuits for Averaged Description of DC-DC Switch-Mode Power Converters Based on Separation of Variables Approach*, Bulletin of the Polish Academy of Sciences, vol. 61, no. 3, pp. 711-723 (2013).

[6] Tajuddin M.F.N., Rahim N.A., *Small-signal AC modeling Technique of Buck Converter with DSP Based Proportional-Integral-Derivative (PID) Controller*, IEEE Symposium on Industrial Electronics and Applications, Kuala Lumpur, Malaysia, October 4-6 (2009).

[7] Janke W., *Characteristic Frequencies in Averaged Description of Step-Down (BUCK) DC-DC Power Converter,* Archives of Electrical Engineering, vol. 65, No. 4, pp. 703-717 (2016).

[8] Reatti A., Kazimierczuk M.K., *Small-signal model for PWM converter for the discontinuous conduction mode and its application for the boost converter*, IEEE Trans. Circuits Syst. I, vol. 50, no. 1, pp. 65-73 (2003).

[9] Czarkowski D., Kazimierczuk M.K., *Energy-conservation approach to modeling PWM dc-dc converters*, IEEE Trans Aerospace and Electron Syst., vol. 29, pp. 1059-63 (1993).

[10] Bryant B., Kazimierczuk M.K., *Voltage-loop power-stage transfer functions with MOSFET delay for boost PWM converter operating in CCM*, IEEE Trans. Industrial Electron., vol. 54, pp. 347-353 (2007).

[11] Luchetta A., Manetti S., Piccirilli M.C., Reatti A., Kazimierczuk M.K., *Effects of parasitic components on diode duty cycle and small-signal model of PWM DC-DC buck converter in DCM*, 15th IEEE International Conference on Environment and Electrical Engineering (EEEIC15), Rome, Italy, pp. 772-777 (2015).

ARCHIVES OF ELECTRICAL ENGINEERING VOL. 66(1), pp. 179-187 (2017)

DOI 10.1515/aee-2017-0013

Third harmonic current injection into highly saturated multi-phase machines

FELIX KLUTE, TORBEN JONSKY

Ostermeyerstraße 11, 31787 Hamelin, Germany
e-mail: fffklute@gmail.com

(Received: 23.09.2016, revised: 14.11.2016)

Abstract: One advantage of multi-phase machines is the possibility to use the third harmonic of the rotor flux for additional torque generation. This effect can be maximised for Permanent Magnet Synchronous Machines (PMSM) with a high third harmonic content in the magnet flux. This paper discusses the effects of third harmonic current injection (THCI) on a five-phase PMSM with a conventional magnet shape depending on saturation. The effects of THCI in five-phase machines are shown in a 2D FEM model in Ansys Maxwell verified by measurement results. The results of the FEM model are analytically analysed using the Park model. It is shown in simulation and measurement that the torque improvement by THCI increases significantly with the saturation level, as the amplitude of the third harmonic flux linkage increases with the saturation level but the phase shift of the rotor flux linkage has to be considered. This paper gives a detailed analysis of saturation mechanisms of PMSM, which can be used for optimizing the efficiency in operating points of high saturations, without using special magnet shapes.

Key words: *dq*-model, non-linear effects, PMSM, saturation, third harmonic current injection, torque improvement

1. Introduction

Multi-phase machines are rarely used in commercial applications due to high inverter costs. But compared to conventional three-phase machines they have the advantage of a higher power density due to higher winding factors and the possibility to use higher harmonics of the rotor flux for torque improvement by third harmonic current injection (THCI). In [1] five-phase machines with special magnet shapes are presented, which are optimised on third harmonic content in the magnet flux for maximizing the torque improvement by THCI. It has been shown in simulation, analytical results and measurement, that the optimal torque improvement can be achieved, if the third harmonic of the magnet flux is 1/6 of the first harmonic. The THCI with the presented magnet shape leads to a higher efficiency compared to motors with conventional magnet shapes without THCI [2] deals with the analytical determina-

tion of optimised THCI. In [3] control methods and systems for five-phase synchronous machines are presented to optimise the third harmonic current in phase and amplitude. With a table containing all operating points the optimal current configuration (direct current i_d, q-current i_q, direct current of the third harmonic i_{d3}, and the q-current of the third harmonic i_{q3}) concerning the motor losses is chosen. Another advantage of THCI is the higher phase control factor of the inverter and the peak voltage reduction.

Up to date no deliberations have been made on the influence of THCI taking into account the non-linear effects of the electromagnetic circuit of Permanent Magnet Synchronous Machines (PMSM). In this paper the THCI into a five-phase PMSM with conventional surface-mounted magnets and concentrated winding is described for different saturation levels concerning the effects on torque improvement, losses and peak voltage reduction by an analytical model, simulation and measurement.

The test drive is fed by an external decentralised inverter consisting of ten SST (smart stator teeth) modules, one for each coil. In the second prototype the SST-modules are integrated into the motor housing. The motor concept is described in [4]. The modeling and parameter identification of this drive is described in [5].

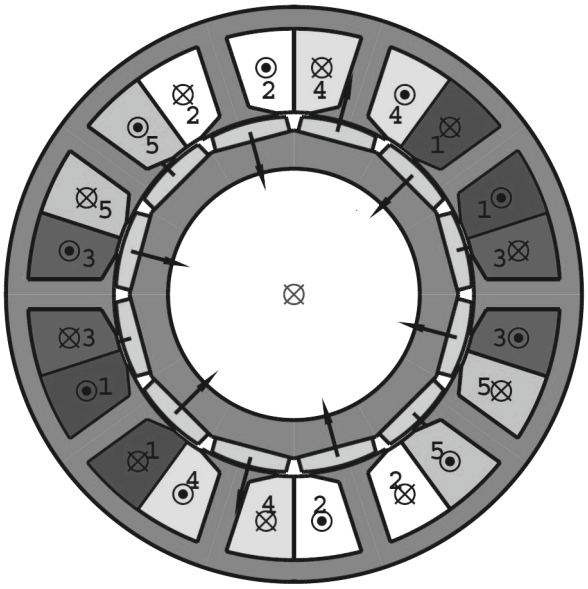

Fig. 1. Cross-section of the test drive with phase numbers

2. Motor concept and magnet shape

As shown in [1] a special magnet shape with a high third harmonic magnet flux is required for a considerable torque improvement by THCI. In this paper a segmented five-phase PMSM with 10 slots and 10 poles with loaf-shaped magnets is presented (Fig. 1). It also requires

a high overload and demagnetization withstand capability. This can only be achieved by conventional magnet shapes with evenly distributed magnet thickness over the pole circumference, for example arc-shaped and loaf-shaped magnets. But these magnets have a relatively low third harmonic component of the permanent magnet flux (about 5% of the first harmonic). Deliberations have been made, that arc-shaped magnets with a wide gap in the pole middle would have a higher percentage of the third harmonic permanent magnet flux. But according to FEM simulations the idea has been proven as ineffective as the first harmonic of the magnet flux has decreased to such a large extent that the motor efficiency decreased by about 4.5% at the same output torque. On the other hand it has been proven by simulation and measurements that the third harmonic of the permanent magnet flux linkage increases from 3 to more than 6% from no-load to double rated current due to saturation effects for the examined motor.

3. Simulation model and experimental setup

The experimental setup consists of a test drive with a rated power of 7.5 kW, a rated speed of 600 rpm and a rated torque of 120 Nm, and a geared load motor. As measurement devices a weighing cell for the torque, a Yokogawa WT 3000 power analyzer for current, voltage and power factor in one stator coil, and PT 100 temperature sensors on both end windings of each stator coil are used. For determination of the efficiency of the whole drive system voltage and current are also measured in the intermediate circuit. The control unit allows to separately provide *d*-current, *q*-current, *d*3-current and *q*3-current. An incremental encoder is used to detect the rotor position. The control unit considers the geometrical symmetry axis of the magnets as *d*-axis and *d*3-axis. All measurements are carried out at constant temperature (42°C).

For simulation the motor is modeled in the FEM-program Ansys Maxwell 2D taking into account the rotor position. The currents are given in the *dq*-system according to the analytical model described in section 5 and internally transformed into phase currents. Induced voltages, the total flux linkages and inductances of all phases as well as the copper losses, magnet losses and core losses and torque are calculated directly in Maxwell for every time step and transformed into the *dq*-system.

As in the control unit of the realised drive system the geometrical symmetry axis of the magnets is assumed to be the *d*-axis and the *d*3-axis. As the maximum current which can be carried by the SST modules does not affect demagnetization, the BH-curve of the permanent magnet material can be assumed as linear, but the non-linear BH-curve of the laminated core is considered. The segmentation of the magnets in axial direction as well as the segment air gap between the single stator tooth modules are neglected.

4. Analytical model

The electromagnetic torque T for m-phase machines is defined according to the Park model by:

$$T = \frac{m}{2} p \boldsymbol{i}^T \boldsymbol{J}\left(\boldsymbol{M}\boldsymbol{i} + \boldsymbol{\Psi}_{PM}\right). \tag{1}$$

Here $\boldsymbol{i}$ is the current vector, $\boldsymbol{J}$ the coefficient matrix from the derivation of the rotation matrix, $\boldsymbol{M}$ the inductance matrix, p the number of pole-pairs and $\boldsymbol{\Psi}_{PM}$ the permanent magnet flux linkage. For five-phase systems the components of the vectors and matrices from Equation (1) are defined as:

$$\boldsymbol{i} = \begin{bmatrix} i_d \\ i_q \\ i_{d3} \\ i_{q3} \\ i_0 \end{bmatrix}; \qquad \boldsymbol{M} = \begin{bmatrix} L_{dd} & L_{qd} & L_{dd3} & L_{dq3} & L_{d0} \\ L_{dq} & L_{qq} & L_{qd3} & L_{qq3} & L_{q0} \\ L_{d3d} & L_{d3q} & L_{d3d3} & L_{d3q3} & L_{d30} \\ L_{q3d} & L_{q3q} & L_{q3d3} & L_{q3q3} & L_{q30} \\ L_{0d} & L_{0q} & L_{0d3} & L_{0q3} & L_{00} \end{bmatrix}. \tag{2}$$

As only static operation points are considered i_d, i_q, i_{d3}, i_{q3} and the zero-current i_0 are constant. The inductances are the absolute inductances:

$$L_{ik} = \frac{\Psi_i}{i_k}. \tag{3}$$

L_{ik} is the absolute inductance between phase i and k, Ψ_i the flux linkage generated by phase k and crossing phase i and i_k is the current of phase k. When the absolute inductances are transformed into the dq-system, the minor elements can be neglected, but for non-linear operating points they have to be considered.

The components of the permanent magnet flux linkage are defined analogously to the current, whereas for ideal linear conditions the q-component and $q3$-component of the permanent magnet flux linkage is 0. But for higher saturation levels, when the d-axis and $d3$-axis are defined as the geometrical symmetry axis of the magnets, the phases of the harmonics of the magnet flux linkage shift so that:

$$\Psi_{PM,q} \neq 0 \quad \text{and} \quad \Psi_{PM,q3} \neq 0, \tag{4}$$

with $\Psi_{PM,q} = 0$ and $\Psi_{PM,q3} = 0$ only i_q and i_{q3} affect the output torque considerably. But when Equation (4) is fulfilled, an additional $d3$-current can be injected to achieve further torque improvement as the phase of the third harmonic current is shifted to fit the phase of the third harmonic of the magnet flux linkage. The permanent magnet flux linkage is calculated out of the total flux linkage Ψ calculated in Maxwell:

$$\Psi_{PM} = \Psi - \boldsymbol{M}\boldsymbol{i}. \tag{5}$$

In the following the different torque generating mechanisms from Equation (1) are distinguished. Firstly, the torque T_{PM} generated by the first and third harmonic of the permanent magnet flux is defined as:

$$T_{PM} = \frac{m}{2} p\left(\Psi_{PM,d} i_q - \Psi_{PM,q} i_d + 3\Psi_{PM,d3} i_{q3} - 3\Psi_{PM,q3} i_{d3}\right). \tag{6}$$

Furthermore the reluctance torque T_{rel} considering the cross-saturation effects is:

$$T_{\text{rel}} = \frac{m}{2} p \boldsymbol{i}^T \boldsymbol{J} \boldsymbol{M} \boldsymbol{i} \,. \tag{7}$$

The total current for a single phase is defined as:

$$I_t = \sqrt{I_d^2 + I_q^2 + I_{d3}^2 + I_{q3}^2} \,. \tag{8}$$

5. Results

5.1 Saturation behavior

To show the saturation behavior of the machine the phase voltage and the torque are calculated in the FEM model for q-current I_q in steps of 20% up to 300% of the rated current (I_r = 16.54 A). In the range of the total phase current given in Equation (8), which can be carried by the SST modules (between 200% and 250% of rated current) measurements and simulation results are in good agreement with each other. According to the simulation results the electromagnetic circuit is fully saturated at total phase currents beginning with 300% of the rated current, where the phase voltages and the torque start to increase linearly with the phase current. That means full saturation cannot be reached with the given SST modules, but nonlinear effects already occur beginning with 140% of the rated current. Simulation results are presented up to 300% of the rated current only to show the behavior at full saturation. According to analytic thermal estimations and measurements the winding insulation can withstand total phase currents of about 180% of the rated current in permanent operation. Concerning the measured thermal capacity of the machine the winding can withstand the highest overload current of 250% which can be carried by the SST modules for about 5 minutes.

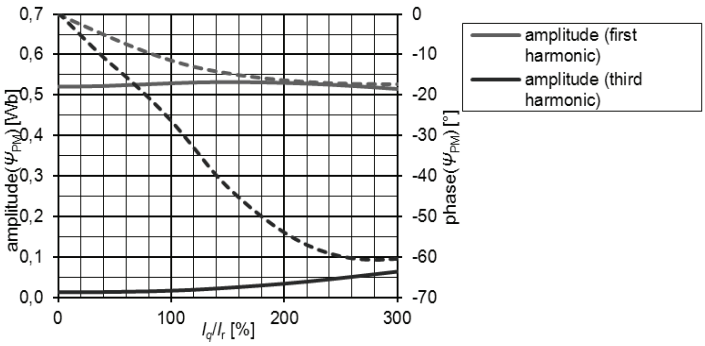

Fig. 2. Amplitude and phase of the first and third harmonic of the permanent magnet flux linkage depending on the q-current from 0 to 300% of rated current in steps of 20%

Another special non-linear effect in five-phase PMSM, which has been mentioned in the previous section, is the phase shift of the permanent magnet flux linkage in the first and third harmonic and the increase of the amplitude of the third harmonic flux linkage depending on saturation, which can be seen in simulation results in Fig. 2.

In Fig. 2 it can be seen, that the amplitude of the first harmonic almost remains constant between 0 and 200% of phase current. For further increase of the phase current the first harmonic decreases linearly. The phase shift of the first harmonic starts to increase until the machine is fully saturated. Much more significant are the changes of the third harmonic of the permanent magnet flux linkage. Here the phase shift increases to a much larger extent, than for the first harmonic. The maximum phase shift is reached at about the same current. The amplitude for the third harmonic permanent magnet flux linkage is negligible for the unsaturated motor, but it starts to increase significantly at $I = 120\%$. The maximum gradient of the third harmonic flux is reached at full saturation.

5.2. Torque improvement

Firstly the torque depending on the *d*- and *q*-current for the first harmonic is examined. In Fig. 3 it can be seen, that for constant *q*-current ($I_q = 150\%$ of rated current) a significant dependence on *d*-current can be observed. Closer examinations with the analytical model show, that the permanent magnet torque T_{PM} almost remains constant, while the reluctance torque T_{rel} considerably rises with negative *d*-current. The torque improvement by *d*-current reaches its maximum at about $i_d = 50\%$ of rated current. Simulation and measurement agree very well with each other.

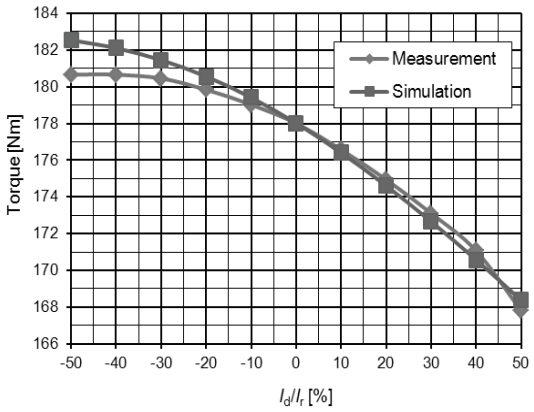

Fig. 3. Simulated and measured torque for $i_q = 150\%$ of rated current in dependence on i_d

In the following the torque output is simulated for i_q from 20 to 240% of rated current in steps of 20%. Furthermore for each value of i_q the effect of third harmonic current is examined and the optimal relation of i_{d3} and i_{q3} concerning torque and the efficiency are determined.

The TCHI is examined for different values of i_{q3} where low values turn out to be more effective because the third harmonic of the permanent magnet flux is rather small. For all

q-current values the efficiency and the torque slightly improve with THCI without $d3$-current. For each value of i_q and i_{q3} the $d3$-current is increased until the efficiency starts to decrease and the torque improvement ΔT compared to the same q-current without THCI is detected. These values of i_{d3} and ΔT are given in Fig. 4 exemplary for a constant $q3$-current (5%). In Fig. 4 it can be seen, that the THCI only has a considerable effect on torque improvement for higher saturation levels (about 1.3% related to the torque value with $i_{d3} = i_{q3} = 0$). But the required value for i_{d3} increases with the saturation level until $i_q = 220\%$ as the phase shift of the third harmonic of the magnet flux linkage increases. At $i_q = 200\%$ and higher, q-component of the flux component even overweighs the d-component. That means $d3$-current injection becomes more effective than $q3$-current injection. The measurements in Fig. 4 agree well with the simulations.

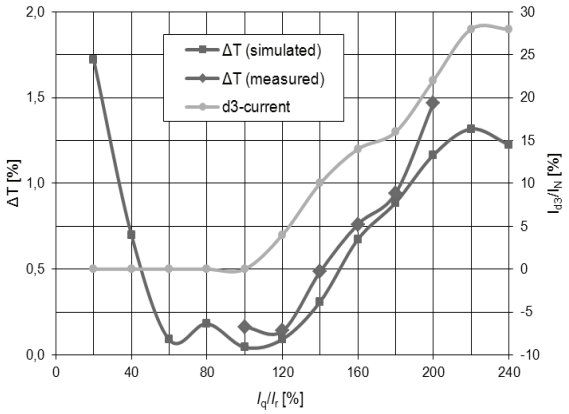

Fig. 4. Relative torque improvement ΔT (to $i_{d3} = i_{q3} = 0$) with $i_{q3} = 5\%$ (of rated current) and optimal value for i_{d3} (constant efficiency)

The dependence of efficiency and torque improvement on $d3$-current is shown more clearly in Fig. 5 and 6 for $I_q = 140\%$ and $I_q = 200\%$ with $I_{q3} = 5\%$. For both operation points the efficiency is increased by THCI. The efficiency for the operation without TCHI is given here as reference (blue line). Here it can be seen that for $I_q = 140\%$ the efficiency decreases at lower $d3$-currents below the reference efficiency than for higher currents ($I_q = 200\%$) and torque improvement is much lower.

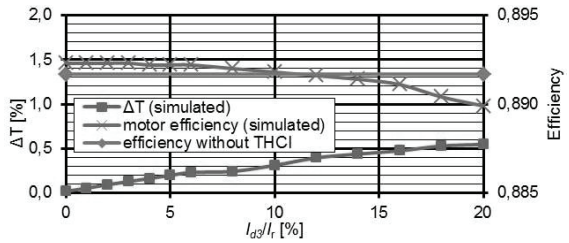

Fig. 5. Relative torque improvement ΔT (to $i_{d3} = i_{q3} = 0$) with $i_q = 140\%$ and $i_{q3} = 5\%$ (of rated current) and efficiency depending on i_{d3}

The torque generating effects are more closely observed in Fig. 7, where different from the *d*-current injection for the first harmonic, the permanent magnet torque has a much greater effect compared to the reluctance torque. This torque improvement is only weakened by reduction of the first harmonic of the permanent magnet flux linkage by increasing $d3$-current. The agreements with the measurement results are acceptable concerning the relatively low torque differences to be measured, the measurement tolerances and high interferences of the technical equipment despite good shielding. The measurements in Fig. 7 show that the motor efficiency and also the total efficiency of the drive system including the rectifier losses almost remain constant with third harmonic current injection in the investigated range of i_{d3}.

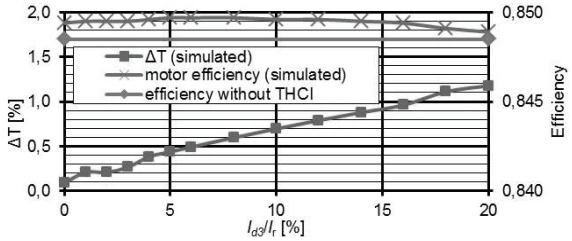

Fig. 6. Relative torque improvement ΔT (to $i_{d3} = i_{q3} = 0$) with $i_q = 200\%$ and $i_{q3} = 5\%$ (of rated current) and efficiency depending on i_{d3}

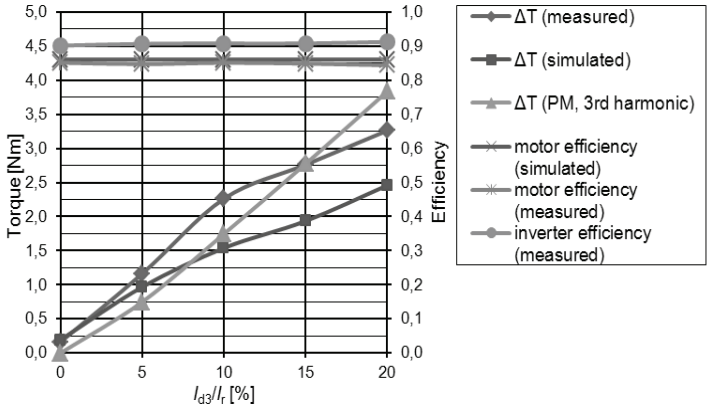

Fig. 7. Torque improvement ΔT, motor efficiency and inverter efficiency (simulation and measurement), torque by the third harmonic of the permanent magnet flux for $i_q = 200\%$ and $i_{q3} = 5\%$ depending on i_{d3}

6. Conclusions

In PMSM with conventional magnet shapes with low third harmonic content in the permanent magnet flux linkage, the effects of THCI with unsaturated electromagnetic circuit are negligible. But for higher saturation levels third harmonic linkage significantly rises and THCI can be very beneficial with consideration of the $q3$-component of the permanent magnet flux linkage. For high overload a higher efficiency in a motor and inverter can be reached.

Acknowledgements
This report is based on the project "EMiLE" which is funded by the German Federal Ministry of Education and Research under promotional reference number 16EMO0007. The authors are responsible for the contents of this publication.

References

[1] Wang K., Zhu A., *Torque Improvement of Five-Phase Surface-Mounted Permanent Magnet Machine Using Third-Order Harmonic*, IEEE Transactions on Energy Conversion, vol. 29, no. 3, pp. 735-747 (2014).
[2] Wang K., Lin D., Zhou P., Zhu Z. Q., Zhang S., *Analytical Determination of 3rd Order Harmonic Current into Five Phase PM Machine for Maximum Torque*, IEEE International Electric Machines & Drives Conference, Coeur d'Alene, ID, USA, pp. 630-636 (2015).
[3] Gallegos-Lopez G., *Methods, Systems and Apparatus for Opimization of Third Harmonic Current Injection in a Multi-Phase Machine*, US Patent, US 8,278,850 B2 (2012).
[4] Wettlaufer J., Borcherding H., Klute F., Jonsky T., *A Compact Servo Drive: Five Phase, Air Cooled, with Highly Integrated Inverter for Industrial Use*, 17th European Conference on Power Electronics and Applications, Geneva, Switzerland, pp. 1-10 (2015).
[5] Jonsky T., Stichweh H., Theßeling M. et al., *Modeling and Parameter Identification of Multiphase Permanent Magnet Synchronous Motors Including Saturation Effects*, 17th European Conference on Power Electronics and Applications, Geneva, Switzerland, pp. 1-10 (2015).

ARCHIVES OF ELECTRICAL ENGINEERING VOL. 66(1), pp. 189-198 (2017)

DOI 10.1515/aee-2017-0014

Thermal analysis of Double Stator Switched Reluctance Machine (DSSRM) with and without a squirrel cage rotor

MOHAMMADALI ABBASIAN[1], HADI JALALI[2]

[1]*Department of Electrical and Computer Engineering, Khorasgan Branch, Islamic Azad University*
P.O. Box 81595-158 Isfahan, Iran

[2]*Department of Electrical Engineering, Khomeinishahr Branch, Islamic Azad University*
P.O. Box 84175-119 Isfahan, Iran
e-mail: {m.abbasian / hadi.jalali}i@iaukhsh.ac.ir

(Received: 26.09.2016, revised: 18.11.2016)

Abstract: Double Stator Switched Reluctance Machine (DSSRM) is a novel switched reluctance machine with limited information about its heat distribution and dissipation. This paper presents a two dimensional (2-D) thermal analysis of Double Stator Switched Reluctance Machine (DSSRM) to observe actual heat distribution in the parts of the machine, using Finite Element Method (FEM). Two topologies for the rotor of DSSRM are considered, Non-Squirrel Cage Double Stator Switched Reluctance Machine (NSC-DSSRM) and Squirrel Cage Double Stator Switched Reluctance Machine (SC-DSSRM). The heat distribution of these two topologies is analyzed, using Computational Fluid Dynamics (CFD). Finally the results are presented and compared.

Key words: Computational Fluid Dynamics (CFD), Finite Element Method (FEM), squirrel cage, double stator, switched reluctance machine, thermal analysis

1. Introduction

The losses in electrical machines generate heat. As a result, temperature of the different parts of the machine rises [1]. It actually decreases the life time of the machine and may even lead to the machine failure [2]. Therefore, thermal modeling and analyzing, plays an important role in the optimal design of electrical machines.

Double Stator Switched Reluctance Machine (DSSRM) is a novel electrical machine with limited information about heat dissipation which makes thermal analysis an essential stage for its design. DSSRM is designed to perform at high torque levels. It is a good candidate for industrial applications operating under harsh environment because it carries the SRM qualities, combining them with the advantages of the double stator topology [3]. As shown in Fig. 1, this machine benefits from two stators which are made of laminated ferromagnetic material and

are equipped with concentrated windings. They are located on the interior and exterior of a cylindrical rotor. The rotor is formed by segments which are hold together using a non-ferromagnetic cage. The cross section of a 4-phase 8/6 DSSRM is illustrated in Figures 2 and 3.

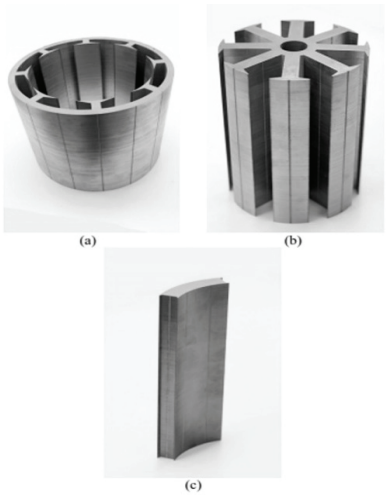

Fig. 1. Outer stator (a), inner stator (b), one rotor segment [7] (c)

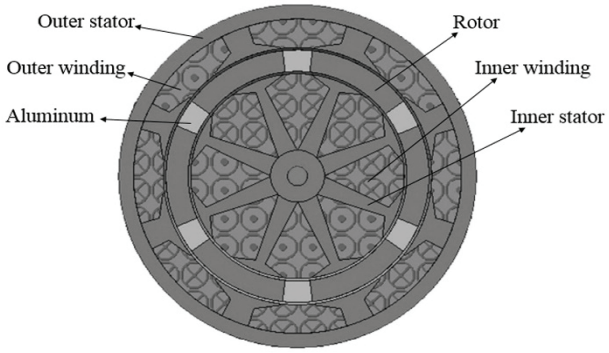

Fig. 2. Squirrel Cage Double Stator Switched Reluctance Machine (SC-DSSRM)

The inner stator of DSSRM is surrounded by the cylindrical rotor and it causes limitation for heat dissipation of the inner stator windings. So, it is necessary to consider the effect of rotor topology in the heat transfer of this machine.

There are two ways to connect the rotor to the output shaft of DSSRM. The first method is implementing a cage. In this method, the rotor segments are placed in a cage and the torque is transmitted to the output shaft by this cage. This topology is named: Squirrel Cage Double Stator Switched Reluctance Machine (SC-DSSRM).

In the second method, their rotor segments are connected together without any cage. In fact, there are two end-plates at either end of the rotor which keeps the rotor segments connected to the shaft. This topology is called: Non-Squirrel Cage Double Stator Switched Reluc-

tance Machine (NSC-DSSRM). Now the main question is that which of these two topologies is better in terms of heat transfer for DSSRM.

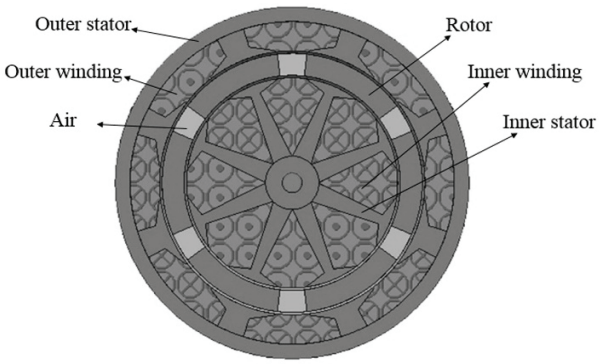

Fig. 3. Non-Squirrel Cage Double Stator Switched Reluctance Machine (NSC-DSSRM)

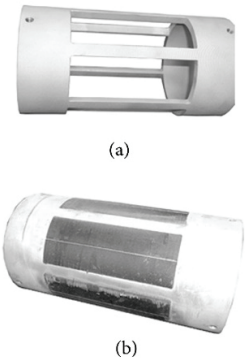

Fig. 4. Squirrel cage for the rotor of DSSRM (a), the rotor of SC-DSSRM (b)

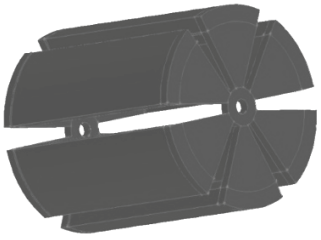

Fig. 5. Rotor of NSC-DSSRM

In [4], thermal modeling and analysis of a 10 kW DSSRM are presented and the temperature distribution in different parts of the machine (including the use of water as coolant) is calculated using FEM. In this paper the heat distribution of two different topologies of DSSRM is studied. The first topology is Non-Squirrel Cage Double Stator Switched Reluctance Machine (NSC-DSSRM) and the second one is Squirrel Cage Double Stator Switched Reluctance Machine (SC-DSSRM). The operation principle of NSC-DSSRM is similar to that of SC-DSSRM

(see Figs. 2-5). The only difference between these two machines is in the design of the rotor. Implementation of the cage in the rotor of DSSRM may influence the heat distribution of the machine, which is studied in this paper using Computational Fluid Dynamics (CFD) [5].

In order to have a more accurate model, a lumped parameter thermal model for DSSRM is proposed in which both modes of heat transfer, conduction and convection are considered. The geometrical model of DSSRM is built up as a parametric model and the simulation results obtained from CFD [6] are presented for an 8/6 DSSRM whose specifications are presented in Table 1.

2. Thermal analysis of Double Stator Switched Reluctance Machine

2.1. Geometrical model

A two dimensional (2-D) model of DSSRM used in this study is shown in Fig. 6. The machine parameters are given in Table 1. The model consists of two stators, one rotor, two stator windings and two airgaps. Drawing the geometrical model of the machine can be a time-consuming task, especially if various different designs have to be investigated. Therefore, the geometrical model is created as a parametric model and mesh generation is done.

2.2. Heat source

The two main components of electromagnetic losses in DSSRM are core losses in the laminations and copper losses in the windings. These losses are the heat source in a thermal analysis [8]. Core losses in DSSRM machine are relatively low, because it benefits from a short flux path. The copper loss and core loss for the different parts of DSSRM are calculated when the rotor speed is 1000 rpm and the phase current is 5 A. The result are presented in Table 2. Moreover, average torque and torque ripple, stator ampere-turn and efficiency at the operating point are mentioned in Table 2. The phase current waveform is assumed as illustrated in Fig. 12 (see Appendix)

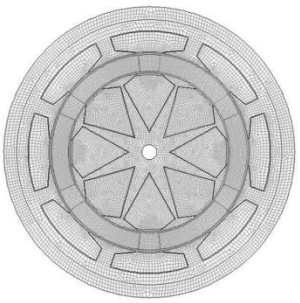

Fig. 6. 2-D Finite element model of DSSRM

In order to predict the temperature distribution in a stator and windings, the thermal analysis of DSSRM using FEM is proposed. Both natural and forced convection are considered for heat transfer through external surface of the machine. Heat transfer from the stator and

windings to an airgap is modeled by forced convection due to the rotation of the rotor. The thermal parameters used in the analysis are given in Table 3.

2.3. Winding model

It is well known that the majority of electrical machines with wound-wire windings have random wire disposition inside the slots, so it is not possible or desirable to model the position of each individual conductor when carrying out thermal analysis. One approach to simplify the model is to use the equivalent thermal conductivity of the system windings and insulation which can be obtained by various methods such as analytical approach, FEM or experiments. Using the numerical and analytical methods an equivalent thermal conductivity of 0.80 W/m/°C is considered for the windings in the proposed thermal analysis.

3. Simulation result analysis

Considering a value of 4 m/s for the air velocity over a frame, the forced convection coefficient over this surface is 30 W/m^2°C. It is noted that since the convection coefficients are rather low, heat transfer by radiation might be important when only natural convection for the external surfaces of the machine is considered in the thermal analysis. For example, it is 30 W/m^2°C, when the air velocity is 4 m/s. When the inside air temperature rise obtained for h = 30 W/m^2 C is considered in the 2-D thermal analysis of the 8/6 DSSRM. For all thermal simulation results in the following external surface of the motor (frame) is 30 W/m^2°C.

The ambient temperature is set as 20°C and thermal analysis was carried out. In the thermal analysis, the temperature increases and reaches the maximum temperature of 65.62°C, at 1000 rpm. The different boundary conditions are shown in Fig. 7. The numeric solution for the thermal analysis is obtained over 140 hours using 8 processors on a Linux cluster with 2.2 GHz. In [10] the thermal analysis of DSSRM is presented in details.

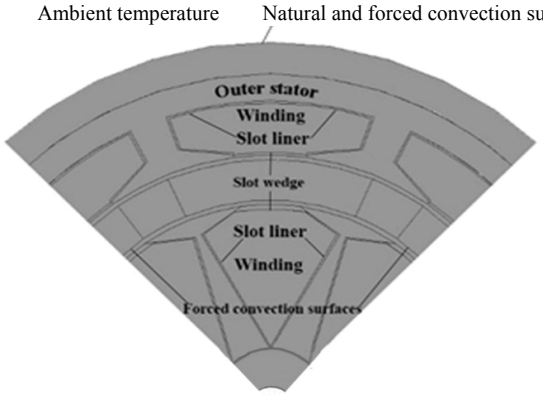

Fig. 7. Machine geometrical model in thermal analysis and different types of boundary conditions

3.1. Analysis result of Squirrel Cage DSSRM (SC-DSSRM)

Figures 8 and Fig. 9 represent the results of thermal analysis of SC-DSSRM. Figure 8 illustrates temperature distribution in the machine and Fig. 9 represents the temperature rise in

different parts of the machine at 1000 rpm and 5 A. It is clear that the maximum temperature of 65.5°C occurs in the inner windings.

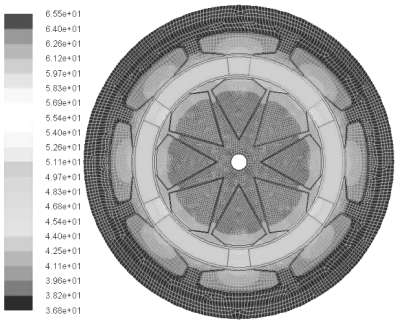

Fig. 8. Temperature distribution at 1000 rpm for SC-DSSRM

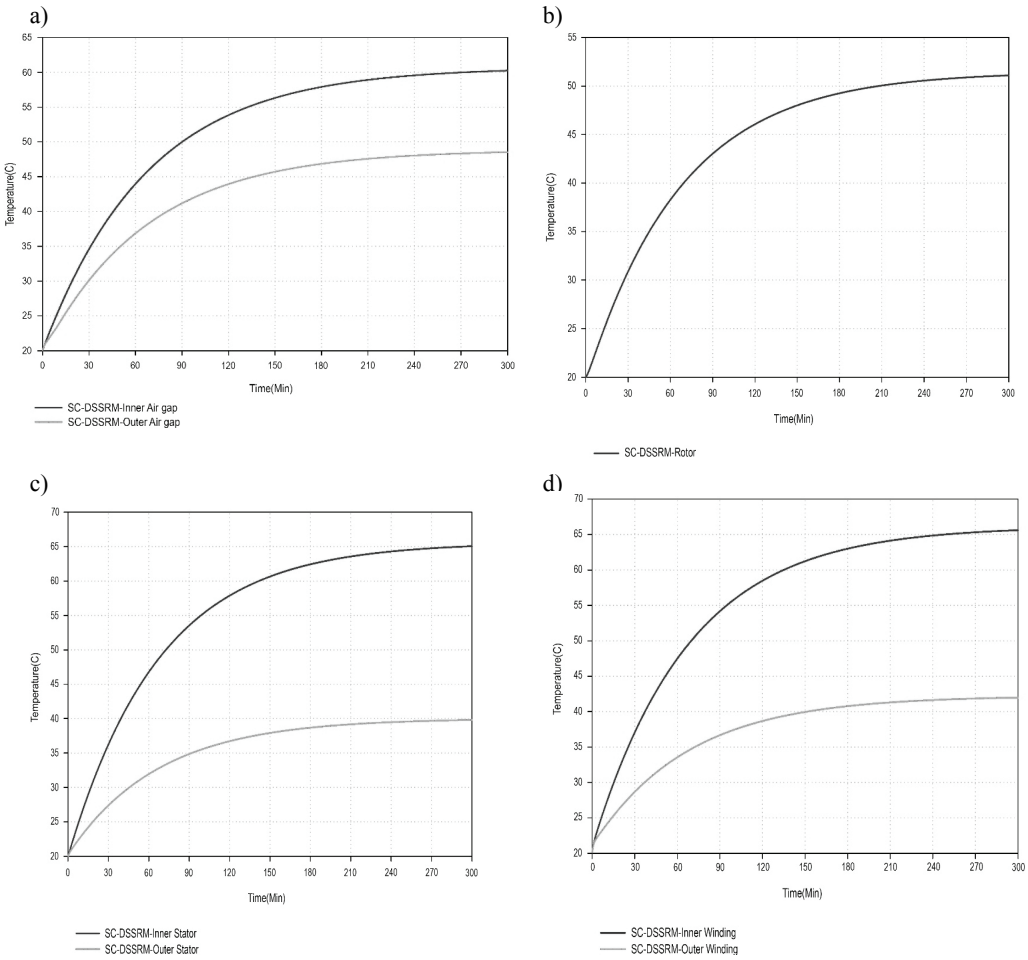

Fig. 9. Temperature-time curve for SC-DSSRM: air gaps (a), rotor (b), stators (c), windings (d)

3.2. Analysis result of Non-Squirrel Cage DSSRM (NSC-DSSRM)

Figures 10 and 11 represent the results of thermal analysis of SC-DSSRM. Figure 10 illustrates temperature distribution in the machine at 1000 rpm and 5 A. Fig. 11 shows the temperature rise in different parts of the machine. It is clear that the maximum temperature of 69.5°C occurs in the inner windings.

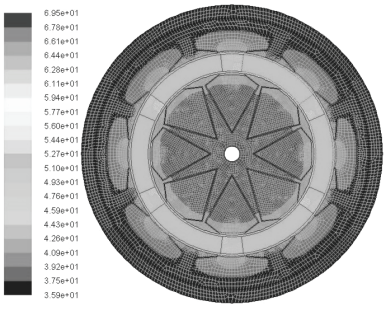

Fig. 10. Temperature distribution at 1000 rpm for NSC-DSSRM

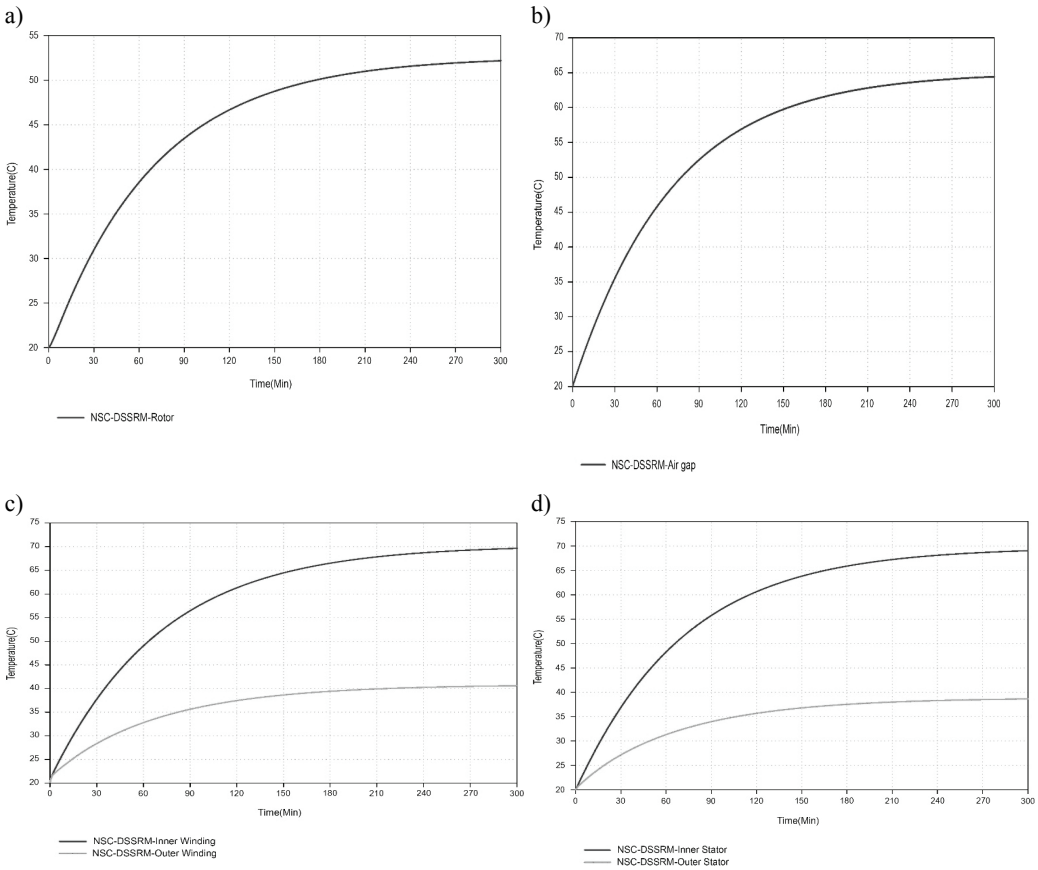

Fig. 11. Temperature-time curve for NSC-DSSRM: air gap (a), rotor (b), stators (c), windings (d)

4. Conclusion

In this paper, the thermal analysis of Double Stator Switched Reluctance Machine (DSSRM) was done, using Finite Element Method (FEM). Two topologies for the rotor of DSSRM were considered: Non-Squirrel Cage Double Stator Switched Reluctance Machine (NSC-DSSRM) and Squirrel Cage Double Stator Switched Reluctance Machine (SC-DSSRM). The heat distribution of these two topologies was analyzed, using Computational Fluid Dynamics (CFD). It was shown that the temperature rise in SC-DSSRM is less, compared to NSC-DSSRM. It can be concluded that the aluminum cage plays an important role in heat transfer of the inner stator winding.

Appendix

Table 1. Specifications of 8/6 DSSRM [3]

No. of phases	4
No. of stator/rotor poles	8/6
Outer radius of outer stator [mm]	72.0
Outer radius of inner stator [mm]	43.9
Rotor segment thickness [mm]	9.0
Airgap	1.0
Stack length [mm]	115.0
Arc of the rotor [deg.]	47
Turns per coil	50
Resistance @ 20°C [Ω]	0.78
Rated speed of motor [rpm]	1000

Table 2. Operating point characteristics of DSSRM

Stator ampere-turn	750
Avarage torque	4.76 Nm
Torque ripple	1.29 Nm
Speed	1000 rpm
Outer stator copper loss	10.21 W
Inner stator copper loss	9.82 W
Outer stator core loss	3.76 W
Inner stator core loss	3.43 W
Rotor core loss	2.21 W
Rotor cage loss	9.63 W
Efficiency (NSC-DSSRM)	94.41%
Efficiency (SC-DSSRM)	92.71%

Table 3. Thermal parameters [9]

	Thermal conductivity (w/m/°C)	**Specific heat (J/kg/°C)**	**Density (kg/m^3)**
Stator lamination (iron)	20	438	7650
Copper	401	385	8933
Slot liner	0.076	1172	2150
Air	0.0263	1007	1.16
Frame (aluminum)	177	875	2770
Slot wedge	0.29	1172	2150

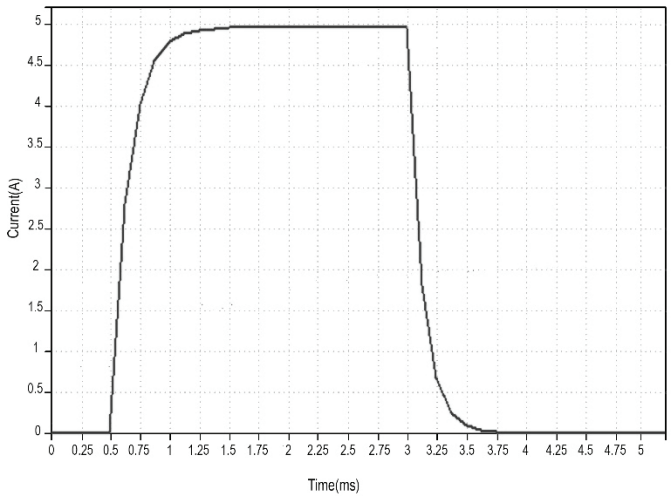

Fig. 12. Phase current waveform of DSSRM

Refrences

[1] Stone G.C., Culbert I., Edward A., *Boulter and Hussein Dhirani, Electrical Insulation for Rotating Machines Design, Evaluation, Aging, Testing and Repair*, Wiley (2004).

[2] Faiz J., Dadgari A., *Heat distribution and thermal calculations for a switched reluctance motor*, Journal of Electrical and Electronics Engineering, Australia, IE Australia & IREE Australia, vol. 12, no (4),pp. 349-361(1992).

[3] Abbasian M., Moallem M., Fahimi B., *Double Stator Switched Reluctance Machines (DSSRM): Fundamentals and Magnetic Force Analysis*, IEEE Transaction on Energy Conversion, vol. 25, no. 3, pp. 589-597 (2010).

[4] Arbab N., Wang W., Lin C., Hearron J., Fahimi B., *Thermal Modeling and Analysis of a Double-Stator Switched Reluctance Motor*, IEEE Transaction on Energy Conversion, vol. 30, no. 3, pp. 1209-1217 (2015).

[5] Anderson J.D. Jr., *Computational Fluid Dynamics*, McGraw-Hill International Editions (1995).

[6] Wood S.E., Greenwood D., *Force ventilated motors advantages in fixed variable speed application*, Proceedings of 5th IECON, pp. 276-280 (1991).

[7] Lin C., Wang W., Fahimi B., *Optimal Design of Double Stator Switched Reluctance Machine (DSSRM)*, Industrial Electronics (ISIE) (2012).
[8] Trigeol J.F., Bertin Y., Lagonotte P., *Coupling control volume modeling in fluid and lumped thermal model-Application to an inductionmachine*, Proceedings of 6th IECON, pp. 4829-4834 (2006).
[9] Incropera F., DeWitt D., *Fundamentals of Heat and Mass Transfer*. New York: Wiley, (1990).
[10] Abbasian M., Jalali H., *Temperature Distribution Analysis of Double Stator Switched Reluctance Machine Using Finite Element Method,* Electrical Machines & Power Electronics (ACEMP), Int. Conference on Optimization of Electrical & Electronic Equipment (OPTIM) & Int. Symposium on Advanced Electromechanical Motion Systems (ELECTROMOTION), Int. Aegean Conference on Electrical Machines & Power Electronics, Ankara, Turkey (2015).

ARCHIVES OF ELECTRICAL ENGINEERING VOL. 66(1), pp. 199-206 (2017)

DOI 10.1515/aee-2017-0015

Asynchronous slip-ring motor synchronized with permanent magnets

TADEUSZ GLINKA, JAKUB BERNATT

Institute of Electrical Drives & Machines KOMEL
188 Rodzieńskiego Ave., 40-203 Katowice, Poland
e-mail: glinka.tadeusz@gmail.com, dyrekcja@komel.katowice.pl

(Received: 16.09.2016, revised: 16.01.2017)

Abstract: The electric LSPMSM motor presented in the paper differs from standard induction motor by rotor design. The insulated start-up winding is located in slots along the rotor circumference. The winding ends are connected to the slip-rings. The rotor core contains permanent magnets. The electromechanical characteristics for synchronous operation were calculated, as were the start-up characteristics for operation with a short-circuited rotor winding. Two model motors were used for the calculations, the V-shaped Permanent Magnet (VPM) – Fig. 3, and the Linear Permanent Magnet (IPM) – Fig. 4, both rated at 14.5 kW. The advantages of the investigated motor are demonstrated in the conclusions.

Key words: motor with permanent magnets, slip-ring rotor winding, asynchronous start

1. Introduction

Synchronized asynchronous motors (SAS) are slip-ring induction motors characterized by the fact that after asynchronous starting they are excited with direct current and can self-synchronize with the power network. The SAS motors are most often used in high power electrical drives. Starting of the motor is achieved by means of a rheostat connected to the rotor circuit via slip-rings and brushes. The start-up current does not usually exceed the double value of the rated current, and the perturbation (transient) current, at the first time instant after connecting the motor to the network does not exceed $4I_N$. The start-up torque can be significantly higher than the rated torque. After start-up the rotor winding is supplied with the direct current and the motor self-synchronizes. After synchronization it operates as a synchronous motor. The SAS motors exhibit the advantages of both induction slip-ring motors and synchronous motors.

When the induction slip-ring motors are compared to squirrel-cage induction motors, it is observed that they are characterized by smooth start-up, the current and torque surges are not as high as in the squirrel-cage motors. The rheostat greatly decreases the start-up current and is also helpful in shaping the torque versus speed curve. During steady-state operation, the

SAS motor exhibits higher efficiency than the induction motor, its power factor is capacitative and $\cos\varphi \leq 1$. The negative feature of the SAS motor is the excitation circuit. Power losses in the excitation circuit result in decreased overall drive efficiency; the rings require periodical inspection and maintenance (cleaning), the brushes wear out and must be replaced from time to time.

The designs of motors with a cage rotor winding and permanent magnets built into a rotor core are known [2, 5, 6]. The cage winding is made up of copper bars placed in slots along the outer rotor circumference; at the coil outhangs the bars are short-circuited with the rings. The permanent magnets are placed in grooves in the interior of the rotor core. The cage winding is used for asynchronous start-up. When near-synchronous speed is attained during starting, the magnetic flux of the permanent magnets tends to self-synchronize the motor, which means that the motor speed increases and arrives at synchronous speed. During synchronous operation this type of motor, in comparison to a standard induction motor working in an identical system, has higher efficiency and its power factor $\cos\varphi \approx 1$. This is a very great advantage, since this is an energy-saving design as opposed to the induction motor.

The disadvantages of cage induction motors synchronized with the magnetic field of permanent magnets may be listed as [3]:

- high start-up current; the steady-state component is *c*. 7 times higher than rated current, and the surge component is *c*. 1.8 times higher than the steady-state component,
- during the start-up heat is generated in the rotor cage; its amount is approximately equal to the kinetic energy of all rotating masses coupled with the motor shaft. This heat causes an increase in the cage rotor temperature and gives rise to possible hazard of thermal demagnetization of permanent magnets (this is particularly dangerous in case of repeated/frequent/start-ups),
- electromagnetic resultant torque, generated by the cage winding and permanent magnets, in the range of speeds from 0 to about half the rated speed ($0 \leq n \approx 0.5n_N$) may be less than motor's rated torque.

The motors with the cage winding and permanent magnets play their role in the drives of mechanical devices and machines with small start-up loads and short start-up times [2, 5]. These conditions are fulfilled by pumps and fans, where the load torque is proportional to the quadratic function of the speed. However, lots of driven machines are characterized by high start-up torque or long start-up time. High load torques, frequently greater than the rated torque, are present in: belt conveyors with belts fully loaded, filled coal pulverizers in power plants, thermal power plants and copper ore preparation plants, traction vehicles. Examples of mechanical devices and machines with high moments of inertia and started under load, characterized by long start-up times, are coal mine shaft fans, forced draft and induced draft fans in power plants and thermal power plants, loaded belt conveyors. The use of the cage induction motors with permanent magnets in rotors in the drives mentioned above is not recommended, since starting may be impeded, in particular in grids with high short-circuit reactance, and the permanent magnets may be exposed to the hazard of thermal de-magnetization, e.g. in the case of frequent start-ups.

2. Rotor design

The stator of the discussed electric motor, i.e. a core and winding, is identical as in an induction motor. The rotor is equipped with the winding wounded into slots and permanent magnets located in the steel yoke [1]. The rotor's winding is three-phase, made of insulated copper wire and connected into star or delta arrangement. Ends of phases are connected to three-slip rings located at the rotor shaft.

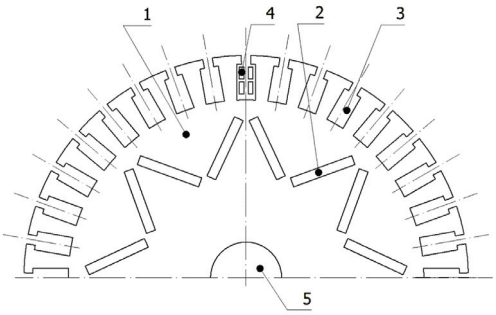

Fig. 1. Cross-section of the VPM motor rotor core with V-shape permanent magnets [1]

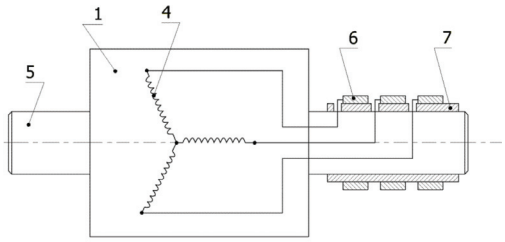

Fig. 2. Star arrangement of the rotor winding, winding ends are connected to slip-rings [1]

The brush holder together with the brush lifting device is attached to the bearing plate of the motor. The design of a slip-ring rotor with the winding and permanent magnets is shown in Figs. 1 and 2. The motor's rotor is laminated, and lamination stack placed at the motor shaft 5 constitutes core 1. Core 1 is grooved (the slits are usually rectangular in shape) and permanent magnets 2 are placed there. In the rotor lamination sheet shown in Fig. 1 the permanent magnets are positioned in the shape of letter "V". The permanent magnets' grooves may also be cut differently. Winding 4 is placed in slots cut into outer circumference of core 1. The winding 4 is three-phase, made of insulated copper wire and connected into delta or star arrangement. The ends of winding 4 are connected to three slip-rings 6, located at insulation sleeve 7, which is positioned at the rotor shaft 5. The wires connecting winding ends 4 with slip-rings 6 may be laid on the surface of shaft 5 or inside the hollowed-out shaft 5. When the motor is assembled, the brushes touch the slip-rings 6. Brushes are copper-graphite type and placed in the brush holder. The brush holder together with the brush lifting device is attached to the bearing plate of the motor.

3. Synchronous characteristics of model motor

The model motor has been designed using laminations of a slip-ring induction motor rated at 14.5 kW, 400 V, 28.6 A, 50 Hz, 1430 rpm, 96.83 N · m, $\cos\varphi = 0.84$. Electromechanical characteristics of two variants of placement of permanent magnets inside the rotor were calculated. The outer/inner diameters of laminations are: stator 246/162 mm and rotor 161/66 mm, core length 194 mm. The slots are trapezoidal in the straight part, and upper and lower parts are shaped as circle arcs. The number of stator slots is 36 and the number of rotor slots is 24. Two variants of magnetic circuit design have been calculated: with V-shape permanent magnets (VPM rotor) and linear magnets "I" (IPM rotor). NdFeB magnets were used: material N42UH, at working temperature 120°C, $B_r = 1.16$ T; $H_{cB} = 848$ kA/m; $\mu = 1.085$. The magnets dimensions are: "V" magnets – 22.85×6 mm and "I" magnets – 51.6×6 mm. The calculations of magnetic flux density distributio in the magnetic circuit of the machine excited by permanent magnets were conducted by a field method, for rotational speed $n = 0$, and current $I = 0$. The results of the calculations are shown in Figs. 3 and 4.

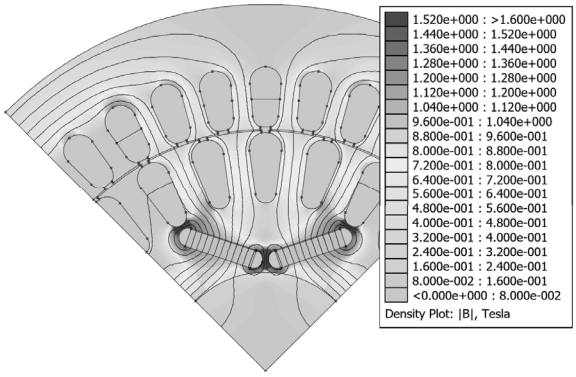

Fig. 3. Distribution of magnetic field in the magnetic circuit of motor excited with V-shape permanent magnets

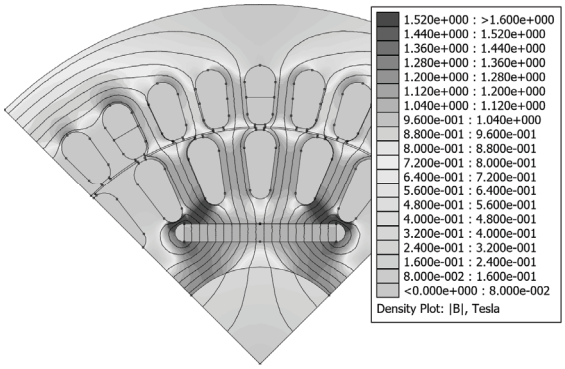

Fig. 4. Distribution of magnetic field in the magnetic circuit of motor excited with linear permanent magnets "I"

Using the magnetic field distributions, the calculations of characteristics for synchronous operation of the motor were performed. The calculations were performed using the circuital method with assumptions:

- slots in the stator of the model motor are straight; in the rotor a skewed slot is equal to one slot pitch,
- data for a stator winding were set the same as for the slip-ring induction motor with the rated data given above,
- supply voltage: 3×400 V,
- steady-state operation.

The synchronous electromechanical characteristics: torque (T_{el}), current (I_{pf}), power factor (cosφ) and efficiency versus angle between magnetomotive force (MMF) of permanent magnets and MMF of the stator winding are shown in Figs. 5 and 6.

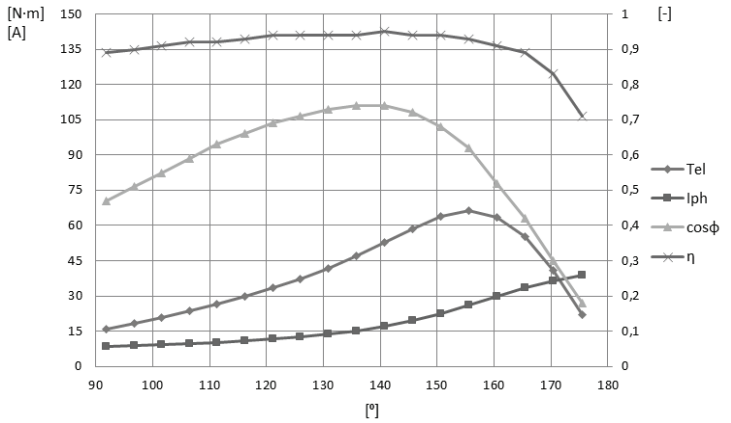

Fig. 5. The electromechanical characteristics of "V" motor: torque (T_{el}), current (I_{ph}), power factor (cosφ) and efficiency (η) versus angle between MMF of permanent magnets and MMF of stator winding

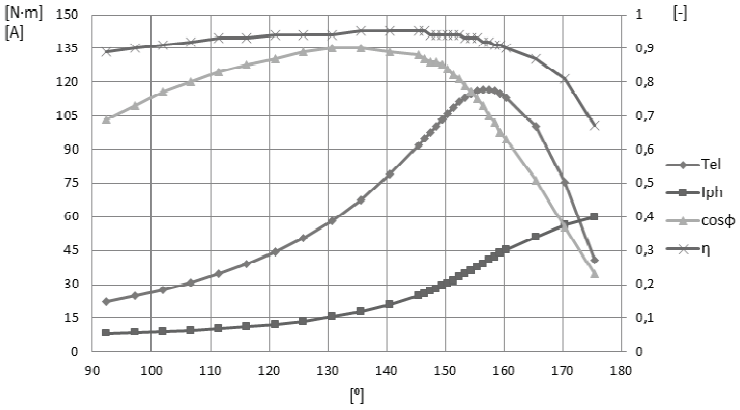

Fig. 6. The electromechanical characteristics of "I" motor: torque (T_{el}), current (I_{ph}), power factor (cosφ) and efficiency (η) versus angle between MMF of permanent magnets and MMF of stator winding

The maximum synchronous torque determines practical use of the motor. The maximal torque of the motor with the VPM rotor is 66 N · m, and in the case of the IPM rotor, the maximal torque is 117 N · m. This means the torque is 56% higher for the IPM motor and 18% higher than the nominal torque of the induction motor. The efficiency of the motor at the maximum torque, in both designs is equal to approximately 93%; power factor cosφ for the VPM motor is 0.64, and for the IPM motor is 0.7.

4. Asynchronous torque of the model motor

The start-up of the motor determines its practical use as a synchronous motor.

During the start-up the magnetic flux generated by permanent magnets during the start-up induces voltage in a stator winding; frequency of the voltage is equal to electrical frequency of rotation $f_2 = n/60p_b$. The current flowing through an armature winding is composed of two components: network component I_1 of f_1 frequency and component I_2 of f_2 frequency. The current component I_1 generates asynchronous torque which determines the motor's start-up, while current component I_2 generates synchronous torque, which varies in accordance with speed during the start-up and impedes the start-up process.

The averaged characteristics of asynchronous torque generated by a short-circuited rotor winding and braking torque caused by permanent magnets were calculated for the model motor. The resultant (averaged) asynchronous starting torque of the model motor was calculated as superposition of the torque mentioned above. The calculations were conducted using the Maxwell software. The results of the calculations are shown in Figs. 7 and 8.

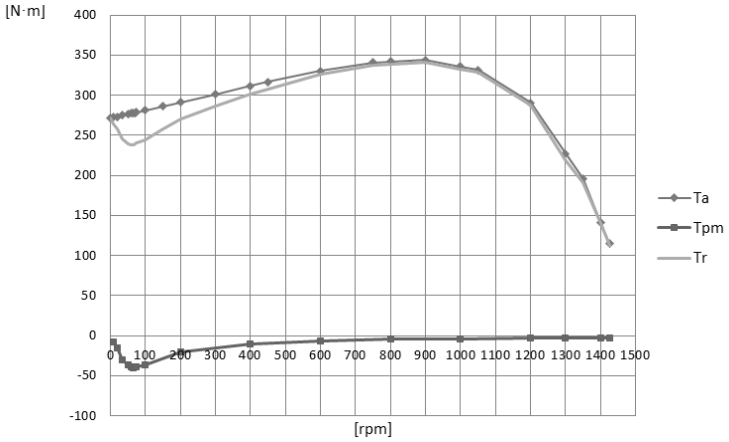

Fig. 7. Torque versus speed curves for "V" motor: asynchronous torque (T_a), braking torque (T_{pm}), resultant (total) torque (T_r)

The start-up of the induction slip-ring motor is carried out using starting resistors that adapt the asynchronous torque-speed curve of the motor to the start-up demands of the load machine. The success of the start-up thus is determined by the maximum torque.

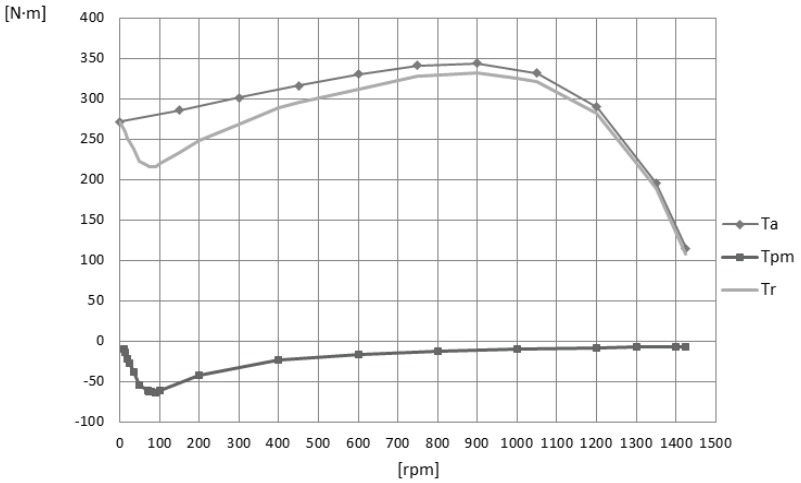

Fig. 8. Torque versus speed curves for "I" motor: asynchronous torque (T_a), braking torque (T_{pm}), resultant (total) torque (T_r)

Figures 7 and 8 show that in the both embodiments of the rotors (VPM and IPM) the maximum torque is about 340 N m, and it is 2.9 times higher, then the maximum torque of synchronous motor type "I". Therefore, there is no danger that the motor will not start.

5. Conclusions

The electric motor excited with permanent magnets and with a slip-ring start-up winding shows improved start-up features in comparison to squirrel-cage induction motors synchronized with permanent magnets, such as:

- the motor start-up is smooth, since a rheostat is used and the start-up current and start-up torque may be set by controlling the value of connected resistance in accordance with the rotational speed; there is no danger of motor stopping in the middle of the start-up,
- the start-up torque in the whole rotational speed range may be significantly greater than the rated torque, since it is appropriately adjusted with the resistance of the rheostat,
- the start-up current usually does not exceed the doubled value of the rated current; the perturbation (transient) current, at the first instant after connecting the motor to the network, does not exceed $4I_N$,
- the torque surge occurring after switching the motor on is proportional to the square of the perturbation (transient) current and is several times less than in the induction cage motor,
- the heat generated during the start-up of the motor driving load machine is generated and dissipated for the most part in the rheostat rather than in the rotor winding, so that there is no danger of overheating the permanent magnets, even in the case of repeated (frequent) start-ups,

- motor may be used for driving machines started under load and with long start-up times,
- the motor with a starting ring winding is more expensive than the motor with a squirrel-cage rotor.

After the start-up, the motor self-synchronizes and operates as a synchronous motor excited with the magnetic field of permanent magnets. After synchronization the brushes contacting the slip-rings may be short-circuited or lifted. It is better to lift the brushes, since brushes and slip-rings do not then wear down; friction is absent and no additional power losses are generated. This type of motor may be used for any type of electrical drive.

If we compare the asynchronous and synchronous characteristics of motor designs "V" and "I", it may be observed that their shapes depend on the rotor construction and the placement of permanent magnets in the rotor core. For each investigated motor design a proper design of a rotor winding and the placement of permanent magnets in a rotor core must be selected, taking into account the criteria of maximum synchronous torque and maximum asynchronous torque. In the case of the discussed model motor, the motor with "I" rotor is characterized by the maximum synchronous torque higher by *c*. 56% with respect to the motor with "V" rotor.

References

[1] Bernatt J., Gawron S., Glinka T. et al., *Rotor of electric motor with permanent magnets,* (in Polish), Polish patent application, P.415273 (2015).
[2] Rossa R., *Reluctance motor with additional permanent magnets excitation,* (in Polish), PhD Thesis, Department of Electrical Machines and Devices, Silesian University of Technology, Gliwice (2006).
[3] Zawilak T., *Utilizing the deep bar effect in direct on start of permanent magnet machines*, Przegląd Elektrotechniczny, vol. 2013, no. 2b, pp. 177-179 (2013).
[4] Zawilak T., Zawilak J., *Line start permanent magnet synchronous motor in ball mill application,* (in Polish), Maszyny Elektryczne – Zeszyty Problemowe, vol. 2016, no. 3, pp. 169-173 (2016).
[5] Ogbuka C., Nwosu C., Agu M., *Dynamic and steady state performance comparison of line-start permanent magnet synchronous motors with interior and surface rotor magnets*, Archives of Electrical Engineering, volume 65, issue 1, pp. 105-116, ISSN (online) 2300-2506, March 2016, DOI: 10.1515/aee-2016-0008
[6] Khazdozian H.A., Jiles D.C., Hadimani R.L., *Magnetic flux focusing for generator designs*, Magnetic Technology International, pp. 24-28, ISSN (print) 2047-0509 (2017).

ARCHIVES OF ELECTRICAL ENGINEERING VOL. 66(1), pp. 207-221 (2017)

DOI 10.1515/aee-2017-0016

Problems related to balancing peak power on the example of the Polish National Power System

HENRYK MAJCHRZAK

Opole University of Technology
ul. Prószkowska, 45-758 Opole
e-mail: henryk.majchrzak13@gmail.com

(Received: 16.08.2016, revised: 17.01.2017)

Abstract: The article discusses issues related to ensuring secure operation of the National Power System. The tasks of transmission system operators in that scope were presented and the power demand of the Polish National Power System on critical days in terms of power generation and demand was characterized. The article also presents the causes and course of events which took place in August 2015 when there was a critical imbalance in the Polish National Power System leading to the introduction of limitations. Then, the possibilities and types of costs connected with the possibilities of balancing the system in the periods of peak loads were characterized. The summary of the article contains the presentation of conclusions related to power balancing in the power system and reduction of related costs.

Key words: cost of energy deliver failure, peak demand of system, system services, power grids

1. Tasks of transmission system operators in the scope of power balancing

One of the basic tasks of transmission system operators (TSOs) is to ensure secure operation of power systems (PSs) managed by them. For this purpose, TSOs undertake a number of actions, including e.g.:

a) the preparation of periodic (current, daily, monthly, annual) coordination plans,
b) the provision of transmission capacities for the cross-border commercial exchange,
c) the conclusion of agreements in the scope of system services for power balancing,
d) the acquisition of cold intervention reserve services, availability of capacities of generating units that are not subject to the central management carried out by TSOs,
e) the conclusion of agreements for demand reduction services at the request of TSOs,
f) the conclusion of agreements with operators from neighboring countries, including agreements for emergency power supplies,
g) the preparation of procedures in case of threats to secure operation of PSs.

Apart from TSOs, entities participating in the performance of the above-mentioned activities are generators, customers and electricity distribution system operators (DSOs) with devices, installations or networks connected directly to the closed grid. TSOs and DSOs operating in the hierarchical order as well as dispatch operation services of the power plants and customers ensure secure operation of the power system. The cooperation between TSOs and transmission system operators from neighboring countries in the scope of the current operation of the grid takes place in accordance with the principles described in the Continental Europe Operation Handbook, i.e. in the document of ENTSO-E, the organization of TSOs from the Continental Europe [1] and the terms and conditions provided in bilateral agreements.

Coordination planning conducted in cooperation with other users of the system is the basic tool used by TSOs to ensure the coherence of activities undertaken by entities participating in the current operation of the grid with safety requirements of the power system. Power balances of the power system presenting its generating capacities, power demand and power surplus necessary for obtaining the required operating reserve as well as the amount of power possible to be provided for the purposes of the cross-border exchange with neighboring PSs, is the basic element of coordination plans. The provision of transmission capacities for the purposes of the cross-border interconnection exchange is an important element affecting the possibilities of covering customers' demands for power and electricity.

The basic task of the Polish TSO – the entity responsible for ensuring secure operation of the Polish National Power System (PNPS) is to balance power. The control of the sufficiency of national generation resources to cover the power demand is provided by power balances prepared by the Polish TSO for different time horizons. They include expected national demand, scheduled power outages and transmission capacities available for the cross-border commercial exchange.

Annual and monthly balances are prepared to determine power surplus available to TSOs for daily peak power demand on working days respectively for specific months of the next year and days of the next month. Daily and current balances are more detailed due to the fact that they are prepared using the Load Distribution Algorithm and based on the commercial and technical data contained in balancing offers, taking system limitations and necessary operating capacity reserve of a given system as well as balances of foreign trade into account.

Coordination plans, apart from the part related to the power balance, also contain shutdown plans for particular components of the closed grid which are prepared, taking overhauls of generating units connected to this grid into consideration. TSOs also identify transmission limitations arising out of applicable criteria for reliable operation of the system and specify the resulting requirements related to the minimum and maximum possible number of generating units in specific nodes of the grid for the entire period covered by the plan.

Detailed arrangements concerning power balancing in the PS are included in internal procedures of the TSO in the form of planning and dispatching instructions. They specify, for instance, resources and the order in which such resources are used for ongoing balancing of the system. The sufficiency of generation capacities occurring in the area of this TSO to cover the demand is of essential importance for the secure operation of the PS in the adopted planing prospects. The criteria for the assessment of the sufficiency of generation capacities in the

Polish National Power System are defined in the Instruction of Transmission System Operation and Maintenance (Instrukcja Ruchu i Eksploatacji Sieci Przesyłowej, IRiESP) [2]. Pursuant to this document, the required power surplus available to the Polish TSO in relation to the demand to be covered by national power plants, i.e. taking the balance of exchanged power into account, should amount to at least 18% of the planned demand to be covered by national power plant for the annual planning horizon, 17% for the monthly planning horizon and not less than 9% for the daily planning horizon.

The requirements in the scope of the management of minimum capacity reserves applicable in the area of ENTSO-E were defined in the documents of this organization applicable in this respect.

2. Characteristics of the power demand in the PNPS

The analysis of the power demand in power systems shows that this demand is different at each hour of the day as well as on each day and in each month of the year. This variability results from the needs of electricity customers which, in turn, depend on a number of other factors, including economic factors such as: conditions of their functioning in the economy of a given country and conditions connected with the time of the year, the day of the week (working days, weekends, bank holidays) and the time of the day (night, intermediate loads, peak loads).

In order to illustrate this phenomenon, Figs. 1-3 present the most important data concerning the variability of the demand in the PNPS in 2014 prepared on the basis of data published in annual reports on the functioning of the PNPS [11] by PSE S.A., performing the role of Polish TSO. Fig. 1 presents the daily demand in the PNPS on days when there was the minimum and maximum power demand.

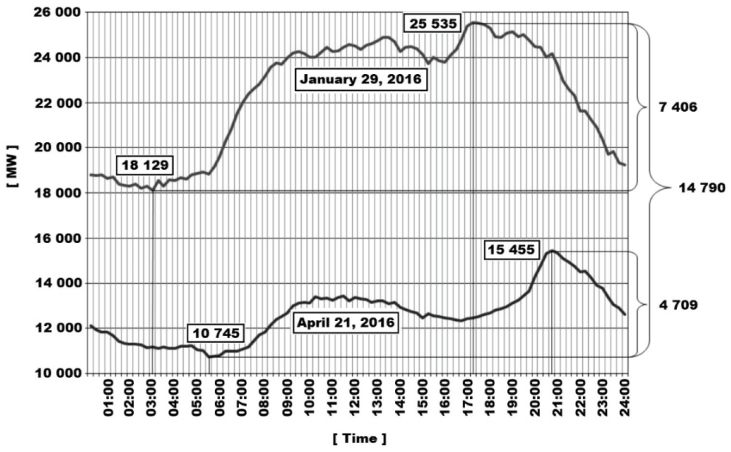

Fig. 1. Power demand on days when there was the minimum and maximum national power demand in the PNPS in 2014

During this period, the maximum power demand in the PNPS occurred on 29 January and amounted to 25 535 MW. The minimum national power demand occurred on 21 April and amounted to 10 745 MW. The difference between the maximum and minimum power demand in the analysed period was 14 790 MW, i.e. approx. 57.9% of the peak demand. The high variability of the power demand was also observed at specific hours of the day. On the day on which the maximum power demand was recorded it changed from 18 129 MW to 25 535 MW. On the day on which the minimum power demand in 2014 was recorded it fluctuated from 10 745 MW to 15 455 MW.

Figs. 2 and 3 present the partial coverage of power demand on days when there was the maximum and minimum power demand in 2014. The demand for power on 29 January 2014 was covered by the generation of electricity in lignite-fired power plants ranging from 5 136 MWh to 7 851 MWh, the generation of electricity in coal-fired utility power plants ranging from 9 938 MWh to 13 510 MWh and the generation of electricity in industrial power plants which was quite stable at all times of the day and which was maintained at the level of approx. 1 300 MWh. Hydro and gas-fired power plants also participated in meeting the power demand - electricity generated by small hydro power plants was low and amounted to approx. 80 MWh on average, and electricity generated by gas-fired power plants amounted to approx. 430 MWh. Electricity generated by wind farms or other renewable energy sources amounted to approx. 2 000 MWh on average. Pumped-storage power plants were started to supply additional electricity during the morning and evening load peak.

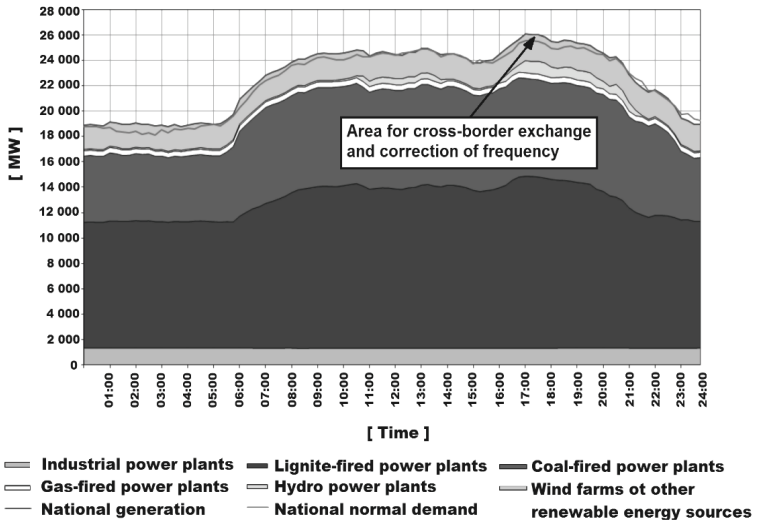

Fig. 2. Power demand in the PNPS on the day on which the maximum national power demand in 2014 was recorded and ways of meeting this demand

On 21 April 2014, electricity generated in industrial power plants was quite stable at all times of the day and amounted to approx. 970 MWh. Electricity generated in lignite-fired utility power plants fluctuated from 3 330 MWh to 5 375 MWh, and in coal-fired utility power

plants from 5 501 MWh to 6 480 MWh. Small hydro power plants generating approx. 100 MWh on average, gas-fired power plants generating approx. 330 MWh and pumped-storage power plants working at the time of peak demand supported the power balance of the PNPS. The total electricity generated by wind farms and other renewable energy sources amounted to approx. 600 MWh per hour on average.

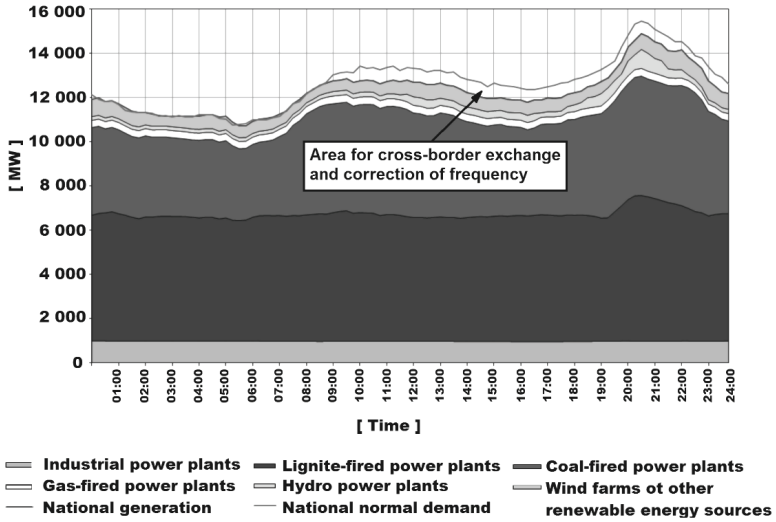

Fig. 3. Power demand in the PNPS on the day on which the minimum national demand in 2014 was recorded and ways of meeting this demand

3. Introduction of limitations of the supply and consumption of electricity in the PNPS in August 2015

In the operational practice concerning issues related to power balancing in the PS, there are a number of examples of occurrence of limitations of the supply of electricity to customers. In 2015, the total amount of electricity not supplied to customers of the PNPS amounted to approx. 95 000 MWh, which constituted approx. 0.06% of the energy consumption in Poland [13]. Such situations are the result of many events, such as e.g.:

a) technical failures in generation, transmission or distribution subsectors [9],
b) extreme weather conditions that cause significant limitations of the operation of key components of the power system or generate extreme increases in the power demand,
c) improperly prepared or too slowly implemented power system development plans leading to the periodic lack of capacity to meet the power demand [3].

In case of possible difficulties with power balancing in the PS, in order to maintain expected supplies to the customers, operators of the PS should undertake all possible activities, such as e.g.: emergency import of electricity from other PSs, overloading of operating generating units, commissioning of emergency units, reduction of voltage in the power supply grid of

a certain group of customers, suspension of works conducted in these parts of the PS which lead to the limitation of the available capacity.

If all possible preventive measures turn out to be insufficient, the TSO is obliged to use other measures, including to implement the limitation of the supply and consumption of electricity, in order to ensure safe and stable operation of the PS. Such limitations are introduced according to the plan previously prepared for this purpose, starting from scheduled limitations and ending, if needed, with emergency limitations.

The heat wave which took place in August 2015, when the air temperature in the afternoon exceeded 35ºC in the entire country, caused a drastic deterioration of power balancing conditions in the PNPS. The average temperature in the country as much higher compared to the previous year, indicated temperature differences reached even 10ºC. These temperatures significantly differed from average long-term temperatures. A strong correlation between the increase in the air temperature and the maximum power demand in the PNPS resulting from the use of cooling equipment on a large scale has been observed for years. As a result, the power demand in the PNPS on 7 August reached its historical maximum level for the summer period amounting to 22 186 MW. High temperatures led to the gradual increase in power outages in centrally dispatched generating units (CDGUs). The reasons for such limitations varied. There were very high emergency outages which reached approx. 3 000 MW on 10 August. This situation was associated with very difficult conditions of operation and cooling of basic and auxiliary equipment forming part of generating units, especially those that have been operated for a very long time. The second group of outages occurring at generating units with open cooling water systems included hydrological limitations. They were caused by low water levels in rivers and exceeded limits of cooling water temperatures during discharges. The most difficult hydrological situation was recorded in the following rivers: Vistula, San and Narew. These outages reached the maximum value of 1 200 MW. High temperatures also led to limitations of the operation of specific systems, for example flue gas desulphurization installation. This resulted in the occurrence of so-called operational outages which reached about 800 MW in the described period. High temperatures resulted in the systematic decrease in the permissible load of 110 kV lines forming part of the distribution grid. This decrease led to limitations of power evacuated from power plants reaching even 1 000 MW. As a result, the total power outages in the analyzed period, caused by the above-mentioned limitations amounted to 4 900 MW.

At the same time, due to technical conditions arising out of unscheduled power flows through the PNPS (so-called loop flows), it was not possible to offer transmission capacities for the purposes of electricity import from neighboring market areas. In spite of using all operational preventive measures available at the planning stage by the Polish TSO, such as:

a) postponement of scheduled overhauls of several units,
b) use of emergency power supplies from neighboring power systems in the Czech Republic and Slovakia,
c) commissioning of available non-centrally dispatched generating units (nCDGUs),
d) reduction of power (DSR).

On 10 August 2015 the expected shortage of generating capacities necessary for balancing the demand of customers of the PNPS reached the value clearly indicating the occurrence of the state of threat to the security of the supply of electricity to customers.

In this situation, the Polish TSO, exercising its statutory rights, made the decision to impose limitations of the supply and consumption of electricity on 10 August from 10:00 am to 09:00 pm and announced applicable power supply levels on a statutory basis. The decision concerning the choice of the power supply level for specific periods was made on the basis of current forecasts of the balance of the PNPS and analyses of consequences of introducing further limitation levels. On their basis it was stated that for the actual conditions of the functioning of the PNPS it is possible to obtain the effect of power reduction for power supply levels above the 16th level; the maximum possible reduction of power consumption is 750 MW for the 17th level, up to 3 360 MW for the 20th level.

Statutory rights authorize the Polish TSO to impose limitations of the supply and consumption of electricity on this basis for the maximum period of 72 hours. Therefore, on 10 August 2015, acting on the basis of article 11c section 3 of the Energy Law Act, the Polish TSO notified the Minister of Economy and the President of the Energy Regulatory Office of the occurrence of threat to the security of the supply of electricity, the measures taken in order to remove this threat and prevent its negative effects. At the same time, the Polish TSO also informed the Minister of Economy that due to forecasted weather conditions, the introduction of limitations of the supply and consumption of electricity at the request of the Polish TSO for the period of 72 hours may be insufficient. Moreover, it informed the Minister that in order to maintain the proper functioning of the NPS, it would be necessary to introduce limitations on the basis of article 11 section 7 of the Energy Law Act, i.e. on the basis of the Regulation of the Council of Ministers. The Polish TSO indicated the 20th level as the maximum requested level of limitations in accordance with § 4 section 3 of the Regulation on the detailed rules and procedures for introducing limitations in the above-mentioned notification. The Polish TSO determined the maximum value of requested limitations of the supply and consumption of electricity at 7 651 MW, indicating at the same time the period from 10 August 2015 to 31 August 2015 as the duration of limitations of the supply and consumption of electricity. On 11 August 2015 the Council of Ministers adopted the Regulation on the introduction of limitations of the supply and consumption of electricity (Journal of Laws of year 2015, item 1136). Pursuant to this Regulation, the limitations of the supply and consumption of electricity were introduced from 11 August 2015 from 00:00 am to 31 August 2015 to 00:00 am on the territory of the Republic of Poland for customers with contracted capacity above 300 kW.

Expected and covered power demand in the PNPS on critical days from 10 to 13 August in the context of introduced power supply levels is presented in Fig. 4 [12].

Power consumption was reduced not only by customers obligated by law, but also by customers not covered by the limitation plan. This was the result of their voluntary response to the TSO's call for the reduction of power consumption by means of mass media. As a result, it changed the daily national power demand in the following way:

a) the effect of the demand reduction started earlier and also lasted after lifting a given power supply level,

b) the full potential of limitations arising out of the 20th power supply level was not revealed on 10 August 2015. As expected, on the first day of limitations a part of customers did not manage to adapt to new conditions (the effect of the power reduction was bigger on 11 August of 2015 when the 19th power supply level was announced),
c) the effect of limitations was also visible on 13 August 2015 despite the fact that the 11th power supply level was announced in which customers may consume electricity up to the level of contracted capacity, which in practice means no limitations.

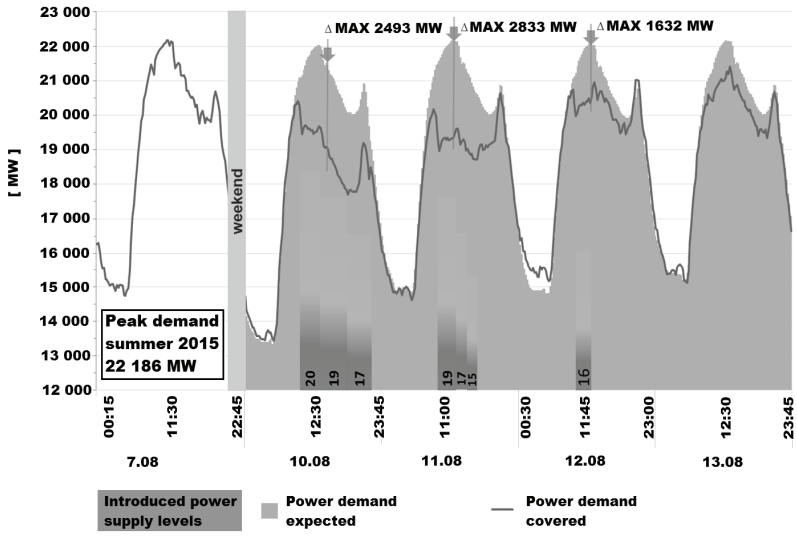

Fig. 4. Expected and covered power demand in the PNPS from 10 to 13 August 2015

The next stabilization of conditions of power balancing in the PNPS was caused by the significant reduction of emergency outages of power generators and hydrological outages in connection with implemented extraordinary measures related to weirs in rivers. It made it possible to prevent the implementation of power supply levels (above the 11th level) on the next days of the month for which the Polish TSO obtained relevant authorizations from the Council of Ministers. The amount of electricity not supplied due to the limitations imposed in the described period was calculated. The difference between the forecasted power demand assumed in daily plans and the actual demand stood at about 55 000 MWh [13], which amounted to 60% of the total electricity not supplied to customers in 2015. On this basis, the total cost of electricity not supplied due to the implementation of planned limitations and other reasons, for example those connected with failures of distribution grids, can be evaluated. For this purposes, the level of unit costs of not supplied electricity should be assumed appropriately to the reason.

Taking the type of measure taken to reduce the power consumption and high uncertainty of possible effects into consideration, implemented power supply levels should be deemed to be properly chosen. It was confirmed by the opinion prepared by the President of the Energy

Regulatory Office on the basis of the report of the Polish TSO. The decisions taken and their efficient implementation at the level of operational activities allowed for safe and stable operation of the PNPS. It was possible to avoid the introduction of emergency limitations, the economic and social consequences of which would be much more serious or, in fact, disastrous.

4. Possibilities of meeting peak power demand of customers

As described above, each power system may experience periodic problems with ensuring safe margin of power balance, which in extreme cases may lead to the implementation of mechanisms of limitations of the supply and consumption of electricity. The probability of the occurrence of such undesirable situations is much higher in the periods of peak loads of the PS which are relatively short. Statistical data collected for the last few years of the operation of the PNPS show that the demand for the last 500 MW of the peak power only lasted about 20 hours and, accordingly, for the last 1 000 MW about 100 hours per year. Such data indicate the assumptions that should be taken into account in the economic analysis presenting different possibilities of covering power demand in the system, including the justification of the feasibility of building peak-load sources. Due to the fact that peak demand lasts for short periods of time, the search for alternative solutions to the construction of generating units designed for peak operation is fully justified. The development of the model allowing for the determination of unit costs of system services for power demand balancing of the system for various variants of possible solutions is very useful for this purpose. It is possible to compare them and identify the optimum solution on the basis of this model.

Available collected data concerning solutions used in the PNPS on the basis of which the comparative analyses were carried out are presented below. Possible solutions were chosen in such a way that they could be used as a model for similar analyses for other power systems. For this purpose, the calculations for the system services available in the PNPS (items 1-5) and potential services in the scope of emergency operation provided by generating sources designed for peak operation (item 6) were made. The following system services were included:

1. overload operation of centrally dispatched generating units (UPP),
2. availability of non-centrally dispatched generating units (GWS),
3. import of electricity by the operator from Sweden (OIs) and synchronous intercomnections (OIps),
4. system service of cold intervention reserve – the result of two public tenders (IRZ1, IRZ2),
5. power consumption reduction at the request of the Polish TSO (DSR – Demand Side Response),
6. intervention operation provided by used (ZISuo, ZISug) and new (ZISno, ZISng) oil- or gas-fired generating sources designed for peak operation.

The following assumptions were taken into account in the above comparative analysis:

a) unit cost were determined on the basis of data published in public tenders or assumed as values estimated on the basis of other source data,

b) determined costs of power balancing services include all costs of the provision of services, i.e. fixed and variable costs [4],
c) all calculated costs were presented in current prices in 2015,
d) analyzed fuel (coal, oil, gas) prices are based on market data applicable in 2015 so significant differences, especially in the area of the calculation of unit variable costs of compared variants should be taken into account,
e) in the case of a new unit, capital expenditures per unit in the amount of 600 000 EUR/MW were assumed for the analysis of costs of peak-load intervention sources. The weighted average cost of the capital was assumed in the amount of 10% and annual operating costs in the amount of 2% of capital expenditures in the entire 30-year period of operation. Data for used generating units were assumed on the basis of the analysis of a rich market offer. The use of open circuits without the use of waste heat was assumed for the calculation of variable costs per unit. Moreover, the use of oil and LPG was assumed, thus maintaining the independence from the operation of gas transmission and distribution grids,
f) electricity is supplied to the PNPS as part of the services acquired by the Polish TSO, referred to in points 1-5, which is then sold on the Balancing Market (BM). The revenue from the sale of electricity is deducted from the purchase cost of these services (the rounded average selling price of electricity on the BM from year 2014, i.e. 160 PLN/MWh was assumed),
g) unit costs of overload operation were calculated on the basis of published data concerning prices on the energy market and increased by the cost increase rate associated with the decrease in the efficiency of the generating unit caused by the mode of operation,
h) unit purchase costs of GWS services were estimated on the basis of variable costs of these sources, taking their structure in the national market into account,
i) unit costs of import of electricity by the operator were established on the basis of the average taken from several years according to the emergency energy exchange mechanism. According to this mechanism, these costs are established on the basis of available electricity prices applicable in markets in which TSOs purchase electricity for the purposes of their neighboring operators (for example spot prices on the Nordpool stock exchange),
j) the same time of using system services, 200 hours per year, was assumed in the calculation of unit costs presented in Table 1. In the case of the reduction of power demand at the request of the Polish TSO (DSR), 60 hours were assumed according to the terms and conditions of concluded agreements, which corresponds to the limitations resulting from technological and organizational conditions of service providers.

Unit costs of system services for power balancing calculated in this way (*jkubm*) are presented in Table 1. They were prepared in two variants: the gross variant including all incurred costs ($jkubm_b$) and the so-called net variant ($jkubm_n$), i.e. the variant in which revenues from the sale of electricity supplied as part of the service provided in the BM are deducted from the costs of system services and avoided costs of purchase of operating capacity reserve were included in the cold intervention reserve service.

Table 1. Unit costs of system services for power balancing of the PNPS in 2015

No.	Type of service	Unit cost of power balancing services		Unit cost of power balancing services	
		fixed [PLN/MWh]	variable [PLN/MWh]	gross [PLN/MWh]	net [PLN/MWh]
1	Overload operation service (UPP)	–	200	200	40
2	Reliability Must Run (GWS)	–	300	300	140
3	Electricity import from Sweden by the operator (OIs)	–	250	250	90
4	Electricity import using synchronous connections (OIps)	–	520	520	360
5	Cold intervention reserve (IRZ1)	770	300	1 070	480
6	Cold intervention reserve (IRZ2)	880	300	1 180	590
7	Reduction of power demand at the request of the Polish TSO (DSR)	–	1 160	1 160	1 160
8	Used oil-fired peak-load intervention source (ZISuo)	1 570	650	2 220	2 060
9	Used gas-fired peak-load intervention source (ZISug)	1 570	940	2 510	2 350
10	New oil-fired peak-load intervention source (ZISno)	2 060	650	2 710	2 550
11	New gas-fired peak-load intervention source (ZISng)	2 060	940	3 000	2 840
12	Unit cost of electricity not supplied due to scheduled limitations ($jknee_{pp}$) – unscheduled limitations ($jknee_{np}$)			7 500-13 500	

Taking the actual conditions of the functioning of the power system into account, the actual time of using specific system services for power balancing in each year is different. For this reason, in the case of optimisation analyses it is useful to prepare the graph presenting the relationship between net unit costs of system services for power balancing of the PS and the time of using such services. The relevant graph for the PNPS and data from Table 1 is presented in Fig. 5.

In spite of unified assumptions, presented unit costs are not fully comparable due to the technical characteristics of specific services. In the case of conventional sources providing the cold intervention reserve service and being peak-load intervention sources (the same also applies to pumped-storage hydro power plants), it is necessary to incur fixed costs of their operation and the actual total unit cost, indeed, depends on the actual time of using such sources.

In the case of services such as: overload operation, use of GWS services, reduction of power demand at the request of the Polish TSO or electricity import by the operator, according to the adopted model of settlement with service providers, fixed costs do not have to be settled with service providers. As a result, the total unit cost does not depend on the actual time of using these services. For reasons given above, it is worth using the unit capacity cost indicator expressed in PLN/MW/year in the process of comparison of costs of various options of obtaining power for the purposes of balancing the PS. To ensure the comparability of various possible solutions, the indicator determined in such a way was calculated on the basis of the

assumption that each of the analysed services will be provided with the same available capacity. Obtained results are presented in Table 2.

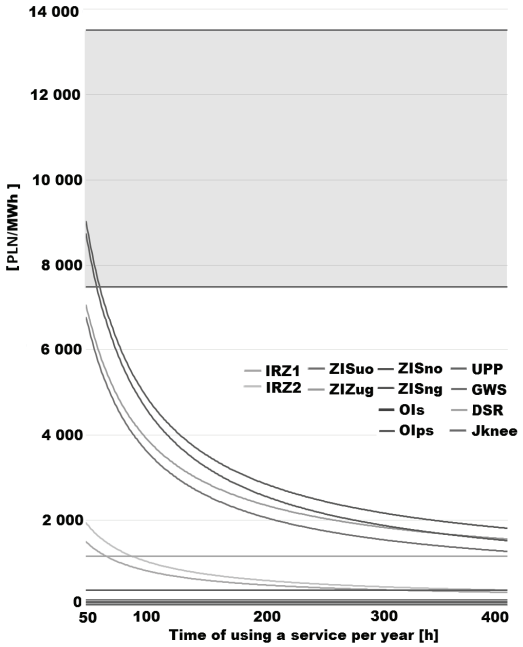

Fig. 5. Relationship between the net unit costs of power balancing services in the PNPS ($jkubm_n$) and the time of using services in the year

Table 2. Unit capacity costs of system services for power balancing of the PNPS in 2015

No.	Type of service	Power to be used by the Polish TSO	Unit capacity cost
		[MW]	[‘000 PLN/MW/year]
1	Cold intervention reserve (IRZ1)	200	154
2	Cold intervention reserve (IRZ2)		176
3	Reduction of power demand at the request of the Polish TSO (DSR)		5.3
4	Used oil-fired peak-load intervention source (ZISuo)		314
5	Used gas-fired peak-load intervention source (ZISug)		314
6	New oil-fired peak-load intervention source (ZISno)		412
7	New gas-fired peak-load intervention source (ZISng)		412

Services provided by sources of cold intervention reserve and the reduction of power demand at the request of the Polish TSO were included in the group of services presented in Table 2 due to the periodic tests of this service generating fixed costs of its provision. The last four items constitute various variants of peak-load intervention sources. It is assumed that these sources would be built for the purposes of the provision of system services for the Polish TSO and not on the basis of their functioning in the electricity market.

The service of intervention operation provided by pumped-storage sources which has not been published in relation to the costs of its provision is also included in the group of services contracted by the Polish TSO. It was assumed that the revenues from the sale of generated electricity in the BM balance variable costs of purchase of electricity in the BM for the purposes of pumping water and costs of the variable component of the distribution fee. However, the nature of this service does not differ much from cold intervention reserve services and does not change the general conclusion regarding the evaluation of the grounds for the purchase of system services for power balancing during peak loads.

Another possible comparison consists in the breakdown of annual costs of purchase of system services for the purposes of power balancing, which however requires making certain assumptions concerning the time of using such services in the analysed period of cost balancing. Costs determined in such a way are reduced by revenues from the sale of generated electricity in the balancing market and in the case of the cold intervention reserve (IRZ) by the avoided costs of purchase of operating capacity reserve services. The breakdown of annual costs is helpful in the calculation of costs of the licensed activity carried out by the TSO, and the choice and purchase of the appropriate service should be the basis for its optimization.

It should also be emphasised that both volumes of available capacity within specific services and the possible time of using such services by the Polish TSO differ much and are not comparable to services the provision of which does not generate fixed costs. For example, capacity available within the overload operation service depending on a given generating unit can be available only for several hours. Also, the volume of available import of electricity by the operator depends on the grid and balancing situation of other TSOs and the duration and frequency of possible reductions are different in case of different providers of this service. Therefore, all these factors should be appropriately taken into account and evaluated in the final comparison and choice of services ensuring the coverage of peak demand for power and electricity.

5. Summary

1. One of the basic tasks of transmission system operators is to ensure the security of operation of power systems managed by them, including power balancing. The analysis of power demand in power systems shows that it is different at different hours of the day as well as on different days of specific months of each year. This variability depends on a number of factors, including conditions of the functioning of customers in the economy of a given country, conditions resulting from the time of the year, week or day – night, intermediate load zones, peak loads.
2. The task of power balancing is particularly difficult in periods of peak loads when the risk on non-supplying electricity to customers is relatively higher than in other periods. The control of the sufficiency of generation resources to cover the demand for power is ensured, for example, by power balances prepared by TSOs for different time horizons.
3. A lot of examples of occurrence of limitations of the supply of electricity to customers were recorded all over the world in the operational practice related to the balancing of power in the PS. The analysis of financial consequences of selected cases of limitations of the

supply and consumption of electricity for customers connected to the PNPS shows that the unit costs of not supplied electricity amounted to 7 500-13 500 PLN/MWh. The amount of these costs in future events will depend on a number of factors such as the nature of limitations – scheduled or emergency limitations, their duration or frequency, ability to foresee them and ability to report possible limitations well in advance, ability to undertake developed preventive measures.

4. The analysis of both direct and indirect financial consequences of limitations of the supply and consumption of electricity for customers clearly shows that possible preventive measures taken well in advance have less serious, economic and social consequences. Appropriate preparation and implementation of measures minimizing the probability of the introduction of limitations is justified.
5. Covering peak power demand by means of generating units designed for peak operation is one of the mechanisms of balancing peak loads. They are characterized by low unit capital expenditures, high availability, short commissioning periods and high flexibility of operation. Fixed costs of such sources and forecasted costs of fuels used by them determine the choice of the optimum technology. However, they do not have a significant impact on the economic calculation determining their construction as an alternative solutions to possible limitations imposed on customers. However, taking into account the fact that peak demand does not last long, the search for alternative solutions to the construction of generating units designed for peak operation is necessary and well-grounded in spite of using cheaper used sources available in the market. It is determined by both technical and economic aspects. For this purpose, it is very helpful to develop the model allowing for the determination of unit costs of system services for power balancing for different variants of possible solutions so that it could be possible to compare them and choose the optimum solution on the basis of this model.
6. The analysis of unit costs of system services for power balancing in the PS from the time of using them shows that the following alternative solutions are more favorable than the construction of generating units designed for peak operation:
   a) possibility of overloading generating units designed for basic and intermediate peak operation, functioning in the market,
   b) use of the possibility of providing system services for power balancing by distributed generation units by TSOs,
   c) system services provided by pumped-storage power plants functioning in the market,
   d) intervention import of electricity from other power systems on the basis of separate interconnection agreements,
   e) temporary use of the intervention operation of old generating units intended for liquidation,
   f) use of the possibilities offered by diversified mechanisms of demand side response (DSR) [6, 8, 10],
   g) use of the electricity storage installations [5, 7].

References

[1] www.entsoe.eu, *Continental Europe Operation Handbook*, ENTSO-E, accessed April 2016.
[2] *Instruction of Transmission System Operation and Maintenance*, Polskie Sieci Elektroenergetyczne S.A. Warszawa (2015).
[3] Jajuga K., Majchrzak H., Weron A., *Integrated risk management of energy producer on the energy market*, Proceedings of 10th scientific-technical conference Rynek Energii Elektrycznej, Kazimierz Dolny (2003).
[4] Majchrzak H., *Power and heat generation on the EU market. Selected issues,* (in Polish), Polska Akademia Nauk – Oddział w Katowicach, Komisja Metrologii, Wydawnictwo Federacji Stowarzyszeń Naukowo-Technicznych, Energetyka i Środowisko, Warszawa (2006).
[5] Majchrzak H., Tomasik G., Kwiatkowski M., *Application of energy storage technology for integration of wind farms with an electric power system*, (in Polish), Energetyka, vol. 10, no. 700, pp. 579-588 (2012).
[6] Majchrzak H., *New tariffs as a way of energy efficiency improvement*, (in Polish), Czysta Energia (2013).
[7] Majchrzak H., *Polish – Japanese cooperation agreement in the area of smart grid development and energy storage*, (in Polish), Czysta Energia (2016).
[8] Malko J., *The Decalogue of the USA power industry development trends,* Energetyka, vol. 6, no. 720, pp. 329-333 (2014).
[9] Report prepared by the team responsible for the investigation of reasons and effects of the disaster in the power industry, appointed under the decision of the Governor of West Pomeranian Voivodeship no. 154/2008 of 22 April 2008, Szczecin, June 2008.
[10] www.entsoe.eu, *Market design for demand side response*, Policy paper. ENTSO-E 2015.
[11] www.pse.pl, *Annual report on the functioning of the PNPS for year 2014*, accessed April 2016.
[12] www.pse.pl, *Daily reports on the operation of the PNPS in year 2015*, accessed April 2016.
[13] www.pse.pl, *Annual report on the functioning of the PNPS for year 2015*, accessed April 2016.

ARCHIVES OF ELECTRICAL ENGINEERING

SPONSORS

Polish Academy of Sciences

Faculty of Electrical Engineering,
Poznan University of Technology

THE AEE JOURNAL IS ALSO CO-SPONSORED BY

Faculty of Electrical, Electronic,
Computer and Control Engineering,
Lodz University of Technology

Faculty of Electrical and Computer Engineering,
Rzeszow University of Technology

Faculty of Electrical and Computer Engineering,
Krakow University of Technology

Faculty of Electrical Engineering,
Automatic Control and Informatics,
Opole University of Technology

Institute of Electrical Drives and Machines
KOMEL

Faculty of Electrical Engineering,
Automatics, Computer Science
and Biomedical Engineering, AGH-UST